



PhD-FSTM-2026-005  
The Faculty of Science, Technology and Medicine

## DISSERTATION

Defence held on 23/01/2026 in Esch-sur-Alzette  
to obtain the degree of

DOCTEUR DE L'UNIVERSITÉ DU LUXEMBOURG

EN SCIENCES EXACTES ET NATURELLES

by

**BARNIK MANDAL**

Born on 12 October 1993 in Karimpur, West Bengal (India)

ADVANCED PROCESSING STRATEGIES FOR  
SOLUTION-BASED FERROELECTRIC  $\text{HfO}_2$  FILMS

### Dissertation defence committee

Dr. Phillip Dale, Chair,  
*Full Professor, University of Luxembourg*

Dr. Beatriz Noheda,  
*Full Professor, University of Groningen*

Dr. Mariona Coll,  
*Tenured Scientist, Institut de Ciència de Materials de Barcelona (ICMAB-CSIC)*

Dr. Uwe Schröder,  
*Senior Scientist, NaMLab gGmbH, Dresden*

### **Supervisor:**

Dr. Sebastjan Glinšek,  
*Head of R&T Group, Luxembourg Institute of Science and Technology*

## Affidavit / Statement of originality

*I declare that this thesis:*

- is the result of my own work. Any contribution from any other party, and any use of generative artificial intelligence technologies have been duly cited and acknowledged;
- is not substantially the same as any other that I have submitted, and;
- is not being concurrently submitted for a degree, diploma or other qualification at the University of Luxembourg or any other University or similar institution except as specified in the text.

*With my approval I furthermore confirm the following:*

- I have adhered to the rules set out in the University of Luxembourg's Code of Conduct and the Doctoral Education Agreement (DEA)<sup>1</sup>, in particular with regard to Research Integrity.
- I have documented all methods, data, and processes truthfully and fully.
- I have mentioned all the significant contributors to the work.
- I am aware that the work may be screened electronically for originality.

I acknowledge that if any issues are raised regarding good research practices based on the review of the thesis, the examination may be postponed pending the outcome of any investigation of such issues. If a degree was conferred, any such subsequently discovered issues may result in the cancellation of the degree.

---

**Approved on 2025-11-01**

<sup>1</sup> If applicable (DEA is compulsory since August 2020)

# Abstract

Ferroelectric hafnium oxide ( $\text{HfO}_2$ ) has emerged as a promising candidate for scalable, lead-free ferroelectric technologies due to its compatibility with complementary metal-oxide-semiconductor (CMOS) fabrication processes. Its ferroelectric behavior originates from the stabilization of a metastable orthorhombic  $Pca2_1$  phase. Although vacuum-based deposition techniques such as Atomic Layer Deposition (ALD) and Pulsed Laser Deposition (PLD) provide excellent control over stoichiometry and film thickness, they exhibit fundamental limitations in sustaining ferroelectricity in films thicker than  $\sim 40$  nm, where the non-polar monoclinic phase becomes energetically favored. Thick ferroelectric films are of particular interest in this PhD, as we aimed to assess the piezoelectric response of  $\text{HfO}_2$  for resonator applications.

Chemical Solution Deposition (CSD) offers a promising route to overcome these constraints by enabling ferroelectric films approaching  $1 \mu\text{m}$  in thickness. This is achieved through fine-grained microstructures, where small grain sizes help to kinetically stabilize the orthorhombic phase. Nonetheless, solution-processed  $\text{HfO}_2$  films still face challenges related to reproducibility and film density, which can in turn limit their dielectric strength.

This thesis systematically investigates solution-derived ferroelectric  $\text{HfO}_2$  films from processing to application. First, annealing atmosphere control and layer-by-layer deposition strategies were developed to enhance fabrication reproducibility and ferroelectric properties. Second, interface engineering using  $\text{HfO}_2$ - $\text{ZrO}_2$  multilayer heterostructures was explored to improve ferroelectric wake-up dynamics and break-down strength. Third, the integration of solution-processed thick  $\text{HfO}_2$  films into high-overtone bulk acoustic resonators was attempted to assess their piezoelectric potential for device applications. The findings establish a framework for solution-derived ferroelectric  $\text{HfO}_2$  and identify pathways for future device application.



# Acknowledgements

I would like to express my sincere gratitude to the Luxembourg National Research Fund (FNR) for supporting my Ph.D. studies through the TRICOLOR project (INTER/NWO/20/15079143/TRICOLOR). I am grateful to the University of Luxembourg for providing an environment that supported my personal and scientific growth. I also thank the Luxembourg Institute of Science and Technology for the infrastructure and support that made most of the experiments in this thesis possible.

Firstly, I would like to express my deepest gratitude to my supervisor and mentor, Dr. Sebastjan Glinsek, for his invaluable guidance and encouragement throughout this work. His trust in my potential and confidence in my ability to take on this project have meant a great deal to me. He consistently created space for me to find and strengthen my own scientific voice. What has mattered most is the genuine care he shows for the person behind the research. In a field where failure is frequent and progress often seems invisible, his empathy made an enormous difference. He taught me how to face problems without being overwhelmed by them, how to step back and see the broader perspective, and how to remain critical while still holding on to a sense of possibility. These lessons will stay with me long after this thesis.

My heartfelt thanks also go to our unit leader, Dr. Emmanuel Defay, for cultivating an environment that encouraged growth in every direction, not only as researchers but as individuals with aspirations beyond science. His support for my entrepreneurial interests, together with that of Sebastjan, is something I will always value. Being part of his group has been a genuine privilege, shaped by scientific freedom, trust, and unwavering intellectual support.

I sincerely appreciate the members of my thesis supervisory committee. Prof. Dr. Jorge Gonzalez Iniguez consistently reminded me of the importance of curiosity in research. Prof.

Dr. Phillip Dale offered key scientific insights, including the suggestion to explore phase identification of hafnia through Raman spectroscopy, an approach that has produced encouraging results and may lead to further publication. Prof. Dr. Beatriz Noheda encouraged me from the very beginning to question assumptions and approach the literature with independence, helping me build confidence as a young scientist. Her warm and supportive presence has meant more to me than I can fully express in formal words. I thank all of them for their thoughtful feedback and guidance throughout these four years.

I am grateful to the external jury members, Dr. Mariona Coll and Dr. Uwe Schroeder, for agreeing to evaluate my dissertation.

I would also like to express my gratitude to Dr. Torsten Granzow, whose depth of knowledge often felt nothing short of magical. No matter how basic my questions were, he always answered them with patience, clarity, and enthusiasm. His careful reviews of my papers and thesis, and his genuine commitment to improving my work, have been invaluable.

I would also like to thank Dr. Stephanie Girod, whose guidance played an important role in shaping my understanding of lithography and the way I work in the clean room. Her lessons on good laboratory practices have become habits I will carry with me throughout my career. I am equally grateful for our many conversations, not only about science but also about life beyond the lab.

I am deeply grateful to Kevin Mengueli, who devoted countless hours to tuning the rapid thermal chemical vapor deposition process for my samples, making possible the reproducible film growth that became central to this thesis. His help in refining the surface of hafnia and in preparing samples for second harmonic generation measurements was truly helpful. My sincere thanks also go to Nathalie Vallé, Adrian Marie Philippe, and Brahime El Adib for their expertise and support with transmission electron microscopy and secondary ion mass spectrometry, and to Patrick Grysan for introducing me to atomic force microscopy. I would also like to thank Yves Fleming for his assistance with x-ray diffraction techniques and Nouredine Adjeroud for his atomic layer deposited hafnia samples.

I would also like to thank all the collaborators from the University of Luxembourg, the University of Groningen, the Jožef Stefan Institute, and the Luxembourg Institute of Science and Technology whose support has shaped this PhD in many ways.

This thesis would not have been possible without the support of all members of the former Ferroic Materials for Transducers group (now, FMEH + CPTM + MFM), as well as my colleagues at LIST. My gratitude goes to Mauro and Angelina, the two other members of chaotic neutral trio. Corsica brought us together, and from that moment on we somehow navigated the long days of the PhD, our late evening group therapy sessions, and every high and low that came with this journey. I would like to thank Veronika and Natalya for the countless evenings at Nonna Nenetta and for the long conversations over cocktails that kept me grounded. Our trip to Rome remains one of the highlights of these past four years, and it means a great deal to me that they made me an uncle to little Kathleen and Evelyn. I thank Hugo for the moments when a change of pace was all I needed. Cooking together and learning guitar from him brought lightness into stressful times. My appreciation also goes to Youri, my biriyani partner. I will never get tired of our food discussions or our unabashedly inappropriate meme exchanges on Instagram. And I thank Uros for getting me into running, a habit I truly cherish now. Because of him, I ended up completing a half marathon, something I am genuinely proud of.

I would also like to express my gratitude to Georgy, Binayak, Christina, Longfei, Alfredo, Naveen, Sangita, Monica, Ashwath, Samuele, Paola, and all the new colleagues turned friends, as well as many others who have accompanied me along the way. Each of them has added something memorable to this chapter of my life, and I am truly thankful for it.

I would also like to thank Dr. Subhro Ghosal, whose teaching of solid state physics during my bachelor studies first sparked my desire to pursue research in physics and eventually a PhD. My gratitude also goes to Dr. Shila Ghosh, who encouraged me to lead the SPIE student chapter and made it possible for me to attend my first scientific conference in Europe, an experience that strongly motivated me to go for higher education.

Most importantly, none of this would have been possible without the dream and determination of my parents. This doctorate is not only my achievement but the fulfilment of a hope they carried long before I even understood what a PhD meant. From our small town in the Indian countryside, they pushed for my education even when it stretched far beyond what we could comfortably afford. For them, my studies were always the priority, and it is their aspiration that has brought me to the point of earning a doctorate from an European university. This accomplishment is as much theirs as it is mine.



# Declaration on the use of generative AI tools

Generative AI tools (ChatGPT, Claude, NotebookLM) were used during the preparation of this thesis for the following purposes:

- **Coding assistance:** Python scripts for data visualization (e.g., matplotlib plots) were generated with AI assistance and manually adapted by the author.
- **Editing and proofreading:** Selected passages were refined for grammar and clarity with AI support.

All scientific content, data analysis, interpretation of results, and conclusions are the original work of the author. AI-generated outputs were reviewed and modified by the author in all cases.

The use of generative AI tools in this thesis complies with the *Guidelines on the Use of Generative AI Tools for Learning and Teaching* issued by the University of Luxembourg (2025).



# Contents

<b>List of Figures</b>	<b>18</b>
<b>List of Tables</b>	<b>20</b>
<b>1 Introduction</b>	<b>21</b>
<b>2 Fundamentals</b>	<b>25</b>
2.1 Theory of polar oxides . . . . .	25
2.1.1 Piezoelectricity . . . . .	26
2.1.2 Ferroelectricity . . . . .	27
2.2 Hafnium oxide and its properties . . . . .	30
2.2.1 Ferroelectricity in HfO <sub>2</sub> thin films . . . . .	32
2.2.2 Defects and their role in ferroelectric HfO <sub>2</sub> . . . . .	35
2.2.3 Wake-up effect in ferroelectric HfO <sub>2</sub> capacitors . . . . .	37
2.2.4 Piezoelectricity in HfO <sub>2</sub> thin films . . . . .	39
2.2.5 Applications . . . . .	41
2.3 Growth techniques . . . . .	42
2.3.1 Atomic layer deposition . . . . .	43
2.3.2 Sputter deposition . . . . .	44
2.3.3 Pulsed laser deposition . . . . .	44
2.3.4 Chemical solution deposition . . . . .	45
2.4 Theory and principles of CSD . . . . .	47
2.4.1 Classical sol–gel systems . . . . .	48
2.4.2 Metal–organic decomposition . . . . .	49
2.4.3 Crystallization mechanisms in CSD . . . . .	50

2.4.4	Stability of oxides during annealing . . . . .	52
<b>3</b>	<b>Fabrication methodologies</b>	<b>55</b>
3.1	Solution preparation . . . . .	55
3.1.1	La:HfO <sub>2</sub> and ZrO <sub>2</sub> solutions . . . . .	55
3.1.2	CeO <sub>2</sub> solution . . . . .	56
3.2	Spin-coating and pyrolysis . . . . .	56
3.3	Rapid thermal annealing process . . . . .	57
3.3.1	System and chamber preparation for crystallization . . . . .	57
3.3.2	Process gas introduction and flow control . . . . .	58
3.3.3	Rapid thermal processing and crystallization . . . . .	59
3.4	Thin film fabrication steps . . . . .	59
3.5	Electrode patterning and deposition . . . . .	60
3.5.1	Electrode preparation for Raman spectroscopy . . . . .	62
<b>4</b>	<b>Study of annealing atmosphere</b>	<b>65</b>
4.1	Motivation . . . . .	65
4.2	Atmosphere conditions for annealing . . . . .	68
4.2.1	Ar atmosphere . . . . .	69
4.2.2	Ar:O <sub>2</sub> atmosphere . . . . .	73
4.2.3	N <sub>2</sub> :O <sub>2</sub> atmosphere . . . . .	74
4.3	Effect of annealing atmosphere on film density and composition . . . . .	77
4.4	Wake-up investigation using Raman spectroscopy . . . . .	80
4.4.1	Spectral response to electrical cycling . . . . .	82
4.5	Summary and outlook . . . . .	84
<b>5</b>	<b>Influence of growth routes on crystallization and orientation</b>	<b>87</b>
5.1	Motivation . . . . .	87
5.2	Film density and organic residuals . . . . .	90
5.3	Crystallographic orientation . . . . .	91
5.4	Enhanced ferroelectricity in L/L films . . . . .	95
5.5	Summary and outlook . . . . .	96

<b>6</b>	<b>Multilayer films</b>	<b>99</b>
6.1	Motivation . . . . .	99
6.2	HfO <sub>2</sub> -ZrO <sub>2</sub> multilayers . . . . .	102
6.2.1	HZO <sub>C50</sub> . . . . .	102
6.2.2	ZHO <sub>C50</sub> . . . . .	107
6.2.3	HZO <sub>C90</sub> . . . . .	107
6.3	HfO <sub>2</sub> -CeO <sub>2</sub> bilayer . . . . .	109
6.4	Effect of interfaces on wakeup . . . . .	111
6.5	Summary and outlook . . . . .	114
<b>7</b>	<b>HfO<sub>2</sub> based resonator</b>	<b>117</b>
7.1	Motivation . . . . .	117
7.2	HBAR theory . . . . .	119
7.2.1	Fundamental architecture and theoretical foundation . . . . .	119
7.2.2	Electromechanical coupling . . . . .	121
7.2.3	Quality factor considerations . . . . .	121
7.2.4	Impedance matching and power transfer . . . . .	122
7.3	HfO <sub>2</sub> HBAR Design . . . . .	122
7.3.1	Target frequency calculation . . . . .	122
7.3.2	Coplanar waveguide probing and impedance matching . . . . .	124
7.3.3	Electric field distribution and voltage breakdown considerations . . . . .	126
7.4	Resonance measurements on HfO <sub>2</sub> thin films . . . . .	127
7.5	Summary and Outlook . . . . .	129
<b>8</b>	<b>Conclusions and perspectives</b>	<b>131</b>
	<b>Publications, Conferences and Activities</b>	<b>137</b>
	<b>Contributions to this thesis</b>	<b>141</b>
<b>A</b>	<b>Characterization techniques</b>	<b>143</b>
A.1	Physical and Structural Characterization . . . . .	143
A.1.1	X-ray diffraction . . . . .	143

A.1.2	X-ray reflectivity . . . . .	144
A.1.3	RAMAN spectroscopy . . . . .	145
A.1.4	Atomic force microscopy . . . . .	145
A.1.5	Scanning electron microscopy . . . . .	146
A.1.6	Transmission Electron Microscopy . . . . .	146
A.1.7	Dynamic Secondary Ion Mass Spectrometry . . . . .	147
A.2	Electrical characterization . . . . .	148
A.2.1	Polarization measurement . . . . .	148
A.2.2	Fatigue measurement . . . . .	149
A.2.3	Breakdown and leakage measurement . . . . .	150
A.2.4	Double beam laser interferometry . . . . .	151
A.2.5	Resonance measurement using Vector Network Analyzer (VNA) . . . . .	151
<b>B</b>	<b>Reproducibility data for La:HfO<sub>2</sub> films</b>	<b>153</b>
	<b>References</b>	<b>155</b>

# List of Figures

2.1	Schematic representation of (a) the direct piezoelectric effect, where applied mechanical stress changes a polarization, $P$ and induces surface charges, and (b) the converse piezoelectric effect, where an applied electric field alters the polarization and produces a mechanical strain. . . . .	27
2.2	(a) Landau free energy as a function of polarization for a ferroelectric material, showing the two stable states at $\pm P_r$ . (b) Corresponding polarization–electric field hysteresis loop, highlighting $P_r$ , $P_s$ , and $E_c$ . . . . .	29
2.3	On the left is the fluorite crystal structure, with hafnium atoms forming a face-centered cubic lattice and oxygen atoms occupying the tetrahedral interstices. On the right are five well-established polymorphs of hafnia, monoclinic (m), orthorhombic-I(o-I), orthorhombic-III (o-III), tetragonal (t), and cubic (c), shown with their respective space groups. For clarity, the polymorphs are shown as 2D projections emphasizing the oxygen sublattice distortions; the Hf positions remain nearly unchanged between phases, and the yellow oxygen atoms highlight the polar displacements characteristic of the ferroelectric o-III phase. The figure is adapted from chapter 6 of [28], based on work by A. Kersch. . . . .	31
2.4	Pressure-temperature phase diagrams of $\text{HfO}_2$ . Panel (A) data taken from [32] and (B) reconstructed from [33]. . . . .	32
2.5	(a) Dopant concentrations corresponding to the maximum remanent polarization ( $P_r$ ), and (b) the width of the concentration window in which ferroelectricity is stabilized in 10 nm-thick $\text{HfO}_2$ films for dopants of different ionic radii. Data include films deposited by ALD, PVD, and CSD techniques, compiled from various studies.[43, 45–49] (c) Unit cell aspect ratio $2c/(a + b)$ as a function of dopant concentration in $\text{HfO}_2$ -based thin films with different dopants. Figure adapted from chapter 3 of [28]. . . . .	34

2.6	Orthorhombic phase fraction as a function of pristine remanent polarization ( $P_r$ ) for atomic layer deposited Si-, Al-, and Gd-doped $\text{HfO}_2$ . Data points correspond to different annealing conditions: 650°C for 10 min, 800°C for 20 s, and 1000°C for 1 s. Dashed lines indicate linear least-square fits for each dopant, with the corresponding slopes displayed in the graph. Figure adapted from [50]. . . . .	35
2.7	a) Switching current versus applied electric field and b) polarization versus applied electric field in the pristine state and in the woken-up state after $10^5$ cycles. Reproduced from [69].	37
2.8	Model of the different stages of the ferroelectric capacitor lifetime a) pristine, b) wake-up. Reproduced from [51]. . . . .	38
2.9	Conventional fabrication procedure includes (1) deposition of bottom electrode, (2) growth of ferroelectric layer (using ALD, sputter deposition, PLD, or CSD), (3) top electrode deposition, (4) crystallization, (5) electrode patterning using photolithography or hard mask, and (6) etching excess electrodes. . . . .	42
2.10	CSD process flow. Reproduced from [111] . . . . .	48
2.11	Free energy–temperature diagram illustrating the metastable nature of CSD-derived amorphous films compared to the equilibrium liquid and crystalline phases. The driving force for crystallization is given by $\Delta G_v$ . Reproduced from [111] . . . . .	50
2.12	Ellingham diagram for $\text{HfO}_2$ showing the standard Gibbs free energy of formation as a function of temperature. The right axis indicates the equilibrium oxygen partial pressure ( $\log p_{\text{O}_2}$ ) [114]. . . . .	53
3.1	CSD growth routes. (a) Conventional, and (b) layer-by-layer route. . . . .	56
3.2	Schematic of the thin films studied in this thesis. (a) $\text{HO}_{C45}$ , (b) $\text{HO}_{C90}$ , (c) $\text{HO}_{C200}$ , (d) $\text{HO}_{L50}$ , (e) $\text{ZO}_{C45}$ , (f) $\text{HZO}_{C50}$ , (g) $\text{HZO}_{C90}$ , (h) $\text{ZHO}_{C50}$ , and (i) $\text{HCO}_{L30}$ . . . . .	61
3.3	(a) Schematic of the metal-insulator-metal stack with a Au(100 nm)/Cr(5 nm) top electrode (100 $\mu\text{m}$ diameter) for electric field treatment. (b) Lithographic mask design used to open the top electrode. (c) Stack after chemical etching of the Au/Cr layers. (d) Optical image showing measurement points for Raman spectra after top electrode removal post-poling. Raman measurements were performed within the bare circular $\text{HfO}_2$ area inside the Au/Cr ring. . . . .	62

4.1	(a) GIXRD patterns and (b, c) ferroelectric hysteresis loops of films annealed in a pure Ar atmosphere at a constant flow rate of 125 sccm, with annealing durations of 45 s, 75 s, and 90 s. For plots (b) and (c), the results are extracted after subjecting the samples to 10 000 rectangular wake-up cycles at 3 kHz. . . . .	70
4.2	(a) GIXRD patterns and (b, c) hysteresis loops of films annealed in pure Ar atmosphere for 90 s with Ar flow rates of 50 sccm, 125 sccm, 200 sccm and 250 sccm. For plots (b) and (c), the results are extracted after subjecting the samples to 10 000 rectangular wake-up cycles at 3 kHz. . . . .	72
4.3	(a) GIXRD patterns and (b, c) hysteresis loops of films annealed in an Ar:O <sub>2</sub> atmosphere with total gas flow fixed at 300 sccm and varying Ar:O <sub>2</sub> ratios of 1:1, 1:2, and 2:1. For plots (b) and (c), the results are extracted after subjecting the samples to 10 000 rectangular wake-up cycles at 3 kHz. . . . .	74
4.4	(a) GIXRD patterns and (b, c) hysteresis loops of films annealed in an N <sub>2</sub> :O <sub>2</sub> atmosphere with total gas flow fixed at 300 sccm and varying N <sub>2</sub> :O <sub>2</sub> ratios of 1:0, 1:1, 1:2, and 2:1. For plots (b) and (c), the results are extracted after subjecting the samples to 10 000 rectangular wake-up cycles at 3 kHz. . . . .	75
4.5	Reproducibility of ferroelectric properties for La:HfO <sub>2</sub> thin films annealed under N <sub>2</sub> :O <sub>2</sub> 1:1 atmosphere. Average coercive field ( $E_c$ ) is plotted against average remanent polarization ( $P_r$ ) for samples of three different thicknesses (HO <sub>C45</sub> , HO <sub>C90</sub> , HO <sub>C200</sub> ). Marker size scales with $n$ , the number of capacitors measured per sample. The shaded area presents tight clustering within each thickness group confirms reproducible ferroelectric behavior. Detailed values are provided in Table B.1. . . . .	76
4.6	X-ray reflectivity patterns of HO <sub>C45</sub> thin films annealed in different atmospheres. Orange line represents Ar annealing (density: 7.5 g/cm <sup>3</sup> ), green line represents Ar:O <sub>2</sub> annealing (density: 8.0 g/cm <sup>3</sup> ), blue line represents N <sub>2</sub> :O <sub>2</sub> annealing (density: 8.0 g/cm <sup>3</sup> ), and gray line shows the theoretical value (density: 9.6 g/cm <sup>3</sup> ).[108] The dashed line intercepts at the density edge are the half maxima of the XRR intensity. . . . .	78
4.7	Secondary ion mass spectrometry depth profiles of (a) Hf, (b) La, (c) O, and (d) C in 45 nm thick HO <sub>C45</sub> thin films annealed in different atmospheres. The vertical dashed lines approximately indicate the interfaces with the top Pt/Ti electrode (left) and the Pt bottom electrode (right). The arrow indicates the direction of film growth (Z-direction). . . . .	79

4.8	The measured Raman spectra of as-deposited HO <sub>C200</sub> thin films, accompanied by the corresponding polarization vs electric field loop. The Raman peak assignments are referenced from Mimura <i>et al.</i> [124]. . . . .	83
4.9	Raman spectra of HO <sub>C200</sub> thin films after partial electrical cycling up to 3 MV/cm, shown alongside the corresponding ferroelectric hysteresis loop. . . . .	84
4.10	Raman spectra of HO <sub>C200</sub> thin films after full electrical cycling up to 3.75 MV/cm, shown alongside the corresponding ferroelectric hysteresis loop. . . . .	85
5.1	Development of microstructure and emergence of a superstructure according to the microstructural zone model of Schuler et al.[131] . . . . .	89
5.2	X-ray reflectivity measurements of the HO <sub>L50</sub> thin films annealed in Ar and N <sub>2</sub> :O <sub>2</sub> atmospheres compared to a simulated curve with the theoretical density of 9.6 g cm <sup>-3</sup> (light grey).[108] The dashed line intercepts at the density edge are the half maxima of the XRR intensity. . . . .	91
5.3	SIMS intensities of carbon in HO <sub>L50</sub> thin films annealed in Ar and N <sub>2</sub> :O <sub>2</sub> atmospheres. . . . .	92
5.4	(a) GIXRD and (b) $\theta$ -2 $\theta$ patterns of the HO <sub>L50</sub> films annealed in Ar and N <sub>2</sub> :O <sub>2</sub> atmospheres. The XRD patterns are compared with the reference patterns from the powder diffraction files. The peaks due to the substrate are marked with *. . . . .	93
5.5	(a) Grazing incident X-ray diffraction (GIXRD) geometry and (b) $\theta$ -2 $\theta$ geometry. In GIXRD incident angle $\omega$ is fixed. . . . .	93
5.6	XRD peak fits of the of HO <sub>L50</sub> films annealed in (a) Ar and (b) N <sub>2</sub> :O <sub>2</sub> atmosphere. . . . .	94
5.7	AFM characterization of surface morphology of HO <sub>L50</sub> films annealed in (a) Ar and (b) N <sub>2</sub> :O <sub>2</sub> atmosphere. . . . .	94
5.8	Hysteresis loops of HO <sub>L50</sub> films: (a) current density–electric field (J–E) characteristics, and (b) polarization–electric field (P–E) characteristics. The results are extracted after subjecting the samples to 3000 rectangular wake-up cycles at 3 kHz. . . . .	95
6.1	(a) Structural schematic and (b) bright-field STEM image of the HZO <sub>C50</sub> multilayer film with the Pt/Ti top electrode and the Pt bottom electrode. . . . .	103
6.2	STEM-energy dispersive X-ray spectroscopy (STEM-EDS) line profile of the HZO <sub>C50</sub> multilayer. Z is the direction of growth. . . . .	103

6.3	(a) Cross-sectional HRTEM image of the field-cycled $\text{HZO}_{C50}$ multilayer film. (b) FFT diffractogram of the highlighted region. (c) Simulated diffraction pattern of orthorhombic $\text{HfO}_2$ along the $[\bar{1}01]$ zone axis (space group $\text{Pca}2_1$ ). (d) Simulated diffraction pattern of tetragonal $\text{HfO}_2$ along the $[\bar{1}11]$ zone axis (space group $\text{P}4_2/\text{nmc}$ ). . . . .	104
6.4	(a) Current density versus electric field loops and (b) polarization versus electric field loops of the $\text{HO}_{C45}$ , $\text{ZO}_{C45}$ and $\text{HZO}_{C50}$ films. . . . .	106
6.5	(a) Schematic illustration of the multilayer structure, and (b) hysteresis loops of the $\text{ZHO}_{C50}$ film after applying 10,000 rectangular voltage pulses with incrementally increasing electric field amplitudes up to 3 MV/cm. . . . .	107
6.6	(a) Structural schematics and (b) dark-field STEM image of the $\text{HZO}_{C90}$ multilayer thick film with Pt electrodes. . . . .	108
6.7	(a) Current density–electric field loops and (b) polarization–electric field loops for $\text{HO}_{C90}$ , $\text{HZO}_{C90}$ , and $\text{HZO}_{C50}$ films. The thick films were measured after 10,000 wake-up cycles with incrementally increasing electric field amplitudes up to approximately 3 MV/cm, while the thin HZO film was measured after 1,000 wake-up cycles at a constant field of 3 MV/cm. . . . .	109
6.8	(a) Structural schematics, (b) GIXRD patterns, (c) current density and polarization loops as a function of electric field (after 20,000 wake-up cycles), of the $\text{HCO}_{L30}$ bilayer thin film with Pt electrodes. The XRD patterns are compared with the reference patterns from the powder diffraction files.[161] . . . . .	110
6.9	(a) Remanent polarization $2P_r$ vs number of wake-up cycles for $\text{HZO}_{C50}$ and $\text{HO}_{C45}$ films. (b) Pristine loops of $\text{HZO}_{C50}$ and $\text{HO}_{C45}$ , acquired from procedures 1 and 2, respectively. (c) $\text{HZO}_{C50}$ and $\text{HO}_{C45}$ loops measured after 1000 cycles following procedures 1 and 2, respectively. (d) $\text{HO}_{C45}$ loop measured after 7000 cycles following procedure 2; for the $\text{HZO}_{C50}$ film, maximum $2P_r$ was achieved by procedure 1 (1000 cycles); therefore, no loop is recorded after 7000 cycles [P1: procedure 1, P2: procedure 2] . . . . .	112
6.10	Breakdown measurements of the pristine $\text{HO}_{C45}$ and $\text{HZO}_{C50}$ films. . . . .	113
7.1	Schematic of an HBAR. (GSG: ground-source-ground) . . . . .	118

7.2	Measured impedance of a LiNbO <sub>3</sub> HBAR showing the dense comb of substrate cavity modes. (a) Wide frequency span illustrating the overall amplitude envelope set by the piezoelectric transducer response. (b) Zoomed view of the shaded region of (a), showing the uniform peak spacing that defines the Free Spectral Range (FSR). This measurement was performed on a LiNbO <sub>3</sub> sample, similar to devices previously demonstrated by Pijolat et al.[193]	120
7.3	Measurement setup of the metal–dielectric–metal trilayer capacitor using a miniature coplanar waveguide (CPW) probe, with a central signal pad (S) surrounded by ground pad (G).	124
7.4	Schematic of the CPW probe tip showing finger geometry and dimensions.	126
7.5	Real and imaginary impedance characteristics of HO <sub>C45</sub> HBAR device swept till 65 GHz.	128
7.6	(a) Real and imaginary impedance of HO <sub>C200</sub> HBAR device swept till 16 GHz, (b) polarization vs. electric field hysteresis, (c) displacement vs. electric field measured at 1 kHz for piezoelectric coefficient $d_{33}$ using double-beam laser interferometry (DBLI). All the measurements were done after wake-up cycling.	129
A.1	Setup configurations for X-ray diffraction: (a) grazing incidence configuration, (b) $\theta$ - $2\theta$ configuration.	144
A.2	(a) Example of the applied electric field waveform and corresponding current density response used for polarization hysteresis loop measurements. (b) Typical resulting polarization–electric field (P–E) hysteresis loop.	149
A.3	Excitation signal for (a) fatigue measurement with bipolar pulses with hysteresis measurement at regular intervals, adapted from [5] (b) Typical result of a fatigue measurement depicted as the remanent polarization versus log cycles of the excitation signal.	150
A.4	Illustration of the electrical breakdown test configurations employed in this work: (a) Linear Ramp Voltage Stress (LRVS) and (b) Constant Voltage Stress (CVS). Adapted from Ref. [203].	151

# List of Tables

3.1	Rapid thermal annealing (RTA) process used for film crystallization. . . . .	58
3.2	List of thin film samples fabricated in this work. The table shows the sample labels, precursor solution concentrations, process flow steps, stack type, and the corresponding schematic figures (see Figure 3.2). . . . .	60
4.1	Ferroelectric properties of $\text{HO}_{C45}$ films annealed in pure Ar atmosphere for different durations, showing coercive field ( $E_c$ ) and remanent polarization ( $2P_r$ ). . . . .	70
4.2	Ferroelectric properties of $\text{HO}_{C45}$ films annealed in pure Ar atmosphere for 90 s for varying gas flow rate, showing coercive field ( $E_c$ ) and remanent polarization ( $2P_r$ ). . . . .	72
4.3	Ferroelectric properties of $\text{HO}_{C45}$ films annealed in $\text{N}_2:\text{O}_2$ atmosphere with different ratios, showing coercive field ( $E_c$ ) and remanent polarization ( $2P_r$ ). The rows corresponding to 1:0 and 1:2 were left blank because high leakage currents prevented accurate determination of the values. . . . .	75
4.4	Reported Raman modes for the polar orthorhombic (o-III) phase from theoretical calculations and experimental measurements. . . . .	82
6.1	Comparison of FFT spot spacing (in $\text{nm}^{-1}$ ) between the $\text{HZO}_{C50}$ sample data and the simulated phases shown in Figure 6.3. . . . .	105
7.1	Target resonance frequencies and corresponding active-layer thicknesses required for $\text{HfO}_2$ HBAR operation. . . . .	123
7.2	Electrode diameter for $50\Omega$ impedance matching. . . . .	125

8.1	Ferroelectric properties of HfO <sub>2</sub> fabricated via CSD, reported in the literature and demonstrated in this work. Two growth routes were used for the solution-processed films: the conventional (conv.) method and the layer-by-layer (L/L) approach. . . . .	132
B.1	Reproducibility of ferroelectric properties for La:HfO <sub>2</sub> thin films grown under N <sub>2</sub> :O <sub>2</sub> 1:1 annealing atmosphere. The table summarizes the number of measured capacitors and the corresponding average coercive field ( $E_c$ ) and remanent polarization ( $P_r$ ) values for each sample type. . . . .	153

# Chapter 1

## Introduction

Ferroelectricity refers to the presence of a spontaneous electric polarization in a material that can be reversed by an applied external electric field and retained as remanent polarization after the field is removed. This property arises in materials lacking inversion symmetry, placing them in the broader category of non-centrosymmetric materials.[1] Ferroelectric materials enable a range of functionalities such as non-volatile memories, sensors, and actuators. Traditionally, materials like  $\text{Pb}(\text{Zr,Ti})\text{O}_3$  (PZT) have dominated these applications. However, since the discovery of ferroelectricity in hafnium oxide ( $\text{HfO}_2$ , commonly referred to as hafnia) thin films in 2011,[2]  $\text{HfO}_2$  has emerged as a promising alternative due to its CMOS compatibility (seamless integration into existing semiconductor fabrication processes), scalability to ultra-thin dimensions,[3] and its potential for lead-free applications. Unlike in conventional perovskite ferroelectrics, ferroelectricity in  $\text{HfO}_2$  originates from a metastable non-centrosymmetric orthorhombic phase, which can be stabilized through doping, mechanical stress, and controlling the grain size. This breakthrough has opened new possibilities for integrating ferroelectric behavior into advanced electronics, particularly for low-power memory and logic applications.

Various techniques are used to fabricate oxide thin films, broadly categorized into chemical methods like Chemical Solution Deposition (CSD) and vacuum-based approaches such as Atomic Layer Deposition (ALD) and Pulsed Laser Deposition (PLD). Chemical methods are generally more cost-effective and suitable for large-area processing, while vacuum-based methods offer high precision and structural uniformity. Among these techniques, CSD is distinguished by its adaptability and its capacity to produce high-quality ferroelectric oxide

films with well-controlled microstructure. A key advantage of CSD is its ability to produce films with thicknesses approaching one micrometer while maintaining stable ferroelectric properties, which is important for achieving the reliable piezoelectric response required in device applications. This capability makes CSD the method of choice for developing ferroelectric HfO<sub>2</sub> thin films in this PhD, where the piezoelectric properties is exploited for practical device implementation.

HfO<sub>2</sub>-based ferroelectric films, despite their promising potential, encounter several challenges in both fabrication and characterization. Reproducibility of ferroelectric properties is difficult to achieve due to the material's sensitivity to processing conditions, especially annealing atmospheres. Although the role of oxygen in stabilizing the polar phase is still a topic of debate, optimizing oxygen presence in annealing conditions is crucial for producing high-quality films. Furthermore, achieving ferroelectricity in thicker films, particularly those beyond 50 nm, remains challenging, which is critical for potential piezoelectric applications. Another significant issue is the wake-up effect. This phenomenon refers to the improvement in remanent polarization over time after repeated polarization switching cycles, driven by factors such as defect redistribution, domain depinning and phase-transition. While this effect can enhance ferroelectric properties, it can also lead to inconsistent remanent polarization over time, negatively impacting device performance. Although significant progress has been made in understanding the formation of the ferroelectric phase, much of the current discussion still centers around the poorly understood wake-up effect.

Most critically, there is a lack of systematic understanding of how annealing conditions, growth strategies, oxide stacking, and interface engineering can influence the ferroelectric properties of HfO<sub>2</sub>, limiting progress on the challenges outlined above. This knowledge gap hinders progress toward developing scalable processes for producing high-quality, solution-processed ferroelectric HfO<sub>2</sub> films that could serve as an alternative to vacuum-based methods while retaining the advantages of cost-effectiveness and large-area processing. Therefore, this thesis aims to answer the following research questions:

1. Can controlled CSD growth conditions, particularly annealing atmospheres, enable reproducible fabrication of high-quality ferroelectric HfO<sub>2</sub> films?
2. Can interface engineering enhance the ferroelectric response and electrical perfor-

mance of HfO<sub>2</sub> thin films?

3. Can solution-processed ferroelectric HfO<sub>2</sub> films achieve the electromechanical properties and integration prospects required for piezoelectric resonator applications?

To address these questions, the thesis is organized into seven chapters. Chapter 1 provides a general introduction, setting the context for the research. Chapter 2 outlines the foundational scientific principles, covering piezoelectricity and ferroelectricity, properties of ferroelectric HfO<sub>2</sub>, its growth techniques with a focus on CSD. Chapter 3 details the experimental approaches employed throughout the work. It elaborates on the synthesis techniques used for HfO<sub>2</sub> films, with particular attention to various CSD growth routes.

The next two chapters tackle research question 1. Chapter 4 investigates how annealing atmosphere controls precursor decomposition, oxygen vacancies, and defect passivation, shaping the ferroelectric behavior of HfO<sub>2</sub> films. Chapter 5 explores layer-by-layer growth route to enhance film density and crystallographic orientation. Together, the chapters show that carefully tuned processing conditions enable reproducible fabrication of high-quality ferroelectric HfO<sub>2</sub> films.

Chapter 6 addresses research question 2 and explores the integration of ZrO<sub>2</sub> and CeO<sub>2</sub> interlayers to engineer multilayer heterostructures via solution deposition. The study examines how variations in layer thickness and stacking order of different oxides influence the overall properties of the film, with particular focus on the role of interfaces in the wake-up process.

Research question 3, is explored in Chapter 7, where we attempted to harness the piezoelectric response of ferroelectric HfO<sub>2</sub> for the fabrication of a high-overtone bulk acoustic resonator (HBAR). The chapter details the design of an HBAR device using HfO<sub>2</sub> as the functional piezoelectric layer, along with theoretical background, fabrication procedures, and characterization techniques. Key results, as well as the associated challenges in device realization, are discussed.

Finally, Chapter 8 summarizes the key findings, links them to the research questions, and outlines future directions for ferroelectric HfO<sub>2</sub> and its device applications.



# Chapter 2

## Fundamentals

This chapter outlines the fundamental background and prior research relevant to the work presented in this thesis. Section 2.1 introduces the fundamental principles of piezoelectricity, and ferroelectricity, in both conventional perovskite-structured polar oxides and the more recent class of simple oxides. Section 2.2 presents an overview of hafnium oxide ( $\text{HfO}_2$ ), outlining its structural and functional characteristics. Section 2.3 discusses various thin-film growth techniques, with particular attention given to Chemical Solution Deposition (CSD) due to its advantages in the fabrication of ferroelectric hafnia thin films. Finally, Section 2.4 describes the principles of the CSD method and elaborates on the crystallization mechanisms involved in solution-processed films.

### 2.1 Theory of polar oxides

Within the framework of crystallography, the 32 point groups encompass all possible symmetry configurations of crystalline solids. Among these, 11 groups are centrosymmetric, meaning they possess an inversion center. The existence of such a symmetry operation precludes the emergence of any net polar behavior, as any polar vector would be reversed under inversion, thereby nullifying macroscopic polarization.

In contrast, the remaining 21 non-centrosymmetric point groups (excluding the cubic point group 432) are capable of exhibiting piezoelectricity—a phenomenon that describes the linear coupling between mechanical stress and electric polarization. Among these 21 non-centrosymmetric classes, 20 are polar point groups characterized by the existence of a

unique polar axis. Crystals belonging to these groups may exhibit spontaneous polarization aligned with the polar axis.[4] Furthermore, in certain polar materials, the direction of spontaneous polarization can be reoriented between crystallographically equivalent states under the influence of an external electric field. This switchability distinguishes a special subclass of polar materials known as ferroelectrics, drawing an analogy to ferromagnetic behavior where the magnetic moment can be similarly reversed. It is therefore not merely the presence of a spontaneous polarization that defines ferroelectricity, but rather its reversibility through the application of an external field.[5]

### 2.1.1 Piezoelectricity

Piezoelectric materials constitute a class of substances that can be polarized not only through the application of an external electric field but also by mechanical stress, as depicted in Figure 2.1. The direct piezoelectric effect refers to the generation of an electric displacement field  $D_i$  in response to an applied mechanical stress  $X_{jk}$ , and is described by the linear relation:

$$D_i = d_{ijk}X_{jk} \quad (2.1)$$

Here,  $d_{ijk}$  is the third-rank piezoelectric tensor with units of C/N (coulombs per newton), representing the piezoelectric coefficients characteristic of the material.[6] The electric displacement  $D_i$  contains contributions from both the vacuum permittivity term  $\varepsilon_0 E_i$  and the material's polarization  $P_i$ , according to

$$D_i = \varepsilon_0 E_i + P_i. \quad (2.2)$$

In the absence of an external electric field ( $E_i = 0$ ), the direct piezoelectric effect manifests as a stress-induced polarization,

$$P_i = d_{ijk}X_{jk}, \quad (2.3)$$

meaning that mechanical stress alters the alignment of electric dipoles within the crystal lattice.

Conversely, piezoelectric materials also exhibit a mechanical deformation—expansion or contraction—when subjected to an electric field. This phenomenon, known as the converse piezoelectric effect, relates the induced strain  $x_{ij}$  to the applied electric field  $E_k$  as follows:

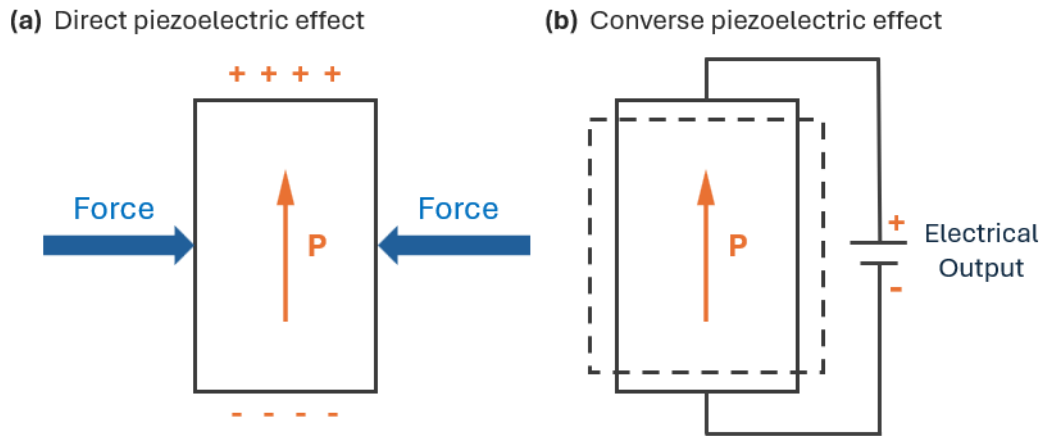


**Figure 2.1** Schematic representation of (a) the direct piezoelectric effect, where applied mechanical stress changes a polarization,  $P$  and induces surface charges, and (b) the converse piezoelectric effect, where an applied electric field alters the polarization and produces a mechanical strain.

$$x_{ij} = d_{kij} E_k = d_{ijk}^t E_k \quad (2.4)$$

where  $d_{ijk}^t$  denotes the transpose of the piezoelectric tensor, and the units of the converse piezoelectric coefficient are in m/V (meters per volt). According to thermodynamic reciprocity, the piezoelectric coefficients for the direct and converse effects are identical, i.e.,  $d_{\text{direct}} = d_{\text{converse}}$ .

It is important to note that both the magnitude and sign of the induced charge density  $D_i$  and the strain  $x_{ij}$  depend on the direction of the applied mechanical stress and electric field, respectively. The piezoelectric coefficient  $d$  may be positive or negative depending on the material and measurement configuration. Coefficients measured in the direction of the applied field are referred to as longitudinal coefficients, those measured perpendicular to the field as transverse coefficients, and others that describe deformation due to shear stresses or fields are classified as shear coefficients.

### 2.1.2 Ferroelectricity

Ferroelectricity can be regarded as a special case of the piezoelectric effect, in which the material not only exhibits a spontaneous electric polarization that is oriented along a specific crystallographic axis but can be reversed under the application of a sufficiently strong

external electric field.[1] The phenomenon of ferroelectricity was first reported by Valasek in 1920 through his investigation of Rochelle salt, where he demonstrated field-induced switching of polarization.[7]

A hallmark of ferroelectric behavior is the structural phase transition from a high-symmetry, non-polar paraelectric phase to a low-symmetry, polar ferroelectric phase. This transition occurs at the Curie temperature ( $T_C$ ) and is typically accompanied by a pronounced increase in dielectric susceptibility.[8]

In the ferroelectric phase, the spontaneous polarization gives rise to bound surface charges. Without sufficient screening from free carriers, charged defects, or metallic electrodes, these charges produce an internal electric field opposing the spontaneous polarization, known as the depolarization field.[9, 10] Upon cooling through  $T_C$  in the absence of an external electric field, the crystal may adopt one of several energetically equivalent polarization orientations. To minimize the sum of electrostatic energy from the depolarization field and elastic energy due to mechanical constraints, the material typically organizes into domains—regions of uniform polarization—separated by domain walls.[11, 12]

The reversal of polarization under an applied electric field  $\vec{E}$  can be understood in terms of the Landau free energy landscape, shown in Figure 2.2(a). The double-well profile represents two stable polarization states at  $\pm P_r$ , corresponding to opposite orientations of the electric dipoles. When the applied field is sufficient to overcome the energy barrier, the polarization flips direction, causing the system to transition from one stable state to the other.

The macroscopic manifestation of this switching process is the ferroelectric hysteresis loop in Figure 2.2(b), which plots polarization as a function of the applied electric field. This characteristic  $P$ - $E$  loop is obtained experimentally by integrating the switching current under a cyclic electric field, often triangular or sinusoidal in waveform.[5, 13] Key parameters extracted from the loop include the remanent polarization  $P_r$  (the polarization at zero applied field after saturation), the saturation polarization  $P_s$  (the maximum achievable polarization), and the coercive field  $E_c$  (the field magnitude required to reduce the polarization to zero during switching).

In addition to these general features of ferroelectricity, hafnia-based materials exhibit quantitative characteristics that differ significantly from conventional perovskites. In hafnia-

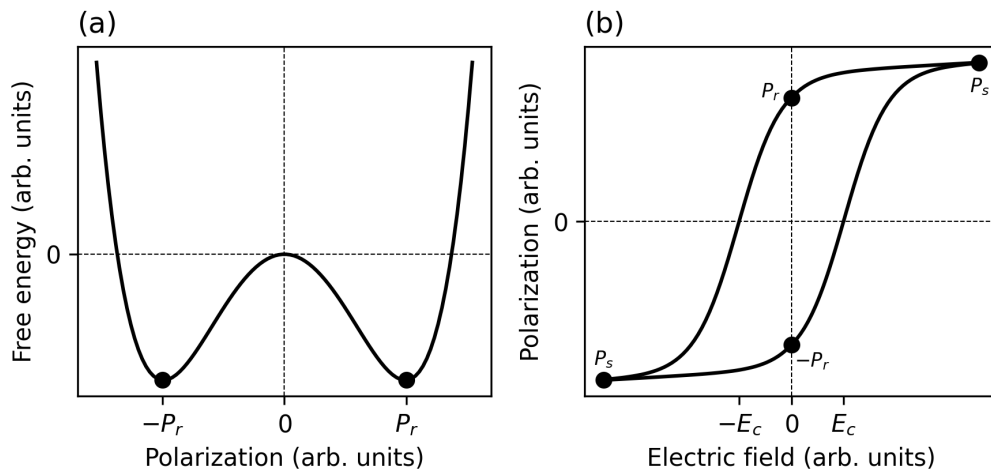


**Figure 2.2** (a) Landau free energy as a function of polarization for a ferroelectric material, showing the two stable states at  $\pm P_r$ . (b) Corresponding polarization–electric field hysteresis loop, highlighting  $P_r$ ,  $P_s$ , and  $E_c$ .

based ferroelectrics, the theoretical spontaneous polarization of the orthorhombic  $Pca2_1$  phase is predicted to be on the order of  $50\text{--}58 \mu\text{C}/\text{cm}^2$ , which corresponds to an ideal polycrystalline  $P_r$  of approximately  $25\text{--}28 \mu\text{C}/\text{cm}^2$ , and up to  $30 \mu\text{C}/\text{cm}^2$  for films exhibiting strong (111) preferential orientation.[14] Experimentally,  $\text{HfO}_2$ -based thin films typically show  $P_r$  values in the range of  $10\text{--}40 \mu\text{C}/\text{cm}^2$ , with the highest reported values approaching  $45 \mu\text{C}/\text{cm}^2$  in doped systems.[15] The coercive field is intrinsically high, with a theoretical limit of about  $13.4 \text{ MV}/\text{cm}$ :[16] however, measured  $E_c$  values in practical thin films generally lie between  $0.8$  and  $2 \text{ MV}/\text{cm}$  due to domain-nucleation-driven switching.[15] These ranges reflect the combined influence of film thickness, crystallographic orientation, dopant concentration, and microstructural factors on the polarization switching behavior of  $\text{HfO}_2$ -based ferroelectrics.

Due to their large dielectric constants and strong piezoelectric responses, ferroelectric materials are integral to technologies such as high-energy-density capacitors and precision actuators.[17] Their reversible polarization switching underpins non-volatile memory devices, particularly ferroelectric random-access memory (FeRAM).[18] Furthermore, their nonlinear polarizability makes them excellent candidates for electro-optic modulation and nonlinear optical processes, including second-harmonic generation.[19, 20]

## 2.2 Hafnium oxide and its properties

Hafnia has been widely acknowledged as a refractory oxide, attributed to its notably high melting temperature of around 2800°C.[21, 22]. Given its higher dielectric permittivity compared to silicon dioxide (SiO<sub>2</sub>), HfO<sub>2</sub> has also been investigated as a potential high-*k* gate dielectric material.[23–25] Extensive research has been conducted over the years to explore its dielectric, electrical, mechanical, and thermal properties in these contexts. The discovery of ferroelectricity in HfO<sub>2</sub>-based thin films in 2011[2] has sparked additional studies, focusing on the material's dielectric, piezoelectric, pyroelectric, and electrocaloric properties.

Hafnium dioxide (HfO<sub>2</sub>) exhibits rich polymorphism, with multiple crystal structures emerging under varying thermodynamic conditions. The high-temperature cubic fluorite phase (space group  $Fm\bar{3}m$ ), illustrated in Fig. 2.3, is characterized by Hf<sup>4+</sup> cations occupying the corners and face centers of the unit cell, while O<sup>2-</sup> anions occupy the eight tetrahedral interstitial sites. This arrangement results in coordination numbers of 8 for Hf<sup>4+</sup> and 4 for O<sup>2-</sup>. [25–27] Similar cubic fluorite structures are also observed in other binary oxides such as ZrO<sub>2</sub> and CeO<sub>2</sub> under specific conditions.[25]

At ambient pressure and temperature, the most thermodynamically stable phase of HfO<sub>2</sub> is monoclinic (space group  $P2_1/c$ ), which is shown in Fig. 2.3. This monoclinic structure can be considered a distorted derivative of the high-symmetry cubic fluorite phase. Upon heating, HfO<sub>2</sub> undergoes a series of phase transitions: from the monoclinic phase to a tetragonal phase (space group  $P4_2/nmc$ ) above approximately 1700°C, and subsequently to the cubic phase above 2600°C.[21, 29–31]

In addition to temperature-induced transitions, HfO<sub>2</sub> exhibits a sequence of pressure-induced polymorphic transformations. With increasing pressure, the material transitions from the monoclinic phase (m) to two orthorhombic phases (denoted oI and oII), and finally to the tetragonal phase (t). A comprehensive pressure-temperature phase diagram detailing these transitions was constructed by Bocquillon (see Figure 2.4).[32] Experimental studies, particularly those using scanning transmission electron microscopy, have identified the noncentrosymmetric orthorhombic-III phase with space group  $Pca2_1$  (see Fig. 2.3) as the best structural representation for many ferroelectric HfO<sub>2</sub> thin films.[34] This structural

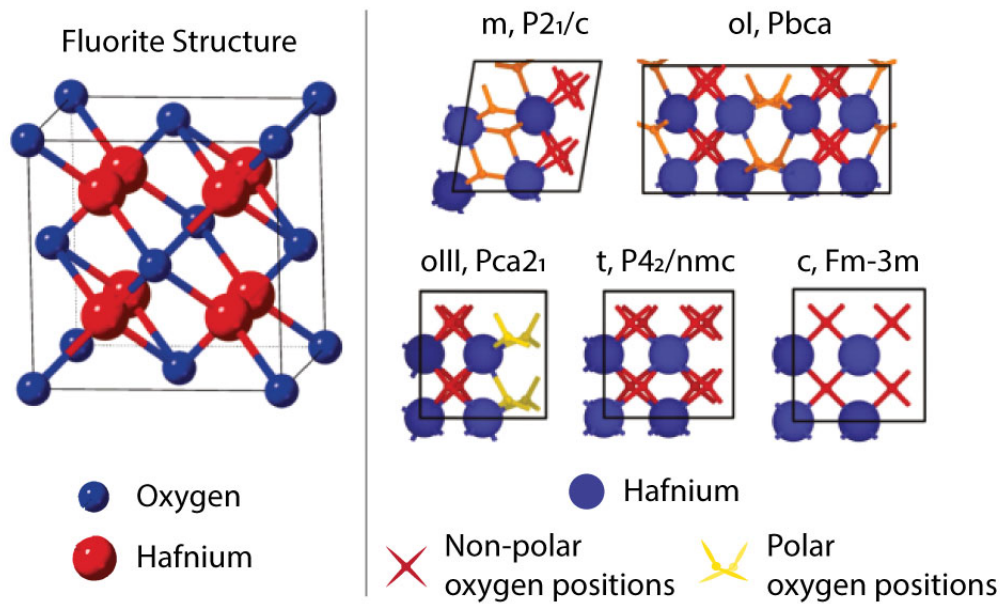


**Figure 2.3** On the left is the fluorite crystal structure, with hafnium atoms forming a face-centered cubic lattice and oxygen atoms occupying the tetrahedral interstices. On the right are five well-established polymorphs of hafnia, monoclinic (m), orthorhombic-I (o-I), orthorhombic-III (o-III), tetragonal (t), and cubic (c), shown with their respective space groups. For clarity, the polymorphs are shown as 2D projections emphasizing the oxygen sublattice distortions; the Hf positions remain nearly unchanged between phases, and the yellow oxygen atoms highlight the polar displacements characteristic of the ferroelectric o-III phase. The figure is adapted from chapter 6 of [28], based on work by A. Kersch.

insight lays the foundation for understanding the ferroelectric behavior observed in  $\text{HfO}_2$  thin films. Throughout this thesis, references to the o-phase will, unless explicitly stated otherwise, generally denote the polar o-III phase.

While X-ray diffraction (XRD) is among the most widely employed techniques for rapid phase identification in crystalline materials, its application to  $\text{HfO}_2$  thin films presents particular difficulties, especially when the focus lies on ferroelectric properties. In this system, distinguishing between the o- and t- phases is inherently challenging due to their pronounced structural similarity and near-identical lattice parameters.[28, 35, 36] This similarity results in substantial overlap of their characteristic Bragg reflections in XRD patterns. For example, the o-111 reflection appears at approximately  $2\theta \approx 30.4^\circ$ , while the t-101 reflection is found near  $2\theta \approx 30.8^\circ$ , often merging into a single broadened peak around  $30.5^\circ$ . These challenges are intensified in thin films, where small grain sizes, random orientation distributions, and

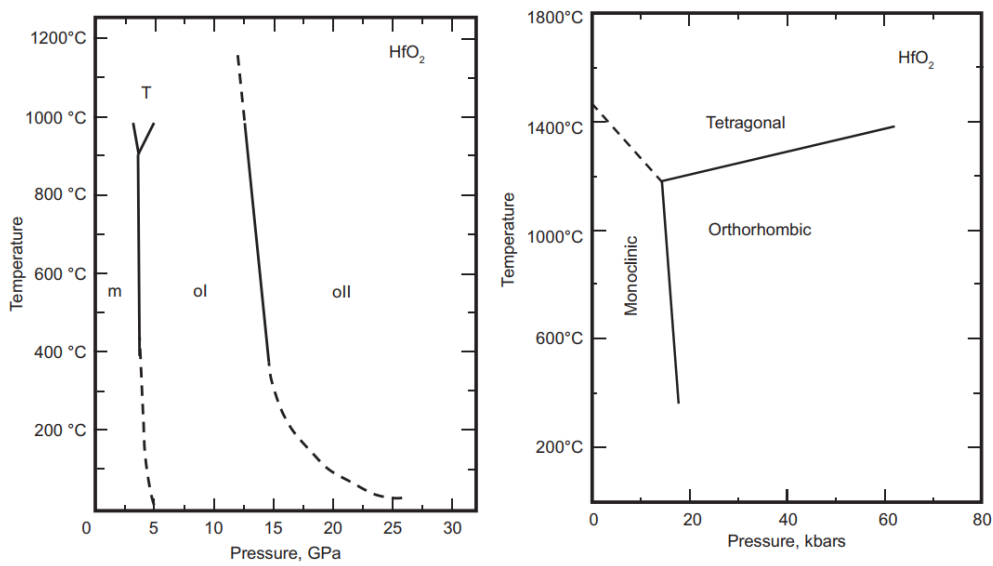


**Figure 2.4** Pressure-temperature phase diagrams of HfO<sub>2</sub>. Panel (A) data taken from [32] and (B) reconstructed from [33].

associated peak broadening hinder unambiguous phase separation.[37, 38] Techniques, such as grazing-incidence x-ray diffraction (GIXRD), can improve peak intensity but rarely achieve definitive resolution between o- and t-phases. Even advanced structural probes, including convergent beam electron diffraction (CBED) and scanning transmission electron microscopy (STEM), typically require targeted analyses such as direct visualization of oxygen sublattice positions to conclusively distinguish the two.[34, 39, 40] This inherent challenge complicates precise quantification of the ferroelectric orthorhombic phase fraction, introducing uncertainty in the correlations between phase composition and functional properties that will be frequently addressed in the results sections.

### 2.2.1 Ferroelectricity in HfO<sub>2</sub> thin films

Ferroelectricity in HfO<sub>2</sub> thin films originates from the stabilization of the polar non-centrosymmetric orthorhombic phase, which does not naturally form in undoped HfO<sub>2</sub> at room temperature but can be induced through suitable doping and post-deposition annealing.[41] Park *et al.* reported that the crystalline phase sequence depends on the dopant concentration, evolving from monoclinic to orthorhombic and, with excessive doping, to tetragonal or cubic.[42]

The optimization of ferroelectric properties requires precise control of dopant concen-

tration, as the remanent polarization ( $P_r$ ) exhibits a strong dependence on doping levels. Figure 2.5a shows the dopant concentrations that produce the highest remanent polarization values (referred to as "best Pr") for each dopant type and deposition method. For ALD- and sputtered PVD-grown films, the optimal range is typically 3–5 %, while CSD layers generally require slightly higher levels of 5–7 %.[43]

The stability window of the ferroelectric phase further depends on the ionic radius of the dopant, ranging from as narrow as  $\sim 2$  % for smaller dopants such as Si and Al to as wide as  $\sim 8$  % for larger dopants like La (Figure 2.5b).[43] Despite these variations, the effective doping ranges remain broadly comparable across ALD-, CSD-, and PVD-deposited films. The broader processing window observed with larger dopants is attributed to their enhanced ability to induce the requisite lattice distortions while maintaining phase stability over a wider concentration range. Computational studies by Batra et al. further support these trends, showing that dopants like La and Sr reduce the free-energy difference between competing phases, thereby favoring orthorhombic stabilization.[44]

Structural effects are evident in the unit cell aspect ratio,  $2c/(a+b)$ . Values of  $\sim 1.01$ – $1.02$  are observed when the oIII-phase fraction is highest, whereas in the tetragonal phase the ratio decreases slightly below 1. Notably, oIII-phase grains embedded within a monoclinic matrix exhibit aspect ratios exceeding 1.02, reflecting the strong structural distortions and internal stresses associated with phase coexistence (Figure 2.5c). This metric serves as a quantitative indicator of the degree of orthorhombic distortion and correlates with the ferroelectric performance of the material.

Annealing plays a critical role in crystallizing the amorphous as-deposited films into the desired ferroelectric phase. The temperature and duration of annealing influence grain growth, texture, and interface chemistry. As annealing temperature increases, both the orthorhombic phase fraction and remanent polarization ( $P_r$ ) generally increase as depicted in Figure 2.6, especially near the phase boundary between the orthorhombic and tetragonal regions.[50]

However, this comes with trade-offs. Higher temperatures can also promote oxygen vacancy formation due to oxygen scavenging by TiN electrodes, thereby degrading endurance through leakage current pathways.[51, 52] La-doped  $\text{HfO}_2$  has shown comparatively better endurance performance than Si-doped variants under similar conditions, with reported

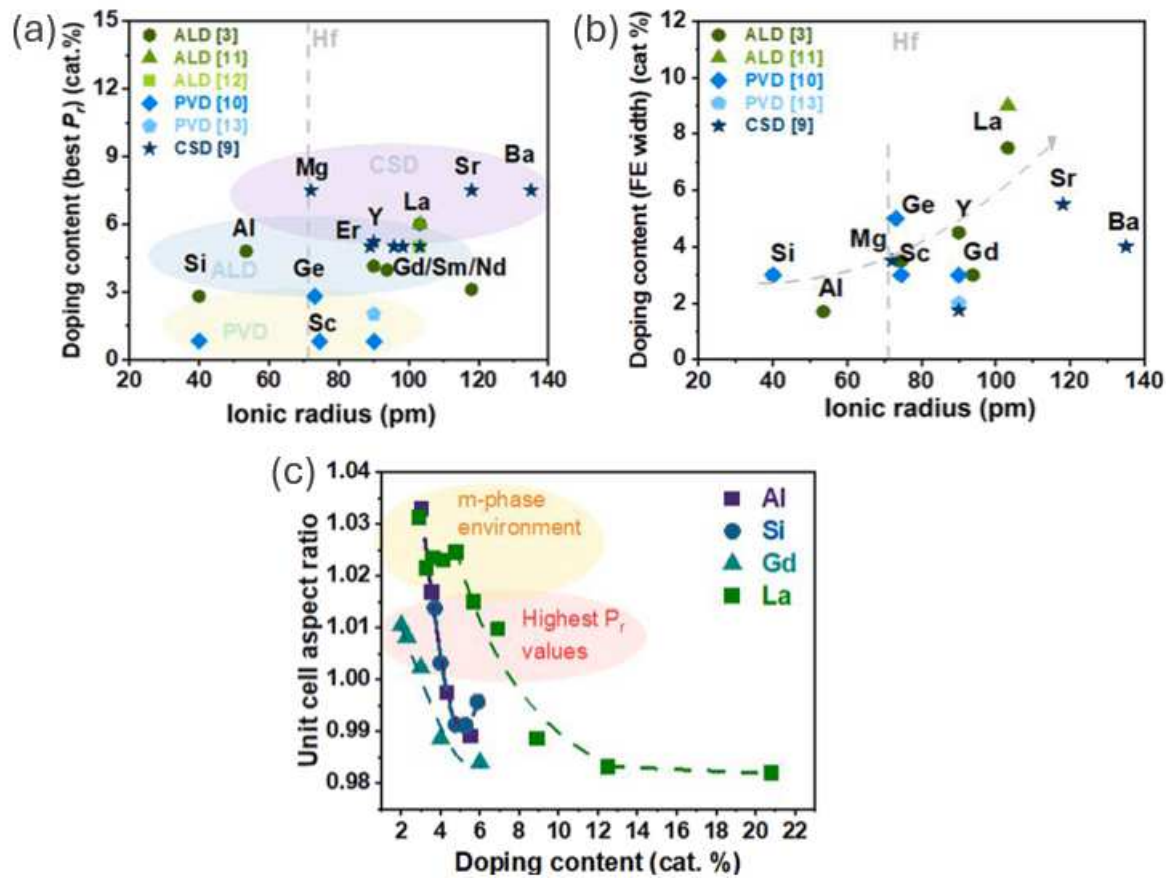


**Figure 2.5** (a) Dopant concentrations corresponding to the maximum remanent polarization ( $P_r$ ), and (b) the width of the concentration window in which ferroelectricity is stabilized in 10 nm-thick  $\text{HfO}_2$  films for dopants of different ionic radii. Data include films deposited by ALD, PVD, and CSD techniques, compiled from various studies.[43, 45–49] (c) Unit cell aspect ratio  $2c/(a+b)$  as a function of dopant concentration in  $\text{HfO}_2$ -based thin films with different dopants. Figure adapted from chapter 3 of [28].

remanent polarization values up to  $45 \mu\text{C}/\text{cm}^2$  and ferroelectricity stable over a broad doping concentration range (8 cat.%).[53, 54] This robust performance is attributed to the formation of trivalent dopant-oxygen vacancy complexes that stabilize the ferroelectric phase. The detailed charge compensation mechanism and its implications for defect engineering are discussed in the next section.

The polarization–electric field (P–E) hysteresis of doped  $\text{HfO}_2$  capacitors reveals characteristic behavior depending on the dopant and processing conditions. For instance, Si-doped films exhibit antiferroelectric-like double hysteresis at high doping concentrations, attributed to a field-induced phase transition between the tetragonal and orthorhombic phases [14, 55]. In contrast, La-doped films show strong, single-loop hysteresis indicative of stable ferroelec-

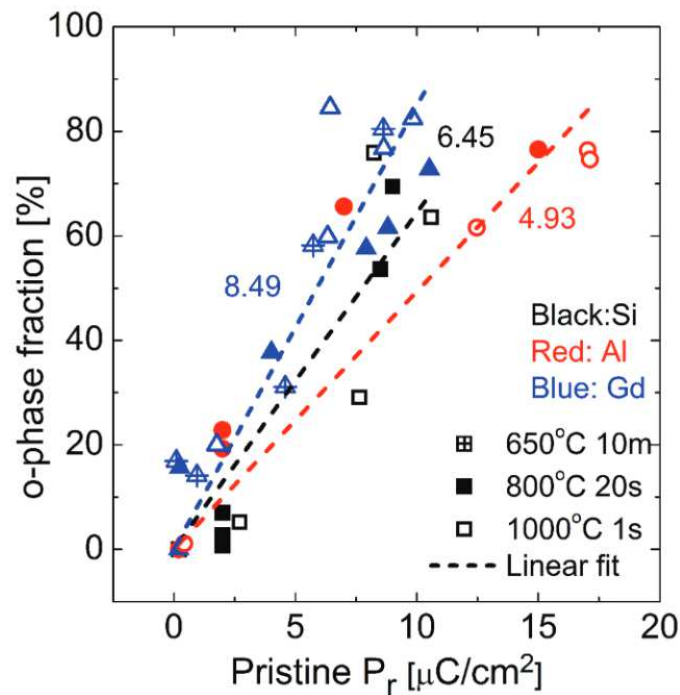


**Figure 2.6** Orthorhombic phase fraction as a function of pristine remanent polarization ( $P_r$ ) for atomic layer deposited Si-, Al-, and Gd-doped  $\text{HfO}_2$ . Data points correspond to different annealing conditions: 650°C for 10 min, 800°C for 20 s, and 1000°C for 1 s. Dashed lines indicate linear least-square fits for each dopant, with the corresponding slopes displayed in the graph. Figure adapted from [50].

tricity with high remanent polarization values, even at modest annealing temperatures.[53]

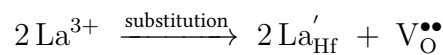
The emergence of ferroelectricity in  $\text{HfO}_2$  thin films has redefined the boundaries of ferroelectric materials, enabling integration into advanced logic and memory devices. Doping and annealing are pivotal in achieving and tuning the ferroelectric properties. Among dopants, La offers one of the most promising pathways due to its broad compositional window, high polarization, and robust endurance. Nevertheless, understanding the interplay of processing conditions, crystallography, and interface chemistry remains vital for optimizing these materials for commercial deployment. A comprehensive investigation into the influence of annealing conditions on the ferroelectric properties of La doped  $\text{HfO}_2$  is presented in Chapter 4, as part of the research conducted in this PhD work.

### 2.2.2 Defects and their role in ferroelectric $\text{HfO}_2$

Defects play a critical role in the ferroelectric properties and performance of hafnium oxide ( $\text{HfO}_2$ ) based materials.[56, 57] Unlike conventional perovskite ferroelectrics where defects

might degrade performance, in  $\text{HfO}_2$ , defects are essential for inducing and enhancing ferroelectricity.[56, 58–61] Oxygen vacancies ( $V_O$ ) are particularly pervasive point defects in oxide thin films, often introduced during fabrication due to low thermal budgets and large area deposition techniques. These vacancies, along with various dopants, are crucial for stabilizing the metastable non-centrosymmetric orthorhombic phase ( $Pca2_1$ ).[28, 62, 63] For instance, oxygen vacancies can lower the formation energy of the orthorhombic phase, making it more energetically favorable.[64–66] The small energy difference between  $\text{HfO}_2$ 's various phases means that even subtle influences from defects can significantly alter phase stability and kinetically favor the transition to the ferroelectric phase during processing.[60] However, while a limited presence of oxygen vacancies can promote polar structures, a high density can lead to disordering of dipole moments, increased polarization switching barriers, and higher leakage currents, which are detrimental to ferroelectric performance.[66]

The controlled introduction of oxygen vacancies through heterovalent doping provides a key mechanism for stabilizing ferroelectricity in  $\text{HfO}_2$ . [28] In the La-doped films investigated in this work, the substitution of trivalent  $\text{La}^{3+}$  (ionic radius 1.160 Å) for tetravalent  $\text{Hf}^{4+}$  (0.83 Å) creates a charge deficiency that must be compensated by oxygen vacancy formation, two  $\text{La}^{3+}$  ions replacing two  $\text{Hf}^{4+}$  atoms generate one doubly positively charged vacancy ( $V_O^{\bullet\bullet}$ ).



These dopant–vacancy complexes reduce the local cation coordination number, kinetically favoring the metastable orthorhombic phase over the thermodynamically stable monoclinic structure.

Critically, the annealing atmosphere can further modulate the oxygen vacancy concentration beyond that intrinsically required by charge compensation.[28] Oxygen-rich atmospheres may suppress additional vacancy formation, while oxygen-deficient conditions (e.g.,  $\text{N}_2$ , Ar, or vacuum) can generate excess vacancies. This atmospheric control over the total defect population influences both the initial ferroelectric properties and the dynamic behavior under electrical cycling, making it a critical processing parameter that extends beyond simply providing thermal energy for crystallization.

### 2.2.3 Wake-up effect in ferroelectric HfO<sub>2</sub> capacitors

In hafnia-based ferroelectrics, distinguishing polar from non-polar phases using diffraction techniques remains a challenge, however electrical characterization can provide direct insight into the presence of ferroelectricity. The most definitive evidence of ferroelectricity arises from the observation of switching currents in current–electric field hysteresis loop as presented in figure 2.7. In HfO<sub>2</sub>-based systems the pristine response often displays a characteristic pinched loop that gradually evolves into a well-saturated hysteresis upon repeated cycling. This so-called wake-up effect, consistently observed across a wide variety of HfO<sub>2</sub> systems regardless of dopant chemistry or processing route, underscores the necessity of electrical conditioning to realize the maximum remanent polarization ( $P_r$ ). [51, 62, 67] Interestingly, this phenomenon is not unique to hafnia but has also been documented in classical perovskite ferroelectrics, suggesting that the wake-up effect is a universal characteristic of ferroelectricity. [68] While such an intrinsic property reflects the dynamic nature of polarization stabilization, it carries important implications for applications, for example in non-volatile memory devices, the change of  $P_r$  with cycling can cause read errors. Thus, understanding and mitigating the wake-up effect is critical for the reliable integration of ferroelectrics into emerging electronic technologies.

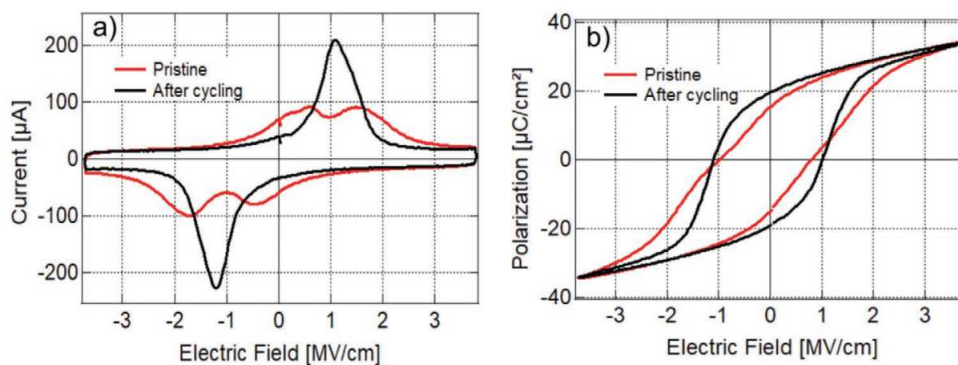


**Figure 2.7** a) Switching current versus applied electric field and b) polarization versus applied electric field in the pristine state and in the woken-up state after  $10^5$  cycles. Reproduced from [69].

The underlying mechanisms driving the wake-up effect involve a complex interplay of defect redistribution and field-induced phase transformations depicted in figure 2.8. The most widely accepted explanation centers on the redistribution of oxygen vacancies, which are inevitably introduced during film growth and subsequent thermal processing. [51] These

defects initially accumulate at electrode–ferroelectric interfaces, particularly when reactive metal nitride electrodes like TiN become partially oxidized during processing, forming  $\text{TiO}_x\text{N}_y$  phases and creating oxygen-deficient regions in the adjacent ferroelectric layer. The asymmetric distribution of these charged defects generates internal bias fields that suppress ferroelectric dipoles near the interfaces and can even force them to polarize in opposing directions, resulting in the characteristic pinched hysteresis loops observed in pristine films. As electrical cycling proceeds, the alternating field facilitates the redistribution of these mobile defects toward more uniform distributions throughout the film volume, progressively diminishing the internal bias fields and allowing ferroelectric domains to align coherently.

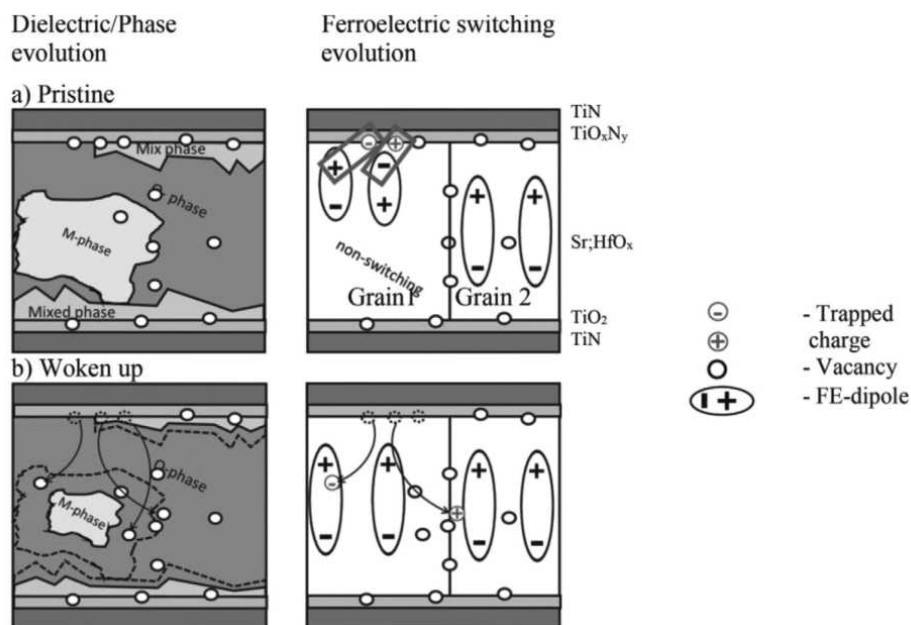


**Figure 2.8** Model of the different stages of the ferroelectric capacitor lifetime a) pristine, b) wake-up. Reproduced from [51].

Complementing defect redistribution, field-induced phase transformations contribute significantly to the wake-up process as can be seen in phase evolution schematic in figure 2.8. The initial film microstructure typically contains a mixture of phases, including the paraelectric monoclinic (m-phase), tetragonal (t-phase), and the desired ferroelectric orthorhombic (o-phase) polymorphs.[51] During electrical cycling, the applied field promotes transformation of non-ferroelectric phases to the polar orthorhombic structure, effectively increasing the volume fraction of ferroelectrically active material. This phase evolution is particularly pronounced in Zr-doped systems, where the formation energy difference

between competing phases is relatively small, making field-induced transformations energetically favorable. The combined effect of defect redistribution and phase transformation manifests as a progressive increase in  $P_r$  until a stable, fully developed hysteresis loop is achieved.

The magnitude of the wake-up effect exhibit strong dependencies on material composition and processing parameters. Among different dopant species, Zr-doped  $\text{HfO}_2$  typically exhibits slight wake-up behavior with small increases in  $P_r$ , attributed to its inherently favorable phase stability and reduced defect concentrations.[70] In contrast, Gd- and Sr-doped films often demonstrate dramatic wake-up effects with substantial polarization enhancement, reflecting their higher initial defect densities and more pronounced internal bias fields.[71, 72] Si-doped systems occupy an intermediate position but frequently exhibit wake-up coupled with imprint effects, where the coercive field shifts systematically due to asymmetric interfacial states.[41, 73] These compositional variations highlight the critical role of dopant chemistry in determining both the initial defect landscape and the subsequent evolution pathways during electrical conditioning.

From a device engineering perspective, mitigating the wake-up effect is a key challenge for the reliable integration of  $\text{HfO}_2$ -based ferroelectrics into memory and logic devices. Suppression strategies include dopant engineering, optimized annealing to minimize parasitic phases, and electrode/interface designs that control oxygen vacancy concentrations. A clear understanding of defect migration, phase transformation, and interfacial reactions is essential for both improving reliability and enabling novel applications. In this PhD, insight into this complex phenomenon has been sought using Raman spectroscopy, as discussed in Chapter 4.

#### 2.2.4 Piezoelectricity in $\text{HfO}_2$ thin films

Having established the ferroelectric nature of  $\text{HfO}_2$ -based thin films, it is natural to turn to their piezoelectric response, particularly since the electromechanical properties of hafnia set it apart from conventional ferroelectrics by exhibiting an unconventional piezoelectric behavior. In contrast to classical ferroelectrics such as perovskite oxides (e.g.,  $\text{PbTiO}_3$ ),  $\text{HfO}_2$  has been theoretically predicted to exhibit a negative longitudinal piezoelectric effect.[74–77] In this unconventional response, compression along the polarization axis enhances the polar

distortion rather than suppressing it. Dutta et al. have confirmed this phenomenon through both, first-principles calculations and experimental investigations, including piezoresponse force microscopy (PFM) studies on HfO<sub>2</sub> thin films.[74] For instance, measurements on La-doped HfO<sub>2</sub> films revealed an anticlockwise rotation of the PFM phase loops, consistent with a negative effective longitudinal coefficient ( $d_{33,\text{eff}}$ ) in the range of  $-2$  pm/V to  $-5$  pm/V, in good agreement with theoretical predictions of  $-0.9$  pm V<sup>-1</sup> to  $-2.5$  pm V<sup>-1</sup>.

The piezoelectric response of HfO<sub>2</sub> can be substantially modified in both magnitude and sign through structural and environmental control. In particular, the sign of the piezoelectric coefficient can be inverted by altering the environment of the active oxygen atoms, for example via epitaxial strain.[74] First-principles simulations predict that in-plane compressive strain can enhance, diminish, or even reverse the sign of the  $e_{33}$  coefficient—transforming it from negative to positive—without reversing the spontaneous polarization, a behavior unprecedented in ferroelectrics. More recently, experiments on Hf<sub>0.5</sub>Zr<sub>0.5</sub>O<sub>2</sub> (HZO) ferroelectric capacitors demonstrated that electrical field cycling can intrinsically tune the piezoelectric response, enabling a smooth transition from a positive  $d_{33}$  in the pristine state to a uniformly negative  $d_{33}$  after sufficient cycling.[78] This evolution proceeds through a continuous reduction in  $d_{33}$  magnitude, passing through zero, followed by sign inversion and subsequent growth in the negative value. Strikingly, the net piezoelectric response can be effectively nullified while preserving fully switchable polarization, suggesting the existence of an intrinsically non-piezoelectric ferroelectric state.

This dynamic tunability explained by density functional theory as a structural evolution from a weakly developed to a strongly developed polar o-phase opens up unprecedented possibilities for electromechanical device engineering. In particular, the ability to reversibly tailor the piezoelectric coefficients of HfO<sub>2</sub>-based ferroelectrics provides a compelling platform for high-performance resonator devices, as discussed in detail in Chapter 7. Such devices can exploit both the unconventional negative piezoelectric response and its tunability to achieve frequency-agile, miniaturized, and CMOS-compatible components for next-generation RF and sensing applications. Beyond resonators, the unique combination of ferroelectricity, piezoelectricity, and structural tunability in HfO<sub>2</sub>-based materials enables a broad spectrum of device concepts across memory, logic, sensing, and energy technologies, as outlined in the following section.

### 2.2.5 Applications

Ferroelectric HfO<sub>2</sub> is gaining traction for advanced semiconductor and energy applications. Their integration into ferroelectric random-access memory (FeRAM) and ferroelectric field-effect transistors (FeFETs) offers compelling benefits, such as non-volatility, low-power operation, and scalability to advanced technology nodes.[15, 79] FeFETs, in particular, leverage the switchable polarization of HfO<sub>2</sub>-based materials to modulate transistor threshold voltages, enabling non-destructive readout and fast switching speeds.[80] Devices have demonstrated endurance up to 10<sup>7</sup> cycles, competing with conventional floating-gate and charge-trapping memory technologies.[81]

Despite these advantages, challenges such as charge trapping and interfacial degradation persist, requiring further optimization of ferroelectric layers and interface engineering. Multi-level cell operation has been explored by exploiting single-domain switching, although the memory window remains constrained by ferroelectric layer thickness and material properties.[82]

Beyond memory technologies, HfO<sub>2</sub>-based ferroelectrics are being applied in energy-related domains. For instance, field-induced phase transitions in HfO<sub>2</sub>-ZrO<sub>2</sub> solid solutions have enabled energy storage densities up to 46 J/cm<sup>3</sup> with good thermal stability, making them suitable for electrostatic supercapacitors.[83] Similarly, doped HfO<sub>2</sub> films have shown strong pyroelectric responses for use in infrared sensing, rivaling traditional materials like lithium niobate.[84] These applications benefit from HfO<sub>2</sub>'s backend-of-line (BEOL) CMOS compatibility, supporting monolithic integration into existing platforms. Furthermore, thick HfO<sub>2</sub> films have demonstrated promising piezoelectric responses,[85] enabling applications in actuators and high overtone bulk acoustic resonator (HBAR) filters, which will be discussed in detail in Chapter 7.

HfO<sub>2</sub>-based ferroelectrics are expected to enable future technologies like neuromorphic computing, reconfigurable logic, and energy-efficient electronics. Ongoing research into 3D FeRAM, negative capacitance, and novel architectures is driving improvements in performance and reliability [15, 86].

## 2.3 Growth techniques

HfO<sub>2</sub>-based thin films are most commonly integrated into a metal–ferroelectric–metal (MFM) capacitor stack, which provides a straightforward platform for electrical characterization such as polarization–electric field (P–E) hysteresis, current–voltage (I–V) measurements, and endurance testing. While other device configurations are possible, here we focus on the MFM architecture, typically realized on silicon substrates in the form Si/SiO<sub>2</sub>/electrode/HfO<sub>2</sub>/electrode. The conventional fabrication sequence, illustrated in Figure 2.9, begins with substrate preparation and bottom electrode deposition, followed by deposition of the HfO<sub>2</sub> layer. After annealing at 400–1000 °C to induce crystallization, a top electrode is deposited—commonly by sputtering or evaporation—and patterned to define the final device. The choice of electrode and substrate materials, along with the annealing conditions, plays a critical role in determining the quality and functionality of the resulting film.

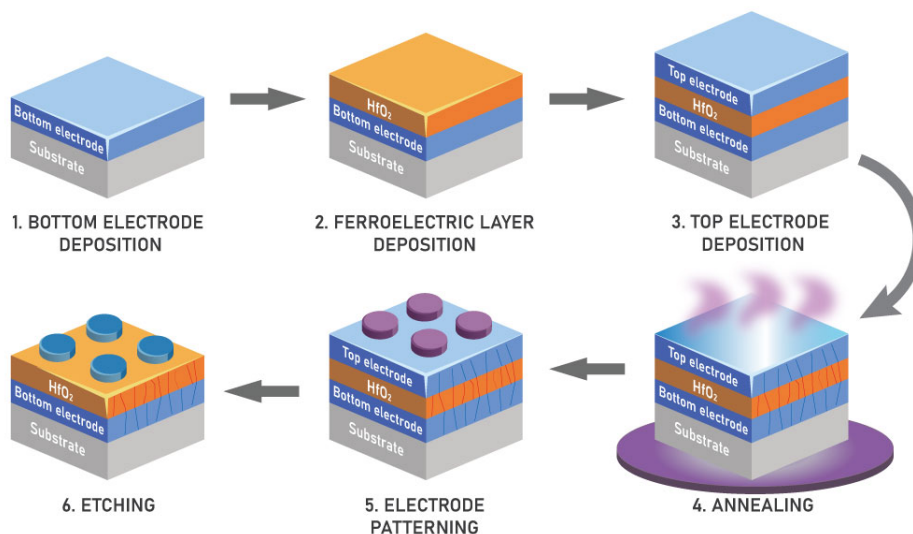


**Figure 2.9** Conventional fabrication procedure includes (1) deposition of bottom electrode, (2) growth of ferroelectric layer (using ALD, sputter deposition, PLD, or CSD), (3) top electrode deposition, (4) crystallization, (5) electrode patterning using photolithography or hard mask, and (6) etching excess electrodes.

A defining challenge for HfO<sub>2</sub> ferroelectrics is stabilization of polar o-phase which depends on film thickness, dopant type and concentration, mechanical stress, and thermal processing. This makes the growth process fundamentally different from that of conventional perovskite ferroelectrics such as Pb(Zr,Ti)O<sub>3</sub> (PZT) or (Ba,Sr)TiO<sub>3</sub> (BST), where the

ferroelectric phase is thermodynamically favored. As a result, the deposition technique is not merely a matter of fabrication convenience but a decisive factor in phase evolution and device performance. The following subsections discuss the main deposition techniques, while a dedicated section is provided on chemical solution deposition, the method employed in this PhD work.

### 2.3.1 Atomic layer deposition

Atomic layer deposition (ALD) has emerged as the predominant technique for fabricating ferroelectric hafnium oxide thin films due to its exceptional thickness control, high conformality, and relatively low process temperatures.[45] The ALD process for  $\text{HfO}_2$  relies on sequential, self-limiting surface reactions using metalorganic precursors such as tetrakis(dimethylamino)hafnium (TDMA-Hf) or tetrakis(ethylmethylamino)hafnium (TEMA-Hf) with oxidizing agents including  $\text{H}_2\text{O}$ ,  $\text{O}_3$ , or  $\text{O}_2$  plasma. The choice of precursor significantly influences the optimal deposition temperature window, which typically ranges from 200–350° C for most Hf-based precursors. TDMA-Hf and TEMA-Hf have become the most widely adopted precursors in ferroelectric  $\text{HfO}_2$  fabrication, with TDMA-based processes generally resulting in lower carbon impurity concentrations and slightly larger grain sizes that favor the o-phase formation.

The optimization of ALD parameters is crucial for achieving robust ferroelectric properties in hafnia-based thin films. Process temperature must be carefully balanced to ensure complete precursor reactions while maintaining amorphous as-deposited films that enable greater control over subsequent crystallization during post-deposition annealing. The selection of oxygen source plays a critical role, with stronger oxidants like  $\text{O}_3$  producing denser films with reduced leakage current but potentially limiting conformality in high-aspect-ratio structures.[87, 88] Oxygen dose time has been identified as a particularly sensitive parameter, where shorter doses (1–5 seconds) typically yield optimal ferroelectric polarization by maintaining appropriate oxygen vacancy concentrations that stabilize the ferroelectric o-phase while suppressing the parasitic monoclinic phase.[89] Additionally, the use of oxygen-scavenging electrodes such as TiN enhances ferroelectric properties by creating beneficial oxygen-deficient conditions that further promote orthorhombic phase stability.[51, 71]

### 2.3.2 Sputter deposition

Sputter deposition offers significant advantages for the fabrication of ferroelectric HfO<sub>2</sub>-based thin films, particularly through its ability to achieve ferroelectricity with substantially lower dopant concentrations compared to ALD-grown films.[45, 90] This physical vapor deposition technique utilizes ceramic targets and can operate at room temperature or below 200°C, making it compatible with temperature-sensitive substrates while minimizing carbon contamination due to the absence of metalorganic precursors.[91] The ballistic nature of the sputtering process creates favorable conditions for oxygen vacancy formation through physical bombardment, which helps stabilize the ferroelectric o-phase. Studies have demonstrated that optimal ferroelectric properties in Y-doped HfO<sub>2</sub> films can be achieved with doping concentrations as low as 1.9 mol.%, significantly lower than the 5 mol.% typically required for ALD or chemical solution-deposited films.[49]

The oxygen stoichiometry during sputter deposition critically influences the ferroelectric properties of HfO<sub>2</sub> films, with oxygen-deficient growth conditions promoting the formation of the o-phase.[92] Research has shown that reducing the O<sub>2</sub>/(Ar + O<sub>2</sub>) ratio during deposition enhances remanent polarization values, with some studies achieving P<sub>r</sub> values of 20 μC/cm<sup>2</sup> under oxygen-lean conditions (O<sub>2</sub>/(O<sub>2</sub> + Ar) = 0).[93] The working pressure during deposition also plays a crucial role, where lower pressures ( $\leq 5 \times 10^{-3}$  mbar) favor the formation of amorphous films that subsequently crystallize into the ferroelectric phase during annealing, while higher pressures promote undesirable monoclinic phase formation.[94, 95] However, sputter deposition has limitations including its line-of-sight nature making it unsuitable for three-dimensional structures, variability in target composition across vendors, and typically higher annealing temperatures (800-1000°C) required for crystallization compared to ALD-grown films.[91]

### 2.3.3 Pulsed laser deposition

Pulsed laser deposition (PLD) has emerged as a powerful technique for synthesizing high-quality epitaxial ferroelectric HfO<sub>2</sub>-based thin films, offering unique advantages over conventional atomic layer deposition (ALD) and sputter deposition methods.[96] The PLD process involves three main stages: laser ablation of the target material using high-fluence

pulsed beams (typically  $1\text{--}2\text{ J/cm}^2$ ), formation of an energetic plume, and subsequent condensation onto heated substrates. [97] This technique enables precise stoichiometric control, high deposition rates ( $\sim 100\text{ \AA/min}$ ), and the ability to access chemically non-equilibrium or metastable compositions under non-thermal conditions. The epitaxial nature of PLD-grown films eliminates complicating factors such as grain boundaries and phase impurities that plague polycrystalline films, making it an ideal platform for fundamental ferroelectric studies.[96, 98–101]

The strain engineering capabilities of PLD have proven crucial for stabilizing the ferroelectric o-phase in  $\text{HfO}_2$ -based films.[101, 102] Epitaxial studies using various substrate materials with lattice parameters ranging from  $3.71$  to  $4.21\text{ \AA}$  have demonstrated that tensile strain states greater than  $0.5\%$  are optimal for o-phase formation, with remanent polarization values reaching up to  $34\text{ }\mu\text{C/cm}^2$  in ultrathin  $\text{Hf}_{0.5}\text{Zr}_{0.5}\text{O}_2$  films grown on  $\text{LSMO/SrTiO}_3$  substrates.[45, 103] In addition to the orthorhombic phase, Wei et al. reported the emergence of a rhombohedral (R3m) ferroelectric phase in epitaxially strained  $\text{Hf}_{0.5}\text{Zr}_{0.5}\text{O}_2$  films grown on  $\text{LSMO/SrTiO}_3$  substrates, which was suggested to originate from a strained cubic phase.[101] Remarkably, PLD-grown films exhibit fundamentally different phase evolution pathways compared to ALD and sputter-deposited counterparts, following the thermodynamically predicted sequence of monoclinic  $\rightarrow$  tetragonal  $\rightarrow$  orthorhombic transformations upon heating.[96, 101, 104] Additionally, PLD enables ferroelectricity in significantly thicker films (up to  $930\text{ nm}$  for Y-doped  $\text{HfO}_2$ ) and shows counterintuitive behavior where increased oxygen pressure during deposition enhances the orthorhombic phase fraction, contrasting sharply with trends observed in other deposition methods.[99, 105]

### 2.3.4 Chemical solution deposition

Unlike vapor-phase techniques such as ALD, sputtering, or PLD, chemical solution deposition (CSD) relies on wet-chemical processing, where metal–organic or inorganic precursors are dissolved in solution and subsequently deposited onto the substrate by methods like spin-coating, dip-coating, or inkjet printing.[106] Starschich et al. first demonstrated ferroelectric Y-doped  $\text{HfO}_2$  films via CSD in 2014, utilizing hafnium 2,4-pentandionate and yttrium 2,4-pentandionate precursors in a propionic acid solution. [37] The process involves multiple spin-coating cycles with intermediary thermal treatments, where each layer undergoes

pre-heating at temperatures ranging from 215–295°C to evaporate solvents and densify the film through the formation of hafnium clusters with bridging oxo-groups and carboxylate ligands.

A distinctive advantage of CSD-grown ferroelectric HfO<sub>2</sub> films is their ability to maintain ferroelectricity at significantly larger thicknesses compared to ALD or sputtered films.[85] While conventional thin film ferroelectric HfO<sub>2</sub> typically exhibits thickness limitations below 30 nm, CSD-based films have demonstrated ferroelectricity in thickness ranges from 34 nm to as high as 1 μm. [107, 108] This enhanced thickness stability is attributed to the fine-grained microstructure characteristic of CSD films, with typical grain sizes of approximately 10 nm that remain relatively insensitive to film thickness. The fine grain structure maintains high grain boundary density throughout the film, which helps stabilize the ferroelectric o-phase over the thermodynamically preferred monoclinic phase. This property was particularly relevant to the present PhD work, where one of the main objectives was to exploit the piezoelectric properties of HfO<sub>2</sub>. Achieving this required thicker films over large substrate areas, and CSD provided a practical route to meet this requirement.

The optimization of CSD process parameters reveals several critical factors for achieving high-quality ferroelectric films. The intermediary annealing step between layer depositions emerges as particularly crucial, where temperature, duration, and atmospheric conditions must be carefully controlled. Studies have shown that pre-annealing temperatures between 215-295°C significantly affect film quality, with lower temperatures maintaining better solution-like homogeneity and resulting in higher remanent polarization values up to 20 μC/cm<sup>2</sup> for 5.2 mol.% Y-doped films. [109] Various dopants including Y, La, Nd, Sm, and Er have been successfully incorporated, with optimal doping concentrations typically around 5 mol.% showing similar ferroelectric responses across different dopant systems.

Despite these advantages, CSD-derived ferroelectric HfO<sub>2</sub> films face significant challenges that limit their practical implementation. Almost all CSD films exhibit pronounced wake-up effects requiring thousands of switching cycles to achieve maximum polarization, along with poor endurance characteristics typically limited to 10<sup>3</sup>–10<sup>4</sup> cycles[45] These issues stem from residual carbon content and oxygen vacancy formation, which contribute to increased leakage currents and degraded switching behavior. Recent advances have focused on multi-step annealing processes in oxygen atmospheres to mitigate oxygen deficiency and

remove wake-up procedure, with some success in improving endurance to  $10^5$  cycles for optimized process conditions. [110] A benchmarking of the results from this PhD against current CSD literature is presented in Chapter 8.

Having introduced CSD in the context of ferroelectric  $\text{HfO}_2$  growth, we now turn to a more detailed discussion of the fundamental principles of this technique in the following section.

## 2.4 Theory and principles of CSD

In the CSD process, metal precursors are initially dispersed and reacted in a liquid medium. The resulting solution is subsequently deposited onto a substrate to form a thin layer. A sequence of thermal treatments is then required to transform the precursor solution into a solid crystalline film. The main stages of the CSD process are illustrated in Fig. 2.10 and summarized as follows:

1. **Solution preparation.** The precursor solution must be homogeneous and stable, consisting of well-dispersed metal cations. Metal precursors are chosen based on their solubility in the solvent and compatibility with subsequent processing steps. In addition, the viscosity of the solution should be tailored to the selected deposition method through appropriate choice of solvents.
2. **Solution deposition.** The solution is deposited onto the substrate using techniques such as spin coating, dip coating, or inkjet printing. This step ensures a uniform liquid layer on the substrate surface, with the film thickness controlled by the deposition parameters.
3. **Low-temperature annealing.** Following deposition, organic components must be removed. Generally, a drying step ( $100\text{--}200^\circ\text{C}$ ) is carried out to evaporate the solvent first. The dried layer is then subjected to pyrolysis ( $350\text{--}500^\circ\text{C}$ ) to eliminate residual organics, although in some processes pyrolysis alone may suffice. After pyrolysis, the film typically consists of an amorphous metal oxide. Multiple deposition–annealing cycles may be performed to achieve the desired thickness.

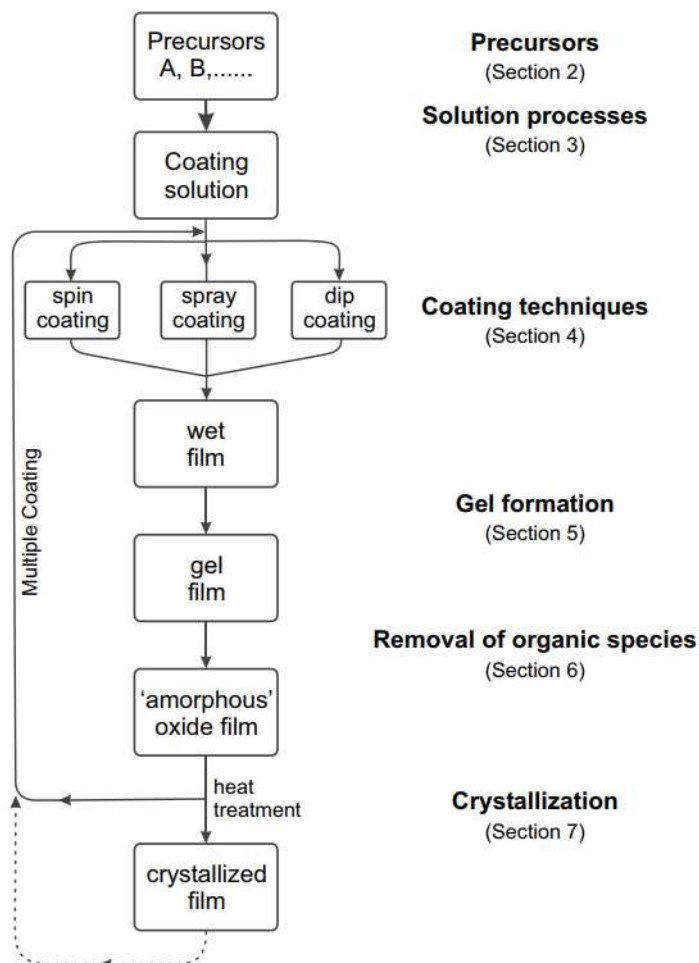


**Figure 2.10** CSD process flow. Reproduced from [111]

- 4. High-temperature annealing.** After pyrolysis, the amorphous film is crystallized by heating at 600–800°C. To avoid cracking during thermal treatment, thick films are generally obtained through repeated deposition and annealing cycles.

CSD methods can be categorized based on the water reactivity of their precursors, with the two most common approaches being sol–gel and metal–organic decomposition (MOD).

### 2.4.1 Classical sol–gel systems

In classical sol–gel systems, metal alkoxides undergo hydrolysis and condensation to form a three-dimensional M–O–M network that entraps solvent molecules.[111] These reactions convert alkoxides into metal hydroxides, which then condense via alcohol or water elimination, producing short-chain oligomers that crosslink to form chemical gels. Such gels are insoluble in their original solvents and can be processed into dense films. After

deposition, the wet films are dried and pyrolyzed at moderate temperatures (200–450 °C) to remove solvents and organic residues, followed by high-temperature annealing to induce crystallization and densification. During annealing, the gel network undergoes structural rearrangements at the atomic level, establishing a stable M–O–M network. Sol–gel systems offer excellent control and reproducibility of the chemical processes, though some commonly used solvents, such as 2-methoxyethanol for perovskite films, pose significant safety and toxicity concerns.

### 2.4.2 Metal–organic decomposition

MOD utilizes precursors such as carboxylates or  $\beta$ -diketonates, which exhibit minimal reactivity towards water or other nucleophiles. In these systems, the precursor molecules remain intact in solution, and oxide formation occurs only during pyrolytic decomposition at elevated temperatures.

#### Hafnia MOD synthesis

For ferroelectric hafnia thin films, the MOD approach is commonly employed.[37] Typical precursors include Hf(IV) acetylacetonate. The precursors are usually dissolved in polar organic solvents such as propionic acid or solvent mixtures, often with small amounts of additives to stabilize the solution and control viscosity. Unlike classical sol–gel systems, no hydrolysis–condensation occurs in solution. Spin-coating these solutions onto substrates produces uniform films, which are subsequently subjected to low-temperature drying, pyrolysis, and high-temperature annealing to crystallize HfO<sub>2</sub>, often with controlled dopant incorporation. The steps are detailed in Chapter 3.

Recent work by Badillio et al.[112] has demonstrated a greener variant of MOD for ferroelectric HfO<sub>2</sub>, in which Hf(acac)<sub>4</sub> and dopants (e.g., Ca(acac)<sub>2</sub>) are dissolved in isopropanol with small amounts of lactic acid and triethylamine. This approach enables dissolution at moderate temperatures (below 100°C) under ambient conditions, avoiding hazardous solvents like propionic anhydride.

### 2.4.3 Crystallization mechanisms in CSD

The crystallization of solution-deposited thin films is governed by thermodynamic principles, where the primary driving force is the reduction in Gibbs free energy as the material transforms from a higher-energy amorphous state to a lower-energy crystalline state. This transformation is illustrated in Figure 2.11, which shows the free energy diagram for a CSD-derived amorphous film, equilibrium liquid, and crystalline phases as a function of temperature. The thermodynamic driving force for crystallization ( $\Delta G_v$ ) represents the free energy difference between the amorphous and crystalline states, providing the energy available to overcome nucleation barriers.

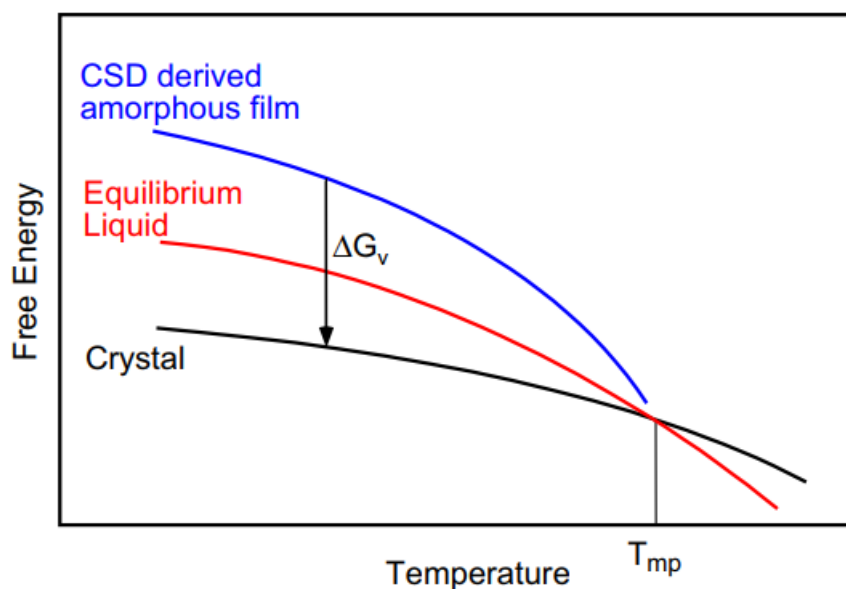


**Figure 2.11** Free energy–temperature diagram illustrating the metastable nature of CSD-derived amorphous films compared to the equilibrium liquid and crystalline phases. The driving force for crystallization is given by  $\Delta G_v$ . Reproduced from [111]

The amorphous state typically possesses higher free energy due to several factors including increased surface area, residual hydroxyl groups, and excess free volume from the solution deposition process. As temperature increases toward the melting point ( $T_{mp}$ ), the driving force for crystallization decreases, affecting the nucleation kinetics and ultimately the film microstructure.

Film crystallization occurs through nucleation and growth processes that can follow two distinct pathways. Homogeneous nucleation within the bulk of the film, or heterogeneous

nucleation at interfaces such as the substrate/film interface, film surface, or at pre-existing seeds and impurity phases. Heterogeneous nucleation generally requires a lower energy barrier and is often the preferred pathway for achieving controlled microstructures.

For solution-deposited hafnia films, the preference between homogeneous and heterogeneous nucleation is significantly influenced by the material's intrinsic properties and processing conditions. While heterogeneous nucleation is generally thermodynamically favorable in thin films, the situation becomes more complex for high melting point materials like BST, ZrO<sub>2</sub> or HfO<sub>2</sub>. The exceptionally high melting temperature of HfO<sub>2</sub> (2700°C) is considerably higher than typical crystallization temperatures used in CSD processing (e.g., 800°C). When the crystallization temperature is significantly lower than the material's melting temperature, the thermodynamic driving force for crystallization becomes very high. Under these conditions, both heterogeneous and homogeneous nucleation events can become equally probable, and homogeneous nucleation may even prevail over heterogeneous nucleation.[106, 111, 113] The prevalence of homogeneous nucleation often leads to the formation of porous films with small, randomly oriented grains, a common challenge observed in HfO<sub>2</sub> and ZrO<sub>2</sub>-based CSD films. Such microstructures are detrimental to ferroelectric properties due to high porosity, grain boundary density, and lack of preferential orientation, ultimately resulting in films with poor electrical performance and high leakage currents.

The crystallization challenges described above are particularly relevant for hafnia-based ferroelectric films, where achieving optimal microstructure is critical for functional device performance. The tendency toward homogeneous nucleation and the resulting porous, randomly oriented microstructures represent significant obstacles that must be addressed through careful process design.

Two primary approaches are employed for hafnia film processing. The first approach, known as the conventional route, involves sequential deposition of amorphous layers followed by a single post-deposition crystallization step. While simpler to implement, this method is particularly susceptible to the nucleation challenges described above and often leads to lower film density and higher leakage currents due to incomplete densification and residual porosity. The second approach, referred to as the layer-by-layer (L/L) method, involves sequential deposition with partial crystallization of each individual layer. This

strategy mitigates crystallization challenges by promoting heterogeneous nucleation at interfaces and reducing the effective film thickness per crystallization event.

The effectiveness of these different processing routes in controlling crystallization behavior, film density, and electrical properties in hafnia-based ferroelectric systems will be demonstrated through specific case studies presented in subsequent chapters, with detailed process flows outlined in Chapter 3.

#### 2.4.4 Stability of oxides during annealing

The annealing atmosphere plays a crucial role in determining the final properties of oxide thin films by controlling the oxygen chemical potential during high-temperature processing. For ferroelectric HfO<sub>2</sub> films, the atmosphere composition directly influences oxygen vacancy formation, which in turn affects both the stabilization of the polar orthorhombic phase and the electrical properties of the resulting devices.

While thin film processing often occurs under non-equilibrium conditions, bulk thermodynamic principles provide a useful framework for understanding the relative stability of different phases and the driving forces for oxidation-reduction reactions. Ellingham diagrams plot the standard Gibbs free energy change ( $\Delta G^\circ$ ) for oxidation reactions as a function of temperature, offering insight into the thermodynamic stability of metal oxides under different oxygen partial pressures ( $pO_2$ ). Figure 2.12 shows the Ellingham diagram for HfO<sub>2</sub>. At equilibrium, the relationship between  $\Delta G^\circ$  and oxygen partial pressure is given by:

$$\log(pO_2) = \frac{\Delta G^\circ}{2.303RT}$$

where R is the gas constant (1.987 cal mol<sup>-1</sup> K<sup>-1</sup>) and T is the absolute temperature in Kelvin, with the right-hand axis showing the corresponding log( $pO_2$ ) values.

From the Ellingham diagram, HfO<sub>2</sub> exhibits very high thermodynamic stability, with equilibrium  $pO_2$  values of approximately 10<sup>-30</sup>–10<sup>-35</sup> atm at typical annealing temperatures (800–1000°C). This indicates that the annealing atmospheres employed in thin film processing—ranging from pure oxygen ( $pO_2 \approx 0.2$  atm) to high-purity inert gases ( $pO_2 \approx 10^{-8}$ –10<sup>-10</sup> atm)—all maintain oxygen partial pressures far above the threshold for bulk HfO<sub>2</sub>

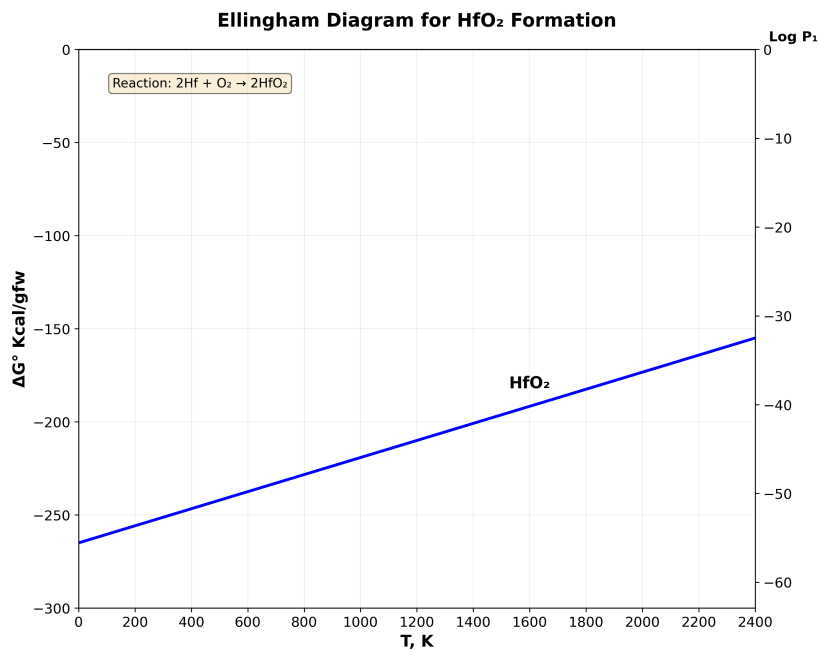
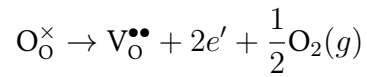


**Figure 2.12** Ellingham diagram for  $\text{HfO}_2$  showing the standard Gibbs free energy of formation as a function of temperature. The right axis indicates the equilibrium oxygen partial pressure ( $\log p_{\text{O}_2}$ ) [114].

reduction. Therefore, complete reduction to metallic hafnium is not thermodynamically favorable under typical processing conditions.

However, it is important to recognize that thin film behavior often deviates significantly from bulk equilibrium thermodynamics. The ferroelectric orthorhombic phase ( $\text{Pca}2_1$ ) is itself a metastable phase stabilized by dopants, finite size effects, and kinetic trapping—none of which are represented in equilibrium phase diagrams. Furthermore, thin films are characterized by high surface-to-volume ratios, interfacial constraints, and limited atomic reservoirs, all of which can lead to non-equilibrium defect concentrations and phase compositions. The Ellingham framework is therefore most useful for understanding relative trends and thermodynamic driving forces rather than absolute predictions of thin film structure.

Despite these limitations, the oxygen partial pressure established by the annealing atmosphere remains a critical process variable. While bulk stoichiometric  $\text{HfO}_2$  is stable across a wide  $p_{\text{O}_2}$  range, the atmosphere significantly influences the concentration of point defects, particularly oxygen vacancies, through the formation of non-stoichiometric phases ( $\text{HfO}_{2-x}$ ). The defect formation reactions in  $\text{HfO}_2$  can be represented using Kröger-Vink notation:



where  $\text{O}_0^\times$  is a lattice oxygen,  $\text{V}_0^{\bullet\bullet}$  is a doubly charged oxygen vacancy, and  $e'$  represents electrons. Higher  $p\text{O}_2$  suppresses vacancy formation (equilibrium shifts left), while lower  $p\text{O}_2$  promotes vacancy generation (equilibrium shifts right). Different gas compositions establish distinct  $p\text{O}_2$  regimes: pure  $\text{O}_2$  provides the highest  $p\text{O}_2$  and suppresses vacancies, inert gases provide lower  $p\text{O}_2$  and promote vacancies, and  $\text{N}_2:\text{O}_2$  mixtures offer intermediate and tunable conditions.

# Chapter 3

## Fabrication methodologies

This chapter outlines the growth process flow for the thin films studied in this work. Section 3.1 describes the synthesis of the solutions necessary for spin-coating  $\text{HfO}_2$  thin films. Section 3.2 discusses the design of rapid thermal annealing recipes used to achieve crystallization. Section 3.3 presents the detailed process flows for different types of films. Finally, Section 3.4 covers the electrode patterning steps required for subsequent electrical characterization.

### 3.1 Solution preparation

The thin films investigated in this thesis are synthesized via chemical solution deposition (CSD), a process previously introduced in Section 2.3. This technique involves two key stages: the preparation of a metal-organic precursor solution, followed by thin film fabrication through spin-coating and subsequent thermal processing. Two distinct deposition strategies were employed to achieve intended thicknesses. As illustrated in Figure 3.1a, the conventional route involved sequential deposition of amorphous layers, followed by a single post-deposition crystallization. In contrast, the layer-by-layer (L/L) method, shown in Figure 3.1b, involved crystallization of each layer.

#### 3.1.1 $\text{La:HfO}_2$ and $\text{ZrO}_2$ solutions

Since the synthesis procedures for  $\text{La:HfO}_2$  and  $\text{ZrO}_2$  solutions are nearly identical, differing only in the choice of precursor powders, they are presented together in this section. For the

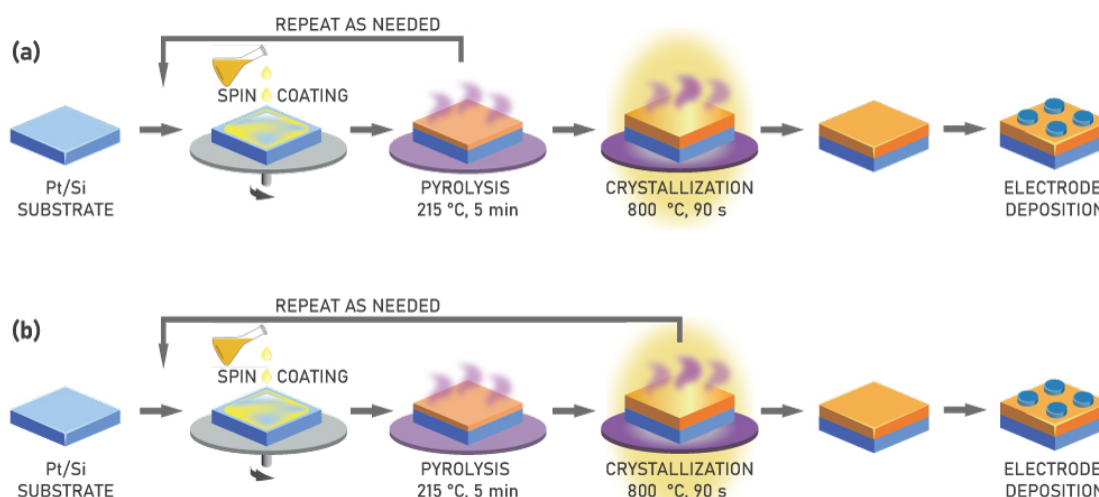


**Figure 3.1** CSD growth routes. (a) Conventional, and (b) layer-by-layer route.

synthesis of 5% La-doped  $\text{HfO}_2$ , Hf(IV)-acetylacetonate (Alfa Aesar, 97%) and La(III)-acetate hydrate (Sigma-Aldrich, 99.9%) were used as metal precursors. Prior to use, La(III)-acetate hydrate was freeze-dried for 16 h to eliminate crystal water. In the case of pure  $\text{ZrO}_2$ , Zr(IV)-acetylacetonate (Sigma-Aldrich, 97%) was used. The precursor powders were dissolved in propionic acid (Sigma-Aldrich, 99.5%) and subjected to reflux at 150 °C for 3 h under an argon atmosphere, using a modified Schlenk line and magnetic stirring to ensure homogeneity. Two distinct precursor concentrations, 0.08 M and 0.28 M, were prepared for La: $\text{HfO}_2$  and  $\text{ZrO}_2$  to achieve target film thicknesses of approximately 5 nm and 15 nm,[109] respectively.

### 3.1.2 $\text{CeO}_2$ solution

For the synthesis of  $\text{CeO}_2$ , cerium nitrate hexahydrate (Sigma-Aldrich, 99.99%) was dissolved in 2-methoxyethanol (2-MOE), stirred in a silicon oil bath at 50 °C for 20 min, followed by continued stirring at room temperature for 4 h. The resulting solution, with a concentration of 0.25 mol/L, was formulated to achieve a target film thickness of approximately 15 nm.

## 3.2 Spin-coating and pyrolysis

Once the solutions were prepared, thin films were grown onto (111)-oriented platinumized silicon substrates. The substrates, measuring  $2.5 \times 2.5 \text{ cm}^2$ , were obtained by manual cleavage of a 6-inch platinumized silicon wafer supplied by Sintef, Norway. Prior to deposition,

the substrates were always degassed on a hot plate at 350 °C for 5 minutes. The solutions were deposited onto the substrates using 3 mL syringes fitted with 0.2 µm PTFE filters (13 mm diameter). The spin-coating program consisted of two steps: (1) 50 rpm for 10 s to ensure homogeneous spreading of the deposited solution, and (2) 3000 rpm for 30 s to remove excess solution and reach the final thickness. After spin coating, the films were pyrolyzed at 215 °C for 5 minutes on hot plates.

### 3.3 Rapid thermal annealing process

The crystallization of thin films was carried out using a rapid thermal chemical vapor deposition (RTCVD) system, the AS-Master 2000 (Annealsys) tool, following a precisely controlled multi-step procedure. The process consisted of system preparation, chamber conditioning, gas flow management, and thermal treatment phases, as summarized in Table 3.1 and described in detail below. Here, we present an example of crystallization performed in a N<sub>2</sub>:O<sub>2</sub> (1:1) atmosphere, which represents the standard configuration employed for film crystallization in this thesis. However, other gas mixture configurations, such as pure Ar or Ar:O<sub>2</sub>, were also used for the study presented in Chapter 4.

#### 3.3.1 System and chamber preparation for crystallization

Prior to each crystallization run, the system underwent preparation to ensure optimal processing conditions. Gas lines were pumped to remove residual gases (step 1 and 2), followed by pressure conditioning through controlled throttle valve positions and vacuum establishment (step 3). The primary pumping chamber was then activated (step 5) to establish the main vacuum for crystallization, followed by a 30 s soft pumping period (step 6) to remove residual gases. Chamber pressure was then adjusted to a position control setpoint of 10° (step 7), followed by another 30 s soft pumping period (step 8) as a transition to the final processing pressure. Finally, the position was set to 90° (step 9), representing the final pressure configuration. A critical pressure monitoring step (step 10) ensured the chamber pressure dropped below 4 mBar before proceeding. An additional 30-s conditioning period (step 11) under active pumping allowed the chamber to reach pressure equilibrium.

No	Operation type	Operation details
1	Pumping gas lines	Pumping in gas line 1 during 10 seconds
2	Pumping gas lines	Pumping in gas line 2 during 10 seconds
3	Pressure	Position control: setpoint = 2°
4	Condition	Waiting for Duration = 2s
5	Pumping	Start primary pumping chamber
6	Condition	Waiting for Duration = 30s
7	Pressure	Position control: setpoint = 10°
8	Condition	Waiting for Duration = 30s
9	Pressure	Position control: setpoint = 90°
10	Condition	Waiting for Capa < 4 mBar
11	Condition	Waiting for Duration = 30s
12	Pumping	Stop
13	Gas	Setpoints (sccm) → Ramp = 30s; N <sub>2</sub> : Ramp to 1000 sccm; O <sub>2</sub> : Ramp to 1000 sccm
14	Condition	Waiting for atmospheric pressure
15	Gas	Setpoints (sccm) → N <sub>2</sub> : 125 sccm; O <sub>2</sub> : 125 sccm
16	Condition	Waiting for Duration = 2s
17	RTP Temp	Pyro control mode to 800°C with ramp at 50°/s
18	Condition	Waiting for Duration = 90s
19	RTP Temp	POWER control mode to 0% during 1s
20	Condition	Waiting for Pyro < 200°C
21	Gas	Setpoints (sccm) → N <sub>2</sub> : 0 sccm; O <sub>2</sub> : 0 sccm

**Table 3.1** Rapid thermal annealing (RTA) process used for film crystallization.

### 3.3.2 Process gas introduction and flow control

Following chamber evacuation, process gases were ramped in to ensure uniform distribution and avoid thermal shock from cooler gases entering the heated chamber. Nitrogen (N<sub>2</sub>) and oxygen (O<sub>2</sub>) flows were simultaneously increased to 1000 sccm over 30 s (step 13), filling the chamber completely. A stabilization phase (step 14) then allowed the system to reach atmospheric pressure, ensuring full displacement of the residual vacuum. Once stabilized,

gas flows were set to processing conditions of  $N_2 = 125$  sccm and  $O_2 = 125$  sccm (step 15), providing the required crystallization environment. A final 2-s stabilization (step 16) ensured steady-state flows before thermal treatment began.

### 3.3.3 Rapid thermal processing and crystallization

The crystallization treatment began with rapid heating under pyrometer (Pyro) control, where lamp power was adjusted to maintain the measured substrate surface temperature. The temperature was ramped to  $800^\circ\text{C}$  at  $50^\circ\text{C}/\text{s}$  (step 17) and held for 90 s (step 18) to enable full crystallization of the film. Cooling was then initiated in POWER control mode, with lamp power set to 0% for 1 s (step 19), followed by monitoring until the Pyro temperature dropped below  $200^\circ\text{C}$  (step 20). Unlike Pyro mode, POWER mode directly sets lamp power, enabling rapid cooling to minimize thermal stress and cracking while preserving crystallinity. Finally,  $N_2$  and  $O_2$  flows were reduced to 0 sccm (step 21), transitioning to an inert atmosphere and terminating reactive gases. This sequence ensured precise control of gas composition, pressure, temperature, and cooling, yielding reproducible crystallization with minimal contamination and stress.

## 3.4 Thin film fabrication steps

In this section, the fabrication steps of the various thin films investigated in this thesis is presented. Table 3.2 summarizes all samples, the concentration of precursor solutions used, and the corresponding process flows, while Figure 3.2 illustrates the schematic diagram of the film stacks.

The samples are labeled as HO, ZO, HZO, ZHO, and HCO, which correspond to  $\text{La:HfO}_2$ ,  $\text{ZrO}_2$ ,  $\text{La:HfO}_2\text{-ZrO}_2$  multilayers,  $\text{ZrO}_2\text{-La:HfO}_2$  multilayers, and  $\text{La:HfO}_2\text{-CeO}_2$  bilayers, respectively. Each sample name carries a subscript denoting the fabrication route, conventional (C) or layer-by-layer (L), followed by the final film thickness in nanometers. For example, the sample  $\text{HZO}_{C50}$  refers to a  $\text{La:HfO}_2\text{-ZrO}_2$  multilayer prepared by the conventional route has a total thickness of 50 nm.

As described earlier, a 0.25 M precursor solution typically yields a thickness of approximately 15 nm per spin-coating cycle, whereas a 0.08 M solution results in about 5 nm.

Sample name	Sol conc. (M)	Process flow	Figure
HO <sub>C45</sub>	0.25	3 (S <sub>Hf</sub> → P) → A	3.2(a)
HO <sub>C90</sub>	0.25	6 (S <sub>Hf</sub> → P) → A	3.2(b)
HO <sub>C200</sub>	0.25	14 (S <sub>Hf</sub> → P) → A	3.2(c)
HO <sub>L50</sub>	0.08	10 (S <sub>Hf</sub> → P → A)	3.2(d)
ZO <sub>C45</sub>	0.25	3 (S <sub>Zr</sub> → P) → A	3.2(e)
HZO <sub>C50</sub>	0.08	5 [(S <sub>Hf</sub> → P) → (S <sub>Zr</sub> → P)] → A	3.2(f)
HZO <sub>C90</sub>	0.25	3 [(S <sub>Hf</sub> → P) → (S <sub>Zr</sub> → P)] → A	3.2(g)
ZHO <sub>C50</sub>	0.08	5 [(S <sub>Zr</sub> → P) → (S <sub>Hf</sub> → P)] → A	3.2(h)
HCO <sub>L30</sub>	0.25	1 [(S <sub>Hf</sub> → P → A) → (S <sub>Ce</sub> → P → A)]	3.2(i)

**Table 3.2** List of thin film samples fabricated in this work. The table shows the sample labels, precursor solution concentrations, process flow steps, stack type, and the corresponding schematic figures (see Figure 3.2).

The “process flow” column in Table 3.2 outlines the sequence of fabrication steps. Here,  $S$  denotes a spin-coating step (with the subscript indicating the specific precursor: Hf for La:HfO<sub>2</sub>, Zr for ZrO<sub>2</sub>, and Ce for CeO<sub>2</sub>),  $P$  corresponds to pyrolysis, and  $A$  represents the final rapid thermal annealing step.

As an example, the process flow for sample HZO<sub>C50</sub> is expressed as:

$$5[(S_{\text{Hf}} \rightarrow P) \rightarrow (S_{\text{Zr}} \rightarrow P)] \rightarrow A.$$

This sequence indicates that one cycle of La:HfO<sub>2</sub> spin-coating and pyrolysis is followed by one cycle of ZrO<sub>2</sub> spin-coating and pyrolysis, and the entire sequence is repeated five times to achieve the target 50 nm multilayer HZO film. Finally, a rapid thermal annealing step is performed to complete the film fabrication.

### 3.5 Electrode patterning and deposition

Circular top electrodes (100 μm diameter) were fabricated using standard photolithography and lift-off processes. The electrode stack consisted of 100 nm Pt with a 5 nm Ti adhesion layer, deposited by electron-beam evaporation (MEB 600 Plassys) at a base pressure of

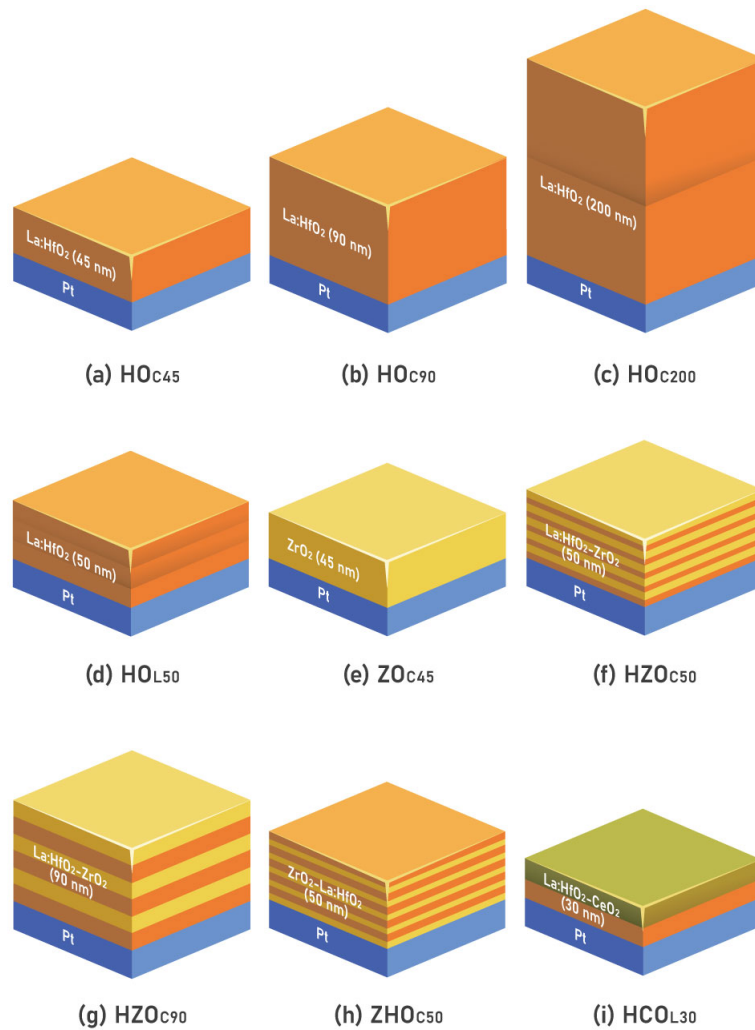


**Figure 3.2** Schematic of the thin films studied in this thesis. (a)  $\text{HO}_{C45}$ , (b)  $\text{HO}_{C90}$ , (c)  $\text{HO}_{C200}$ , (d)  $\text{HO}_{L50}$ , (e)  $\text{ZO}_{C45}$ , (f)  $\text{HZO}_{C50}$ , (g)  $\text{HZO}_{C90}$ , (h)  $\text{ZHO}_{C50}$ , and (i)  $\text{HCO}_{L30}$ .

$5 \times 10^{-8}$  mbar. Photolithography patterns were designed using KLayout software and transferred using a maskless aligner (Heidelberg MLA150). The resist stack comprised LOR3A lift-off resist (baked at  $160^\circ\text{C}$  for 5 min) and Shipley S1813 photoresist (baked at  $115^\circ\text{C}$  for 1 min). Following exposure and development in MF319 developer for 60 seconds, metal deposition and subsequent lift-off defined the final electrode geometry for the metal–insulator–metal (MIM) device structures.

For advanced characterizations, such as Raman spectroscopy and resonance measurements, Au(100 nm)/Cr(5 nm) electrodes were instead employed. These were also deposited

by electron-beam evaporation under the same base pressure conditions. The specific details of these fabrications are described in the following sections.

### 3.5.1 Electrode preparation for Raman spectroscopy

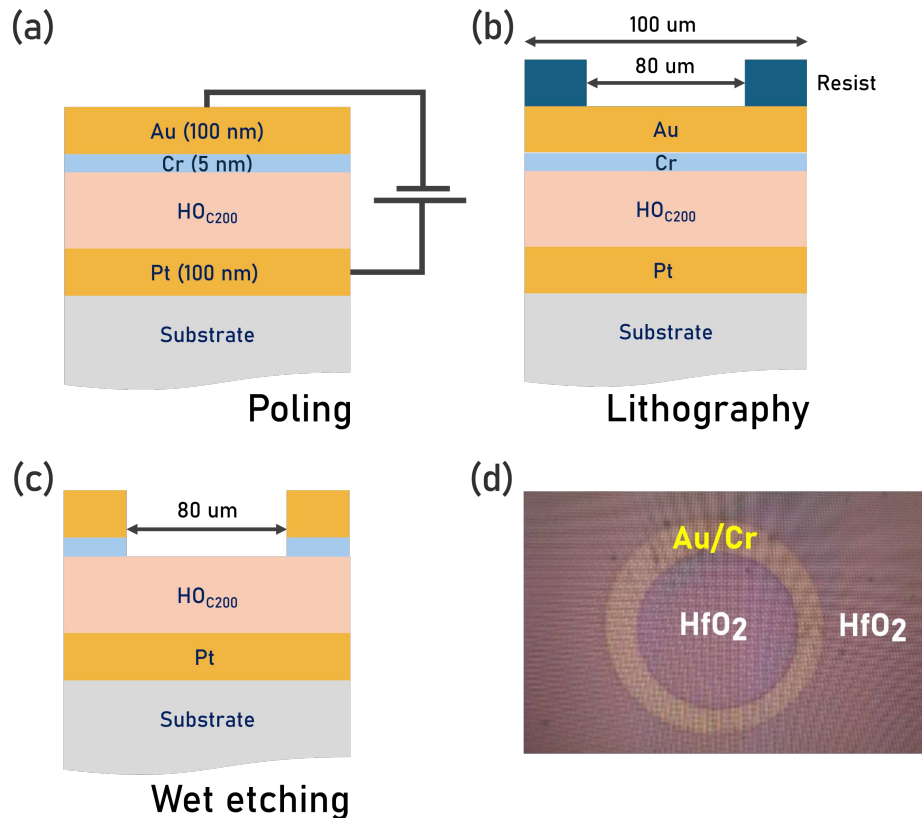


**Figure 3.3** (a) Schematic of the metal-insulator-metal stack with a Au(100 nm)/Cr(5 nm) top electrode (100  $\mu\text{m}$  diameter) for electric field treatment. (b) Lithographic mask design used to open the top electrode. (c) Stack after chemical etching of the Au/Cr layers. (d) Optical image showing measurement points for Raman spectra after top electrode removal post-poling. Raman measurements were performed within the bare circular  $\text{HfO}_2$  area inside the Au/Cr ring.

For Raman spectroscopy measurements on electrically cycled capacitors, a modified electrode configuration was employed consisting of 100 nm Au with a 5 nm Cr adhesion layer in a circular geometry of 100  $\mu\text{m}$  diameter, as shown in Figure 3.3(a). This Au/Cr electrode stack was specifically chosen to enable selective removal through wet chemical etching, allowing access to the underlying ferroelectric film for spectroscopic analysis. Following electrical poling of the capacitors to the desired field conditions, standard photolithography was used to pattern the top electrode area for partial removal (Figure 3.3(b)). The exposed

electrode regions were then selectively etched using a two-step wet chemical process: first, gold removal using potassium iodide (KI) in aqueous solution, followed by chromium removal using ammonium cerium(IV) nitrate and nitric acid. This process selectively exposed portions of the electrically poled ferroelectric film while preserving adjacent electrode areas.

This process resulted in a clean circular opening of approximately 80  $\mu\text{m}$  in diameter within the top electrode, providing direct access to the underlying La:HfO<sub>2</sub> film for Raman measurements (Figure 3.3(c)). The final structure, shown in Figure 3.3(d), consisted of an exposed region of the ferroelectric film surrounded by a ring-shaped Au/Cr electrode, which enabled localized post-poling Raman spectroscopy with minimal optical interference.



# Chapter 4

## Study of annealing atmosphere

Achieving reproducible processing outcomes often depends on careful optimization of each step, with annealing conditions playing a particularly important role. This chapter investigates the impact of the annealing atmosphere on the ferroelectric properties of  $\text{HfO}_2$  thin films. Section 4.1 presents the motivation for this study together with a brief review of relevant literature. The different annealing gas compositions examined in this work are described in Section 4.2. Section 4.3 discusses the structural and compositional modifications induced by varying annealing atmospheres, based on X-ray reflectivity and secondary ion mass spectrometry analyses. Section 4.4 then focuses on the wake-up behavior of thick films processed under the optimized annealing conditions. Finally, Section 4.5 summarizes the main findings and provides an outlook for future investigations.

### 4.1 Motivation

The annealing atmosphere represents one of the most critical yet poorly understood parameters in the fabrication of ferroelectric  $\text{HfO}_2$  thin films via chemical solution deposition. This thermal treatment step not only facilitates the removal of residual organics and film densification but also governs the crystallization pathway from an initially amorphous state to the desired ferroelectric phase. The atmospheric composition during annealing significantly influences the stabilization of the polar *o*-phase, which is essential for desirable ferroelectric properties. A thermodynamic background on oxide stability and oxygen partial pressure during annealing is provided in Chapter 2 (Section 2.4.4). However, the

precise role of oxygen during annealing remains debated in the literature.[110, 115] Some studies indicate that oxygen-rich atmospheres reduce oxygen vacancies and mitigate the wake-up effect,[115] whereas others report that oxygen deficiency enhances ferroelectricity by increasing vacancy concentrations in  $\text{HfO}_2$  thin films.[110]

Recent investigations have revealed that the atmospheric environment creates far more complex effects than simple oxygen stoichiometry control. The electrochemical state of hafnia surfaces is highly sensitive to atmospheric composition, with different gases creating distinct surface interaction mechanisms that fundamentally alter ferroelectric behavior.[116] Studies on uncapped hafnia films demonstrated that atmospheric species can passivate oxygen vacancies through surface adsorption, leading to environment-dependent transitions between ferroelectric and non-ferroelectric states. These findings suggest that the annealing atmosphere may establish persistent surface electrochemical states that influence not only initial crystallization but also long-term device stability and reproducibility.

The complexity of the relationship between annealing atmosphere and film property becomes particularly pronounced in solution-processed films, where organic precursor decomposition might occur simultaneously with crystallization. The kinetics of carbon removal, oxygen incorporation, and defect formation are intrinsically coupled and highly atmosphere-dependent. Furthermore, the industrial viability of solution-processed ferroelectric hafnia depends heavily on process robustness. Minor variations in annealing atmosphere composition, humidity, or trace contaminants can lead to substantial property variations between batches. Understanding the mechanistic origins of these sensitivities is essential for developing reliable manufacturing protocols. The environmental control required during annealing may extend beyond the commonly investigated oxygen partial pressure to include considerations of gas purity, moisture content, and even the sequence of atmospheric exposure during heating and cooling cycles.

Prior research on  $\text{Hf}_{0.5}\text{Zr}_{0.5}\text{O}_2$  films deposited by CSD has shown that the annealing atmosphere can dictate the resulting crystal phase. Specifically, nitrogen ( $\text{N}_2$ ) annealing tends to promote the orthorhombic phase, while air annealing favors the monoclinic phase.[117] This has been attributed to oxygen deficiency under  $\text{N}_2$ , which destabilizes the monoclinic phase and promotes the orthorhombic/tetragonal structures.[117] More recently, yttrium-doped  $\text{Hf}_{0.5}\text{Zr}_{0.5}\text{O}_2$  films annealed under vacuum at 800 °C demonstrated improved ferroelectric

properties and reduced leakage currents compared to films annealed in  $N_2$  or  $O_2$ .<sup>[115]</sup> These effects were linked to increased oxygen vacancy concentrations which is considered favorable for stabilizing the ferroelectric phase and suppressing leakage.

Conversely, multi-step CSD processes with repeated oxygen annealing cycles have been shown to reduce oxygen-vacancy-related defects and enable wake-up-free ferroelectricity in  $Y:HfO_2$  films.<sup>[115]</sup> These findings highlight the critical interplay between annealing-induced defect chemistry and both initial ferroelectric properties and their subsequent evolution under electrical cycling.

Beyond establishing the initial ferroelectric properties, understanding how these properties evolve under electrical cycling is essential for ensuring device reliability. However, the structural transformations that occur in CSD-derived films during the wake-up process remain poorly understood. Although conventional X-ray diffraction is useful for initial phase identification, it faces significant limitations in probing the effect of field-cycling on phases of  $HfO_2$  thin-films. The large X-ray spot size in laboratory diffractometers (typically several hundred micrometers) is fundamentally incompatible with the small dimensions of ferroelectric capacitors ( $< 100 \mu m$ ), preventing the extraction of phase information from electrically cycled regions. Raman spectroscopy provides a powerful alternative, offering both superior phase discrimination through vibrational fingerprints and spatial resolution on the order of a few micrometers—well matched to device-scale electrodes. This enables the investigation of wake-up behavior in capacitors with electrodes as small as a few micrometers.

In this chapter, we systematically investigate the influence of annealing atmosphere on the structural and ferroelectric properties of La-doped  $HfO_2$  45 nm thin films deposited via CSD. By examining various annealing gas compositions and their influence on film crystallization, defect formation, and ferroelectric behavior, we identify processing conditions that yield reproducible films with stable ferroelectric properties. Building upon these results, we leverage our capability to fabricate high-quality thick (200 nm)  $La:HfO_2$  films to investigate the wake-up mechanism using Raman spectroscopy.

## 4.2 Atmosphere conditions for annealing

Initial studies on solution-processed  $\text{HfO}_2$  films were conducted under  $\text{Ar}:\text{O}_2$  atmospheres.[43, 109] Such mixed-gas environments are widely employed during annealing to achieve a controlled balance between oxidation and crystallization. While pure  $\text{O}_2$  can lead to excessive oxidation and potential structural degradation, pure Ar may promote undesirable reduction of metal precursors. The  $\text{Ar}:\text{O}_2$  mixture provides moderated oxygen activity, facilitating controlled precursor decomposition, effective removal of organic residues, and improved phase purity and crystallinity. The optimal gas ratio is typically tailored to the specific precursor chemistry and the desired film properties.

However, when using oxygen-containing precursors such as metal acetates, nitrates, or alkoxides, annealing is often carried out in an inert atmosphere to avoid unwanted oxidation during decomposition. In practice,  $\text{N}_2$  is frequently used for this purpose and is particularly common in studies on  $\text{HfO}_2$  thin films grown by atomic layer deposition (ALD).[45, 118, 119]

Recent studies have explored the effects of annealing in pure  $\text{O}_2$ , pure  $\text{N}_2$ , and vacuum environments, demonstrating that the annealing atmosphere can significantly influence film properties. Schenk *et al.*, employed an  $\text{Ar}:\text{O}_2$  ratio of 1:1 for the annealing of  $\text{La}:\text{HfO}_2$  thin films.[85] However, in our experiments, similar conditions led to elevated leakage currents and inconsistent ferroelectric performance, underscoring the need for further optimization.

In this study, we systematically investigated the impact of three annealing atmospheres, pure Ar,  $\text{Ar}:\text{O}_2$ , and  $\text{N}_2:\text{O}_2$ , on the structural and ferroelectric properties of La-doped  $\text{HfO}_2$  films of  $\text{HO}_{C45}$  type (refer to Table 3.2 for sample nomenclature and process flow). In addition to gas composition, two key processing parameters, gas flow rate and annealing duration, were varied to evaluate their influence on film characteristics. For annealing in pure Ar, the gas flow rate was varied between 50 and 250 sccm. The effect of annealing duration was examined under a constant Ar flow rate of 125 sccm. In the case of mixed-gas environments ( $\text{Ar}:\text{O}_2$  and  $\text{N}_2:\text{O}_2$ ), the total gas flow was fixed at 300 sccm. The gas flow ratios were systematically varied to assess their impact on the structural and ferroelectric properties of the films.

The subsequent sections present and discuss the experimental findings, emphasizing the

influence of annealing atmosphere, flow rate, and duration on phase formation, crystallinity, and electrical performance of HO<sub>C45</sub> thin films.

### 4.2.1 Ar atmosphere

This section focuses on films annealed in a pure Ar atmosphere, with systematic variation in annealing time and gas flow rate. Three annealing durations, 45 s, 75 s, and 90 s, were selected for comparison. The corresponding GIXRD patterns are shown in Figure 4.1(a). All samples exhibit the characteristic pattern of polar orthorhombic phase, including a prominent (111) peak at 30.6° and a weaker (002) reflection at 35.5°, as discussed in Section 2.2 in Chapter 2. Additionally, a broad shoulder extending to approximately 31°–31.5° is observed on the high-angle side of this peak. Although this feature has frequently been attributed to the monoclinic phase in the literature, it is more accurately associated with the tetragonal (101) contribution. The monoclinic ( $P2_1/c$ ) phase, if present, would instead appear as two separate peaks at approximately 28.5° ( $-111_m$ ) and 31.5° ( $111_m$ ), located on either side of the composite o/t/c peak.[28] The GIXRD patterns show negligible variation across the three annealing durations. The absence of notable changes indicates that the equilibrium crystal structure and grain size are already achieved during the shortest annealing time, with extended durations offering no additional benefit.

The influence of varying annealing duration on ferroelectric switching is demonstrated in Figure 4.1(b) and Figure 4.1(c). Prominent switching current peaks are observed in all the films, which exhibit a coercive field ( $E_c$ ) of 2 MV/cm. For the films annealed in an Ar atmosphere for 45 s, 75 s, and 90 s, the remanent polarization ( $2P_r$ ) values are 17  $\mu\text{C}/\text{cm}^2$ , 19  $\mu\text{C}/\text{cm}^2$ , and 23  $\mu\text{C}/\text{cm}^2$ , respectively. However, all samples exhibit signs of leakage current, as indicated by the rounded shape of the hysteresis loops, particularly near the saturation region. The values of coercive field and remanent polarization with annealing time is summarized in Table 4.1.

Therefore, structural analysis confirms that crystallization in pure Ar atmosphere is effectively complete within 45 s, as indicated by minimal changes in GIXRD patterns. This rapid phase formation suggests that the orthorhombic phase is both thermodynamically and kinetically favored under the applied conditions. However, electrical measurements reveal a more nuanced behavior: although remanent polarization increases with longer annealing,

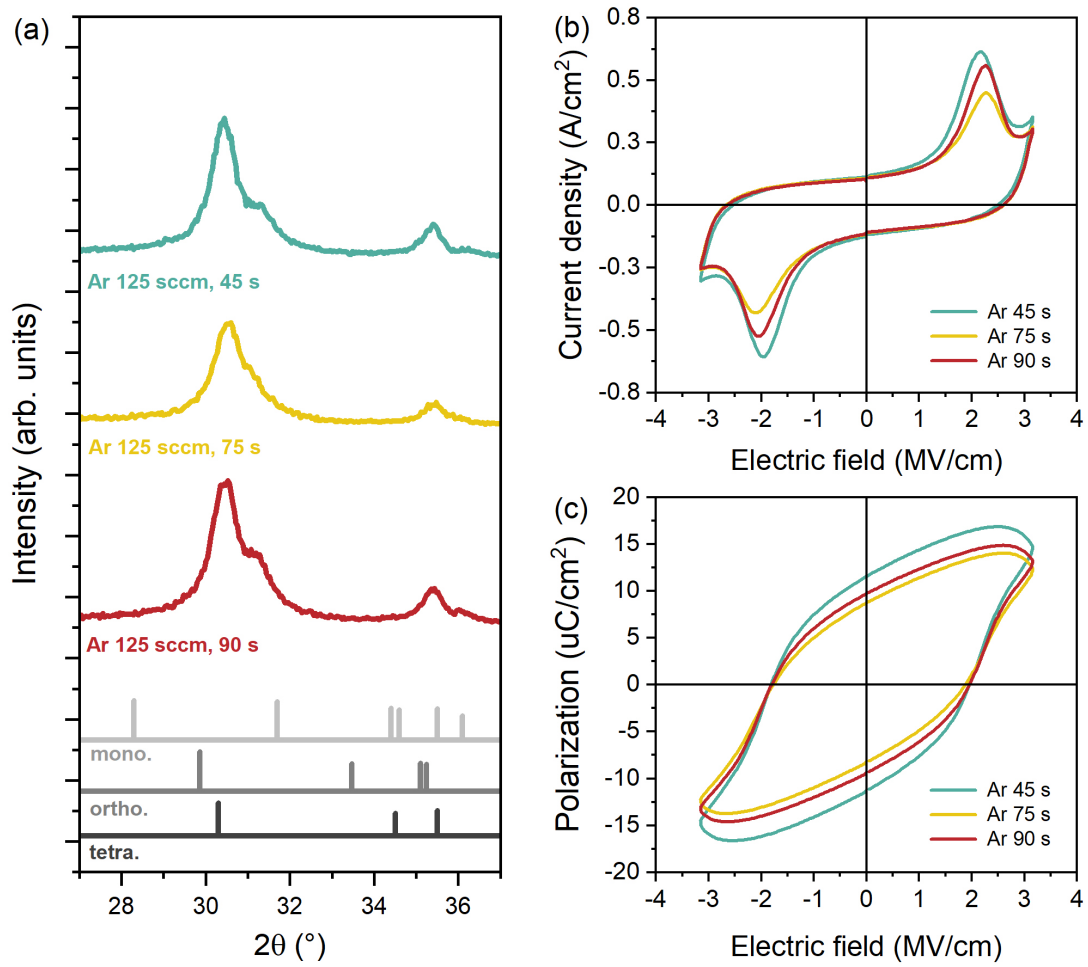


**Figure 4.1** (a) GIXRD patterns and (b, c) ferroelectric hysteresis loops of films annealed in a pure Ar atmosphere at a constant flow rate of 125 sccm, with annealing durations of 45 s, 75 s, and 90 s. For plots (b) and (c), the results are extracted after subjecting the samples to 10 000 rectangular wake-up cycles at 3 kHz.

Time (s)	Coercive field (MV/cm)	Remanent polarization ( $\mu\text{C}/\text{cm}^2$ )
45	2	23
75	2	17
90	2	19

**Table 4.1** Ferroelectric properties of  $\text{HO}_{C45}$  films annealed in pure Ar atmosphere for different durations, showing coercive field ( $E_c$ ) and remanent polarization ( $2P_r$ ).

this is likely due to enhanced leakage rather than improved ferroelectricity. For the shortest annealing condition investigated, device reliability was poor: of the approximately 12 capac-

itors tested, only 3 could be measured without premature electrical breakdown. In contrast, 90 s annealing yielded far more consistent electrical performance—10 of the 11 capacitors survived the full measurement sequence and exhibited reproducible polarization–electric field loops, despite the higher leakage current.

In the second part of the Ar atmosphere study, four  $\text{HO}_{C45}$  samples were annealed under varying Ar gas flow rates of 50, 125, 200, and 250 sccm. The annealing duration was fixed at 90 s, as determined from the previous experiment. The GIXRD patterns of these films, shown in Figure 4.2(a), exhibit the characteristic features of  $\text{HfO}_2$  thin films with only minor differences across the samples. Notably, the shoulder near  $31^\circ$  appears relatively weak in the films annealed at 50 and 200 sccm, suggesting slight variations in the phase composition.

The corresponding current density and polarization hysteresis loops are presented in Figures 4.2(b) and 4.2(c). Distinct switching current peaks are observed in all samples except the one annealed at 50 sccm, which experienced dielectric breakdown before reaching the coercive field. In contrast, the samples annealed at 125, 200, and 250 sccm demonstrate stable ferroelectric switching behavior, with coercive fields ( $E_c$ ) of approximately 2 MV/cm and remanent polarization ( $2P_r$ ) values around  $18 \mu\text{C}/\text{cm}^2$ . However, all these films also show signs of leakage, as indicated by the rounded polarization loops near the saturation region. The values of coercive field and remanent polarization with different gas flow rate is summarized in Table 4.2.

Based on this investigation, it is evident that while the Ar gas flow rate has little impact on the structural properties of the films, it plays a crucial role in their electrical performance. The minimal variation in the GIXRD patterns suggests that the crystallization behavior and phase composition remain largely unaffected by flow rate. However, the film annealed at 50 sccm exhibits severe dielectric breakdown, indicating that insufficient gas exchange during annealing may lead to poor removal of decomposition byproducts and incomplete precursor conversion ultimately degrading the dielectric property.

In contrast, higher gas flow rates (125–250 sccm) facilitate effective removal of volatile species, leading to improved ferroelectric behavior and electrical stability. The convergence of electrical characteristics at higher flow rates suggests that beyond a certain threshold, increase in the flow rate provide no additional benefit. Thus, identifying an optimal Ar flow rate is essential to ensure efficient annealing, maintain structural quality, and enhance the

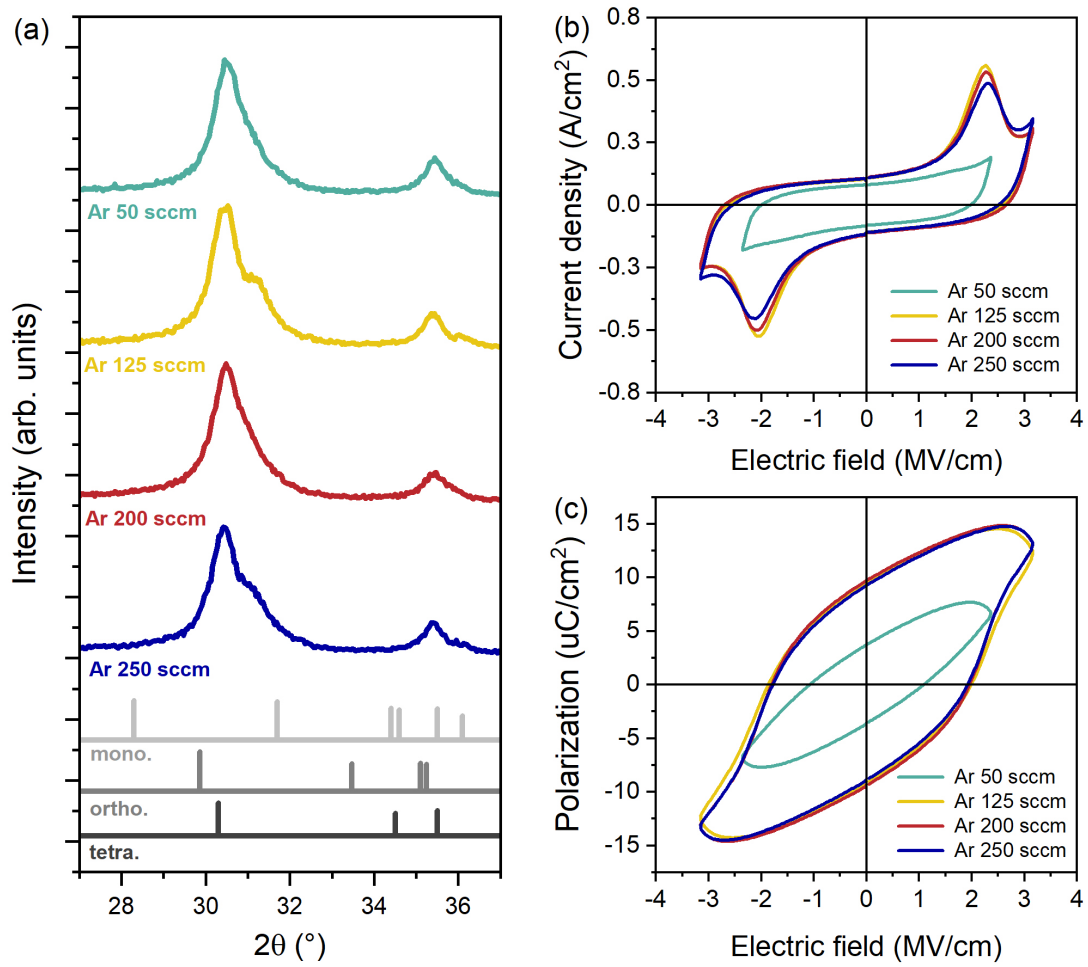


**Figure 4.2** (a) GIXRD patterns and (b, c) hysteresis loops of films annealed in pure Ar atmosphere for 90 s with Ar flow rates of 50 sccm, 125 sccm, 200 sccm and 250 sccm. For plots (b) and (c), the results are extracted after subjecting the samples to 10 000 rectangular wake-up cycles at 3 kHz.

Gas flow rate (sccm)	Coercive field ( $\text{MV}/\text{cm}$ )	Remanent polarization ( $\mu\text{C}/\text{cm}^2$ )
50	–	–
125	2	18
200	2	18
250	2	18

**Table 4.2** Ferroelectric properties of  $\text{HO}_{\text{C}45}$  films annealed in pure Ar atmosphere for 90 s for varying gas flow rate, showing coercive field ( $E_c$ ) and remanent polarization ( $2P_r$ ).

electrical reliability of La:HfO<sub>2</sub> thin films.

### 4.2.2 Ar:O<sub>2</sub> atmosphere

This section examines films grown in an Ar:O<sub>2</sub> mixed-gas atmosphere with a total gas flow rate of 300 sccm. Three different Ar:O<sub>2</sub> ratios, 1:1, 1:2, and 2:1, were used. The GIXRD patterns, shown in Figure 4.3(a), exhibit the characteristic features of HfO<sub>2</sub> thin films with no significant variation across different atmospheres. However, notable differences arise in the electrical properties. Figures 4.3(b) and 4.3(c) present the current-density and polarization hysteresis loops as functions of the applied field. Switching current peaks are observed in all films except for the Ar:O<sub>2</sub> 2:1 sample. However, all films exhibit significant leakage. Due to the substantial leakage contribution, extracting reliable ferroelectric properties from the measured loops is challenging. Furthermore, all the films exhibited early breakdown, with the Ar:O<sub>2</sub> 1:2 sample failing beyond 2 MV/cm. This suggests that the presence of O<sub>2</sub> alongside Ar negatively impacts the ferroelectric properties of HfO<sub>2</sub> thin films.

The study of Ar:O<sub>2</sub> mixed-gas annealing reveals that increased oxygen content negatively affects the electrical performance of HfO<sub>2</sub> thin films, despite minimal changes in structural properties. GIXRD results show consistent phase composition across all gas ratios, indicating that crystallization is largely unaffected by oxygen partial pressure, or that possible changes cannot be resolved by XRD. However, electrical measurements reveal significant degradation with oxygen-containing atmospheres, including increased leakage, reduced breakdown strength, and suppressed ferroelectric switching. The 2:1 Ar:O<sub>2</sub> sample shows no switching, and the 1:2 sample breaks down at 2 MV/cm. These trends suggest that excess oxygen reduces the concentration of oxygen vacancies that help stabilize the ferroelectric orthorhombic phase, leading to weakened ferroelectric switching and compromised electrical performance. As a result, reliable ferroelectric behavior is obscured.

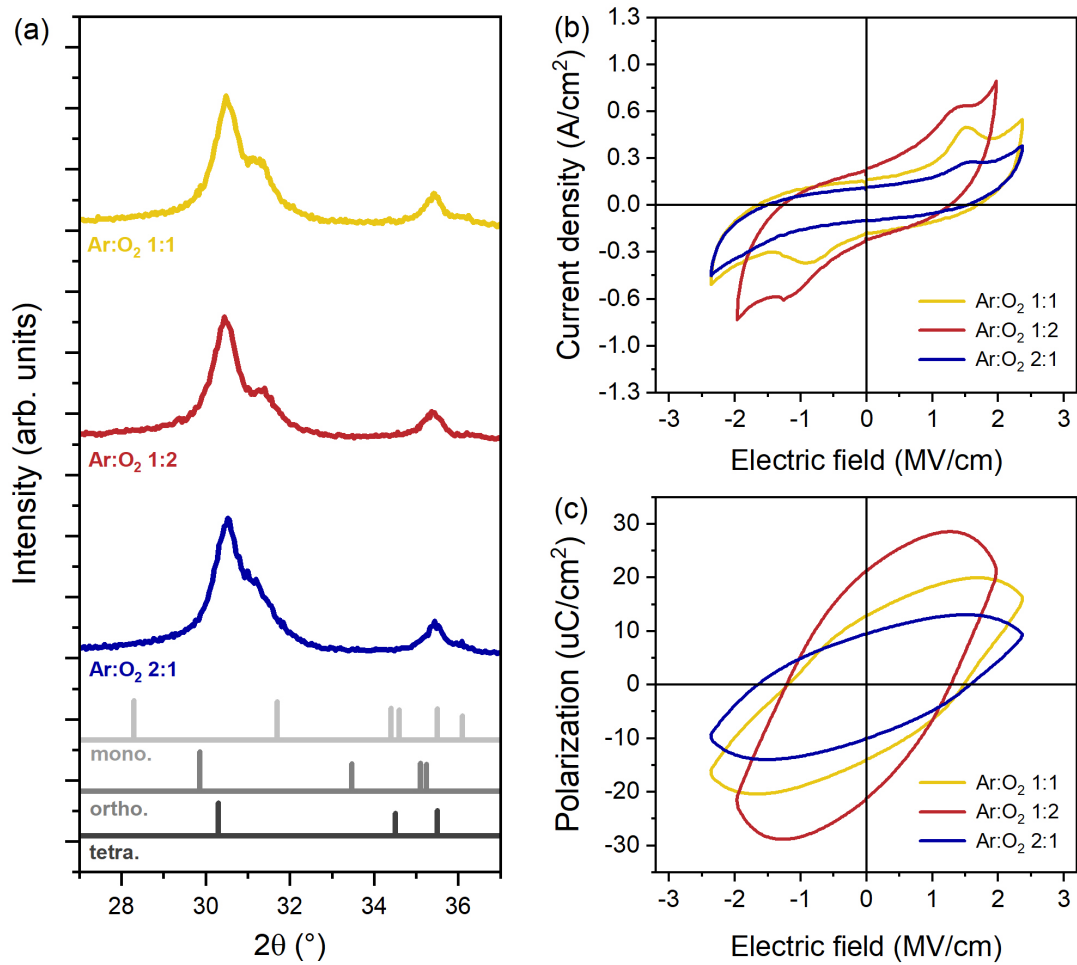


**Figure 4.3** (a) GIXRD patterns and (b, c) hysteresis loops of films annealed in an Ar:O<sub>2</sub> atmosphere with total gas flow fixed at 300 sccm and varying Ar:O<sub>2</sub> ratios of 1:1, 1:2, and 2:1. For plots (b) and (c), the results are extracted after subjecting the samples to 10 000 rectangular wake-up cycles at 3 kHz.

### 4.2.3 N<sub>2</sub>:O<sub>2</sub> atmosphere

This section focuses on the investigation of N<sub>2</sub>:O<sub>2</sub> atmospheres with controlled gas ratios of 1:0, 1:1, 1:2, and 2:1, while maintaining a total gas flow rate of 300 sccm for annealing duration of 90 s. Notably, the 1:0 ratio corresponds to a pure N<sub>2</sub> atmosphere at 300 sccm. The GIXRD patterns, presented in Figure 4.4(a), exhibit no significant variations across the different gas ratios.

Figures 4.4(b) and 4.4(c) illustrate the current-density and polarization hysteresis loops under varying annealing atmospheres, revealing a strong dependence of ferroelectric performance on oxygen content. Films annealed in oxygen-deficient (pure N<sub>2</sub>) or oxygen-rich

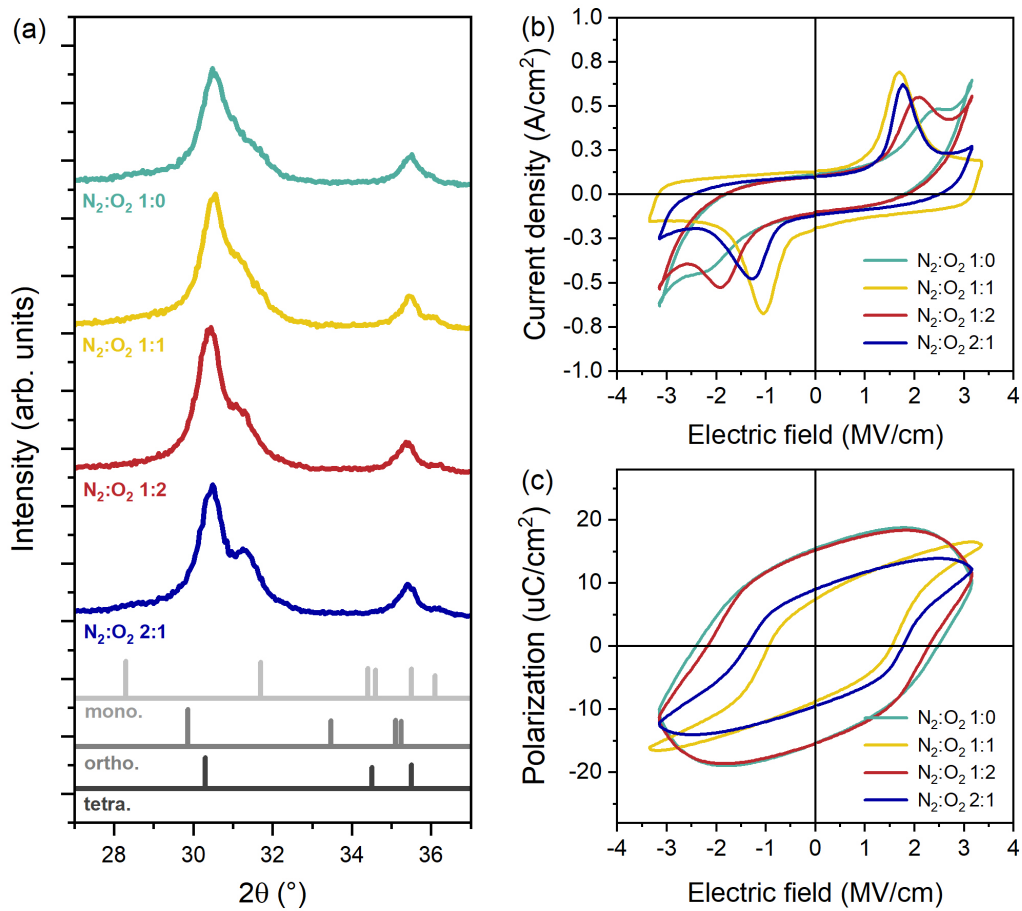


**Figure 4.4** (a) GIXRD patterns and (b, c) hysteresis loops of films annealed in an  $N_2:O_2$  atmosphere with total gas flow fixed at 300 sccm and varying  $N_2:O_2$  ratios of 1:0, 1:1, 1:2, and 2:1. For plots (b) and (c), the results are extracted after subjecting the samples to 10 000 rectangular wake-up cycles at 3 kHz.

Ratio	Coercive field (MV/cm)	Remanent polarization ( $\mu C/cm^2$ )
1:0	–	–
1:1	1.3	16
1:2	–	–
2:1	1.8	17

**Table 4.3** Ferroelectric properties of  $HO_{C45}$  films annealed in  $N_2:O_2$  atmosphere with different ratios, showing coercive field ( $E_c$ ) and remanent polarization ( $2P_r$ ). The rows corresponding to 1:0 and 1:2 were left blank because high leakage currents prevented accurate determination of the values.

(N<sub>2</sub>:O<sub>2</sub> 1:2) environments exhibit pronounced leakage currents that obscure ferroelectric switching, whereas intermediate compositions, particularly N<sub>2</sub>:O<sub>2</sub> 1:1 and 2:1, demonstrate well-defined ferroelectric behavior. The N<sub>2</sub>:O<sub>2</sub> 1:1 film achieves the most favorable electrical characteristics, with a low coercive field (1.3 MV/cm), robust breakdown strength exceeding 3 MV/cm, and remanent polarization of 16  $\mu\text{C}/\text{cm}^2$ . The 2:1 sample exhibits slightly higher remanent polarization (17  $\mu\text{C}/\text{cm}^2$ ), likely attributable to marginally increased leakage. The values of coercive field and remanent polarization for different gas ratios are summarized in Table 4.3. For each sample, approximately 20 capacitors were characterized, providing a consistent basis for comparing electrical behavior across different gas ratios. These results highlight the importance of controlling oxygen partial pressure to achieve reliable ferroelectric switching; balanced N<sub>2</sub>:O<sub>2</sub> atmospheres appear most effective, while both oxygen-poor and oxygen-rich environments lead to degraded electrical performance. Having identified N<sub>2</sub>:O<sub>2</sub> 1:1 as the optimal annealing atmosphere, we reproduced multiple samples of varying thicknesses under these conditions, confirming consistent ferroelectric behavior as shown in Figure 4.5.

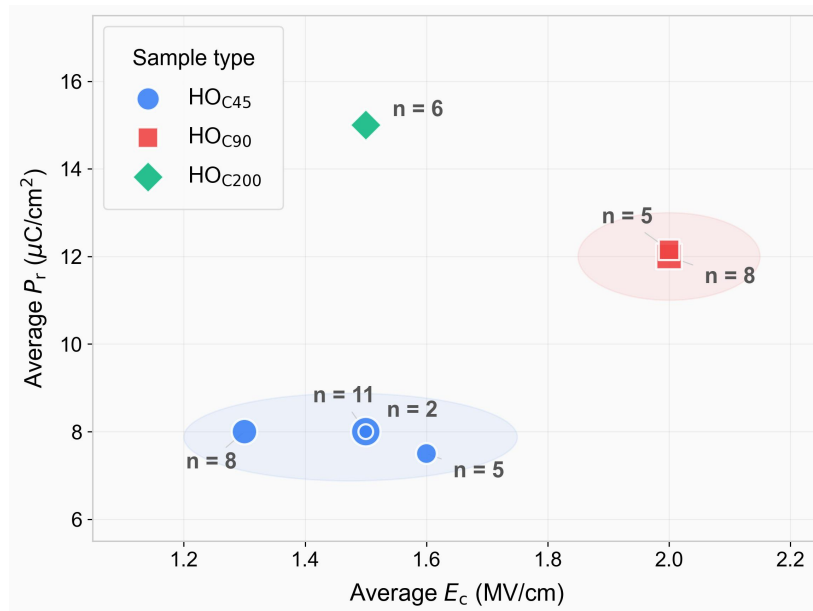


**Figure 4.5** Reproducibility of ferroelectric properties for La:HfO<sub>2</sub> thin films annealed under N<sub>2</sub>:O<sub>2</sub> 1:1 atmosphere. Average coercive field ( $E_c$ ) is plotted against average remanent polarization ( $P_r$ ) for samples of three different thicknesses (HO<sub>C45</sub>, HO<sub>C90</sub>, HO<sub>C200</sub>). Marker size scales with  $n$ , the number of capacitors measured per sample. The shaded area presents tight clustering within each thickness group confirms reproducible ferroelectric behavior. Detailed values are provided in Table B.1.

### 4.3 Effect of annealing atmosphere on film density and composition

To further investigate the impact of annealing atmosphere on film properties, particularly density and elemental composition, three samples from the annealing atmosphere study that demonstrated comparatively promising characteristics were selected for detailed analysis: HO<sub>C45</sub> samples annealed in Ar atmosphere (125 sccm for 90 s), Ar:O<sub>2</sub> (1:1), and N<sub>2</sub>:O<sub>2</sub> (1:1). The X-ray reflectivity results in Figure 4.6 reveal clear density variations between films annealed under different conditions. The critical angle for total external reflection, determined at half-maximum intensity where X-rays transition from surface reflection to material penetration, serves as a direct measure of film density. The Ar-annealed sample exhibits a lower critical angle (0.71°) compared to oxygen-containing atmospheres (~0.74°), corresponding to a reduced density of 7.5 g/cm<sup>3</sup> versus 8.0 g/cm<sup>3</sup> for both Ar:O<sub>2</sub> and N<sub>2</sub>:O<sub>2</sub> films. Notably, all experimental densities fall significantly below the simulated theoretical value of 9.6 g/cm<sup>3</sup>, consistent with previously reported challenges in achieving full densification during chemical solution deposition of HfO<sub>2</sub> and ZrO<sub>2</sub> films, as evidenced by SEM,[120, 121] transmission electron microscopy,[75] atomic force microscopy observations,[122] and limited XRR studies.[85, 123] This density deficit reflects the inherent difficulties in completely eliminating porosity and organic residues during crystallization of solution-derived oxide films.

To understand the origin of this reduced density in Ar-annealed films, secondary ion mass spectrometry (SIMS) was performed to investigate the compositional differences. The SIMS depth profiles in Figure 4.7 reveal compositional variations between films annealed under different conditions, providing key insights into organic byproduct removal mechanisms and interfacial compositions during thermal processing. The hafnium and lanthanum profiles (Figures 4.7a and 4.7b) show relatively uniform distribution across all annealing conditions, indicating that cation distribution remains stable regardless of atmospheric composition. However, the hafnium profile exhibits notable accumulation at the bottom interface, which could indicate interfacial reactions with the underlying platinum electrode.

The oxygen profiles (Figure 4.7c) display higher intensity at both the interfaces regardless of annealing atmosphere, while the central region maintains consistent distribution.

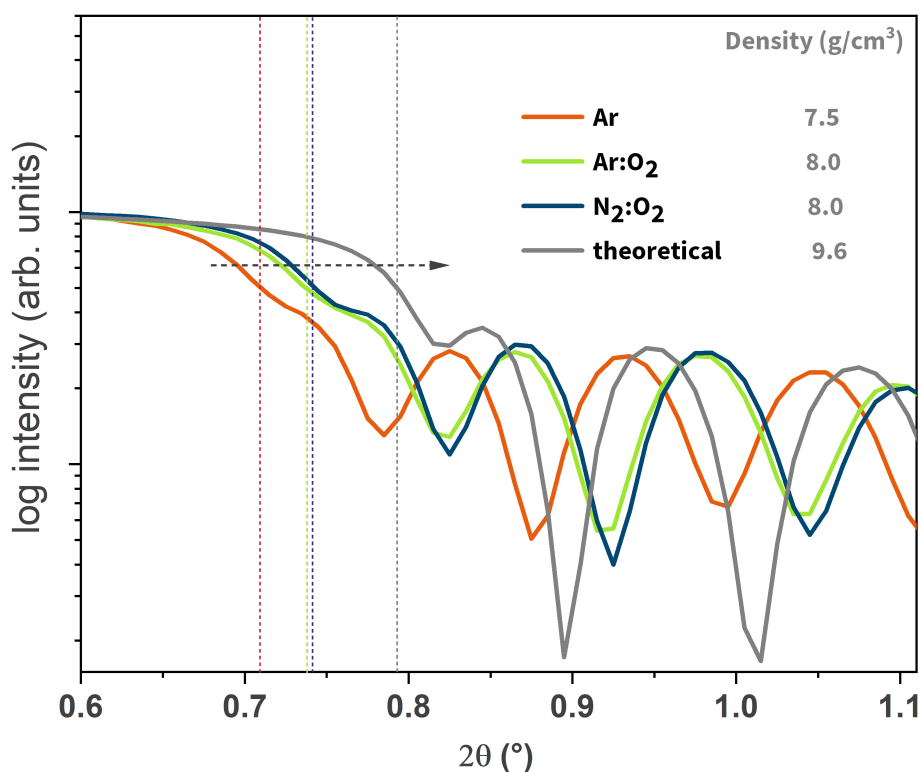


**Figure 4.6** X-ray reflectivity patterns of  $\text{HO}_{C45}$  thin films annealed in different atmospheres. Orange line represents Ar annealing (density:  $7.5 \text{ g/cm}^3$ ), green line represents Ar:O<sub>2</sub> annealing (density:  $8.0 \text{ g/cm}^3$ ), blue line represents N<sub>2</sub>:O<sub>2</sub> annealing (density:  $8.0 \text{ g/cm}^3$ ), and gray line shows the theoretical value (density:  $9.6 \text{ g/cm}^3$ ).<sup>[108]</sup> The dashed line intercepts at the density edge are the half maxima of the XRR intensity.

The most significant effect of annealing atmosphere is observed in the carbon profiles (Figure 4.7d), where Ar-annealed films retain substantially higher carbon content throughout the bulk compared to oxygen-containing atmospheres (Ar:O<sub>2</sub> and N<sub>2</sub>:O<sub>2</sub>), indicating incomplete decomposition of organics from Hf(IV)-acetylacetonate and propionic acid during annealing. The carbon content in both films (1000 counts/s) approaches the SIMS detection threshold, indicating that the overall carbon concentration is insufficient to significantly affect the density measurements obtained through XRR. Nevertheless, the elevated residual carbon content shows a direct relationship with the density reduction observed via XRR in the Ar-annealed film. This increased carbon presence likely indicates persistent residual carbon at grain boundaries, which contributes to porosity formation. Remarkably, these films continue to demonstrate strong switching currents, implying that partial decomposition may kinetically stabilize the polar phase by modulating grain growth processes, a behavior previously observed by Chen et al.<sup>[107]</sup>

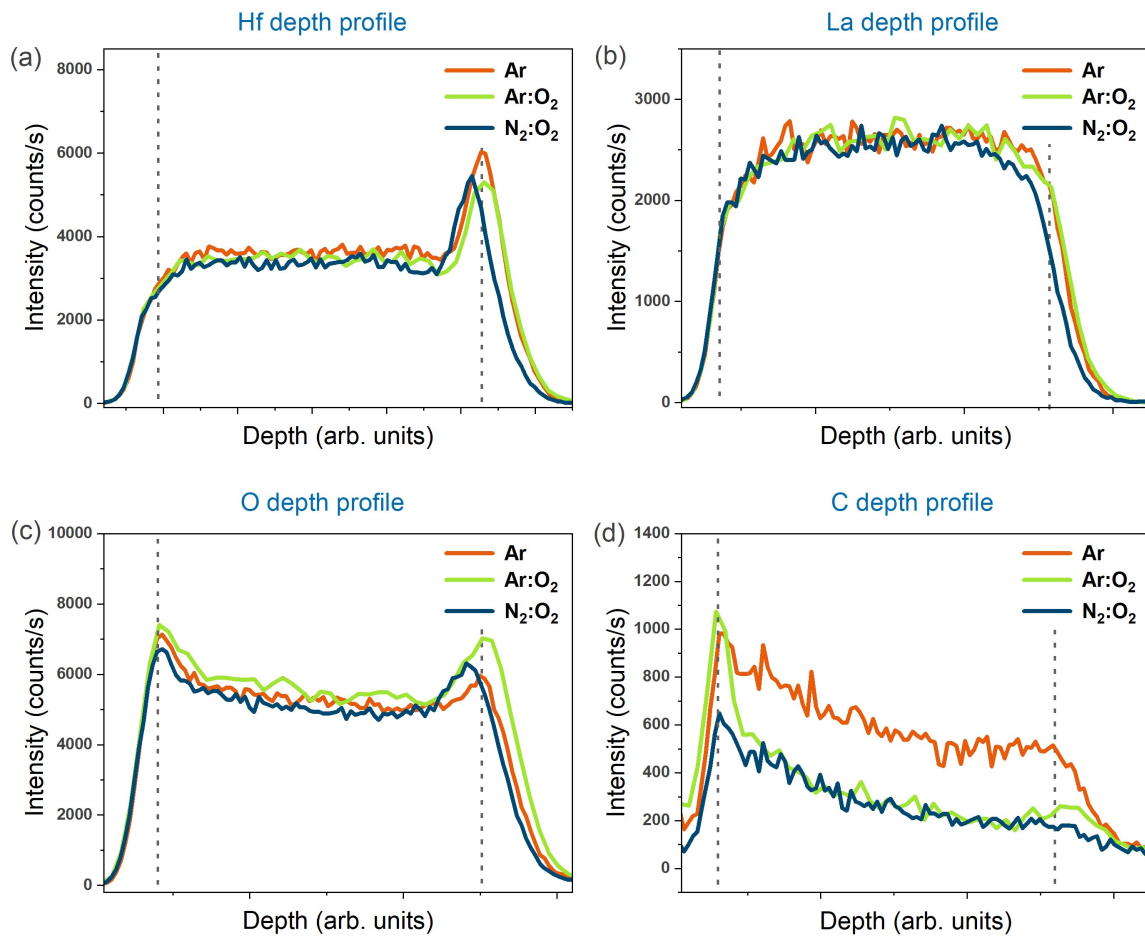


**Figure 4.7** Secondary ion mass spectrometry depth profiles of (a) Hf, (b) La, (c) O, and (d) C in 45 nm thick  $\text{HO}_{\text{C}45}$  thin films annealed in different atmospheres. The vertical dashed lines approximately indicate the interfaces with the top Pt/Ti electrode (left) and the Pt bottom electrode (right). The arrow indicates the direction of film growth (Z-direction).

The excess hafnium, combined with oxygen accumulation, at the bottom electrode interface can act as a dielectric layer or modify the local electric field distribution, potentially contributing to observed leakage current in ferroelectric hysteresis loops. Furthermore, this interfacial composition variation may be related to the wake-up phenomenon, where the interfacial layer acts as a dead layer that initially suppresses ferroelectric switching, requiring multiple voltage cycles to optimize local composition for improved ferroelectric behavior. The varying oxygen content at this interface, depending on annealing atmosphere, may also influence oxygen vacancy density, which affects both leakage mechanisms and wake-up processes in ferroelectric thin films.

In conclusion, while pure Ar conditions promote stable ferroelectric switching, incom-

plete organic decomposition and lower film density limit their effectiveness. In contrast, oxygen-rich environments improve organic removal but tend to suppress ferroelectricity by over-passivating oxygen vacancies. The balanced  $N_2:O_2$  (1:1) atmosphere offers an optimal compromise, ensuring efficient precursor decomposition while preserving the defect structures necessary for polarization switching. Having established processing conditions that yield reproducible ferroelectric films, we next investigate the wake-up phenomenon using Raman spectroscopy to gain insight into the structural changes that accompany electrical cycling.

#### 4.4 Wake-up investigation using Raman spectroscopy

In this section, Raman spectroscopy is employed to investigate the wake-up phenomenon in 200 nm  $La:HfO_2$  ( $HO_{C200}$ ) films processed under the optimized  $N_2:O_2$  (1:1) atmosphere. The 200 nm thickness was selected after multiple unsuccessful attempts to obtain a measurable Raman signal from thinner 45 nm ( $HO_{C45}$ ) and 90 nm ( $HO_{C90}$ ) films. Raman measurements were performed using a confocal configuration with an effective laser spot size of approximately 0.3–1  $\mu m$  (FWHM), depending on the objective lens used (50x–100x). Spectra were collected from four independently fabricated capacitors to assess measurement repeatability, and the resulting data showed highly consistent peak positions and relative intensities across all devices. This reproducibility confirms that the observed spectral evolution is characteristic of the film rather than device-to-device variation. The increased film thickness therefore provides sufficient signal intensity for reliable phase analysis while preserving the phase composition established during annealing.

Recent advances in the growth of thicker ferroelectric films have enabled more reliable phase analysis using Raman spectroscopy, primarily due to improved signal-to-noise ratios. Mimura *et al.* demonstrated the effective use of cross-sectional and surface Raman spectroscopy on pulsed-laser deposited 850 nm-thick  $YO_{1.5}-HfO_2$  films, achieving clear discrimination among the tetragonal, antipolar orthorhombic (Pbca), and polar orthorhombic phases. Notably, they observed a field-induced transition from the tetragonal to the ferroelectric orthorhombic phase.[124]

Fan *et al.* studied the vibrational properties of yttrium-stabilized  $HfO_2$  using a combi-

nation of Raman and infrared spectroscopy alongside first-principles calculations. Their work provided spectral insights consistent with the presence of multiple polymorphs, including features attributed to the ferroelectric orthorhombic phase, though exact phase identification remains challenging due to overlapping modes.[125] By growing bulk single crystals using a laser-diode-heated floating zone technique, they stabilized both polar and antipolar orthorhombic phases and provided a comprehensive spectroscopic fingerprint database, offering a valuable reference for phase identification in thin films. Beyond HfO<sub>2</sub>, Materano *et al.* demonstrated the use of Raman spectroscopy to reliably distinguish the polar orthorhombic phase from competing tetragonal and monoclinic phases in CSD and ALD grown ZrO<sub>2</sub> thin films of 100 nm and 30 nm, respectively.[126] These results highlight Raman spectroscopy as a powerful technique for monitoring phase evolution in these oxide systems. In addition, several studies have employed Raman spectroscopy for phase identification in hafnia- and zirconia-based systems.[61, 127, 128]

Despite the demonstrated utility of Raman spectroscopy for phase identification in ferroelectric hafnia and zirconia systems, the literature reveals significant inconsistencies in reported vibrational modes for the polar o-III phase. This variability stems from multiple factors including differences in material composition (pure HfO<sub>2</sub>, ZrO<sub>2</sub>, or mixed Hf<sub>1-x</sub>Zr<sub>x</sub>O<sub>2</sub>), dopant types and concentrations, experimental conditions such as film thickness and deposition methods, mechanical stress states, and the computational approaches employed for theoretical predictions. As illustrated in Table 4.4, different research groups report markedly different sets of characteristic peaks for the ferroelectric phase. In this work, the Raman modes reported by Mimura *et al.*[124] showed better agreement with our experimentally observed values and were therefore used as the reference for comparison.

The measurements were carried out in three stages: (i) the as-deposited state, (ii) after partial electrical cycling just above the coercive field up to 3 MV/cm, and (iii) after full wake-up treatment at 3.75 MV/cm, which is close to the dielectric breakdown limit. Raman spectra were collected following each treatment to monitor the evolution of phase composition and identify characteristic vibrational features associated with the monoclinic, tetragonal, and polar orthorhombic phases.

Study	Material System	Reported Modes (cm <sup>-1</sup> )	Type
Materano et al.[126]	ZrO <sub>2</sub>	199, 309, 341, 545, 579	Calc.
		200, 320, 340, 550, 580, 620	Exp.
Mimura et al.[124]	7%YO <sub>1.5</sub> -93%HfO <sub>2</sub>	156, 267, 319, 384, 600	Exp.
Schroeder et al.[61]	HfO <sub>2</sub>	353/342/354, 397/390/395,	Calc.
		500/490/497, 565/555/560	
		340, 360, 620	Exp.
Fan et al.[125]	HfO <sub>2</sub>	354, 396, 471 (A <sub>1</sub> )	Calc.
		532, 562 (B <sub>2</sub> )	

**Table 4.4** Reported Raman modes for the polar orthorhombic (o-III) phase from theoretical calculations and experimental measurements.

#### 4.4.1 Spectral response to electrical cycling

Figure 4.8 shows the Raman spectrum of the as-deposited film alongside the corresponding ferroelectric hysteresis loop, which indicates paraelectric behavior. Owing to the relatively large film thickness, a high signal-to-noise ratio was achieved, enabling clear identification of characteristic peaks associated with multiple phases.

In the as-deposited state, prominent peaks are observed at approximately 499 cm<sup>-1</sup>, which is characteristic of the monoclinic phase, and at 261, 308, and 650 cm<sup>-1</sup>, associated with the tetragonal phase. Notably, a pronounced peak near 384 cm<sup>-1</sup> is also evident, which corresponds to the polar orthorhombic phase. The Raman spectroscopy results indicate that the polar orthorhombic phase exists in the as-deposited film, a distinction that cannot be made using X-ray diffraction techniques as observed in Chapters 4 and Chapters 5. Additional Raman signatures of the polar orthorhombic phase are expected at 267, 319, and 600 cm<sup>-1</sup>. Interestingly, the spectral feature around 310 cm<sup>-1</sup> may indicate contributions from both the tetragonal and orthorhombic phases, reflecting a degree of phase competition or mixed-phase character. Moreover, despite the apparent presence of the ferroelectric phase in the as-deposited film, no switching current is observed in the pristine state.

Figure 4.9 presents the Raman spectra obtained after electrical cycling up to 3 MV/cm, showing an increase in the intensity of the peak near 500 cm<sup>-1</sup>, characteristic of the polar orthorhombic phase. The corresponding ferroelectric hysteresis loop, also shown in the

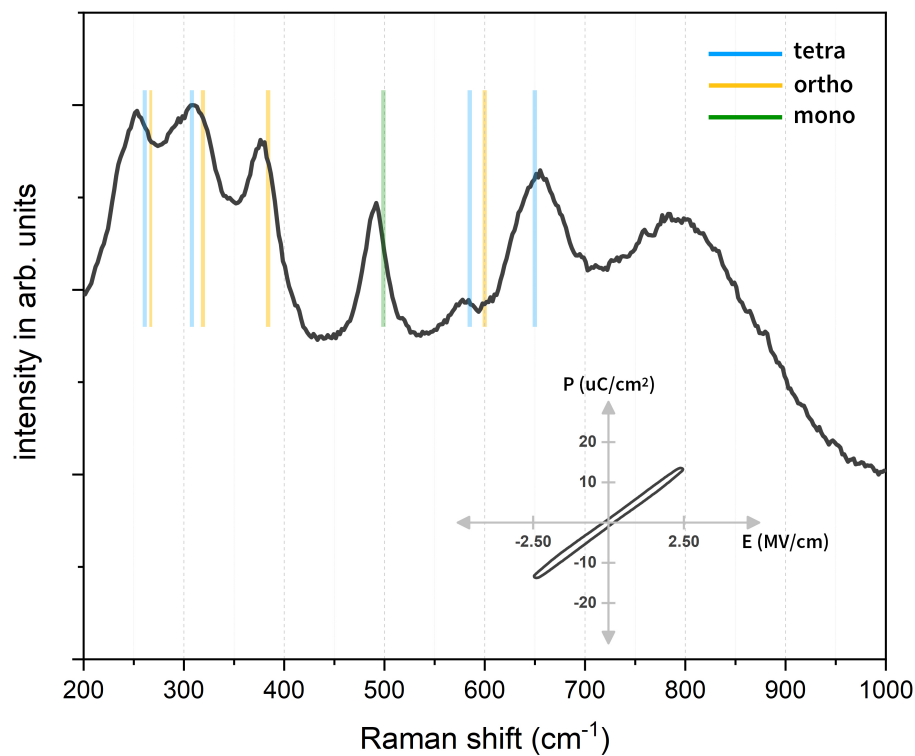


**Figure 4.8** The measured Raman spectra of as-deposited  $\text{HfO}_{200}$  thin films, accompanied by the corresponding polarization vs electric field loop. The Raman peak assignments are referenced from Mimura *et al.* [124].

figure, reveals a remanent polarization of  $7 \mu\text{C}/\text{cm}^2$ . A reduction in the intensity of the peak around  $310 \text{ cm}^{-1}$  was also noted. Additionally, an increase in the intensity of the tetragonal peak near  $650 \text{ cm}^{-1}$  was observed.

To further enhance the ferroelectric behavior, the film was subjected to electrical cycling at a higher field of  $3.75 \text{ MV}/\text{cm}$ , which is close to the dielectric breakdown limit. As illustrated in Figure 4.10, the Raman spectra show a clear increase in the intensity of peaks near  $310$  and  $384 \text{ cm}^{-1}$ . The accompanying ferroelectric hysteresis loop demonstrates a corresponding improvement in switching behavior, with the remanent polarization increasing to approximately  $15 \mu\text{C}/\text{cm}^2$ .

The evolution of Raman spectra during progressive electrical cycling provides insights into the wake-up mechanism in ferroelectric hafnia. The  $384 \text{ cm}^{-1}$  peak observed in the as-deposited state indicates that the polar orthorhombic phase is already present but inactive due to defect pinning, a behavior typical of solution-derived  $\text{HfO}_2$  (see Chapter 2). With increasing field strength, the enhancement of orthorhombic peaks ( $310$  and  $384 \text{ cm}^{-1}$ )

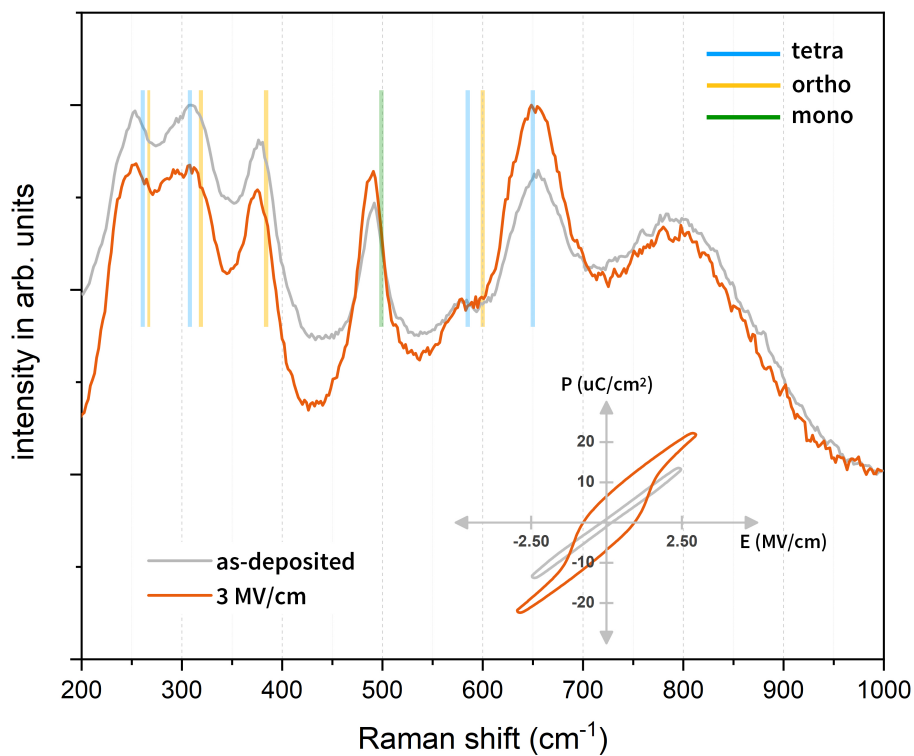


**Figure 4.9** Raman spectra of  $\text{HO}_{C200}$  thin films after partial electrical cycling up to 3 MV/cm, shown alongside the corresponding ferroelectric hysteresis loop.

correlates with improved ferroelectric switching, supporting a defect de-pinning mechanism. Full wake-up at 3.75 MV/cm further strengthens these signatures, consistent with enhanced defect redistribution. Importantly, the absence of peak shifts or splitting suggests that wake-up in our films probably does not involve structural phase transitions but rather activation of existing polar domains. The reduced intensity of the  $310\text{ cm}^{-1}$  peak during partial cycling may result from cycling-induced defects or oxygen vacancies, while the enhancement of the tetragonal peak near  $650\text{ cm}^{-1}$  points to additional phase interactions. This complexity highlights the need for complementary techniques such as Fourier Transform Infrared Spectroscopy (FTIR) to fully unravel the structural changes underlying wake-up.

## 4.5 Summary and outlook

This comprehensive investigation of annealing atmosphere effects on La-doped  $\text{HfO}_2$  thin films prepared by chemical solution deposition has revealed critical insights into the complex interplay between atmospheric composition, structural properties, and ferroelectric

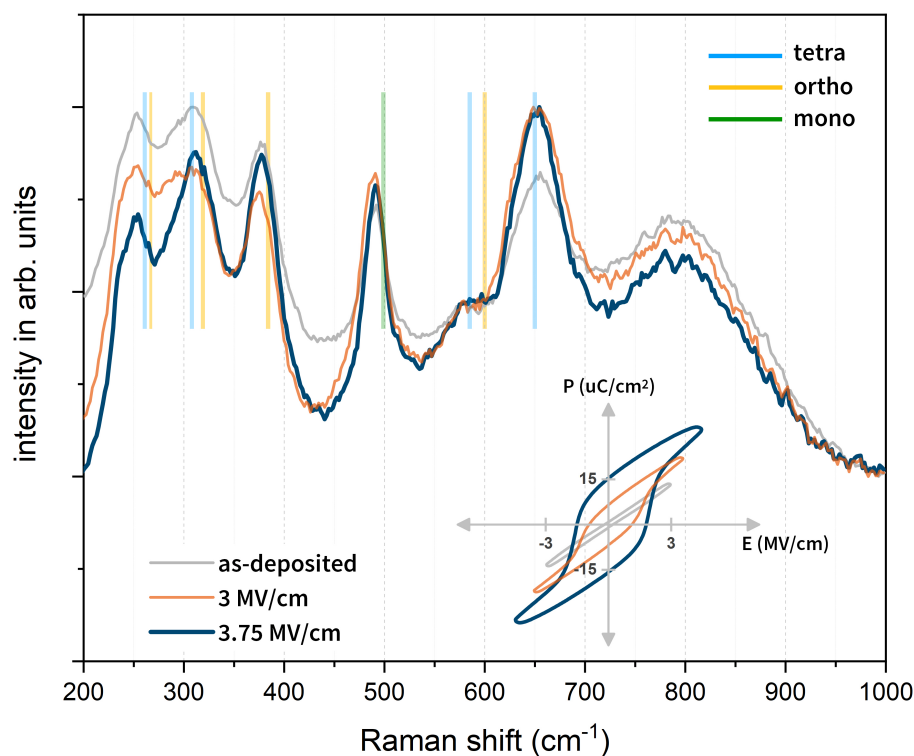


**Figure 4.10** Raman spectra of  $\text{HO}_{C200}$  thin films after full electrical cycling up to 3.75 MV/cm, shown alongside the corresponding ferroelectric hysteresis loop.

performance. The systematic study of pure Ar, Ar: $\text{O}_2$ , and  $\text{N}_2$ : $\text{O}_2$  atmospheres demonstrated that while crystallization occurs rapidly (within 45 s) and shows no observable differences in X-ray diffraction patterns, the electrical properties exhibit profound sensitivity to oxygen partial pressure and gas flow parameters. Pure Ar atmospheres, particularly at optimized flow rates of 125–250 sccm, enable stable ferroelectric switching with coercive fields of  $\sim 2$  MV/cm, though residual carbon content and lower film density ( $7.5 \text{ g/cm}^3$ ) indicate incomplete organic decomposition. Conversely, oxygen-containing atmospheres, while promoting more effective organic removal and higher film densities ( $8.0 \text{ g/cm}^3$ ), generally degrade electrical performance through excessive oxygen vacancy passivation, with the notable exception of balanced  $\text{N}_2$ : $\text{O}_2$  (1:1) conditions that achieve optimal ferroelectric characteristics including reduced coercive fields (1.3 MV/cm) and enhanced breakdown strength. Films processed under  $\text{N}_2$ : $\text{O}_2$  (1:1) exhibited excellent reproducibility in ferroelectric response.

Building upon these optimized processing parameters, the structural evolution of ferroelectric hafnia under electrical cycling was examined using Raman spectroscopy to elucidate the wake-up mechanism. The results revealed that as-deposited films exhibit mixed-phase

structures with pinned dipoles that inhibit polarization switching. Partial cycling at moderate fields (3 MV/cm) led to the activation of ferroelectric behavior accompanied by an increase in the polar orthorhombic phase signal, while full wake-up treatment at higher fields (3.75 MV/cm) produced a stable remanent polarization of approximately  $15 \mu\text{C}/\text{cm}^2$ . The Raman data indicated that the wake-up process primarily involves defect redistribution and dipole de-pinning rather than field-induced phase transformation, highlighting Raman spectroscopy as a sensitive probe for studying dynamic structural processes in ferroelectric hafnia.

The insights gained from this study establish that the annealing atmosphere governs the delicate balance between organic decomposition, oxygen vacancy formation, and defect passivation—key factors in stabilizing ferroelectric behavior in solution-processed hafnia. These findings provide a framework for optimizing processing parameters and scaling up CSD-based ferroelectric film fabrication with improved reproducibility. Future work should focus on in-situ monitoring of structural and interfacial changes during annealing and cycling to further clarify the mechanisms driving wake-up and long-term device reliability.

# Chapter 5

## Influence of growth routes on crystallization and orientation

Controlling crystallographic orientation in thin films is essential for optimizing their functional performance. This chapter investigates how adopting a layer-by-layer growth route can influence both the densification and orientation of HfO<sub>2</sub> thin films, ultimately affecting their ferroelectric properties. Section 5.1 outlines the motivation for exploring alternative crystallization strategies. Section 5.2 details the layer-by-layer growth approach employed in this work. Section 5.3 examines the impact of this growth method on film density and the presence of organic residuals. Section 5.4 discusses the influence of the growth route on the crystallographic orientation of the films. Section 5.5 presents the enhancement of ferroelectric properties observed in layer-by-layer films. Finally, Section 5.6 summarizes the key findings and provides an outlook for future research directions.

### 5.1 Motivation

The development of high-performance functional oxide thin films via CSD faces fundamental microstructural challenges that severely limit their practical application in electronic devices. While CSD provides notable advantages in cost-effectiveness, scalability, and compositional flexibility over vacuum-based deposition techniques, conventional processing often produces films with suboptimal properties that limit device performance, as demonstrated in Chapter 4, where low-density films exhibiting significant leakage currents were observed.

As discussed in the Chapter 2, the crystallization behavior in solution processed hafnia films is dominated by the thermodynamic conditions, where homogeneous nucleation prevails because of the crystallization temperatures being significantly lower than the material's melting temperature. This nucleation behavior leads to two critical microstructural deficiencies that must be addressed:

(a) Low density and porosity: Solution-derived films consistently exhibit porous microstructures with low relative densities, typically below 80% of theoretical values for  $\text{HfO}_2$ . [108] This pervasive issue arises from the fundamental mismatch between processing temperatures (typically  $800^\circ\text{C}$ ) and the high melting temperatures of functional oxides outlined above. For materials like  $\text{HfO}_2$ , with melting temperatures around  $2700^\circ\text{C}$ , the limited thermal budget severely restricts diffusion-mediated grain growth and coalescence processes necessary for densification, similar to the challenges observed in BST (melting point  $1600\text{-}2000^\circ\text{C}$ ) where columnar growth was difficult to achieve on Pt-Si substrates at  $800^\circ\text{C}$ . [129] The resulting porosity directly translates to high leakage currents and poor endurance in ferroelectric devices. [108]

(b) Lack of orientation control: Conventional CSD processes produce randomly oriented polycrystalline films with small grain sizes, typically  $\leq 20$  nm in the case of  $\text{HfO}_2$ . [85] This random orientation represents a fundamental limitation because the functional properties of these materials are highly anisotropic, and for ferroelectric applications, alignment of the polar axis is crucial to maximize remanent polarization. This challenge is exemplified in PZT films, where achieving the (001) orientation is essential for maximum polarization but is typically not possible on platinized silicon substrates due to the tensile stress ( $150$  MPa) that develops in the crystallized film during cooling through the Curie temperature, leading instead to suboptimal (111) textures. [111] Despite extensive efforts to control orientation through various processing modifications, achieving the preferential orientation required for optimal performance in ferroelectric oxides like  $\text{HfO}_2$  remains highly challenging with conventional CSD methods.

To initiate heterogeneous nucleation and overcome these limitations, one approach is to follow the microstructural zone model developed by Schuler et al., which provides a theoretical framework for understanding and controlling microstructure in CSD films. [130, 131] This model predicts microstructural evolution based on the dimensionless ratio  $q$

= ICS/SLT, where ICS is the intrinsic crystallite size (determined from X-ray diffraction using the Scherrer equation or TEM measurements) and SLT is the single layer thickness. The model identifies three fundamental morphologies as depicted in figure 5.1: granular structures form when  $q \ll 1$  (SLT much greater than ICS), layered structures emerge when  $0.42 < q < 1$ , and columnar structures with characteristic dendritic grains develop when  $q > 1$  (SLT less than ICS). This framework is unique to sol-gel processing since layered and granular structures are not typically observed in PVD or CVD processes, which inherently operate at very high  $q$  values due to continuous, low-rate deposition. For conventional CSD processing of  $\text{HfO}_2$ , typical grain sizes around 20 nm place most systems in the undesirable granular regime ( $q \ll 1$ ). By utilizing dilute solutions and crystallization of every layer, the SLT can be systematically reduced, increasing the  $q$  value and transitioning from granular to layered or columnar microstructures, thereby promoting heterogeneous nucleation and dense microstructure formation.

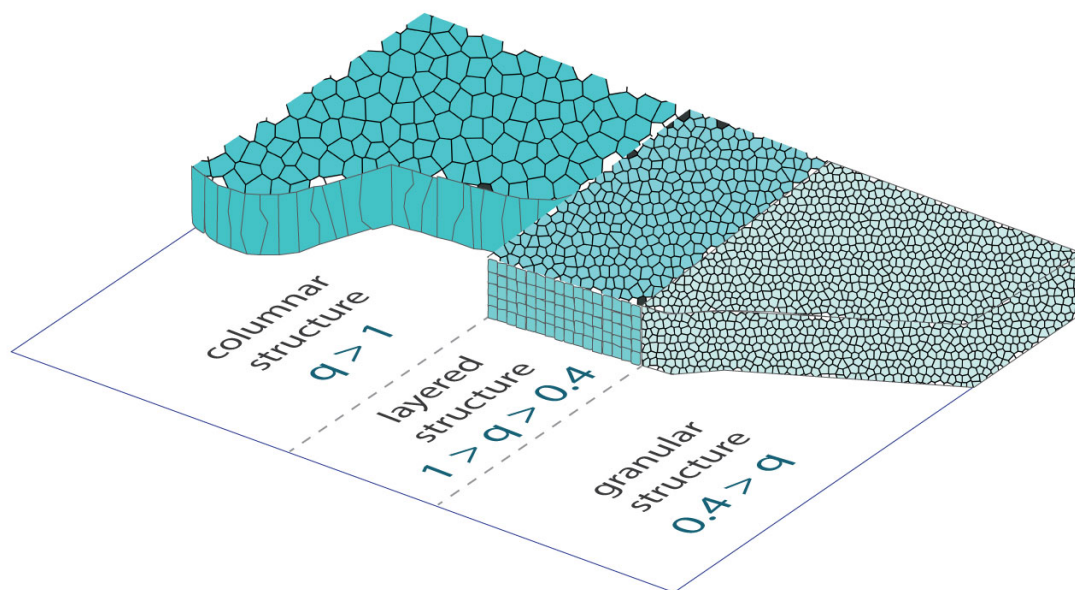


**Figure 5.1** Development of microstructure and emergence of a superstructure according to the microstructural zone model of Schuler et al.[131]

Based on this theoretical framework, this chapter systematically investigates the implementation of a layer-by-layer(L/L) growth approach to promote heterogeneous nucleation and achieve columnar microstructure. This alternative growth route is designed to simultaneously promote preferential orientation and enhance film density, while utilizing annealing

atmospheres identified as optimal for achieving superior ferroelectric properties in Chapter 4.

To implement the L/L crystallization strategy within the optimal  $q$  regime, processing was adapted from the conventional  $\text{HO}_{C45}$  sample to a layer-by-layer  $\text{HO}_{L50}$  sample. This modification involved diluting the precursor solution from 0.25 M to 0.08 M, thereby reducing the single-layer thickness from 15 nm to 5 nm. Such thin layers satisfy the  $q > 1$  condition, as they are significantly smaller than the typical 20 nm grain size in conventional  $\text{HfO}_2$  films,[121, 132–134] which promotes the development of a columnar microstructure. Details of the sample nomenclature and processing workflows are provided in Chapter 3. For this study, two  $\text{HO}_{L50}$  samples were subjected to RTA under  $\text{N}_2:\text{O}_2$  (1:1) and pure Ar atmosphere (125 sccm flow rate).

## 5.2 Film density and organic residuals

Film density represents a critical parameter in CSD-derived ferroelectric films, as it directly impacts electrical performance and device reliability. X-ray reflectivity (XRR) measurements were performed to determine the film density, as shown in Figure 5.2. Both the L/L films exhibit a density of  $8.4 \text{ g cm}^{-3}$ , corresponding to 87% of the theoretical value, which is notably higher than the 78% and 80% measured for conventional films annealed in Ar and  $\text{N}_2:\text{O}_2$ , respectively. This improvement in density is likely associated with enhanced heterogeneous nucleation. [108, 130] While reduced density and porosity have been reported to improve the longitudinal piezoelectric response in  $\text{Pb}(\text{Zr,Ti})\text{O}_3$  thin films [135], such effects are generally detrimental in hafnia-based ferroelectrics, where poor densification promotes early dielectric breakdown.[108]

To further investigate the correlation between density and processing conditions, SIMS was performed on the L/L films. Figure 5.3 presents the depth profiles of carbon concentrations within the films. A higher overall carbon content is observed in Ar-annealed films compared to the  $\text{N}_2:\text{O}_2$ , consistent with the behavior observed in conventional films. This finding suggests that the absence of oxygen during annealing inhibits complete decomposition of organic precursors, irrespective of the growth route. A remaining question, however, is why L/L Ar film show carbon signal comparable to conventional film yet displays improved

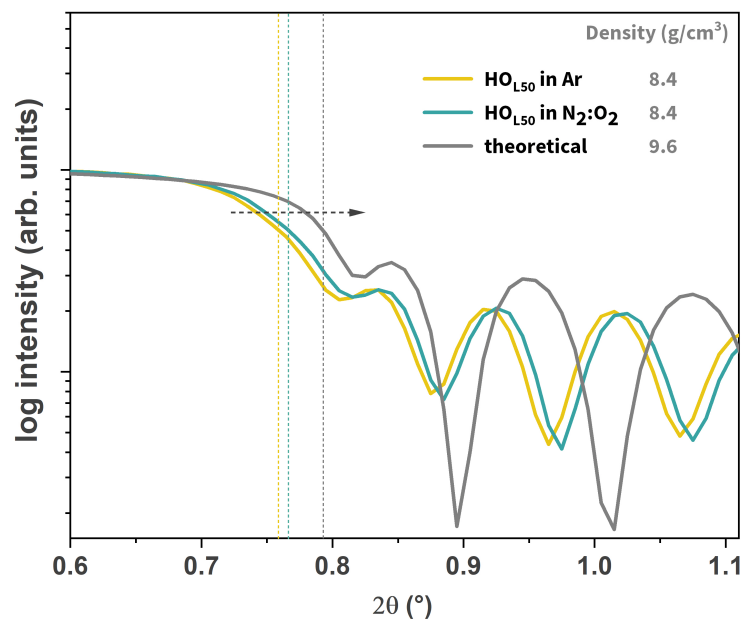


**Figure 5.2** X-ray reflectivity measurements of the HO<sub>L50</sub> thin films annealed in Ar and N<sub>2</sub>:O<sub>2</sub> atmospheres compared to a simulated curve with the theoretical density of 9.6 g cm<sup>-3</sup> (light grey).[108] The dashed line intercepts at the density edge are the half maxima of the XRR intensity.

density. One possible explanation is that carbon residues still persist at grain boundaries, but the adoption of the L/L route substantially reduces porosity, thereby yielding a denser microstructure.

### 5.3 Crystallographic orientation

As discussed earlier, heterogeneous nucleation at interfaces significantly influences the crystallographic orientation of solution processed films by providing a thermodynamically preferred pathway with lower energy barriers compared to bulk nucleation.[106, 111] The GIXRD patterns of HO<sub>L50</sub> films annealed in N<sub>2</sub>:O<sub>2</sub> and Ar atmospheres are shown in Figure 5.4(a). Although the diffraction peaks appear at the expected  $2\theta$  positions, their intensities are notably weak for both films. In contrast, the  $\theta$ - $2\theta$  XRD patterns (Figure 5.4b) more clearly reveal the preferential orientations, with films annealed in N<sub>2</sub>:O<sub>2</sub> exhibiting a pronounced (002) peak at 35.4°, while Ar-annealed film preferentially crystallized along the (111) orientation at 30.4°.

To explain why weak peaks are observed in GIXRD compared to the sharp peaks in  $\theta$ - $2\theta$

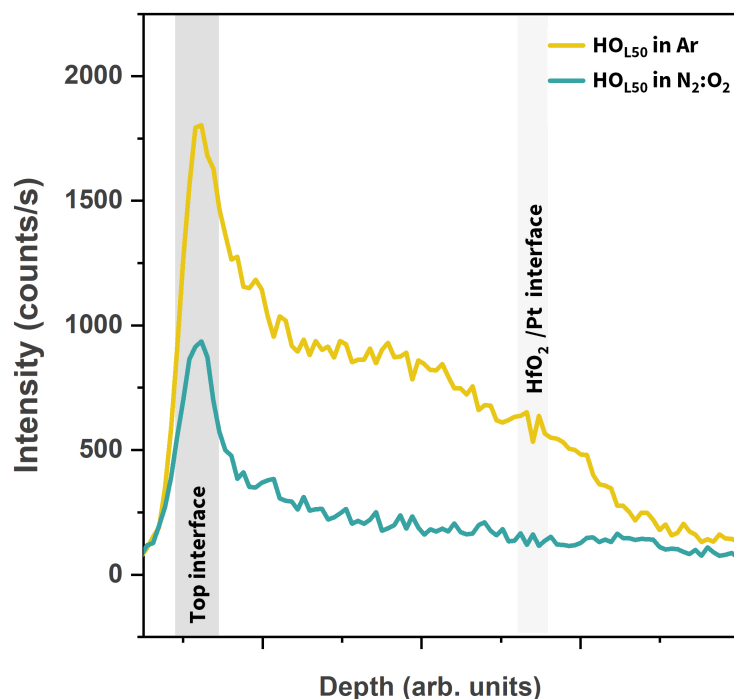


**Figure 5.3** SIMS intensities of carbon in  $\text{HO}_{L50}$  thin films annealed in Ar and  $\text{N}_2:\text{O}_2$  atmospheres.

scans, the measurement geometries are illustrated in Figure 5.5. In GIXRD, the scattering vector is tilted relative to the surface normal by an angle  $\Psi = |\theta - \omega|$ , where  $\omega$  is the fixed incident angle and  $\theta$  is the diffraction angle (Figure 5.5a). For example, within the  $2\theta$  range of  $26^\circ$ – $36^\circ$  (Figure 5.4a),  $\Psi$  varies between  $12.5^\circ$  and  $17.5^\circ$  when  $\omega$  is fixed at  $0.5^\circ$ . As a result, when the scattering vector is tilted by more than  $12.5^\circ$  from the surface normal, diffraction from strongly out-of-plane oriented films produces weak peak intensities. In contrast, in the  $\theta$ – $2\theta$  geometry (Figure 5.5b) the scattering vector is aligned normal to the film surface, enabling strong diffraction signals from preferentially oriented films.

Beyond crystallographic orientation, understanding the microstructural characteristics of these films requires assessing the grain size, as it plays a crucial role in stabilizing the desired ferroelectric phases. The grain size was estimated using both XRD peak analysis and atomic force microscopy (AFM). Pseudo-Voigt fitting in Figure 5.6 was applied to the XRD data to determine the average crystallite size using the Scherrer equation.[136] The L/L films annealed in  $\text{N}_2:\text{O}_2$  and Ar atmospheres had sizes of 21 nm and 14 nm, respectively. AFM imaging in Figure 5.7 revealed grain sizes of  $12 \pm 4$  nm for both films. The relatively large error bars arise from the fine microstructure of the films, which makes accurate grain

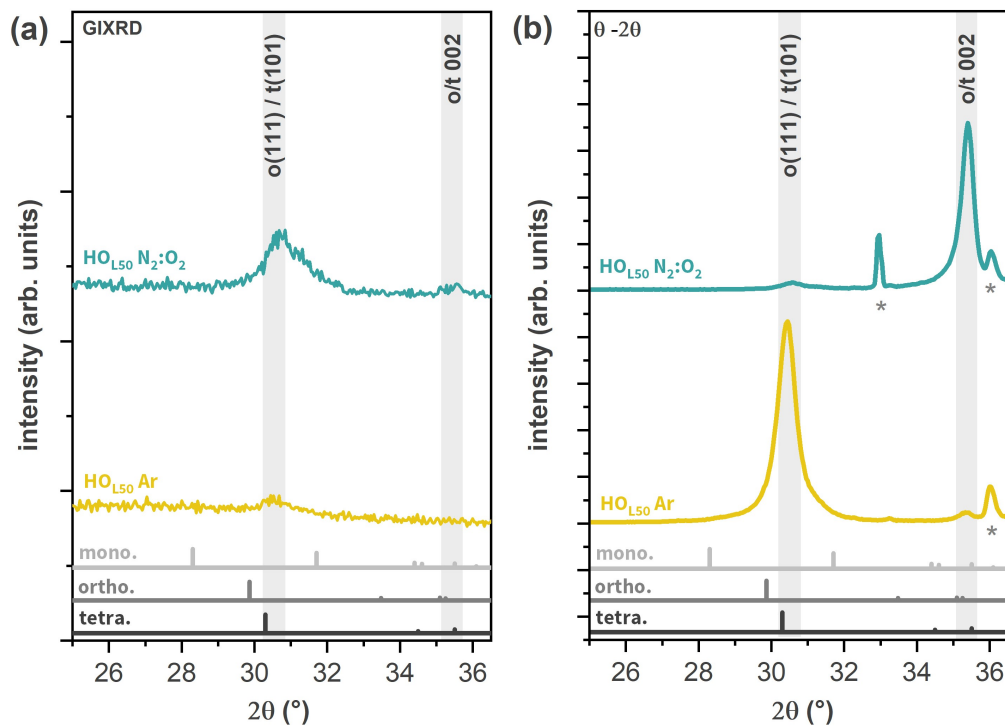


**Figure 5.4** (a) GIXRD and (b)  $\theta$ - $2\theta$  patterns of the  $\text{HO}_{L50}$  films annealed in Ar and  $\text{N}_2:\text{O}_2$  atmospheres. The XRD patterns are compared with the reference patterns from the powder diffraction files. The peaks due to the substrate are marked with \*.

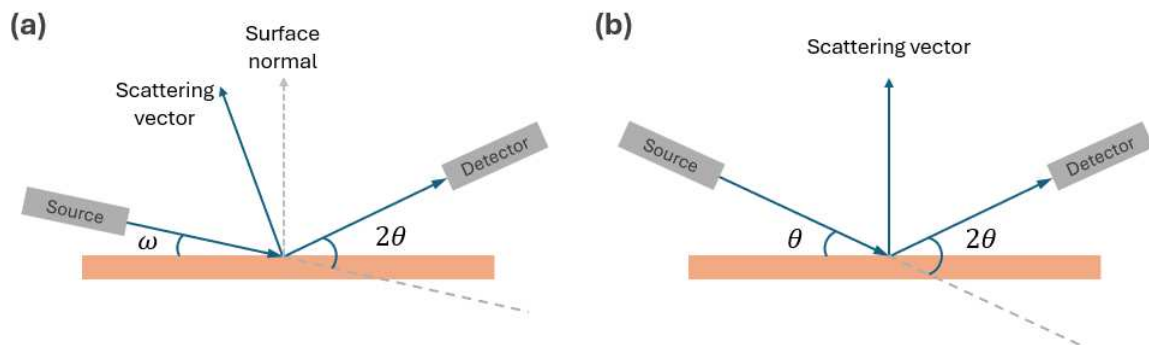


**Figure 5.5** (a) Grazing incident X-ray diffraction (GIXRD) geometry and (b)  $\theta$ - $2\theta$  geometry. In GIXRD incident angle  $\omega$  is fixed.

size determination difficult.

The influence of residual carbon on the microstructure and phase formation of  $\text{HfO}_{L50}$  thin films has been an active topic of investigation. Chen et al. [107] previously reported that undoped CSD-grown  $\text{HfO}_2$  films retained significant carbon, which they proposed was responsible for reducing grain size and thereby stabilizing the polar phase. In our study,

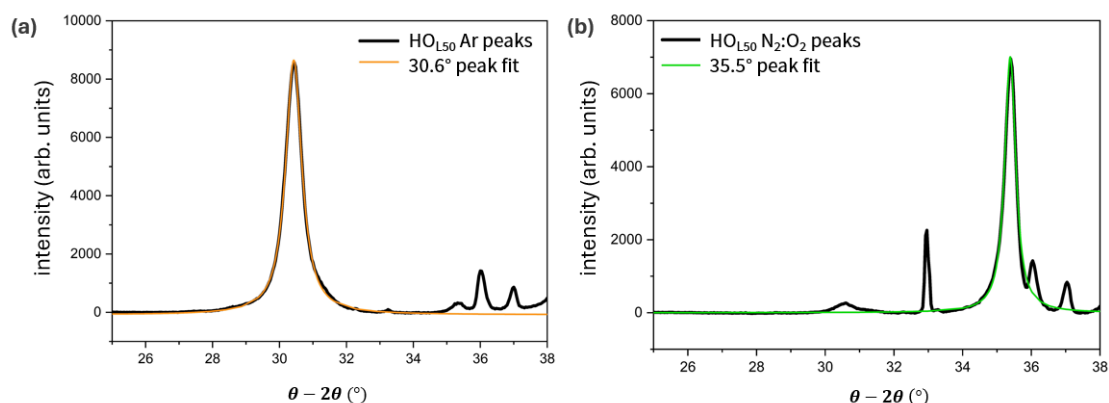


**Figure 5.6** XRD peak fits of the of  $HO_{L50}$  films annealed in (a) Ar and (b)  $N_2:O_2$  atmosphere.

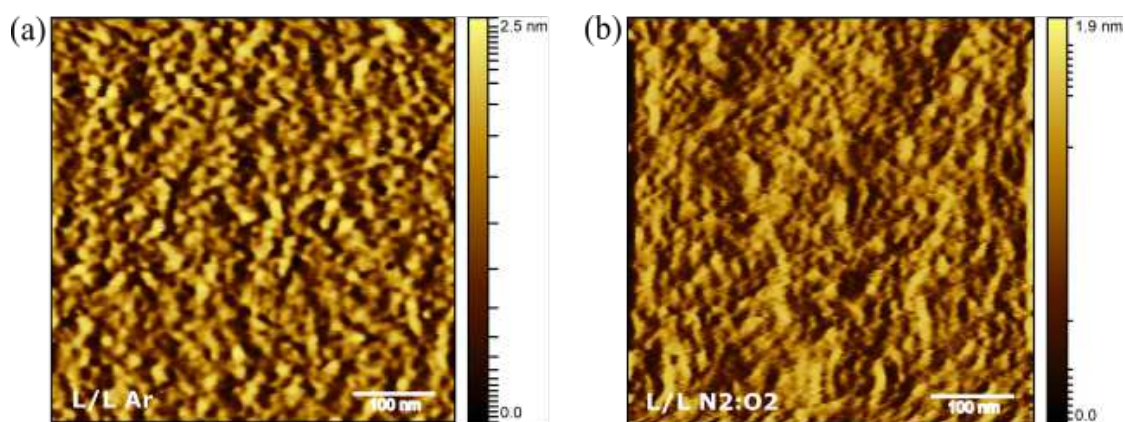


**Figure 5.7** AFM characterization of surface morphology of  $HO_{L50}$  films annealed in (a) Ar and (b)  $N_2:O_2$  atmosphere.

however, establishing such a direct link is difficult, and the relationship appears to be more nuanced. Our results indicate that in L/L films, residual carbon exerts a pronounced effect on crystallographic orientation rather than solely on grain size. Specifically, films with low residual carbon content preferentially crystallize with a (002) orientation, whereas higher carbon levels are associated with a shift toward a (111) texture. We hypothesize that when residual carbon alters the local diffusion processes, it effectively shifts the nucleation temperature or driving force magnitude, consequently influencing the resulting crystallographic orientation. This suggests that residual carbon, acts as a critical parameter governing the texture evolution in L/L films.

## 5.4 Enhanced ferroelectricity in L/L films

The current-density hysteresis loops and polarization hysteresis loops as functions of the applied field are presented in Figure 5.8. Leakage-free switching behavior is observed in the  $\text{HO}_{L50} \text{N}_2:\text{O}_2$  film, which exhibits an enhanced  $P_r$  of  $15 \mu\text{C cm}^{-2}$ . The increase in  $P_r$  from  $7.5 \mu\text{C cm}^{-2}$  in the conventional  $\text{N}_2:\text{O}_2$  1:1 film (see Chapter 4) to  $15 \mu\text{C cm}^{-2}$  in the L/L  $\text{N}_2:\text{O}_2$  film can be attributed to the preferential (002) orientation of the polar phase and improved film density. On the other hand, the  $\text{HO}_{L50}$  Ar-annealed film exhibits no detectable ferroelectricity, likely due to the absence of the polar phase. In the orthorhombic (111)-oriented phase, polarization is inclined at approximately  $55^\circ$ , which would contribute to a measurable perpendicular polarization component. Previously Schenk et al. [108] has reported, L/L films annealed in an Ar: $\text{O}_2$  atmosphere exhibited significant remanent polarization, emphasizing that oxygen is essential for stabilizing ferroelectricity in L/L films. Furthermore, the study reported a piezoelectric coefficient ( $d_{33,\text{eff}}$ ) of  $7.7 \text{ pm V}^{-1}$  in  $1 \mu\text{m}$ -thick La: $\text{HfO}_2$  films, comparable to AlN. Thinner La: $\text{HfO}_2$  films exhibited a 30% decrease in  $d_{33}$ , attributed to a reduced fraction of the o-002 phase. Thus, strongly (002)-oriented, thick L/L films represent a promising avenue for improving piezoelectric performance.

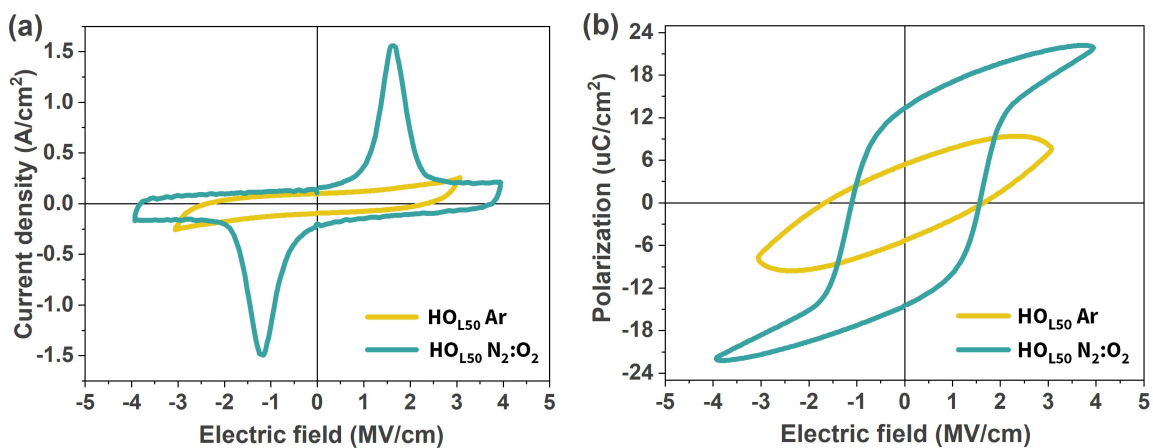


**Figure 5.8** Hysteresis loops of  $\text{HO}_{L50}$  films: (a) current density–electric field (J–E) characteristics, and (b) polarization–electric field (P–E) characteristics. The results are extracted after subjecting the samples to 3000 rectangular wake-up cycles at 3 kHz.

The ferroelectric performance of  $\text{HO}_{L50}$  films is governed by a complex interplay between carbon content, crystallite size, and crystallographic orientation, with each parameter exerting distinct but interconnected effects on the remanent polarization and coercive field.

Carbon content emerges as a critical factor influencing both phase stability and texture development, where films with reduced carbon residuals ( $\text{N}_2:\text{O}_2$  annealing) not only promote the formation of the polar orthorhombic phase but also drive preferential (002) orientation, ultimately enabling enhanced ferroelectric switching. Conversely, higher carbon content in Ar-annealed films correlates with (111) texture and complete suppression of ferroelectricity, suggesting that organic residuals act as orientation-directing agents that fundamentally alter the crystallization pathway. The crystallite size, while remaining relatively similar across both annealing conditions (14–21 nm), appears to be less influential on ferroelectric properties compared to orientation effects. Most significantly, crystallographic orientation demonstrates the most pronounced impact on  $P_r$ , with the dramatic enhancement from  $7.5 \mu\text{C cm}^{-2}$  in conventional films to  $15 \mu\text{C cm}^{-2}$  in (002)-oriented L/L films directly attributable to the optimal alignment of the polar axis perpendicular to the film surface. This orientation-driven improvement, combined with the enhanced film density (87% vs. 78–80% in conventional films), creates a synergistic effect that not only doubles the remanent polarization but also enables leakage-free switching behavior, demonstrating that microstructural optimization through controlled nucleation and growth represents a viable pathway toward high-performance ferroelectric hafnia thin films.

## 5.5 Summary and outlook

This chapter has systematically investigated strategies for overcoming fundamental microstructural limitations in solution-processed  $\text{HfO}_2$  thin films, specifically addressing the critical challenges of poor densification, uncontrolled porosity, and random crystallographic orientation that severely compromise ferroelectric device performance. Through implementation of a layer-by-layer growth approach guided by the microstructural zone model, this work demonstrates that controlled reduction of single-layer thickness from  $\sim 15$  nm to  $\sim 5$  nm effectively transitions the growth regime from granular to more layered structure, promoting heterogeneous nucleation and enhanced film quality.

The L/L methodology yielded substantial improvements across multiple performance metrics. Film density increased from 78–80% to 87% of theoretical values, while crystallographic texture could be systematically controlled through annealing atmosphere, with

$\text{N}_2:\text{O}_2$  atmospheres promoting preferential (002) orientation and Ar atmospheres favoring (111) texture. Most significantly, the synergistic effects of enhanced density and optimal (002) orientation resulted in a doubling of remanent polarization from  $7.5 \mu\text{C cm}^{-2}$  to  $15 \mu\text{C cm}^{-2}$ , accompanied by leakage-free switching behavior. These findings establish a clear structure-property relationship where carbon residue content acts as a critical parameter governing texture evolution, with reduced carbon levels facilitating both polar phase stabilization and preferential orientation.

Moving forward, the demonstrated control over microstructure and orientation through the L/L approach opens several promising research directions. The achievement of strong (002) orientation and enhanced ferroelectric properties suggests significant potential for advanced device applications, particularly given the scalability advantages of solution processing over vacuum-based techniques. Future investigations should focus on optimizing the  $q$  parameter through systematic variation of solution concentration and layer thickness to achieve even stronger (002) textures, while exploring alternative annealing atmospheres to further minimize carbon content without compromising phase stability. Additionally, the extension of this methodology to other ferroelectric oxide systems could establish L/L processing as a general strategy for achieving high-performance functional thin films via cost-effective solution routes, ultimately enabling broader adoption of ferroelectric devices in emerging technologies.



# Chapter 6

## Multilayer films

This chapter is focused on the design and fabrication of multilayer films composed of hafnia and other simple oxides, with the aim of enhancing phase stability, polarization behavior, and overall electrical performance. A literature overview and motivation are first provided to establish the context for the work presented in Section 5.1. In Section 5.2,  $\text{HfO}_2\text{-ZrO}_2$  multilayer films with varying individual layer thicknesses are discussed. Section 5.3 is dedicated to the investigation of  $\text{HfO}_2\text{-CeO}_2$  bilayer structure. In Section 5.4, the role of interfaces on the wake-up behavior in these multilayer systems is examined. Finally, Section 5.5 presents a summary along with potential applications of multilayer thin films.

### 6.1 Motivation

Among the various dopants explored for  $\text{HfO}_2$ -based ferroelectrics, zirconium (Zr) has proven particularly advantageous. Owing to its similar physical and chemical properties to hafnium (Hf), Zr enables stable ferroelectric polarization at approximately 50% substitution.[35, 79, 137] Compositional studies across the full  $\text{Hf}_{1-x}\text{Zr}_x\text{O}_2$  range have shown that ferroelectricity is most pronounced in compositions where  $x = 0.3\text{-}0.5$ . Within this window, the material exhibits characteristic butterfly-shaped dielectric constant–electric field hysteresis loops and remanent polarization values reaching up to  $30 \mu\text{C}/\text{cm}^2$ . [35, 137] Furthermore, the ferroelectric properties of  $\text{Hf}_{1-x}\text{Zr}_x\text{O}_2$  can be achieved at relatively low processing temperatures (400–500°C), which is significantly lower than other doped  $\text{HfO}_2$  systems that require temperatures exceeding 650°C.[137, 138] This makes HZO solid solution

films well-suited for CMOS process flows with strict back-end-of-line (BEOL) thermal budgets. These characteristics make  $\text{Hf}_{1-x}\text{Zr}_x\text{O}_2$  highly suitable for a wide range of applications, including ferroelectric random-access memory (FeRAM), ferroelectric field-effect transistors (FeFETs), and emerging neuromorphic computing devices.[138]

In addition to  $\text{HfO}_2$  and  $\text{Hf}_{1-x}\text{Zr}_x\text{O}_2$  solid solutions,  $\text{ZrO}_2$  itself has garnered considerable interest for its ferroelectric properties. In 2014, density functional theory calculations suggested that the ferroelectric orthorhombic (o) phase of  $\text{ZrO}_2$  could be stabilized over the dielectric monoclinic (m) and antiferroelectric-like tetragonal (t) phases by applying epitaxial strain.[139] Ferroelectricity in  $\text{ZrO}_2$  thin films was experimentally demonstrated using a Pt/ $\text{ZrO}_2$  (6.1–19.6 nm)/Pt capacitor structure, where the  $\text{ZrO}_2$  layer was deposited by remote plasma atomic layer deposition.[140] Fan et al. in 2016, demonstrated the stabilization of the ferroelectric orthorhombic phase in  $\text{ZrO}_2$  thin films via radio frequency magnetron sputtering.[141] This was achieved by leveraging substrate-induced strain to drive the transition from the paraelectric tetragonal phase to the ferroelectric orthorhombic phase. Starschich et al, successfully realized thicker ferroelectric  $\text{ZrO}_2$  and Hf-doped  $\text{ZrO}_2$  films using chemical solution deposition (CSD) with organometallic precursors.[43]

While early studies on  $\text{HfO}_2$ -based ferroelectrics primarily focused on solid solutions to stabilize the ferroelectric orthorhombic phase, multilayer architectures, particularly superlattices composed of fluorite-structured oxide layers have recently emerged as a promising alternative.[142] Similar strategies in perovskite systems have already demonstrated that artificial layering can provide distinct advantages.[143–147] First-principles calculations predict that artificial perovskite superlattices can exhibit enhanced functionalities through interface engineering. For instance,  $\text{PbTiO}_3/\text{SrTiO}_3$  1/1 superlattices are theoretically expected to display spontaneous polarization of  $26 \mu\text{C cm}^{-2}$  and dielectric constants approaching  $\sim 600$ , driven by improper ferroelectric coupling mechanisms.[144] Experimental realizations in perovskite superlattices further confirm such enhancements, including voltage tunability as high as 94% in  $\text{BaTiO}_3/\text{SrTiO}_3$  superlattices,[145] dielectric permittivities exceeding 10,000 at 110 MHz in  $\text{SrZrO}_3/\text{SrTiO}_3$  systems,[146] and even artificial ferroelectricity induced in paraelectric/paraelectric superlattices through lattice distortion effects.[146, 147]

In 2014, Park et al. demonstrated that both intrinsic and field-induced ferroelectricity could be successfully realized in atomic layer deposited  $\text{HfO}_2/\text{ZrO}_2$  nanolaminates.[148]

Using pulsed-laser-deposited  $\text{HfO}_2/\text{ZrO}_2$  superlattices, Li et al. reported robust and stable ferroelectricity across a wide thickness range (4–100 nm) with reduced coercive fields ( $\sim 0.85$  MV/cm). This behavior was attributed to interfacial energy and kinetic barriers that inhibit phase transitions, where the energy cost required for the crystal structure to transform from the polar orthorhombic phase to the stable monoclinic phase becomes significantly elevated, thereby stabilizing the ferroelectric state in otherwise paraelectric materials.[149] Similarly, J. van Gent et al. observed strong ferroelectricity in epitaxial  $\text{Hf}_{1-x}\text{Zr}_x\text{O}-\text{ZrO}_2$  superlattices, where a polar rhombohedral (R3m) phase was stabilized.[150] These structures exhibited enhanced remnant polarization ( $2P_r$  of  $84 \mu\text{C cm}^{-2}$ ) and endurance of up to  $10^9$  switching cycles at high Zr content.  $\text{HfO}_2-\text{ZrO}_2$  superlattice structures have also been reported using alternative techniques such as RF magnetron sputtering, demonstrating increased remanent polarization (up to  $25 \mu\text{C/cm}^2$  for 1 nm sublayers versus  $20 \mu\text{C/cm}^2$  for solid-solution reference films), reduced coercive fields (2.1 MV/cm for 2.5 nm sublayers compared to 3.1 MV/cm for reference films), and improved high-temperature endurance exceeding  $10^3$  cycles at  $150^\circ\text{C}$  for optimized sublayer thicknesses. [151]

In addition to  $\text{HfO}_2-\text{ZrO}_2$  multilayer,  $\text{HfO}_2-\text{CeO}_2$  systems have also garnered attention for their ferroelectric potential.[152–156] Zheng et al. demonstrated that Ce doping in  $\text{Hf}_{1-x}\text{Ce}_x\text{O}_2$  thin films enhances remanent polarization and endurance by stabilizing the orthorhombic phase.[156] Cüppers et al. further showed that annealing atmospheres significantly impact switching kinetics in epitaxial Hf–Ce–O films via modulation of the oxygen vacancy profile, which is the spatial distribution and concentration of missing oxygen atoms that act as defect sites affecting domain nucleation and switching uniformity.[152]

Complementing these experimental efforts, density functional theory (DFT) calculations by Dutta et al. revealed that small-radius dopants, such as Si (radius  $1.11 \text{ \AA}$  vs  $1.87 \text{ \AA}$  for Hf), preferentially segregate into distinct layers within the orthorhombic ferroelectric phase of  $\text{HfO}_2$ , rather than mixing uniformly with Hf.[157] This tendency promotes the stabilization of the polar phase over competing nonpolar polymorphs, thereby highlighting the potential of multilayer architectures over conventional solid solutions. Kumar et al. employed first-principles DFT calculations to predict a novel hybrid-improper ferroelectric  $P2_1$  phase in  $\text{CeO}_2-\text{HfO}_2$  superlattices, exhibiting a spontaneous polarization of  $30.3 \mu\text{C/cm}^2$  and a remarkably low switching barrier of  $8.5 \text{ meV/atom}$ .[158] These findings underscore the

promise of engineered multilayers in advancing the functional properties of polar fluorite oxides. Building on this, we investigated solution-processed HfO<sub>2</sub>-ZrO<sub>2</sub> and HfO<sub>2</sub>-CeO<sub>2</sub> multilayers with varying oxide growth order, layer thicknesses and film thicknesses to explore their structural and ferroelectric behavior.

## 6.2 HfO<sub>2</sub>-ZrO<sub>2</sub> multilayers

This section presents a study on La:HfO<sub>2</sub>-ZrO<sub>2</sub> multilayer thin films, focusing on the influence of individual layer thickness and growth sequence on ferroelectric phase stabilization. While previous reports have explored thick solid-solution Hf<sub>0.5</sub>Zr<sub>0.5</sub>O<sub>2</sub> films, investigations into comparable multilayer architectures remain limited. In the following sections, we examine multilayer films consisting of alternating La:HfO<sub>2</sub> and ZrO<sub>2</sub> layers annealed in a 1:1 N<sub>2</sub>:O<sub>2</sub> atmosphere. For reference, HO<sub>C45</sub> and ZO<sub>C45</sub> films deposited under the same conditions are used as benchmarks. The sample nomenclature and processing procedures are described in detail in Chapter 3.

### 6.2.1 HZO<sub>C50</sub>

Figure 6.1a illustrates the structural schematic of the HZO<sub>C50</sub> multilayer, comprising ten alternately deposited 5 nm-thick layers of La:HfO<sub>2</sub> and ZrO<sub>2</sub>, beginning with La:HfO<sub>2</sub> and terminating with ZrO<sub>2</sub>. The bright-field STEM image in Figure 6.1b clearly shows the expected multilayer stack, as evidenced by the contrast variation between the alternating La:HfO<sub>2</sub> and ZrO<sub>2</sub> layers. This contrast variation arises because Hf has a higher atomic number than Zr, causing it to scatter more electrons. As a result, the La:HfO<sub>2</sub> layers appear darker than the ZrO<sub>2</sub> layers in bright-field TEM images, since increased scattering reduces the intensity of transmitted electrons reaching the detector. The stack is enclosed between two Pt electrodes.

Elemental analysis using energy-dispersive X-ray spectroscopy (EDS) was carried out to assess potential cation inter-layer diffusion resulting from high-temperature crystallization of the 5 nm-layered amorphous film at 800 °C. The EDS line profile is shown in Figure 6.2. The periodic modulation in the Hf M and Zr K signals validates the preservation of the layered structure. The observed overlap of Hf M and Zr K signals at the interfaces may partially

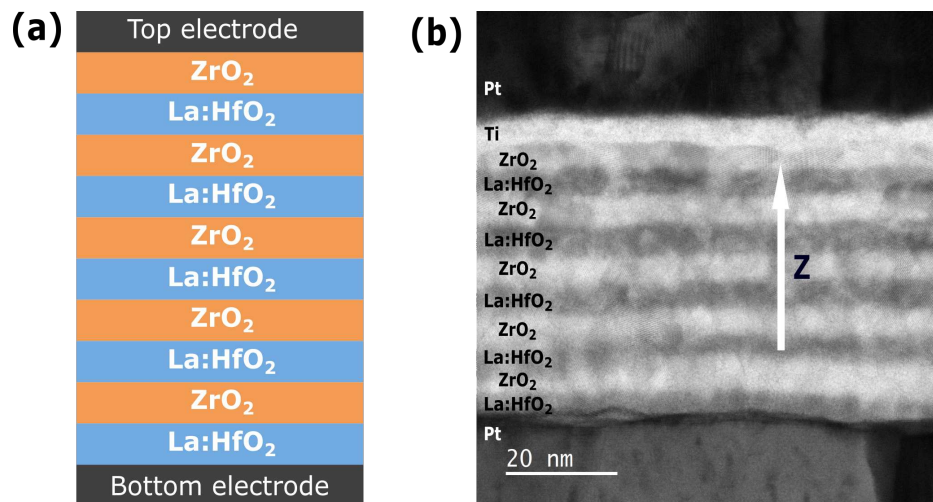


**Figure 6.1** (a) Structural schematic and (b) bright-field STEM image of the  $\text{HZO}_{C50}$  multilayer film with the Pt/Ti top electrode and the Pt bottom electrode.

arise from instrumental artifacts, and thus prevents a definitive quantitative assessment of inter-layer diffusion. The Ti K signal marks the upper boundary of the film.

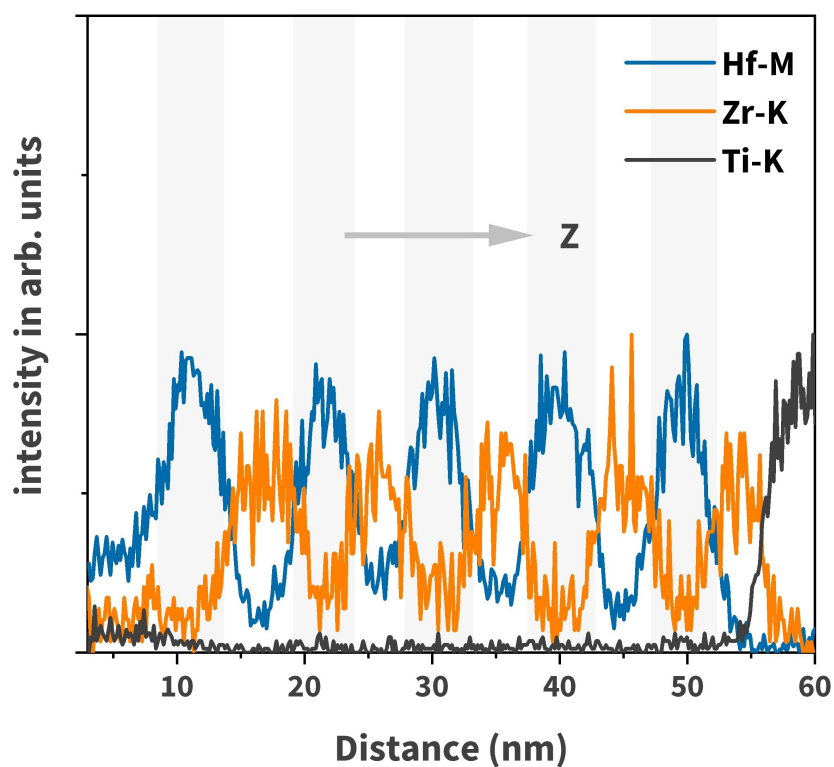


**Figure 6.2** STEM-energy dispersive X-ray spectroscopy (STEM-EDS) line profile of the  $\text{HZO}_{C50}$  multilayer. Z is the direction of growth.

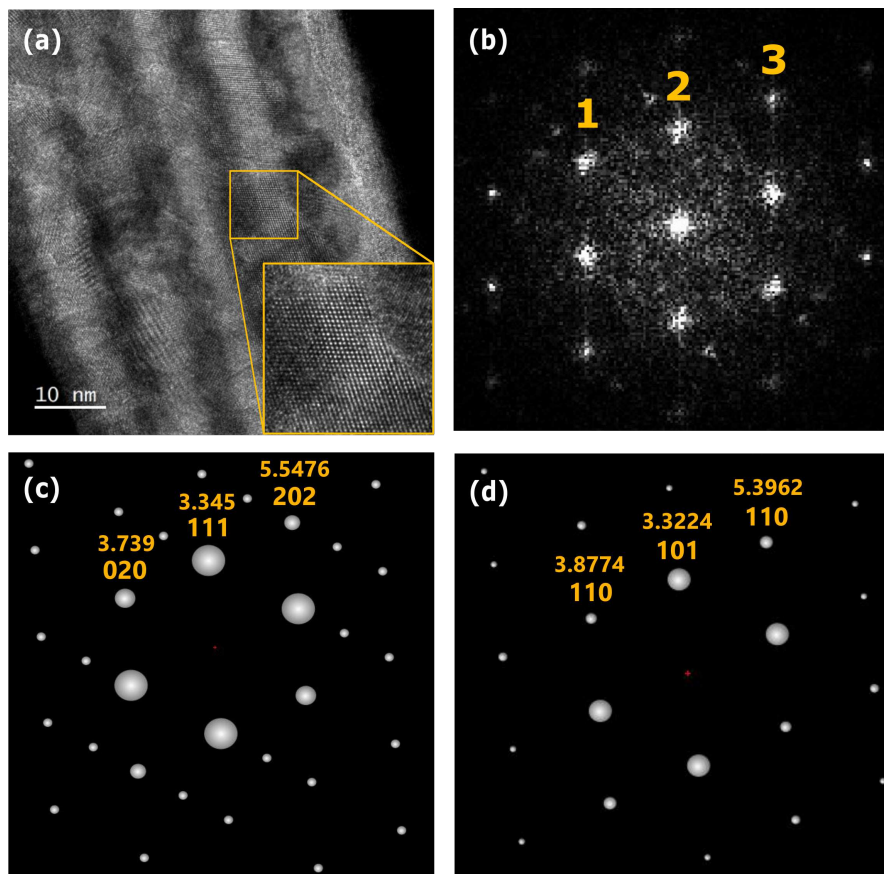


**Figure 6.3** (a) Cross-sectional HRTEM image of the field-cycled HZO<sub>C50</sub> multilayer film. (b) FFT diffractogram of the highlighted region. (c) Simulated diffraction pattern of orthorhombic HfO<sub>2</sub> along the  $[\bar{1}01]$  zone axis (space group Pca2<sub>1</sub>). (d) Simulated diffraction pattern of tetragonal HfO<sub>2</sub> along the  $[\bar{1}\bar{1}1]$  zone axis (space group P4<sub>2</sub>/nmc).

To further investigate the phase composition and grain orientation within the HZO<sub>C50</sub> multilayers, cross-sectional high-resolution transmission electron microscopy (HRTEM) was performed, as shown in Figure 6.3. The presence of continuous lattice fringes across several layers with alternating compositions indicates that grains extend through multiple sublayers, maintaining coherent crystallographic orientation. The corresponding fast Fourier transform (FFT) diffractogram from a representative region (Figure 6.3b) was compared against simulated diffraction patterns based on standard PDF cards for monoclinic (P2<sub>1</sub>/c), orthorhombic (Pca2<sub>1</sub>), and tetragonal (P4<sub>2</sub>/nmc) phases. In the FFT diffractogram, the central spot corresponds to the zero spatial frequency component, representing the average image intensity. It should not be confused with the unscattered transmitted beam observed in the center of reciprocal-space TEM images. The surrounding spots arise from the periodic lattice

	HZO multilayer	o-phase	t-phase	m-phase
Spot 1	5.29	5.54	5.39	5.87
Spot 2	3.25	3.34	3.32	3.51
Spot 3	3.77	3.73	3.87	3.86
Ratio (spot 1/ spot 2)	1.62	1.65	1.62	1.67
Ratio (spot 2/ spot 3)	0.86	0.89	0.85	0.90

**Table 6.1** Comparison of FFT spot spacing (in  $\text{nm}^{-1}$ ) between the  $\text{HZO}_{C50}$  sample data and the simulated phases shown in Figure 6.3.

fringes in the real-space HRTEM image and correspond to the reciprocal lattice vectors of the underlying crystal structure. Their positions and relative intensities are governed by the lattice spacing, crystal symmetry, and grain orientation, thereby enabling phase identification and zone-axis determination.

The experimental FFT shows strong agreement with simulated patterns of the ferroelectric orthorhombic phase viewed along the  $[\bar{1}01]$  zone axis (Figure 6.3c) and the tetragonal phase along the  $[\bar{1}11]$  direction (Figure 6.3d). The ratios of the distances from the center to spots 1 and 2, and from spots 2 to 3 in the experimental FFT, are measured to be 1.62 and 0.86, respectively. These values closely match those derived from the simulated diffraction patterns of the orthorhombic and tetragonal phases. As summarized in Table 6.1, the absolute spot spacings from the  $\text{HZO}_{C50}$  multilayer are also consistent with both phases, further supporting the coexistence of orthorhombic and tetragonal domains in the films. In contrast, the monoclinic phase shows larger deviations, particularly in the spot 1 spacing, making it less likely to account for the observed FFT pattern.

Figure 6.4 displays the current density–electric field and polarization–electric field hysteresis loops measured after electrical wake-up cycling. For comparison, the electrical properties of the  $\text{HO}_{C45}$  and  $\text{ZO}_{C45}$  films are also included as references. The  $\text{ZO}_{C45}$  film exhibits no observable switching current, confirming its paraelectric nature. In contrast, both the  $\text{HO}_{C45}$  and  $\text{HZO}_{C50}$  films display pronounced switching currents, characteristic of ferroelectric behavior. The  $\text{HO}_{C45}$  film shows a remanent polarization ( $P_r$ ) of  $8 \mu\text{C}/\text{cm}^2$  and a coercive field ( $E_c$ ) of  $1.5 \text{ MV}/\text{cm}$ , while the  $\text{HZO}_{C50}$  multilayer exhibits a slightly

higher  $P_r$  of  $9 \mu\text{C}/\text{cm}^2$  and a reduced  $E_c$  of  $1.2 \text{ MV}/\text{cm}$ . If the ZrO<sub>2</sub> layers in the HZO<sub>C50</sub> stack were purely dielectric, they would act as electrically passive "dead layers," diminishing the effective electric field across the ferroelectric film. This would typically result in a reduction of remanent polarization and an increase in coercive field,[159] neither of which are observed here. The comparable ferroelectric performance of the HZO<sub>C50</sub> and HO<sub>C45</sub> samples suggests that the active ferroelectric layer thickness is nearly identical in both cases. The findings raise the possibility that ferroelectric phase may be induced in ZrO<sub>2</sub> layers when integrated into a multilayer structure with HfO<sub>2</sub>, despite the paraelectric nature of the ZO<sub>C45</sub> film in its standalone form. It is likely that the current processing parameters for the ZrO<sub>2</sub> film are not optimal for stabilizing a ferroelectric phase independently. However, the presence of HfO<sub>2</sub> layer, with a closely matching lattice parameter, may promote phase stabilization through interfacial strain.

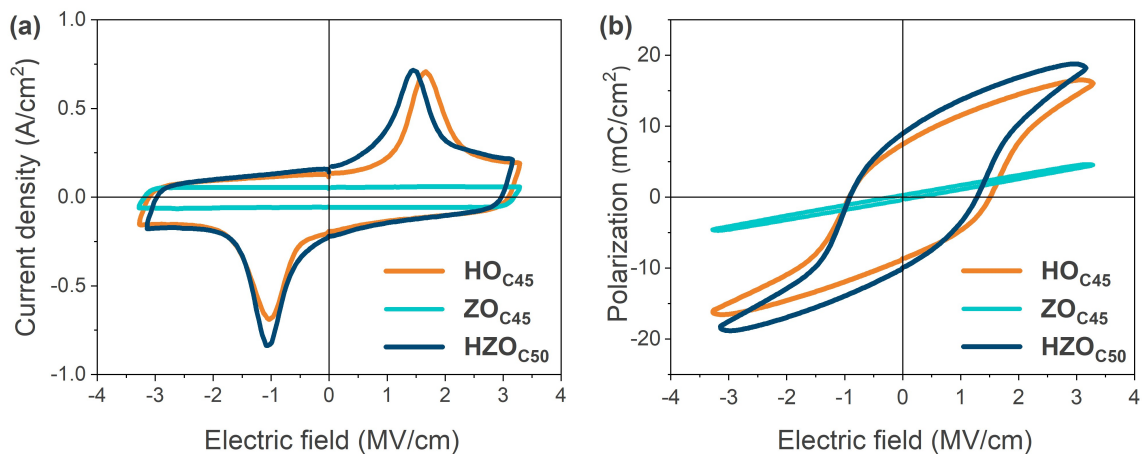


**Figure 6.4** (a) Current density versus electric field loops and (b) polarization versus electric field loops of the HO<sub>C45</sub>, ZO<sub>C45</sub> and HZO<sub>C50</sub> films.

The observed phase composition in the HZO<sub>C50</sub> multilayers may be strongly influenced by the specific sublayer where homogeneous nucleation is initiated. Given the alternating deposition of La:HfO<sub>2</sub> and ZrO<sub>2</sub>, variations in the resulting crystallographic phase may arise depending on whether nucleation occurs within the HfO<sub>2</sub> or ZrO<sub>2</sub> layers. The sublayer that acts as the primary nucleation site could govern the dominant phase that subsequently propagates throughout the multilayer stack. As such, layer-selective nucleation may play a critical role in determining whether ferroelectric or non-ferroelectric phases are stabilized in the final structure.

### 6.2.2 ZHO<sub>C50</sub>

The ZHO<sub>C50</sub> multilayer stack initiated with a ZrO<sub>2</sub> layer, the resulting structure displays poor ferroelectric performance (see Figure 6.5b), likely due to the stabilization of a nonpolar phase in the initial ZrO<sub>2</sub> layer. Nevertheless, the switching peaks in the current response indicate partial polarization switching, likely arising from polar grains nucleated within the HfO<sub>2</sub> layer. It is plausible that optimizing the processing conditions to favor a polar phase at the bottom interface could mitigate this effect. However, a comparable phenomenon has been observed by van Gent *et al.*, who studied epitaxial rhombohedral Hf<sub>1-x</sub>Zr<sub>x</sub>O<sub>2</sub> superlattices fabricated via pulsed laser deposition.[150] These results suggest that the initial layer's phase plays a critical role in determining ferroelectric response, independent of the deposition technique, crystal structure, or type of ferroelectric phase. Van Gent *et al.* suggested this occurs because the necessary interface for ferroelectric phase stabilization is disrupted when ZrO<sub>2</sub> rather than Hf-containing layers contact the bottom electrode.

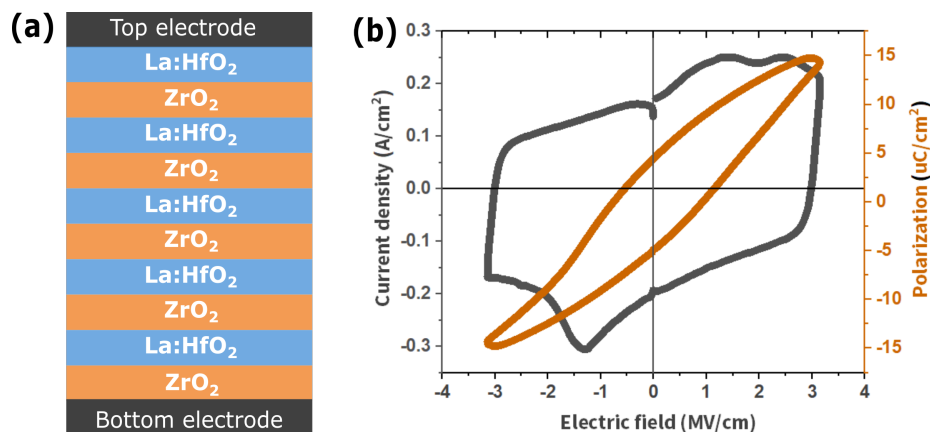


**Figure 6.5** (a) Schematic illustration of the multilayer structure, and (b) hysteresis loops of the ZHO<sub>C50</sub> film after applying 10,000 rectangular voltage pulses with incrementally increasing electric field amplitudes up to 3 MV/cm.

### 6.2.3 HZO<sub>C90</sub>

Figure 6.6a presents the structural schematic of the thick HZO<sub>C90</sub> multilayer film, consisting of six alternately deposited 15 nm-thick layers of La:HfO<sub>2</sub> and ZrO<sub>2</sub>, beginning with La:HfO<sub>2</sub> and terminating with ZrO<sub>2</sub>, resulting in a total film thickness of approximately 90 nm. The dark-field STEM image in Figure 6.6b confirms the formation of the intended multilayer

architecture, as evidenced by the periodic contrast variation between the La:HfO<sub>2</sub> and ZrO<sub>2</sub> layers. Unlike the HZO<sub>C50</sub> multilayer, where bright-field STEM imaging was employed, the HZO<sub>C90</sub> structure shown in Figure 6.6b was imaged using dark-field STEM. In this imaging mode, contrast is reversed relative to bright-field, heavier elements such as Hf scatter electrons more strongly and therefore appear brighter, while lighter elements like Zr appear darker. This results in La:HfO<sub>2</sub> layers appearing brighter than the ZrO<sub>2</sub> layers.

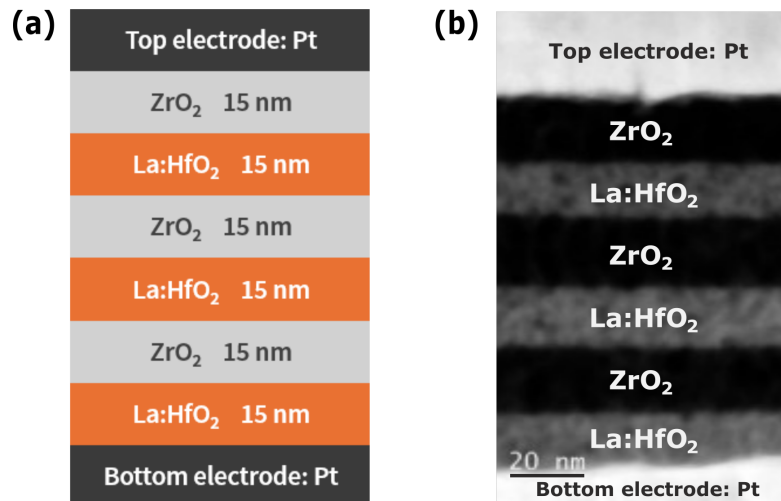


**Figure 6.6** (a) Structural schematics and (b) dark-field STEM image of the HZO<sub>C90</sub> multilayer thick film with Pt electrodes.

Figure 6.7 presents the current density–electric field and polarization–electric field hysteresis loops of the HZO<sub>C90</sub> film measured after 10,000 electrical wake-up cycles. For comparison, the hysteresis loops of the thick HO<sub>C90</sub> and thin HZO<sub>C50</sub> films are also included. The HO<sub>C90</sub> and HZO<sub>C90</sub> samples exhibit nearly identical ferroelectric behavior, each demonstrating a remanent polarization ( $P_r$ ) of 13  $\mu\text{C}/\text{cm}^2$  and a coercive field ( $E_c$ ) of 2 MV/cm. The comparable switching characteristics of the HO<sub>C90</sub> and HZO<sub>C90</sub> films, despite the inclusion of ZrO<sub>2</sub> layers in the latter, strongly suggest that the ZrO<sub>2</sub> sublayers contribute actively to the overall ferroelectric response, rather than acting as passive dielectric layers, similar to that observed in HZO<sub>C50</sub> film.

The enhanced  $P_r$  in the thicker HZO<sub>C90</sub> film in comparison to thin HZO<sub>C50</sub> may be attributed to the formation of larger, more continuous ferroelectric domains across the multilayer structure. On the other hand, the increase in coercive field with thickness could result from increased domain wall pinning. This increased pinning is consistent with the

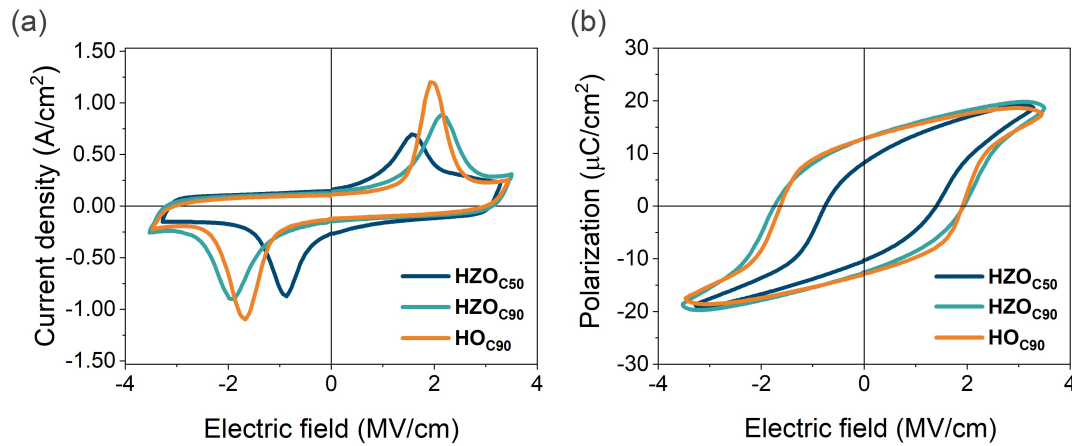


**Figure 6.7** (a) Current density–electric field loops and (b) polarization–electric field loops for  $\text{HO}_{\text{C}90}$ ,  $\text{HZO}_{\text{C}90}$ , and  $\text{HZO}_{\text{C}50}$  films. The thick films were measured after 10,000 wake-up cycles with incrementally increasing electric field amplitudes up to approximately 3 MV/cm, while the thin HZO film was measured after 1,000 wake-up cycles at a constant field of 3 MV/cm.

Al-Shareef model, where thicker films provide greater volume for electronic charge carrier trapping at domain wall regions, thereby restricting domain wall movement and requiring higher fields for switching.[160]

### 6.3 $\text{HfO}_2\text{--CeO}_2$ bilayer

Figure 6.8a illustrates the structural schematic of the  $\text{HfO}_2\text{--CeO}_2$  ( $\text{HCO}_{\text{L}30}$ ) bilayer thin film, comprising a 15 nm  $\text{HfO}_2$  bottom layer and a 15 nm  $\text{CeO}_2$  top layer, sandwiched between Pt electrodes. The corresponding GIXRD pattern shown in Figure 6.8b exhibits distinct diffraction peaks attributable to both materials. Sharp reflections at  $28.5^\circ$  and  $33.0^\circ$  are indexed to the (111) and (200) planes of cubic  $\text{CeO}_2$ , consistent with a highly crystalline fluorite phase. In addition, a broad peak centered around  $30.3^\circ$  is observed, corresponding to the (111) reflection of either the orthorhombic or tetragonal phase of  $\text{HfO}_2$ , as both share similar diffraction signatures in this angular range. Figure 6.8c shows the current density–electric field and polarization–electric field hysteresis loops of the  $\text{HCO}_{\text{L}30}$  bilayer film, measured after 20,000 electrical wake-up cycles. The loops exhibit a remanent polarization ( $P_r$ ) of  $3 \mu\text{C}/\text{cm}^2$  and a coercive field ( $E_c$ ) of 800 kV/cm. The relatively low  $P_r$  may result from depolarizing field effects introduced by the  $\text{CeO}_2$  layer, which could screen or destabilize the polarization in the adjacent  $\text{HfO}_2$ . Interestingly, the reduced  $E_c$  suggests that integrating

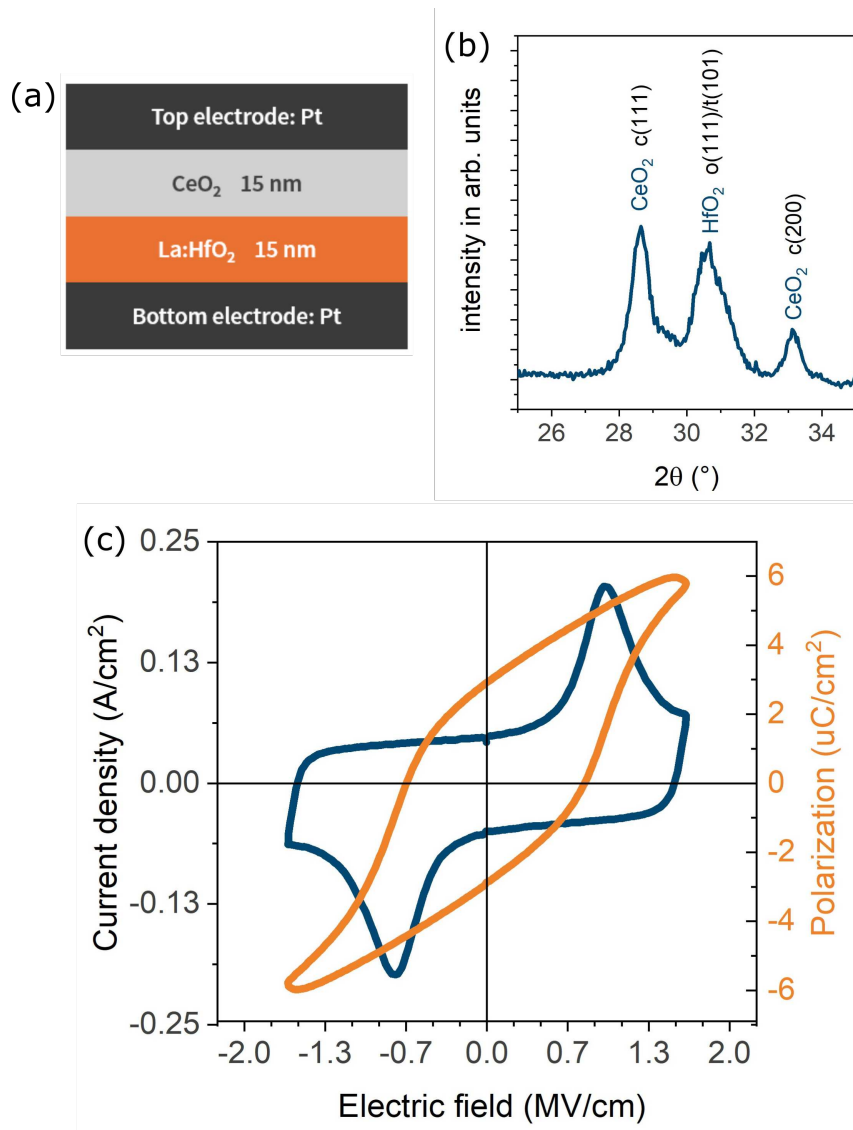


**Figure 6.8** (a) Structural schematics, (b) GIXRD patterns, (c) current density and polarization loops as a function of electric field (after 20,000 wake-up cycles), of the HfO<sub>2</sub>-CeO<sub>2</sub> bilayer thin film with Pt electrodes. The XRD patterns are compared with the reference patterns from the powder diffraction files.[161]

HfO<sub>2</sub> with CeO<sub>2</sub> may offer a pathway to lowering switching fields. However, we were unable to consistently reproduce high-quality bilayer films due to poor wetting behavior of the cerium nitrate hexahydrate precursor solution (dissolved in 2-methoxyethanol) on both Pt-Si substrates and HfO<sub>2</sub> surfaces, resulting in non-uniform film deposition and poor CeO<sub>2</sub> film morphology. These challenges raise the possibility that the CeO<sub>2</sub> layer may behave partially as a conductive path. If the majority of the applied voltage drops across the HfO<sub>2</sub> layer alone, the effective field in HfO<sub>2</sub> would correspond to approximately 1.4 MV/cm, which aligns

with the typical coercive field of our solution-processed HfO<sub>2</sub> films. Further investigation is needed to clarify the electrical role of the CeO<sub>2</sub> layer and its influence on the overall ferroelectric behavior of the bilayer system.

## 6.4 Effect of interfaces on wakeup

Although both HO<sub>C45</sub> and HZO<sub>C50</sub> films exhibit similar ferroelectric properties across different thickness regimes, their behavior under electrical cycling, particularly in the thin-film configuration, shows distinct differences. In the case of HZO<sub>C50</sub> film, the response to electrical wake-up cycling diverges significantly from that of HO<sub>C45</sub> film. This contrast is illustrated in Figure 6.9a, which presents the evolution of remanent polarization ( $2P_r$ ) as a function of wake-up cycles. To investigate this behavior, two wake-up protocols were employed. *Procedure 1* consisted of 1000 cycles applied at a relatively high electric field of approximately 3 MV/cm, which exceeds the typical coercive field ( $E_c$ ) observed in HfO<sub>2</sub>-based ferroelectric films. *Procedure 2*, in contrast, involved a gradual field ramping approach, where 7000 cycles were applied in seven sequential sets of 1000 cycles. In each set, the electric field was incrementally increased from approximately 0.8 MV/cm up to 3 MV/cm. This comparative analysis was aimed at gaining deeper insight into how the presence of interfaces in the HZO<sub>C50</sub> multilayer structure influences its electrical response during wake-up cycling under varying electric field conditions.

The HO<sub>C45</sub> films demonstrated poor endurance under immediate application of high fields and typically experienced dielectric breakdown within the first 10 cycles of Procedure 1, rendering this wake-up protocol unsuitable for such films. In contrast, the HZO<sub>C50</sub> multilayer structure exhibited greater endurance to the applied high electric field and displayed a clear wake-up effect. The initial polarization–electric field ( $P$ – $E$ ) hysteresis loops for the HZO<sub>C50</sub> film subjected to Procedure 1 and the HO<sub>C45</sub> film subjected to Procedure 2 are presented in Figure 6.9b. The HZO<sub>C50</sub> sample exhibits a characteristic "propeller-shaped" loop with a nonzero remanent polarization, a signature commonly reported in Hf<sub>*x*</sub>Zr<sub>1–*x*</sub>O<sub>2</sub> systems. This distinctive shape is typically associated with a field-induced phase transition from the nonpolar tetragonal (T) phase to the ferroelectric orthorhombic (o-III) phase, and is further influenced by factors such as defect pinning and the motion of charged domain walls.[162,

163] Following 1000 wake-up cycles, the  $\text{HZO}_{\text{C}50}$  film achieves a maximum  $2P_r$  value of  $18 \mu\text{C}/\text{cm}^2$  (Figure 6.9c), whereas the  $\text{HO}_{\text{C}45}$  film requires approximately 7000 cycles to reach a comparable polarization level (Figure 6.9d). When subjected to Procedure 2, the  $\text{HZO}_{\text{C}50}$  film exhibits a wake-up response nearly identical to that of the  $\text{HO}_{\text{C}45}$  film. These observations underscore the influence of interfacial effects within the  $\text{HZO}_{\text{C}50}$  stack on its electrical performance and suggest enhanced wake-up dynamics.

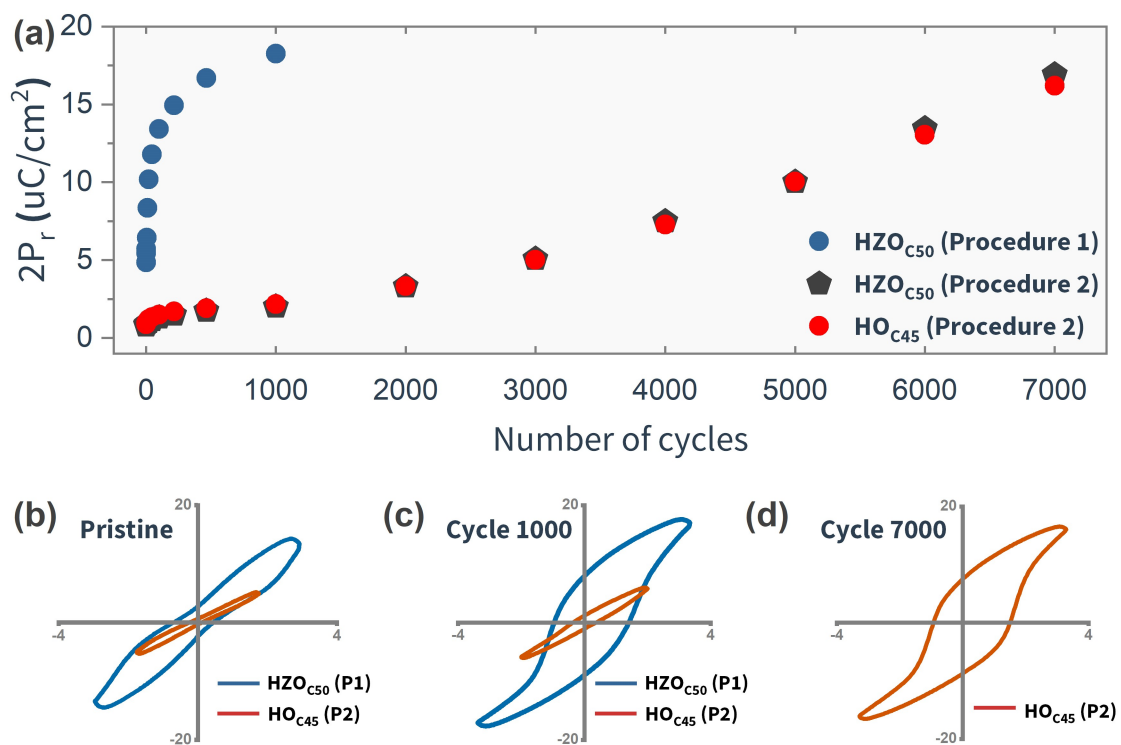


**Figure 6.9** (a) Remanent polarization  $2P_r$  vs number of wake-up cycles for  $\text{HZO}_{\text{C}50}$  and  $\text{HO}_{\text{C}45}$  films. (b) Pristine loops of  $\text{HZO}_{\text{C}50}$  and  $\text{HO}_{\text{C}45}$ , acquired from procedures 1 and 2, respectively. (c)  $\text{HZO}_{\text{C}50}$  and  $\text{HO}_{\text{C}45}$  loops measured after 1000 cycles following procedures 1 and 2, respectively. (d)  $\text{HO}_{\text{C}45}$  loop measured after 7000 cycles following procedure 2; for the  $\text{HZO}_{\text{C}50}$  film, maximum  $2P_r$  was achieved by procedure 1 (1000 cycles); therefore, no loop is recorded after 7000 cycles [P1: procedure 1, P2: procedure 2]

Wake-up field cycling is a common technique used in hafnia-based ferroelectrics to enhance their polarization response by redistributing defects, particularly oxygen vacancies.[51, 62] However, these defects—often localized at grain boundaries, interfaces, or domain walls—can also facilitate the formation of conductive filaments under high electric fields.[164–166] As a result, wake-up cycling at or above the coercive field ( $E_c$ ) can be detrimental to the dielectric integrity of conventional  $\text{La:HfO}_2$  ( $\text{HO}_{\text{C}45}$ ) films. It is hypoth-

esized that the ability of multilayer  $\text{HZO}_{C50}$  films to withstand the direct application of high electric fields stems from the presence of multiple  $\text{La:HfO}_2\text{-ZrO}_2$  interfaces, which act as barriers that disrupt the vertical formation of conductive filaments across the film thickness. To investigate this hypothesis, breakdown measurements presented in Figure 6.10 were conducted on both the  $\text{HO}_{C45}$  and  $\text{HZO}_{C50}$  samples under identical electrical stress conditions. The results demonstrate a stark contrast in dielectric robustness. The  $\text{HO}_{C45}$  film undergoes catastrophic breakdown at approximately 2.0 MV/cm, as evidenced by the sharp vertical spike in leakage current density reaching  $3.0 \times 10^{-1} \text{ A/cm}^2$ . In contrast, the  $\text{HZO}_{C50}$  multilayer maintains stable dielectric behavior with low leakage current density (below  $1.0 \times 10^{-1} \text{ A/cm}^2$ ) even at electric fields exceeding 4.0 MV/cm—twice the breakdown field of the  $\text{HO}_{C45}$  film.

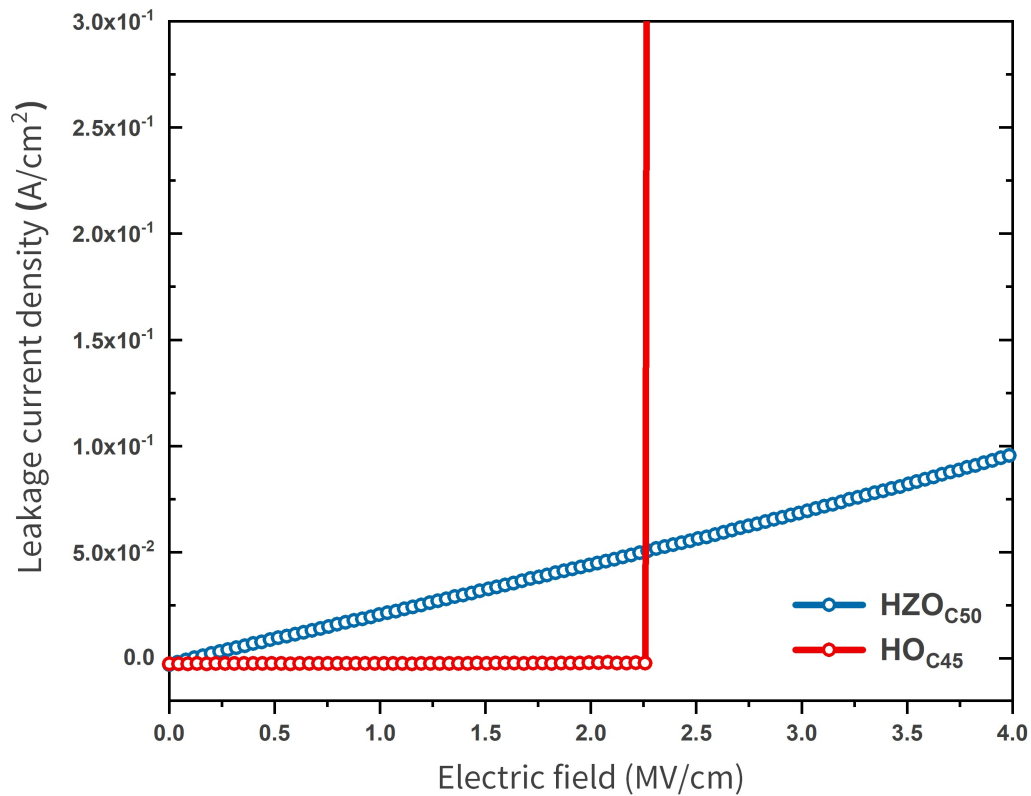


**Figure 6.10** Breakdown measurements of the pristine  $\text{HO}_{C45}$  and  $\text{HZO}_{C50}$  films.

The observation aligns with previous reports on epitaxial rhombohedral  $\text{Hf}_{1-x}\text{Zr}_x\text{O}_2$  superlattices, which show cycling endurance as high as  $10^6$  to  $10^9$  cycles,[150] further affirming that multilayer engineering is an effective strategy for enhancing the durability of ferroelectric hafnia-based films. Similar benefits have been observed beyond hafnia systems

as well, Sun et al.[167] reported a breakdown strength of 4.5 MV/cm in BZT-BCT multilayer films, compared to just 1 MV/cm in single-layer BZT and BCT films of equivalent thickness. This enhancement was attributed to the suppression of “electric tree” formation due to the presence of engineered interfaces. In addition to multilayering, other approaches to mitigating early fatigue in ferroelectric thin films include defect engineering, inhibition of vacancy diffusion, and the introduction of compositional inhomogeneities.[58, 168, 169]

Notably, this interface-mediated improvement in electrical properties was observed specifically in thin  $\text{HZO}_{C50}$  multilayers with 5 nm individual layer thicknesses (total thickness 50 nm), but was not replicated in thick  $\text{HZO}_{C90}$  multilayers with 15 nm individual layers (total thickness 90 nm). This thickness-dependent behavior can be attributed to the relationship between individual layer thickness and the average grain size in our films (15–20 nm). When individual layer thicknesses are smaller than the characteristic grain size ( $\sim 5$  nm layers), the engineered interfaces effectively disrupt filamentary growth pathways because grains span multiple layers, creating a tortuous path for defect migration and filament formation. In contrast, when individual layer thickness approaches or exceeds the grain size ( $\sim 15$  nm layers), complete grains can form within single layers, reducing the interface density per grain and thereby diminishing the effectiveness of interface engineering in disrupting vertical percolation paths. This grain size–interface spacing relationship explains why the protective effect of multilayering becomes less pronounced in thicker individual layers, where the interfaces are too sparse relative to the microstructural length scale to effectively interrupt conductive pathways.

## 6.5 Summary and outlook

This chapter investigated the design and fabrication of hafnia-based multilayer films as an alternative to conventional solid solution approaches for enhancing ferroelectric properties and electrical performance. The study focused on  $\text{HfO}_2\text{--ZrO}_2$  multilayers with varying individual layer thicknesses and  $\text{HfO}_2\text{--CeO}_2$  bilayer structures, with particular emphasis on understanding the role of interfaces in determining electrical behavior.

Key findings demonstrate that multilayer architectures offer distinct advantages over solid solution films. Thin  $\text{HZO}_{C50}$  multilayers (5 nm individual layers) exhibited comparable

ferroelectric properties to conventional  $\text{HO}_{C45}$  films while showing superior electrical endurance and enhanced wake-up dynamics. The presence of  $\text{ZrO}_2$  layers, despite being paraelectric in isolation, contributed actively to the ferroelectric response when integrated into the multilayer stack, suggesting strain-mediated phase stabilization across interfaces. Cross-sectional HRTEM analysis revealed continuous grain growth across multiple sublayers, indicating strong crystallographic coupling between alternating compositions. Importantly, the initial layer composition was found to be critical, with  $\text{HfO}_2$ -initiated stacks ( $\text{HZO}_{C50}$ ) demonstrating robust ferroelectricity, while  $\text{ZrO}_2$ -initiated structures ( $\text{ZHO}_{C50}$ ) showed poor performance.

The interface-mediated improvement in electrical properties was thickness-dependent and directly related to the grain size–interface spacing relationship. While thin multilayers (5 nm individual layers) benefited from enhanced breakdown resistance due to interfaces disrupting filamentary conduction paths, thick multilayers (15 nm individual layers) showed reduced effectiveness as complete grains formed within single layers, diminishing the protective role of interfaces.

Future research directions should focus on optimizing processing conditions to stabilize ferroelectric phases in  $\text{ZrO}_2$ -initiated multilayers and exploring the potential of  $\text{CeO}_2$ -based systems once morphological challenges are resolved. The demonstrated grain size–interface engineering principle opens pathways for designing multilayer stacks with tailored electrical properties by controlling the ratio of layer thickness to characteristic microstructural length scales. Furthermore, these findings demonstrate a novel strategy for enhancing the wake-up behavior of ferroelectric  $\text{HfO}_2$ - and  $\text{ZrO}_2$ -based thin films through the deliberate introduction of interfaces, offering an alternative to traditional solid solution approaches. This interface engineering method can be effectively extended to the fabrication of thicker multilayer films for piezoelectric applications, as it not only improves wake-up characteristics but also mitigates early dielectric breakdown during prolonged electrical cycling—two key challenges commonly faced in thicker film architectures.



# Chapter 7

## HfO<sub>2</sub> based resonator

This chapter is dedicated to the application of the ferroelectric thin film developed over the course of this doctoral research. The intrinsic piezoelectric response of ferroelectric hafnium oxide is harnessed for the fabrication of a high-overtone bulk acoustic resonator (HBAR) device. In Section 7.1, a review of the relevant literature is presented, along with the underlying motivation for pursuing a hafnia-based resonator architecture. Section 7.2 outlines the fundamental operating principles of the HBAR. Section 7.3 addresses key design considerations that influence device performance. In Section 7.4, the experimental results are systematically discussed. Finally, Section 7.5 offers a summary of the chapter, and potential avenues for future research are identified, with particular emphasis on strategies to enhance the quality factor of the device.

### 7.1 Motivation

High-overtone bulk acoustic resonators (HBARs) are attracting attention due to their excellent scalability, high operational frequencies, elevated quality ( $Q$ )-factors, and the ability to support multiple phonon modes.[170–175] These attributes make HBARs highly suitable for a variety of applications, including low-phase-noise frequency reference oscillators and high-resolution material characterization.[176–180] Furthermore, the presence of multiple resonant modes allows for interaction with quantum systems such as superconducting qubits[181, 182] and color centers,[183, 184] enabling the storage and manipulation of quantum information within the resonator structure.

A conventional HBAR consists of a thin piezoelectric film between electrodes on a thick passive substrate (Figure 7.1). An applied alternating electric field excites longitudinal bulk acoustic waves (BAWs), which propagate through the substrate and reflect at interfaces to form discrete high-overtone modes. To enable efficient excitation and sustainment of these GHz-range acoustic modes, piezoelectric materials with low dielectric and acoustic losses—such as AlN,[185] AlScN,[186, 187]  $\text{Ba}_{0.5}\text{Sr}_{0.5}\text{TiO}_3$ ,[179] and ZnO[188]—are commonly employed. The key figures of merit for HBARs are the quality factor ( $Q$ ), which quantifies energy storage relative to dissipation, and the electromechanical coupling coefficient ( $k_t^2$ ), which determines electrical-to-mechanical energy conversion efficiency.

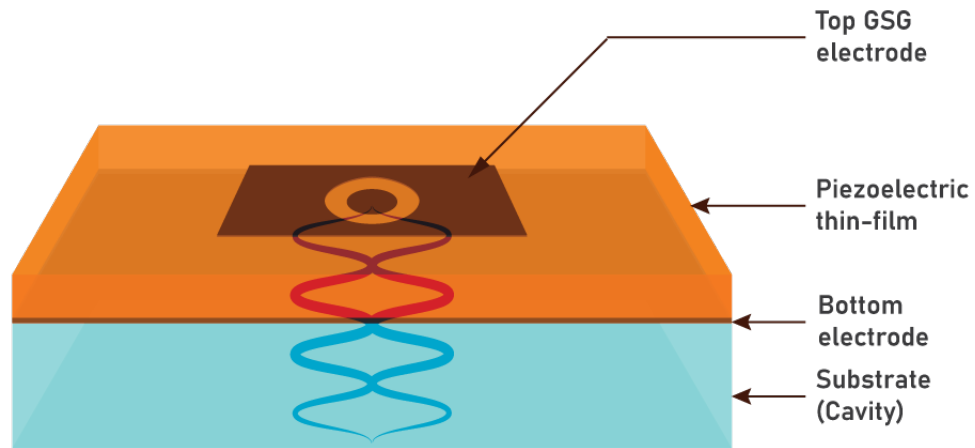


**Figure 7.1** Schematic of an HBAR. (GSG: ground-source-ground)

The ferroelectric properties, combined with excellent scalability, make  $\text{HfO}_2$  thin films a particularly promising material for high-frequency electromechanical transduction. To date, only a limited number of studies have reported on resonators based on ferroelectric hafnia. Ghatge et al. have demonstrated integrated nano-electromechanical resonators based on 10 nm-thick ferroelectric  $\text{Hf}_{0.5}\text{Zr}_{0.5}\text{O}_2$  (HZO) films, achieving resonance frequencies from 340 kHz to 13 GHz with a maximum  $f_0Q$  product of  $3.97 \times 10^{12}$ , where electromechanical transduction is primarily governed by the electrostrictive effect.[189] Another study by Ghatge et al. demonstrated 30 nm-thick HZO-based nano-electromechanical resonators with ultra-high aspect ratio membranes, operating at 195 kHz with large vibration amplitude and a maximum  $Q$  of 3300 under high vacuum, enabled by strong electrostrictive coupling.[190] Tharpe et al. have demonstrated switchable nanoelectromechanical resonators based on 50

nm-thick Hf<sub>0.5</sub>Zr<sub>0.5</sub>O<sub>2</sub>-Al<sub>2</sub>O<sub>3</sub> superlattice transducers, operating in lateral and thickness-oriented bulk acoustic wave modes, achieving resonance frequencies from 0.39 GHz to 17.32 GHz with a maximum  $f_0Q$  product of  $4.04 \times 10^{12}$  Hz and electromechanical couplings of 2.5%, where electromechanical transduction is primarily governed by linear piezoelectric transduction induced by pulsed poling.[191] These results collectively underscore the material's promise for chip-scale transduction in both classical and quantum domains, though the demonstrated devices remain limited to flexural and extensional modes.

In contrast, the HBAR presents a more suitable architecture for exploiting the full piezoelectric and ferroelectric potential of hafnia-based films at GHz-range frequencies. HBARs offer a high-Q, multi-mode acoustic platform with minimal energy dissipation, ideally suited for RF filtering and frequency control.[192] Ferroelectric hafnia, with its demonstrated piezoelectric coefficient ( $d_{33}$ ) of 7.7 pm/V,[85] comparable to that of aluminum nitride (AlN) at 5 pm/V,[17], the current industry standard, emerges as a strong candidate for next-generation, monolithically integrable HBAR devices.

## 7.2 HBAR theory

### 7.2.1 Fundamental architecture and theoretical foundation

Unlike Film Bulk Acoustic Resonators (FBARs) or Solidly Mounted Resonators (SMRs), the substrate in an HBAR is not acoustically decoupled; instead, it actively functions as a resonant cavity for acoustic waves. When an alternating electric field is applied across the electrodes, the piezoelectric layer generates acoustic waves that couple into the substrate, exciting its numerous bulk acoustic modes, which then couple back to the piezoelectric transducer. Because the substrate is much thicker than the piezoelectric film, the majority of the acoustic energy is stored within the substrate, making its acoustic properties the dominant factor in determining the resonator's quality ( $Q$ ) factor.

The fundamental physics governing HBAR operation is based on acoustic wave propagation, where the relationship between wave velocity ( $c$ ), wavelength ( $\lambda$ ), and frequency ( $f$ ) is expressed as  $c = \lambda f$ . The speed of wave propagation in the composite structure is determined by the effective material properties:

$$c = \sqrt{\frac{K_{eff}}{\rho_{eff}}} \quad (7.1)$$

where  $K_{eff}$  is the effective Young's modulus and  $\rho_{eff}$  is the effective density.

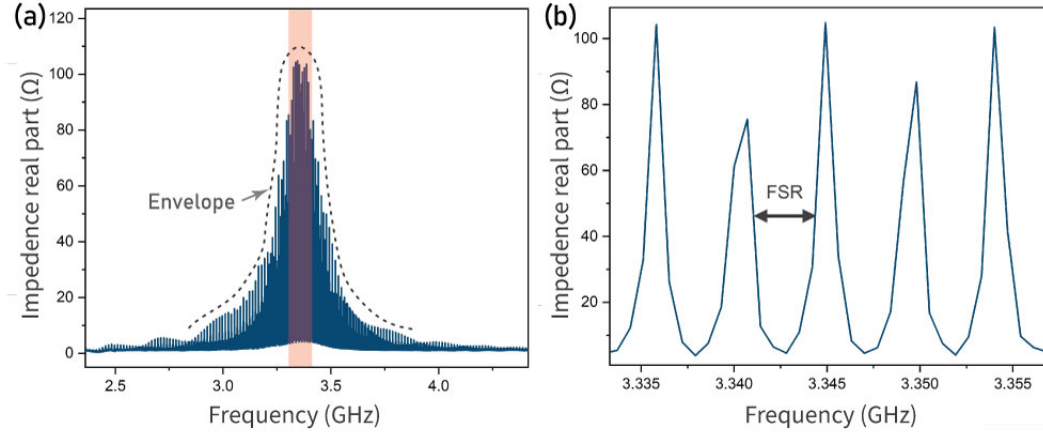


**Figure 7.2** Measured impedance of a LiNbO<sub>3</sub> HBAR showing the dense comb of substrate cavity modes. (a) Wide frequency span illustrating the overall amplitude envelope set by the piezoelectric transducer response. (b) Zoomed view of the shaded region of (a), showing the uniform peak spacing that defines the Free Spectral Range (FSR). This measurement was performed on a LiNbO<sub>3</sub> sample, similar to devices previously demonstrated by Pijolat et al.[193]

In an HBAR structure, acoustic waves propagate through the thick substrate and reflect at the interfaces, creating standing wave patterns that define the device's resonant behavior. The substrate acts as an acoustic cavity, supporting multiple resonant modes when its thickness corresponds to integer multiples of half-wavelengths. This gives rise to a dense comb of substrate bulk modes (Figure 7.2a) with resonant frequencies approximately given by:

$$f_n \approx \frac{nv_s}{2d_s} \quad (7.2)$$

where  $n$  is the harmonic order,  $v_s$  is the acoustic velocity in the substrate, and  $d_s$  is the substrate thickness. These modes are observed most strongly around the resonance envelope of the piezoelectric transducer, which governs the overall amplitude profile of the comb. The uniform spacing between adjacent modes defines the Free Spectral Range (FSR) as  $\Delta f = v_s/(2d_s)$ , depicted in Figure 7.2b. The multi-mode structure distinguishes HBARs

from conventional single-mode resonators and enables applications requiring closely spaced resonances or broadband operation.

### 7.2.2 Electromechanical coupling

A key metric for HBAR performance is the electromechanical coupling coefficient ( $k^2$ ), which quantifies the efficiency of energy conversion between electrical and mechanical domains, give by:

$$k_{eff}^2 = \frac{f_A^2 - f_R^2}{f_A^2} \quad (7.3)$$

where  $f_A$  and  $f_R$  represent the anti-resonance and resonance frequencies, respectively.

Electromechanical coupling coefficient is influenced by material choice, electrode design, and interfaces. For instance, aluminum nitride (AlN) typically exhibits  $k^2$  values around 6.5-7%,[17] while lithium niobate (LiNbO<sub>3</sub>) can reach 43%.[193]

### 7.2.3 Quality factor considerations

High-Overtone Bulk Acoustic Resonators (HBARs) are recognized for their exceptionally high quality factors (Q), which are crucial for stable frequency control applications and ultra-stable frequency sources. The composite structure, where a thin piezoelectric film acts as a transducer on a substantially thicker, low-loss substrate, ensures that the majority of acoustic energy is stored within the substrate. Consequently, the overall quality factor can be approximated as a weighted average of the constituent layers:

$$Q_{total} \approx Q_s \left(1 - \frac{E_p}{E_{total}}\right) + Q_p \left(\frac{E_p}{E_{total}}\right) \quad (7.4)$$

where  $Q_s$  and  $Q_p$  represent the quality factors of the substrate and piezoelectric layer, respectively, and  $E_p/E_{total}$  denotes the fraction of acoustic energy stored in the piezoelectric layer.

Achieving high Q in HBARs critically depends on the substrate's acoustic properties, including low viscoelastic and dielectric losses, and precise parallelism and mirror-quality polishing of its faces. Additional factors influencing the overall Q include electrode material

and geometry, ohmic losses, intrinsic material dissipation mechanisms, and air damping at lower frequencies.[17]

A key performance metric for HBARs is the quality factor-frequency product ( $Q \cdot f$ ), which typically exceeds  $10^{14}$  Hz for well-designed devices:

$$Q \cdot f > 10^{14} \text{ Hz} \quad (7.5)$$

This superior performance makes HBARs advantageous over other acoustic devices like FBARs or SMRs, whose  $Q \cdot f$  products are often an order of magnitude lower.[17] Notable achievements include a record  $Q \cdot f$  product of  $1.1 \times 10^{14}$  Hz with Aluminum Nitride (AlN) on sapphire substrates,[171] and  $Q$  factors of 53,000 at 1.5 GHz using Lithium Niobate (LiNbO<sub>3</sub>), yielding  $Q \cdot f$  products above  $8 \times 10^{13}$  Hz.[193, 194]

## 7.2.4 Impedance matching and power transfer

Efficient acoustic power transfer between the piezoelectric layer and substrate depends on the acoustic impedance mismatch, which is determined by the material properties.[17] The reflection coefficient at the interface is given by:

$$R = \left| \frac{Z_2 - Z_1}{Z_2 + Z_1} \right|^2 \quad (7.6)$$

where  $Z_1 = \rho_1 v_1$  and  $Z_2 = \rho_2 v_2$  represent the acoustic impedances of adjacent layers. Material selection aims to minimize this reflection coefficient to maximize acoustic energy transfer into the substrate cavity.

The theoretical framework presented here provides the foundation for understanding and optimizing hafnia-based HBAR performance, with particular emphasis on achieving high  $Q$ -factor operation and efficient electromechanical coupling across the desired frequency spectrum.

## 7.3 HfO<sub>2</sub> HBAR Design

### 7.3.1 Target frequency calculation

The design of high-overtone bulk acoustic wave resonators (HBARs) based on hafnium dioxide (HfO<sub>2</sub>) thin films requires careful consideration of multiple parameters to achieve

optimal performance at a target frequency. This section presents the design methodology for HfO<sub>2</sub> HBAR devices build upon theoretical framework presented above. The design methodology includes film thickness optimization, impedance matching considerations, and electrical field distribution analysis.

For thickness-mode resonators, the boundary condition for resonance is satisfied when:

$$n \cdot \frac{\lambda}{2} = d \quad (7.7)$$

where  $n$  is the mode number, and  $d$  is the film thickness.

Combining equations 7.1, and 7.7, the resonance frequency for the fundamental mode ( $n = 1$ ) is:

$$f_r = \frac{1}{2d} \sqrt{\frac{K_{eff}}{\rho_{eff}}} \quad (7.8)$$

For the HfO<sub>2</sub> thin film resonator design, the following material properties were considered:

- Effective Young's modulus:  $K_{eff} = 300$  GPa
- Effective density:  $\rho_{eff} = 8000$  kg/m<sup>3</sup>

Using Equation 7.8, the required thicknesses to achieve the target frequencies were calculated and are summarized in Table 7.1.

Thickness (nm)	$f_r$ (GHz)
45	68
100	30
200	15
500	6
1000	3

**Table 7.1** Target resonance frequencies and corresponding active-layer thicknesses required for HfO<sub>2</sub> HBAR operation.

### 7.3.2 Coplanar waveguide probing and impedance matching

Proper impedance matching is crucial for efficient energy transfer between the resonator and external measurement systems. For our HfO<sub>2</sub> HBAR characterization, a concentric electrode configuration was employed, following the RF measurement technique developed for thin dielectric film characterization.[195] This design offers several advantages: simplified fabrication requiring only single-step lithography on the top electrode, elimination of direct contact requirements to the bottom electrode, and effective isolation of the active resonator area from parasitic effects.

The concentric electrode design consists of a central circular patch serving as the signal electrode (S) surrounded by a ground ring (G), as illustrated in Figure 7.3. This configuration enables coplanar waveguide (CPW) probe measurements while maintaining controlled impedance characteristics. The electrical path to the bottom electrode is established through the large capacitance formed between the outer ground ring and the bottom metal layer, eliminating the need for direct bottom contact.

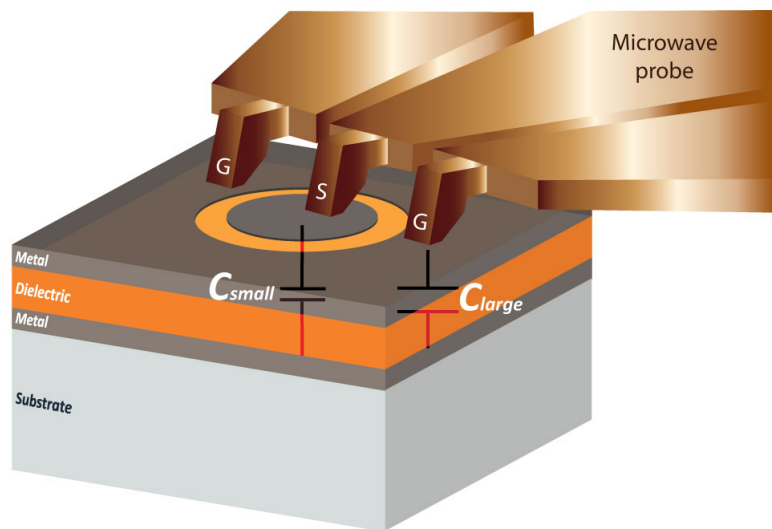


**Figure 7.3** Measurement setup of the metal–dielectric–metal trilayer capacitor using a miniature coplanar waveguide (CPW) probe, with a central signal pad (S) surrounded by ground pad (G).

The measurement principle relies on the capacitive coupling hierarchy within the concentric structure, as presented in Figure 7.3. The capacitance between the central signal electrode and the bottom metal layer is significantly smaller ( $C_{small}$ ) than the capacitance formed between the large outer ground ring and the bottom electrode ( $C_{large}$ ). This capaci-

tance ratio ensures that the electrical response of the complete circuit is dominated by the smaller central capacitor, effectively isolating the active resonator area for characterization. The characterization employs a one-port reflection measurement approach using a vector network analyzer (VNA). The measurement technique using VNA is detailed in Appendix A. Following calibration with a standard reference wafer, the CPW probe measures the reflection coefficient of incident microwaves from the device under test. This reflection data is subsequently converted to impedance values, enabling extraction of the resonator's capacitive and resistive characteristics across the frequency range of interest.

Based on the HBAR stack and the dielectric properties of hafnia, impedance matching calculations can be carried out. The capacitance of the central circular electrode is given by:

$$C = \frac{\varepsilon_r \varepsilon_0 \pi r^2}{d} \quad (7.9)$$

where  $\varepsilon_r$  is the relative permittivity of HfO<sub>2</sub> (taken as 25),  $\varepsilon_0$  is the permittivity of free space ( $8.854 \times 10^{-12}$  F/m),  $r$  is the electrode radius, and  $d$  is the film thickness.

The impedance relationship

$$Z = \frac{1}{2\pi f C} \quad (7.10)$$

can be rearranged to solve for the required electrode radius. For 50  $\Omega$  impedance matching at the target frequency, the required electrode radius is:

$$r = \sqrt{\frac{d}{2\pi^2 f \varepsilon_r \varepsilon_0 50}} \quad (7.11)$$

Table 7.2 summarizes the calculated electrode diameters required to achieve 50  $\Omega$  impedance matching for different target frequencies of the HBAR stack.

Thickness (nm)	$f_r$ (GHz)	Diameter ( $\mu\text{m}$ )
45	68	$\sim 2$
100	30	$\sim 8$
200	15	$\sim 16$
500	6	$\sim 40$
1000	3	78

**Table 7.2** Electrode diameter for 50 $\Omega$  impedance matching.

However, a challenge arises from the CPW probe tip which has a width of  $20\ \mu\text{m}$ , for films thinner than  $300\ \text{nm}$ , the required source electrode diameter falls below  $20\ \mu\text{m}$ , preventing proper impedance matching.

### 7.3.3 Electric field distribution and voltage breakdown considerations

A key requirement for extracting ferroelectric and, consequently, piezoelectric properties from HfO<sub>2</sub> is electrical poling. Due to the relatively large coercive field of hafnia, the DC bias needed to pole thick films can approach or exceed the air breakdown limit. For instance, achieving a coercive field of  $\sim 2\ \text{MV/cm}$  in a  $500\ \text{nm}$  film requires a DC bias of approximately  $100\ \text{V}$ .

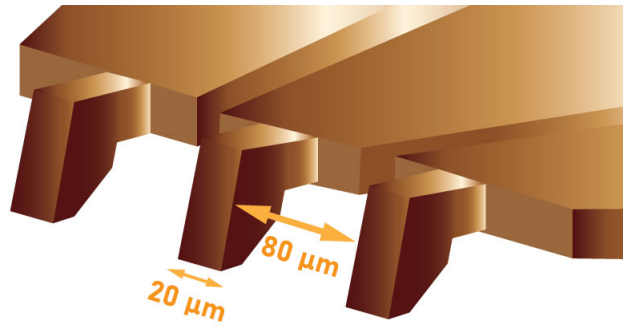


**Figure 7.4** Schematic of the CPW probe tip showing finger geometry and dimensions.

However, air gaps between the ground (G) and signal (S) fingers of the probe is  $80\ \mu\text{m}$  (Figure 7.4), which imposes additional voltage breakdown constraints. The critical gap distance can be estimated from the dielectric strength of air as

$$gap = \frac{\text{Voltage}}{\text{Dielectric strength of air}} \quad (7.12)$$

For a  $100\ \text{V}$  bias and an air dielectric strength of  $1\ \text{kV/mm}$ , the required gap is

$$gap = \frac{100\ \text{V}}{1\ \text{kV/mm}} = 100\ \mu\text{m}. \quad (7.13)$$

To ensure reliable operation without probe tip damage, thinner films requiring DC voltages below  $80\ \text{V}$  for poling were selected. Although the initial approach involved

applying DC offset in-situ using the VNA during frequency sweeping, this method resulted in probe damage and electrode pad failure. Consequently, a conventional poling methodology was adopted, wherein the capacitor structure was first poled using a single probe contact on the source electrode, followed by separate resonance measurements.

## 7.4 Resonance measurements on HfO<sub>2</sub> thin films

Two La:HfO<sub>2</sub> HBAR devices were fabricated with our highest quality thin-films, a 45 nm film (HO<sub>C45</sub> annealed in N<sub>2</sub>:O<sub>2</sub> 1:1) targeting 60 GHz frequency and a 200 nm film (HO<sub>C200</sub> annealed in N<sub>2</sub>:O<sub>2</sub> 1:1) designed for resonance at ~15 GHz. Both HO<sub>C45</sub> and HO<sub>C200</sub> were grown on double-side polished platinized silicon substrates to minimize acoustic losses and ensure efficient energy coupling. Based on the impedance matching calculations, the HO<sub>C45</sub> and HO<sub>C200</sub> devices required source electrode diameters of 4 μm and 16 μm, respectively, to achieve proper 50 Ω matching. These dimensions are significantly smaller than the 20 μm probe tip width, creating fabrication constraints that prevented optimal impedance matching. However, this impedance mismatch alone should not have completely suppressed the resonant behavior. Both devices underwent ferroelectric poling prior to RF testing to activate the piezoelectric properties of the hafnia layer. The impedance characteristics were measured using a vector network analyzer with coplanar waveguide probing.

Figure 7.5 shows the measured impedance response for the HO<sub>C45</sub> HBAR device. Although the real and imaginary components of impedance exhibit smooth, monotonic variations without the characteristic sharp resonance features expected for a functioning bulk acoustic resonator. The impedance magnitude remains relatively low throughout the frequency range, with both real and imaginary parts showing gradual frequency-dependent changes typical of a purely capacitive response.

The impedance characteristics of the HO<sub>C200</sub> HBAR device are presented in Figure 7.6(a), revealing predominantly capacitive behavior consistent with the previous observations. The imaginary impedance component exhibits the characteristic 1/*f* frequency dependence expected for a capacitive response. While a sharp drop in real impedance occurs near 16 GHz, potentially indicating parasitic resonance effects, no distinct acoustic resonance signatures are evident within the target frequency range of approximately 16 GHz. To

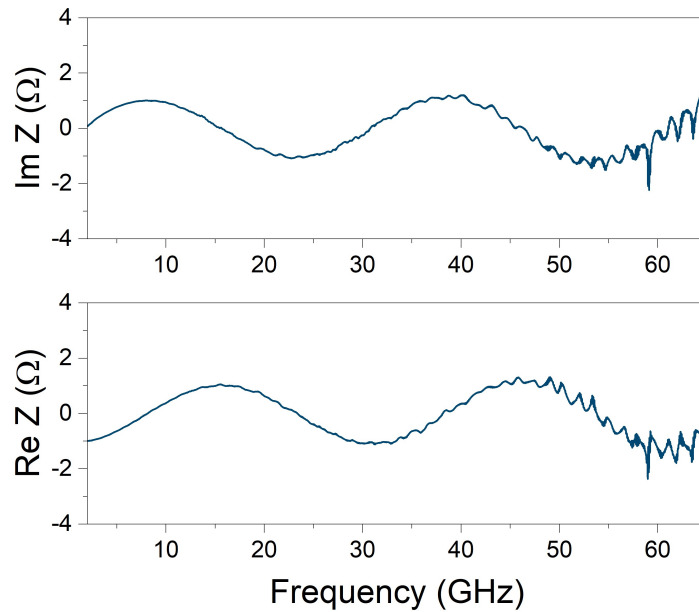


**Figure 7.5** Real and imaginary impedance characteristics of HO<sub>C45</sub> HBAR device swept till 65 GHz.

investigate the underlying cause of the absent resonance behavior, the piezoelectric properties of the poled HO<sub>C200</sub> film were characterized using double-beam laser interferometry (DBLI). The polarization-electric field hysteresis loop, measured after electrical poling and shown in Figure 7.6(b), exhibits a significantly degraded ferroelectric response compared to the same sample characterized in Chapter 4 for Raman spectroscopy. This deterioration can be attributed to the large electrode dimensions (400  $\mu\text{m}$  diameter) required for DBLI measurements. In polycrystalline HfO<sub>2</sub> films, such large electrodes tend to exhibit poor switching behavior due to the presence of numerous grains with varying coercive fields, making complete polarization reversal difficult.[196] The displacement-electric field measurement, presented in Figure 7.6(c), confirms the poor piezoelectric performance with a piezoelectric coefficient ( $d_{33}$ ) value of less than 1 pm/V.

The exceptionally low  $d_{33}$  provides a clear explanation for the absence of resonance in the HBAR devices. The intrinsically low electromechanical coupling of our solution-processed hafnia films hinders efficient conversion between electrical and acoustic energy even after ferroelectric poling. Schenk et al.[85] reported that the piezoelectric coefficient  $d_{33}$  of HfO<sub>2</sub> decreases from about 7.7 pm/V to 3.5 pm/V upon cycling, pointing to possible degradation of piezoelectric performance. To exclude poling-related loss of  $d_{33}$ , we also tested electrically untreated film stacks, but no resonance was detected. The inherently low

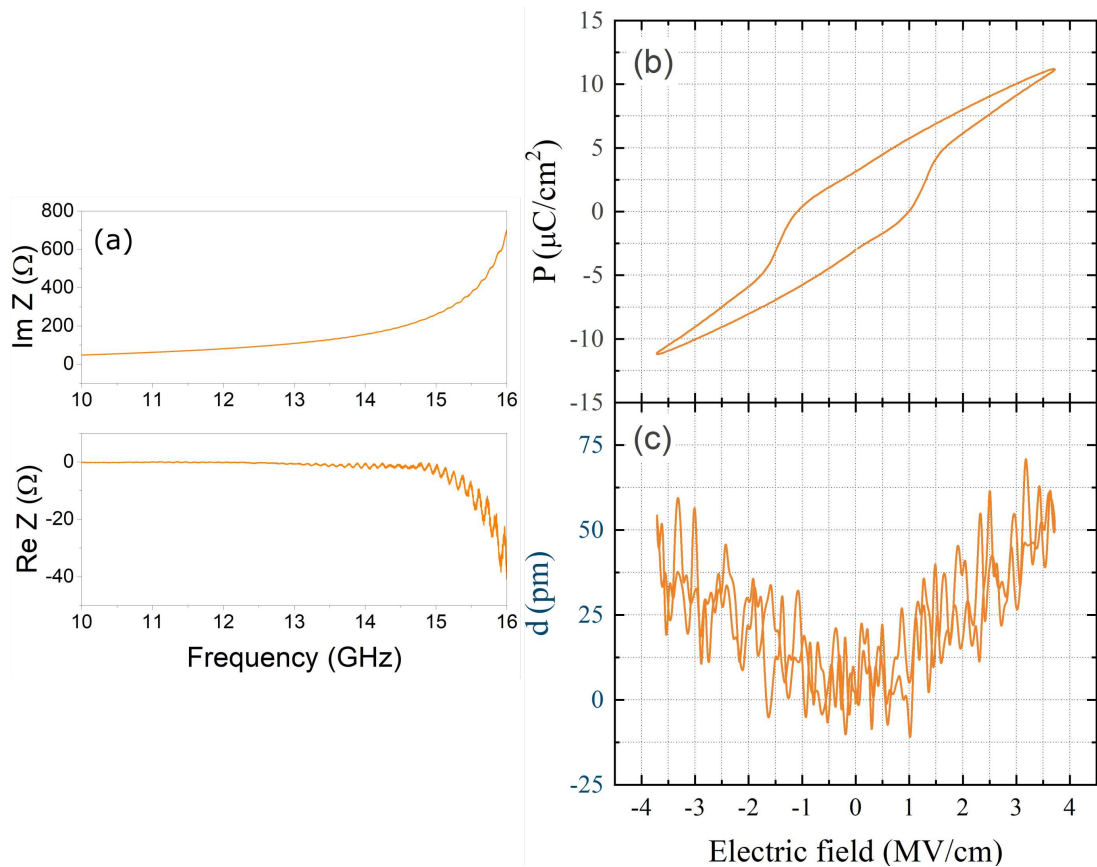


**Figure 7.6** (a) Real and imaginary impedance of HO<sub>C200</sub> HBAR device swept till 16 GHz, (b) polarization vs. electric field hysteresis, (c) displacement vs. electric field measured at 1 kHz for piezoelectric coefficient  $d_{33}$  using double-beam laser interferometry (DBLI). All the measurements were done after wake-up cycling.

piezoelectric coefficients likely suppress acoustic wave generation, leaving resonances buried beneath the system noise floor. The predominantly capacitive response further suggests that device impedance is governed by electrode geometry rather than electromechanical coupling, indicating poor acoustic interaction with the substrate and/or masking by parasitic capacitance.

## 7.5 Summary and Outlook

This chapter demonstrated an attempt to develop high-overtone bulk acoustic resonators (HBARs) using ferroelectric La:HfO<sub>2</sub> thin films, targeting frequencies of  $\sim 15$  GHz and  $\sim 60$  GHz through optimized film thickness design and impedance matching considerations. Despite successful device fabrication with proper electrode geometries and ferroelectric pol-

ing protocols, no acoustic resonance signatures were observed in either the 45 nm or 200 nm devices. The absence of resonant behavior is attributed to insufficient piezoelectric response, with measured  $d_{33}$  values below 1 pm/V well below the threshold required for efficient electromechanical coupling in HBAR architectures. This highlights the critical need to enhance hafnia's intrinsic piezoelectric properties and identify strategies to reduce acoustic losses. Future research should prioritize systematic optimization of hafnia's piezoelectric properties by controlling crystallographic orientation, employing dopant engineering strategies, and tailoring thermal processing conditions to achieve a stable, high-performance piezoelectric response suitable for practical acoustic resonator applications. In parallel, exploring alternative device architectures that incorporate substrates with favorable acoustic characteristics, such as sapphire ( $\text{Al}_2\text{O}_3$ ) or lithium niobate ( $\text{LiNbO}_3$ ), to minimize acoustic losses may be essential for unlocking hafnia's full potential in next-generation RF and quantum acoustic technologies.

# Chapter 8

## Conclusions and perspectives

This thesis provides comprehensive insights into the fabrication and optimization of solution-processed ferroelectric hafnia thin films, establishing new pathways for achieving high-quality HfO<sub>2</sub> thin films with enhanced ferroelectric properties. Importantly, we now return to the research questions introduced in Chapter 1, providing clear answers based on the results presented throughout this work.

1. Can controlled CSD growth conditions, particularly annealing atmospheres, enable reproducible fabrication of high-quality ferroelectric HfO<sub>2</sub> films?

Yes. Chapter 4 establishes annealing atmosphere as a decisive factor governing the balance between organic precursor decomposition, defect chemistry, and ferroelectric performance in HfO<sub>2</sub> films. Pure Ar atmospheres enable stable ferroelectric switching ( $E_c \sim 2$  MV/cm) but suffer from residual carbon and lower film density, while oxygen-rich conditions improve decomposition and densification yet typically suppress ferroelectricity through excessive vacancy passivation. The optimal solution is achieved under balanced N<sub>2</sub>:O<sub>2</sub> (1:1) atmospheres, which combine effective organic removal with preservation of beneficial defect structures, yielding superior properties including reduced coercive fields (1.3 MV/cm) and enhanced breakdown strength. The reproducibility achieved under these optimized conditions also enabled reliable Raman measurements, confirming stable phase formation across samples.

Microstructural engineering in Chapter 5, using the layer-by-layer methodology, highlights the effectiveness of controlling growth kinetics to overcome inherent

limitations of solution processing. Reducing the individual layer thickness from  $\sim 15$  nm to  $\sim 5$  nm shifted the growth regime from granular to layered, increasing film density from 78–80% to 87% of the theoretical value and enabling systematic control of crystallographic texture. Under optimized  $N_2:O_2$  atmospheres, this approach promoted preferential (002) orientation, which, together with improved density, doubled the remanent polarization from  $7.5 \mu\text{C}/\text{cm}^2$  to  $15 \mu\text{C}/\text{cm}^2$  while achieving switching with negligible leakage current. These values position the films developed in this work among the higher-performing CSD studies reported in the literature (Table 8.1).

No	Material	Thickness (nm)	$P_r$ ( $\mu\text{C cm}^{-2}$ )	$E_c$ ( $\text{MV cm}^{-1}$ )	Wake-up cycles	Ref
1	HfO <sub>2</sub>	136	22.56	-	$10^5$	[107]
2	CeO <sub>2</sub> -HfO <sub>2</sub>	78	20	1.5	-	[156]
3	Y:HfO <sub>2</sub>	42	19	1.6	$10^3$	[109]
4	Y:HfO <sub>2</sub>	40	17	1.5	-	[115]
5	Mg:HfO <sub>2</sub>	26	16.4	3.2	$10^3$	[197]
6	Y:HfO <sub>2</sub>	55	15	5.5	wake-up free	[110]
7	Y:HfO <sub>2</sub>	35	13	2.1	$10^3$	[37]
8	La, Nd, Sm,	35	12.5	1.6	$10^3$	[109]
9	La:HfO <sub>2</sub> (Conv.)	45	8	1.5	$10^4$	This work
10	La:HfO <sub>2</sub> (Conv.)	90	12	2	$10^4$	This work
11	La:HfO <sub>2</sub> (Conv.)	200	15	1.5	$10^4$	This work
12	La:HfO <sub>2</sub> (L/L)	45	15	1.5	$10^4$	This work
13	HZO (Conv.)	50	9	1.2	$10^3$	This work
14	HZO (Conv.)	90	13	2	$10^4$	This work
15	HZO	100	8	1	$10^4$	[43]
16	La:HfO <sub>2</sub>	1000	7.7	1	460	[85]
17	La:HfO <sub>2</sub>	45	15	$\sim 1.5$	-	[108]
18	HZO	40	7.5	1	$10^4$	[121]
19	Ca:HfO <sub>2</sub>	90	11.1	1.1	$10^3$ - $10^4$	[112]
20	Sr:HfO <sub>2</sub>	40	17	1.85	$10^3$ - $10^4$	[198]

**Table 8.1** Ferroelectric properties of HfO<sub>2</sub> fabricated via CSD, reported in the literature and demonstrated in this work. Two growth routes were used for the solution-processed films: the conventional (conv.) method and the layer-by-layer (L/L) approach.

This work establishes a systematic framework that not only resolves reproducibility

challenges in solution-processed hafnia but also provides transferable principles for tuning the annealing atmosphere in other solution-derived ferroelectric oxides. The mechanistic understanding developed here highlights the central role of annealing atmosphere in balancing precursor decomposition, oxygen vacancy formation, and defect passivation—factors critical for reliable ferroelectric behavior. Beyond atmosphere optimization, precise microstructural engineering through layer-by-layer processing enables enhanced density, crystallographic alignment, and strong ferroelectric response. Building on this foundation, future work should exploit the capability for controlled atmosphere and microstructure to mitigate defect redistribution, particularly oxygen vacancies that drive wake-up and imprint phenomena, with in situ STEM/TEM studies offering direct insights into defect dynamics during cycling. To overcome the persistently high coercive fields ( $\sim 1.3$  MV/cm) that hinder low-power operation, the flexibility of CSD should be harnessed to manipulate deposition kinetics and stabilize microstructures that promote lower switching fields and enhanced breakdown strength. Extending these approaches to epitaxial growth on single-crystal substrates could further reduce grain boundary effects, enable thick, fully oriented hafnia films for resonator applications, and ultimately support the integration of ferroelectric  $\text{HfO}_2$  into neuromorphic computing architectures, where enhanced reliability and finely tunable polarization responses are essential for efficient artificial intelligence hardware.

2. Can interface engineering enhance the ferroelectric response and electrical performance of  $\text{HfO}_2$  thin films?

Addressing research question 2, the multilayer studies in Chapter 6 demonstrate that interface engineering can significantly enhance the ferroelectric response and electrical performance of  $\text{HfO}_2$  thin films. Thin  $\text{HfO}_2$ - $\text{ZrO}_2$  multilayers ( $\text{HZO}_{C50}$ , 5 nm individual layers, 50 nm total thickness) achieved  $P_r$  of  $9 \mu\text{C}/\text{cm}^2$ , reduced  $E_c$  of 1.2 MV/cm, and breakdown strength up to 4.0 MV/cm—double that of conventional single-layer films (2.0 MV/cm). These films also showed accelerated wake-up dynamics, reaching maximum polarization within  $10^3$  cycles compared to  $7 \times 10^3$  cycles for solid-solution counterparts. In contrast, thick multilayers ( $\text{HZO}_{C90}$ , 15 nm layers) exhibited

higher  $P_r$  of  $13 \mu\text{C}/\text{cm}^2$  but at the cost of increased  $E_c$  (2 MV/cm), highlighting the grain size–interface spacing relationship as a governing factor. The  $\text{HfO}_2$ – $\text{CeO}_2$  bilayer system displayed only modest ferroelectricity ( $P_r = 3 \mu\text{C}/\text{cm}^2$ ,  $E_c = 800 \text{ kV}/\text{cm}$ ). Importantly,  $\text{HfO}_2$ -initiated stacks outperformed  $\text{ZrO}_2$ -initiated ones, demonstrating that the bottom interface critically influences phase stabilization. Collectively, these results establish interface engineering as an effective pathway for tailoring wake-up behavior, breakdown resistance, and ferroelectric performance in hafnia-based systems.

Future research should also build on the multilayer interface engineering strategies established here. Exploring interlayers beyond  $\text{ZrO}_2$  and  $\text{CeO}_2$ , such as  $\text{TiO}_2$  or  $\text{Al}_2\text{O}_3$ , offers the potential to exploit interfacial strain to further enhance ferroelectric, piezoelectric, and electromechanical performance. In parallel, real-time monitoring of carbon removal kinetics and interfacial composition during annealing will be essential to deepen mechanistic understanding and guide predictive process control. Together, these directions chart a pathway from fundamental processing insights toward reliable, scalable, and multifunctional ferroelectric hafnia devices.

3. Can solution-processed ferroelectric  $\text{HfO}_2$  films achieve the electromechanical properties and integration prospects required for piezoelectric resonator applications?

In Chapter 7, we tried tackling research question 4 by assessing the feasibility of  $\text{La}:\text{HfO}_2$  films for high-overtone bulk acoustic resonators (HBARs). Despite optimized device geometries and poling protocols, the fabricated resonators exhibited predominantly capacitive impedance responses with no distinct acoustic resonances, consistent with the exceptionally low piezoelectric coefficient ( $d_{33} < 1 \text{ pm}/\text{V}$ ) measured in the films. These results confirm that the intrinsically weak electromechanical coupling of our solution-processed hafnia, limits efficient acoustic wave generation, even after electrical poling.

While the current results preclude immediate HBAR operation, they highlight critical pathways for future development. Enhancing the electromechanical response could involve dopant engineering, crystallographic orientation control, or hybrid device architectures that combine hafnia's CMOS compatibility with substrates offering su-

perior piezoelectric coupling. The layer-by-layer approach, although time-consuming for thick films, remains a promising route to achieve improved microstructural control and alignment. First-principles calculations predict that the piezoelectric coefficient ( $d_{33}$ ) of  $\text{HfO}_2$  can be dramatically enhanced through structural softening mechanisms, with theoretical values reaching  $-45$  pm/V under epitaxial strain, while more practical enhancements may be realized through  $\text{HfO}_2$ -based superlattices incorporating  $\text{SnO}_2$  or  $\text{PbO}_2$ .<sup>[199]</sup> A particularly promising direction involves growing thick  $\text{HfO}_2$  films on substrates with low acoustic losses and high electromechanical coupling, such as sapphire ( $\text{Al}_2\text{O}_3$ ), lithium niobate ( $\text{LiNbO}_3$ ), quartz ( $\text{SiO}_2$ ), silicon carbide ( $\text{SiC}$ ), or nanocrystalline diamond (NCD). Moreover, collecting samples produced using different techniques and sourced from multiple laboratories could complement these efforts, enabling systematic optimization of HBAR performance. The combination of optimized substrate selection, strategic superlattice design, and the multilayer processing methodologies established in this work could potentially overcome current limitations in electromechanical coupling and enable successful implementation of CMOS-compatible  $\text{HfO}_2$ -based acoustic devices for next-generation applications.



# Publications, Conferences and Activities

## Articles in Peer-Reviewed Journals

### As First Author

1. **B. Mandal**, N. Valle, B. E. Adib, S. Girod, K. Mengueli, Y. Fleming, P. Grysan, E. Defay, S. Glinsek, 'Control of Ferroelectricity in Solution-Processed Hafnia Films Through Annealing Atmosphere'. *Advanced Electronic Materials*, **2024**, 10, 2300893.
2. **B. Mandal**, A. M. Philippe, N. Valle, E. Defay, T. Granzow, and S. Glinsek, 'Ferroelectric HfO<sub>2</sub>-ZrO<sub>2</sub> Multilayers with Reduced Wake-Up'. *ACS Omega*, **2025**, 10 (13), 13141-13147.

### As Co-Author

1. S. Glinsek, L. Song, M. Gerard, O. Bouton, S. Girod, M. El Hachemi, **B. Mandal**, E. Defay, T. Granzow, and J. Polesel-Maris, "Autonomous low-energy communication module based on inkjet-printed transparent antenna," *Cell Reports Physical Science*, **2023**, 4 (12), 101685.
2. S. W. Konsago, K. Žiberna, A. Matavž, **B. Mandal**, S. Glinšek, Y. Fleming, A. Benčan, G. L. Brennecka, H. Uršič, and B. Malič, "Engineering the Microstructure and Functional Properties of 0.5Ba(Zr<sub>0.2</sub>Ti<sub>0.8</sub>)O<sub>3</sub>-0.5(Ba<sub>0.7</sub>Ca<sub>0.3</sub>)TiO<sub>3</sub> Thin Films," *ACS Applied Electronic Materials*, **2024**, 6 (6), 4467-4477.
3. S. W. Konsago, K. Žiberna, A. Matavž, **B. Mandal**, S. Glinšek, G. L. Brennecka, H. Uršič, and B. Malič, "High energy storage density and efficiency of 0.5Ba(Zr<sub>0.2</sub>Ti<sub>0.8</sub>)O<sub>3</sub> -

- 0.5(Ba<sub>0.7</sub>Ca<sub>0.3</sub>)TiO<sub>3</sub> thin films on platinized sapphire substrates,” *Journal of Materials Chemistry A*, **2025**, 13 (4), 2911–2919.
4. A. Blázquez Martínez, **B. Mandal**, S. Glinšek, and T. Granzow, “Defect engineering of charge transport and photovoltaic effect in BiFeO<sub>3</sub> films,” *Acta Materialia*, **2025**, 283, 120481.
  5. N. R. Alluri, L. Song, S. Girod, **B. Mandal**, J. Cardoletti, V. Bobnar, T. Granzow, V. Kovacova, A.-M. Philippe, E. Defay, and S. Glinšek, “Solution-Based Fabrication of High-Performance K<sub>0.5</sub>Na<sub>0.5</sub>NbO<sub>3</sub> Thin Films for Surface Haptics,” *arXiv*, **2025**, arXiv:2502.21066.
  6. L. Song, S. Glinšek, N. R. Alluri, V. Kovacova, M. Melchiorr, A. Blázquez Martínez, **B. Mandal**, J. Cardoletti, and E. Defay, “Highly transparent lead-free piezoelectric haptic device,” *Communications Materials*, **2025**, 6 (1), 81.
  7. S. W. Konsago, M. Koblar, K. Žiberna, A. Matavž, **B. Mandal**, S. Glinšek, V. Bobnar, A. Benčan, and B. Malič, “Microstructure, crystalline orientation evolution and electromechanical properties of 0.5Ba(Zr<sub>0.2</sub>Ti<sub>0.8</sub>)O<sub>3</sub> – 0.5(Ba<sub>0.7</sub>Ca<sub>0.3</sub>)TiO<sub>3</sub> thin films on platinized sapphire substrate,” *Journal of Alloys and Compounds*, **2025**, 1047, 185124.

## Conferences

### Oral Presentations

1. **B. Mandal**, J. Íñiguez, and S. Glinšek, “Effect of annealing atmosphere on ferroelectricity of solution-processed La:HfO<sub>2</sub> thin films,” *Photovoltaics: Advanced Concepts for high Efficiency (PACE) Young Scientists Conference*, University of Luxembourg, Luxembourg, October 10–12, 2022.
2. **B. Mandal**, N. Valle, A.-M. Philippe, B. El Adib, E. Defay, and S. Glinšek, “Ferroelectricity in solution-processed La:HfO<sub>2</sub>/ZrO<sub>2</sub> multilayers,” *European Materials Research Society (E-MRS) Fall Meeting*, Warsaw, Poland, September 18, 2023.
3. **B. Mandal**, A.-M. Philippe, N. Valle, E. Defay, T. Granzow, and S. Glinšek, “Ferroelectric La:HfO<sub>2</sub>–ZrO<sub>2</sub> multilayers with reduced wake-up,” *IEEE International Symposium on*

*Applications of Ferroelectrics (ISAF) Conference, Graz, Austria, July 17, 2025.*

### Poster Presentations

1. **B. Mandal**, J. Íñiguez, and S. Glinšek, “Study of HfO<sub>2</sub> thin-film-based heterostructures with optimal functional properties,” *PhD Day*, University of Luxembourg, 2022.
2. **B. Mandal**, J. Íñiguez, E. Defay, and S. Glinšek, “Effect of annealing atmosphere on ferroelectricity of solution-processed La:HfO<sub>2</sub> thin films,” *High-K Workshop*, NaMLab, Dresden, Germany, 2023.
3. **B. Mandal**, N. Valle, A.-M. Philippe, B. El Adib, E. Defay, and S. Glinšek, “Ferroelectricity in solution-processed La:HfO<sub>2</sub>/ZrO<sub>2</sub> multilayers,” *International School of Oxide Electronics (ISOE) Conference*, Cargèse, Corsica, 2023.

### Awards

- **Best Poster Award**, PhD Day, University of Luxembourg, Luxembourg, 2022. Awarded for the poster titled “Study of HfO<sub>2</sub> thin-film-based heterostructures with optimal functional properties.”

### Summer schools

- **6<sup>th</sup> International School of Oxide Electronics (ISOE)**, Cargèse, France, August 29–September 8, 2023.

### Science outreach activities

- **LIST Open Day 2022**, Luxembourg Institute of Science and Technology (LIST), Belvaux, Luxembourg, June 18, 2022. Participated in the institute’s public outreach event showcasing ongoing research in materials science and nanotechnology. Event link]
- **Luxembourg Researchers’ Days 2022**, Rockhal, Esch-sur-Alzette/Belval, November 25–26, 2022. Contributed to the national science communication event organized by the Luxembourg National Research Fund (FNR).

- **Luxembourg Researchers' Days 2024**, Rockhal, Esch-sur-Alzette/Belval, November 28–30, 2024.

## **Entrepreneurial Activities**

- **Founder Academy, LIST Ventures**. Selected as one of the candidates in the first cohort of the Founder Academy organized by LIST Ventures.
- **FNR JUMP Proposal (in preparation)**. Developing a proposal for the Luxembourg National Research Fund (FNR) JUMP program, based on a data analytics tool for R&D conceived during the PhD. The tool addresses key challenges in managing and interpreting experimental data workflows.
- **Nexus 2025**, Luxembourg, June 17–18, 2025. [Event link]
- **Luxembourg Venture Days 2025**, Luxembourg, October 22–23, 2025. [Event link]

# Contributions to this thesis

The work presented in this thesis is the result of scientific collaborations. The contributions of the collaborators are outlined below:

- **Chapter 3:** The electrode patterning for Raman spectroscopy, including the development of the lithography process, was carried out by S. Girod from the Luxembourg Institute of Science and Technology.
- **Chapter 4:** SIMS profiles were conducted by N. Valle and B. El-Adib from the Luxembourg Institute of Science and Technology.
- **Chapter 5:** SIMS profiles were conducted by N. Valle and B. El-Adib from the Luxembourg Institute of Science and Technology. AFM images were obtained in collaboration with P. Grysan from the Luxembourg Institute of Science and Technology.
- **Chapter 6:** TEM measurements were performed by A. M. Philippe from the Luxembourg Institute of Science and Technology.
- **Chapter 7:** HBAR design and resonance measurements were carried out in collaboration with T. Granzow from the Luxembourg Institute of Science and Technology.  $d_{33}$  measurements were performed by V. Bobnar from the Jozef Stefan Institute.

The work was supervised by S. Glinsek. All work not mentioned above was performed solely by the author of this thesis.



# Appendix A

## Characterization techniques

### A.1 Physical and Structural Characterization

#### A.1.1 X-ray diffraction

X-ray diffraction (XRD) is a technique used to analyze crystalline materials. The electron densities of atoms within a crystal lattice can diffract an incident X-ray beam in specific directions, following the conditions for constructive interference. These conditions are described by Bragg's law:

$$2d \sin \theta = n\lambda \quad (\text{A.1})$$

Where:

- $d$  is the interplanar spacing,
- $\theta$  is the incident angle,
- $n$  is an integer (order of diffraction), and
- $\lambda$  is the wavelength of the incident X-ray radiation.

Modern diffractometers commonly use copper  $K\alpha$  radiation with a wavelength of 0.15406 nm. When the conditions for constructive interference are met, peaks appear in a plot of X-ray intensity as a function of the deviation angle  $2\theta$ . The intensity of these peaks depends on the chemical composition of the crystal planes.

Two standard configurations for XRD measurements are:

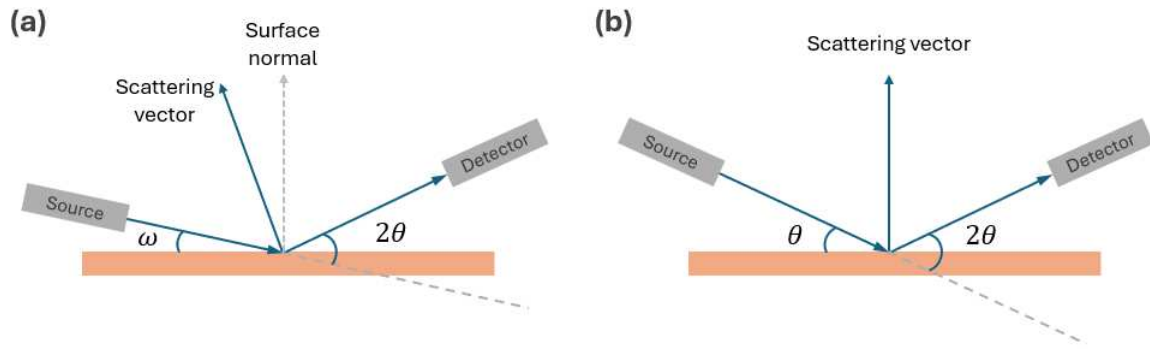


**Figure A.1** Setup configurations for X-ray diffraction: (a) grazing incidence configuration, (b)  $\theta$ - $2\theta$  configuration.

1. Grazing incidence setup (Figure A.1a)– The X-ray source remains fixed at a small angle ( $\sim 1^\circ$ ), while the detector moves. This setup is particularly sensitive to surface of the sample due to its unique geometry.

2.  $\theta$ - $2\theta$  configuration (Figure A.1b) – The X-ray tube and detector move synchronously, probing only crystal planes parallel to the sample surface.

To analyze the crystal structure of the films shown in this thesis, diffraction measurements were performed on a Bruker D8 diffractometer (Bruker, USA) using Cu  $K\alpha$  radiation ( $\lambda=0.15406$  nm).

### A.1.2 X-ray reflectivity

X-ray reflectivity (XRR) is a technique used to characterize the density, thickness, and roughness of thin films by analyzing the reflection of X-rays from the surface as a function of the incidence angle. XRR operates at low angles, near the critical angle of total reflection ( $\theta_c$ ). The position of  $\theta_c$  corresponds to a sharp intensity drop in a plot of  $\log(\text{intensity})$  vs.  $2\theta$  and can be used to determine the material's density ( $\rho$ ) using the following equation:

$$\rho = \frac{\theta_c^2 \pi}{r_e \lambda^2 N_A} \sum_i x_i \frac{f_i}{M_i} \quad (\text{A.2})$$

Where:

- $r_e$  is the **classical electron radius** ( $2.818 \times 10^{-5}$  Å),
- $\lambda$  is the **X-ray wavelength**,

- $N_A$  is **Avogadro's constant** ( $6.626 \times 10^{23} \text{ mol}^{-1}$ ),
- $x_i$  are the **stoichiometric coefficients**,
- $M_i$  are the **molar masses of the elements**, and
- $f_i$  represents the **real part of the atomic scattering factors**.

The X-ray reflectivity (XRR) measurements presented in this thesis were conducted using a PANalytical X'Pert Pro instrument equipped with Cu  $K\alpha$  radiation ( $\lambda=0.15406 \text{ nm}$ ), and the XRR data were fitted using the GenX software.[200]

### A.1.3 RAMAN spectroscopy

Raman spectroscopy is a non-destructive optical technique used to probe the vibrational modes of materials. It is based on the inelastic scattering of monochromatic light, known as the Raman effect, where incident photons interact with molecular or lattice vibrations and are scattered with an energy shift corresponding to the vibrational energy levels of the material. The resulting Raman spectrum provides a characteristic fingerprint of the material's structural and chemical composition. In crystalline solids, Raman scattering is sensitive to crystal symmetry, phase, strain, and defects, making it particularly suitable for identifying different polymorphs and probing local structural changes in ferroelectric thin films.

Raman measurements were carried out using a confocal *inVia* Renishaw Raman microspectrometer operating in backscattering configuration. A continuous-wave He–Cd laser with an excitation wavelength of 442 nm was employed at full output power. The scattered light was dispersed using a diffraction grating with 2400 lines/mm and subsequently imaged onto a CCD detector. The system was operated in micro-Raman mode, providing high spatial resolution for localized analysis of the thin-film regions. The confocal configuration enhanced depth selectivity and reduced background contributions from underlying layers. All measurements were performed at room temperature under ambient conditions.

### A.1.4 Atomic force microscopy

Atomic Force Microscopy (AFM) is a high-resolution imaging technique that utilizes a sharp tip, typically with a radius below 10 nm, to scan the surface of a sample at the nanoscale.

By interacting with the sample's surface, the probe generates a detailed topographical map, providing insights into surface morphology and roughness. All AFM images presented here were recorded using an Bruker Innova AFM in tapping mode.

### A.1.5 Scanning electron microscopy

Electron microscopy enables the visualization of features that optical microscopy cannot resolve due to the limitations of visible light. Owing to the wave-particle duality, electrons exhibit wave-like behavior, with wavelengths shorter than those of visible light, allowing for significantly higher resolution. In a scanning electron microscope, electrons are accelerated through a column and directed onto the sample. Various interactions can occur between the incident electrons and the sample, leading to the emission of secondary electrons, back-scattered electrons, Auger electrons, and X-rays, all of which can be detected. Secondary electron detection is specifically used to generate a magnified topographical image of the sample. All SEM images presented here were extracted using an FEI Helios NanoLab 650.

### A.1.6 Transmission Electron Microscopy

Transmission Electron Microscopy (TEM) is a high-resolution characterization technique that enables the investigation of material structure, morphology, and composition at the nanometer to atomic scale. In TEM, a high-energy electron beam is transmitted through an electron-transparent specimen, and the interaction between the electrons and the atoms within the sample generates various contrast mechanisms. The resulting image carries information about the internal structure, crystal orientation, and defects.

Different imaging modes in TEM and Scanning Transmission Electron Microscopy (STEM) allow complementary insights into the sample:

- **Bright-Field STEM (BF-STEM):** In BF-STEM, the image is formed using electrons that are transmitted through the sample without significant deviation from the incident beam direction. These low-angle transmitted electrons are collected by a small on-axis detector. Contrast in BF-STEM mainly arises from differences in sample thickness and diffraction conditions, allowing visualization of general morphology, interfaces, and defects such as dislocations or grain boundaries.

- **Dark-Field STEM (DF-STEM):** In DF-STEM, only the high-angle scattered electrons are collected using an annular detector placed off-axis. The resulting image highlights regions of the sample with strong scattering—typically areas of higher atomic number (Z-contrast) or crystallographic variations. This imaging mode provides enhanced compositional and structural contrast, making it particularly useful for mapping interfaces and identifying local variations in atomic structure.
- **High-Resolution TEM (HRTEM):** HRTEM utilizes phase contrast generated by the interference of the directly transmitted and diffracted electron waves to produce images at atomic resolution. Lattice fringes corresponding to specific crystallographic planes become visible, allowing direct observation of atomic arrangements, interplanar spacings, and structural defects such as dislocations or stacking faults. HRTEM is therefore invaluable for studying crystallinity, interface coherence, and local strain fields in thin films.

Samples for TEM analysis were prepared using a focused ion beam (FIB) lamella preparation technique with an FEI Nanolab Helios 650 system. Conventional TEM investigations were carried out using a JEOL JEM-2100 microscope operated at 200 kV and equipped with a JED-2300 energy-dispersive X-ray spectroscopy (EDXS) detector. Additional high-resolution and analytical studies were performed using a probe Cs-corrected JEOL ARM 200CF microscope fitted with a Centurio EDX system. Both bright-field (BF) and dark-field (DF) STEM imaging modes were employed to enhance contrast and visualize nanoscale structural features. High-resolution TEM (HRTEM) imaging was conducted to examine atomic-scale structure, lattice ordering, and crystallinity in selected regions of the samples.

### A.1.7 Dynamic Secondary Ion Mass Spectrometry

Secondary Ion Mass Spectrometry (SIMS) is a powerful surface analysis technique used to determine the elemental and isotopic composition of materials with high sensitivity. In SIMS, the surface of a sample is bombarded by a focused primary ion beam, causing the ejection (sputtering) of secondary ions from the near-surface region. These secondary ions are then analyzed by a mass spectrometer to obtain information about the sample's composition as a function of depth. Dynamic SIMS (D-SIMS) extends this principle by continuously

sputtering the sample surface during analysis, allowing the construction of depth profiles that reveal elemental distributions throughout the film thickness.

Depth profiling presented was performed using a CAMECA SC-Ultra D-SIMS instrument. Measurements were carried out with a low-impact energy caesium ( $\text{Cs}^+$ ) primary ion beam operating at 1 keV. The analytical conditions were optimized to enable quantitative comparison of elements between samples. The intensities, detected as Cs-based molecular clusters, was collected from a circular analysis area with a diameter of approximately  $60 \mu\text{m}$ . This configuration ensured uniform sputtering across the analysis region and reliable quantification of elemental distribution through the entire film thickness.

## A.2 Electrical characterization

Electrical characterization of a ferroelectric thin film capacitor involves measuring its ferroelectric properties, primarily focusing on polarization through switching current. Additionally, reliability studies are conducted to assess the polarization degradation during fatigue cycling and the dielectric breakdown of the material. All these measurements were performed using the Ferroelectric Thin Film Analyzer aixACCT TFA 2000. Probe tips were employed to make contact with both the top and bottom electrodes. For metal-insulator-metal (MIM) samples, contact with the bottom electrode was established by applying silver paint along the edges of the substrate, ensuring reliable electrical connections. These tests provide critical information on the material's performance and durability under varying conditions.

### A.2.1 Polarization measurement

Polarization hysteresis measurements are performed by applying a triangular voltage signal (shown in Figure A.2a) at a specific frequency while continuously recording the polarization current response. For an ideal, non-leaky ferroelectric capacitor, the polarization can be expressed as:

$$\frac{1}{A} \int_0^{\Delta t} i(t) dt = P(\Delta t) - P(0) = \Delta P \quad (\text{A.3})$$

where  $\Delta P$  represents the change in polarization over time  $\Delta t$ . The polarization hysteresis loop, as shown in Figure A.2b, is obtained by plotting polarization  $P$  as a function of the electric field  $E$ . The shape of the hysteresis loop is influenced by the frequency of the measurement and can be altered by factors such as defect chemistry, dopants, mechanical stresses, and poling history [201, 202].

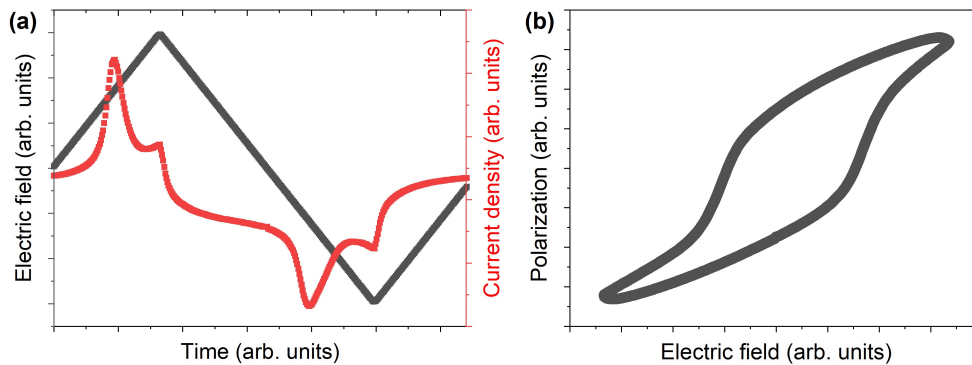


**Figure A.2** (a) Example of the applied electric field waveform and corresponding current density response used for polarization hysteresis loop measurements. (b) Typical resulting polarization–electric field (P–E) hysteresis loop.

## A.2.2 Fatigue measurement

'Fatigue' refers to the degradation of material properties due to repetitive cycling. In the case of ferroelectric materials, it typically involves the deterioration of piezoelectric coefficients, remanent polarization, or electrical permittivity when subjected to cyclic electric fields. The fatigue cycling is carried out by applying a bipolar or unipolar excitation signal at a specific frequency, typically for several hundred to millions of cycles. However, the shape and sequence of the excitation signal can be adjusted to meet the specific requirements of the application. Polarization and permittivity hysteresis are measured in situ at regular intervals during the fatigue cycling to monitor the evolution of material properties. When selecting the cycling signal's amplitude, frequency, waveform, and the number of switching cycles, it's important to ensure that complete switching occurs at higher frequencies, while also considering the limitations of the measurement device to provide sufficient driving power. The schematic of the fatigue measurement sequence and an example of remanent polarization degradation of a thin film are shown in Figure A.3. The cycling parameters are

chosen to simulate the intended operating conditions. The results from the fatigue cycling provide insight into the lifetime of the material or device under test. Typically, higher frequencies and cycling amplitudes are selected to demonstrate material degradation within a reasonable time frame, and the results are then extrapolated to the operating conditions.

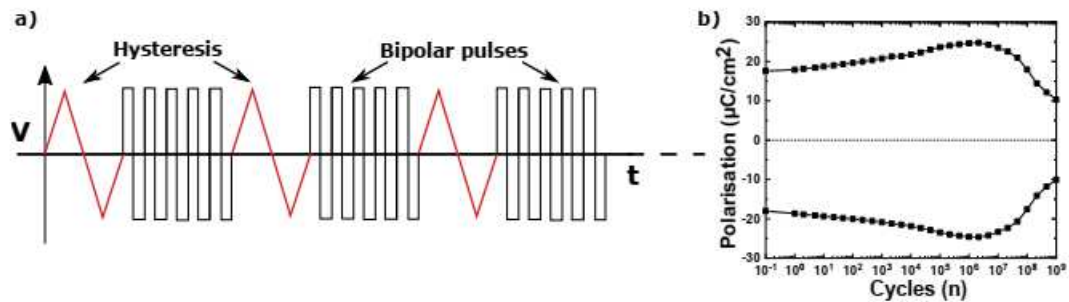


**Figure A.3** Excitation signal for (a) fatigue measurement with bipolar pulses with hysteresis measurement at regular intervals, adapted from [5] (b) Typical result of a fatigue measurement depicted as the remanent polarization versus log cycles of the excitation signal.

### A.2.3 Breakdown and leakage measurement

In the context of ferroelectric materials, breakdown refers to the dielectric breakdown that occurs when an electrical field of sufficient magnitude is applied. The dielectric breakdown strength is determined by the material's intrinsic properties or the presence of defects and free charge carriers. Breakdown tests are specifically designed and adapted to study the mechanisms and effects that lead to dielectric breakdown in a given material. There are two primary methods for measuring a material's breakdown characteristics: applying a linearly varying voltage (staircase mode) until the material breaks down (see Figure A.4a) or applying a constant voltage over time and monitoring the evolution of current (see Figure A.4b).

In this thesis, linear ramp voltage stress (LRVS) tests were used to assess breakdown behavior. It is essential to accurately define the operational parameters, including the ramp rate (step size and duration), as well as the sample's initial poling state or electrical history. The electrode geometry and material selection can also have a significant influence on the measured breakdown characteristics. In LRVS tests, the breakdown voltage ( $V_{bd}$ ) is determined by monitoring the current response at each voltage step, where a sudden increase in current by several orders of magnitude indicates the breakdown event. Careful control

and definition of the measurement parameters are therefore critical to ensure reliable and reproducible results.

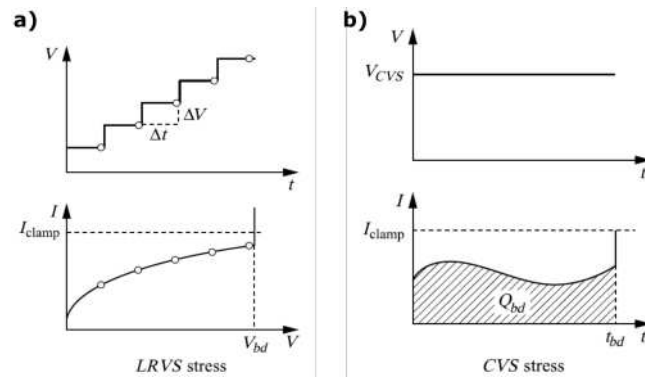


**Figure A.4** Illustration of the electrical breakdown test configurations employed in this work: (a) Linear Ramp Voltage Stress (LRVS) and (b) Constant Voltage Stress (CVS). Adapted from Ref. [203].

## A.2.4 Double beam laser interferometry

Double-beam laser interferometry (DBLI) is a technique commonly used to measure the out-of-plane piezoelectric coefficient ( $d_{33,f}$ ) of thin piezoelectric films in a metal–insulator–metal (MIM) capacitor configuration. However, accurate measurement poses significant challenges due to wafer bending, which can introduce substantial errors in the detected displacement. Wafer bending effects can be mitigated either by attaching the wafer to a rigid substrate or by employing a dual-interferometer configuration that performs differential displacement measurements, achieving sub-picometer resolution [204]. Nevertheless, expansion or compression of the substrate itself may still influence the measured response, leading to variations in the extracted  $d_{33,f}$  values with electrode size. Sivaramakrishnan *et al.* demonstrated that reliable  $d_{33,f}$  determination requires the ratio between electrode diameter and substrate thickness to be approximately unity [205].

## A.2.5 Resonance measurement using Vector Network Analyzer (VNA)

A vector network analyzer (VNA) is an instrument used to characterize the electrical response of a device by measuring the relationship between an applied stimulus signal and the

resulting reflected and/or transmitted signals. The VNA contains both a signal source and a set of receivers that compare the transmitted or reflected signals to the known input. In a one-port configuration, the device under test (DUT) is connected to a single port of the VNA, and only the reflected signal is measured, yielding the reflection coefficient ( $S_{11}$ ). Resonance behavior in the DUT is typically identified from frequency-dependent variations in  $|S_{11}|$  magnitude or phase, where a resonance condition corresponds to a local minimum in the reflection response.

Resonance measurements were carried out using an Anritsu VectorStar broadband vector network analyzer operating from 70 kHz to 145 GHz within a single coaxial connection. The setup was configured for one-port DUT measurements. Electrical probing was performed on an MPI probe station equipped with ground–signal–ground (GSG) RF probe tips (MPI RF T110A-GSG100 and MPI RF T26A-GSG100), enabling precise and repeatable high-frequency contact with the sample electrodes. The VNA generated the stimulus signal through its internal source and measured the reflected signal using integrated receivers. This configuration provides broadband capability and high sensitivity for investigating the electromechanical resonance characteristics of the thin-film capacitors.

# Appendix B

## Reproducibility data for La:HfO<sub>2</sub> films

Table B.1 summarizes the ferroelectric properties of La:HfO<sub>2</sub> samples reproduced under the optimized N<sub>2</sub>:O<sub>2</sub> 1:1 annealing conditions discussed in Chapter 4.

#	Sample type	# of measured cells	Average $E_c$ (MV/cm)	Average $P_r$ ( $\mu\text{C}/\text{cm}^2$ )
1	HO <sub>C45</sub>	11	1.5	8
2	HO <sub>C45</sub>	2	1.5	8
3	HO <sub>C45</sub>	8	1.3	8
4	HO <sub>C45</sub>	5	1.6	7.5
5	HO <sub>C90</sub>	5	2	12
6	HO <sub>C90</sub>	8	2	12
7	HO <sub>C200</sub>	6	1.5	15

**Table B.1** Reproducibility of ferroelectric properties for La:HfO<sub>2</sub> thin films grown under N<sub>2</sub>:O<sub>2</sub> 1:1 annealing atmosphere. The table summarizes the number of measured capacitors and the corresponding average coercive field ( $E_c$ ) and remanent polarization ( $P_r$ ) values for each sample type.



# References

- [1] Lines, M. E. and Glass, A. M. *Principles and Applications of Ferroelectrics and Related Materials*. Oxford University Press, 2001.
- [2] Böske, T. S., Müller, J., Bräuhaus, D., Schröder, U., and Böttger, U. “Ferroelectricity in hafnium oxide thin films”. In: *Applied Physics Letters* 99.10 (Sept. 2011), p. 102903. ISSN: 0003-6951. DOI: 10.1063/1.3634052.
- [3] Cheema, S. S., Shanker, N., Wang, L.-C., Hsu, C.-H., Hsu, S.-L., Liao, Y.-H., San Jose, M., Gomez, J., Chakraborty, W., Li, W., Bae, J.-H., Volkman, S. K., Kwon, D., Rho, Y., Pinelli, G., Rastogi, R., Pipitone, D., Stull, C., Cook, M., Tyrrell, B., Stoica, V. A., Zhang, Z., Freeland, J. W., Tassone, C. J., Mehta, A., Saheli, G., Thompson, D., Suh, D. I., Koo, W.-T., Nam, K.-J., Jung, D. J., Song, W.-B., Lin, C.-H., Nam, S., Heo, J., Parihar, N., Grigoropoulos, C. P., Shafer, P., Fay, P., Ramesh, R., Mahapatra, S., Ciston, J., Datta, S., Mohamed, M., Hu, C., and Salahuddin, S. “Ultrathin ferroic HfO<sub>2</sub>-ZrO<sub>2</sub> superlattice gate stack for advanced transistors”. In: *Nature* 604.7904 (Apr. 2022), pp. 65–71. ISSN: 1476-4687. DOI: 10.1038/s41586-022-04425-6.
- [4] Fraser, B. C., Danner, H., and Papinsky, R. “Untitled”. In: *Physical Review* 100 (1955), p. 745.
- [5] Waser, R., Böttger, U., and Tiedke, S., eds. *Polar Oxides: Properties, Characterization, and Imaging*. Weinheim: Wiley-VCH, 2005, p. 391. ISBN: 978-3-527-40532-9.
- [6] Damjanovic, D. “Ferroelectric, dielectric and piezoelectric properties of ferroelectric thin films and ceramics”. In: *Reports on Progress in Physics* 61.9 (1998), pp. 1267–1324. DOI: 10.1088/0034-4885/61/9/002.
- [7] Valasek, J. “Piezo-Electric and Allied Phenomena in Rochelle Salt”. In: *Physical Review* 17.4 (1921), pp. 475–481. DOI: 10.1103/PhysRev.17.475.

- 
- [8] Strukov, B. A. and Levanyuk, A. P. *Ferroelectric Phenomena in Crystals: Physical Foundations*. Berlin, Heidelberg: Springer, 1998, p. 308. ISBN: 978-3-540-63132-1. DOI: 10.1007/978-3-642-60293-1.
- [9] Mehta, R. R., Silverman, B. D., and Jacobs, J. T. “Depolarization Fields in Thin Ferroelectric Films”. In: *Journal of Applied Physics* 44.8 (Aug. 1973), pp. 3379–3385. DOI: 10.1063/1.1662770.
- [10] Wurfel, P., Batra, I. P., and Jacobs, J. T. “Polarization Instability in Thin Ferroelectric Films”. In: *Physical Review Letters* 30.24 (June 1973), pp. 1218–1221. DOI: 10.1103/PhysRevLett.30.1218.
- [11] Tagantsev, A. K., Stolichnov, I., Colla, E. L., and Setter, N. “Polarization fatigue in ferroelectric films: Basic experimental findings, phenomenological scenarios, and microscopic features”. In: *Journal of Applied Physics* 90.3 (Aug. 2001), pp. 1387–1402. DOI: 10.1063/1.1386407.
- [12] Meier, D., Seidel, J., Gregg, M., and Ramesh, R. *Domain Walls: From Fundamental Properties to Nanotechnology Concepts*. Vol. 24. Series on Semiconductor Science and Technology. Oxford: Oxford University Press, 2020, p. 368. ISBN: 978-0-19-886249-9. DOI: 10.1093/oso/9780198862499.001.0001.
- [13] Wang, L., Wang, X., and Shi, J. “Measurement and estimation of ferroelectric hysteresis loops”. In: *Ferroelectrics* 411.1 (2011), pp. 86–92.
- [14] Materlik, R., Künneth, C., and Kersch, A. “The origin of ferroelectricity in  $\text{Hf}_{1-x}\text{Zr}_x\text{O}_2$ : a computational investigation”. In: *J. Appl. Phys.* 117.13 (2015), p. 134109.
- [15] Mikolajick, T., Slesazeck, S., Mulaosmanovic, H., Park, M. H., Fichtner, S., Lomenzo, P. D., Hoffmann, M., and Schroeder, U. “Next generation ferroelectric materials for semiconductor process integration and their applications”. In: *Journal of Applied Physics* 129.10 (2021), p. 100901. DOI: 10.1063/5.0037617.
- [16] Clima, S., Wouters, D. J., Adelman, C., Schenk, T., Schroeder, U., Jurczak, M., and Pourtois, G. “Identification of the ferroelectric switching process and dopant-dependent switching properties in orthorhombic  $\text{HfO}_2$ : A first principles insight”. In: *Applied Physics Letters* 104.9 (Mar. 2014). ISSN: 1077-3118. DOI: 10.1063/1.4867975.

- [17] Defay, E., ed. *Integration of Ferroelectric and Piezoelectric Thin Films: Concepts and Applications for Microsystems*. London: Wiley-ISTE, 2011. ISBN: 978-1-84821-239-8.
- [18] Ishiwara, H., Okuyama, M., and Arimoto, Y., eds. *Ferroelectric Random Access Memories*. Vol. 93. Topics in Applied Physics. Berlin, Heidelberg: Springer, 2004. ISBN: 978-3-540-21020-4.
- [19] Kaminow, I. P. *An Introduction to Electrooptic Devices*. New York: Academic Press, 1974. ISBN: 978-0-12-394850-2.
- [20] Boyd, R. W. *Nonlinear Optics*. 3rd. Burlington, MA: Academic Press, 2008, p. 640. ISBN: 978-0123694706.
- [21] Wang, J., Li, H. P., and Stevens, R. “Hafnia and hafnia-toughened ceramics”. In: *Journal of Materials Science* 27.20 (1992), pp. 5397–5430. DOI: 10.1007/BF00541770.
- [22] Matsumoto, K., Itoh, Y., and Kameda, T. “EB-PVD process and thermal properties of hafnia-based thermal barrier coating”. In: *Science and Technology of Advanced Materials* 4.2 (2003), pp. 153–158. DOI: 10.1016/S1468-6996(03)00018-8.
- [23] Zhao, J. et al. “Fabrication of high-performance  $Y_2O_3$  stabilized hafnium dioxide refractories”. In: *Ceramics International* 41 (2015), pp. 5232–5238.
- [24] Demkov, A. A. and Navrotsky, A. *Materials Fundamentals of Gate Dielectrics*. Springer Science & Business Media, 2005. ISBN: 9780387233602.
- [25] Navrotsky, A. “Thermochemical insights into refractory ceramic materials based on oxides with large tetravalent cations”. In: *Journal of Materials Chemistry* 15.19 (2005), pp. 1883–1890.
- [26] Carter, C. B. and Norton, M. G. *Ceramic Materials: Science and Engineering*. New York: Springer, 2008. ISBN: 978-0-387-46270-7.
- [27] Jr., W. D. C. and Rethwisch, D. G. *Materials Science and Engineering: An Introduction*. 8th ed. Hoboken, NJ: John Wiley & Sons, 2009. ISBN: 978-0-470-41997-7.
- [28] Schroeder, U., Hwang, C. S., and Funakubo, H., eds. *Ferroelectricity in Doped Hafnium Oxide: Materials, Properties and Devices*. English. 2nd ed. Cambridge, UK: Woodhead Publishing, Aug. 2025, p. 850. ISBN: 9780443291821.

- [29] Shin, D., Arroyave, R., and Liu, Z.-K. "Thermodynamic modeling of the Hf-Si-O system". In: *Calphad* 30.4 (2006), pp. 375–386.
- [30] Huan, T. D., Sharma, V., Rossetti, G. A., and Ramprasad, R. "Pathways towards ferroelectricity in hafnia". In: *Physical Review B* 90.6 (2014), p. 064111.
- [31] Wolten, G. M. "Diffusionless phase transformations in zirconia and hafnia". In: *Journal of the American Ceramic Society* 46.9 (1963), pp. 418–422.
- [32] Bocquillon, G., Susse, C., and Vodar, B. "Allotropie de L'Oxyde d'Hafnium sous Haute Pression". In: *Revue Internationale des Hautes Températures et des Refractaires* 5.4 (1968), pp. 247–251.
- [33] Tang, S. E. J., Kai, M., and Kobayashi, Y. "A high-pressure high-temperature X-ray study of phase relations and polymorphism of HfO<sub>2</sub>". In: *Properties of Earth and Planetary Materials at High Pressure and Temperature*. 1998, pp. 401–407.
- [34] Sang, X., Grimley, E. D., Schenk, T., Schroeder, U., and LeBeau, J. M. "On the structural origins of ferroelectricity in HfO<sub>2</sub> thin films". In: *Applied Physics Letters* 106.16 (2015), p. 162905.
- [35] Park, M. H., Lee, Y. H., Kim, H. J., Kim, Y. J., Moon, T., Kim, K. D., Müller, J., Kersch, A., Schroeder, U., Mikolajick, T., and Hwang, C. S. "Ferroelectricity and Antiferroelectricity of Doped Thin HfO<sub>2</sub>-Based Films". In: *Advanced Materials* 27.11 (Feb. 2015), pp. 1811–1831. ISSN: 1521-4095. DOI: 10.1002/adma.201404531.
- [36] Kashir, A., Oh, S., and Hwang, H. "Defect Engineering to Achieve Wake-up Free HfO<sub>2</sub>-Based Ferroelectrics". In: *Advanced Engineering Materials* 23.1 (Sept. 2020). ISSN: 1527-2648. DOI: 10.1002/adem.202000791.
- [37] Starschich, S., Griesche, D., Schneller, T., Waser, R., and Böttger, U. "Chemical solution deposition of ferroelectric yttrium-doped hafnium oxide films on platinum electrodes". In: *Applied Physics Letters* 104.20 (May 2014). ISSN: 1077-3118. DOI: 10.1063/1.4879283.
- [38] Mueller, S., Mueller, J., Singh, A., Riedel, S., Sundqvist, J., Schroeder, U., and Mikolajick, T. "Incipient Ferroelectricity in Al-Doped HfO<sub>2</sub> Thin Films". In: *Advanced Functional*

- Materials* 22.11 (Mar. 2012), pp. 2412–2417. ISSN: 1616-3028. DOI: 10.1002/adfm.201103119.
- [39] Campanini, M., Erni, R., Yang, C.-H., Ramesh, R., and Rossell, M. D. “Periodic giant polarization gradients in doped BiFeO<sub>3</sub> thin films”. In: *Nano Letters* 18.2 (2018), pp. 717–724. DOI: 10.1021/acs.nanolett.7b03817.
- [40] Campanini, M., Eimre, K., Bon, M., Pignedoli, C. A., Rossell, M. D., and Erni, R. “Atomic-resolution differential phase contrast STEM on ferroelectric materials: A mean-field approach”. In: *Physical Review B* 101 (2020), p. 184116. DOI: 10.1103/PhysRevB.101.184116.
- [41] Schroeder, U., Richter, C., Park, M., et al. “Lanthanum doped hafnium oxide: a robust ferroelectric material”. In: *Inorganic Chemistry* 57.5 (2018), pp. 2752–2765.
- [42] Park, M., Schenk, T., Fancher, C., et al. “A comprehensive study on the structural evolution of HfO<sub>2</sub> thin films doped with various dopants”. In: *J. Mater. Chem. C* 5.18 (2017), pp. 4677–4690.
- [43] Starschich, S., Schenk, T., Schroeder, U., and Boettger, U. “Ferroelectric and piezoelectric properties of Hf<sub>1-x</sub>Zr<sub>x</sub>O<sub>2</sub> and pure ZrO<sub>2</sub> films”. In: *Applied Physics Letters* 110.18 (May 2017). ISSN: 1077-3118. DOI: 10.1063/1.4983031.
- [44] Batra, R., Huan, T., Rossetti Jr, G., and Ramprasad, R. “Factors favoring ferroelectricity in hafnia: a first-principles computational study”. In: *Chemistry of Materials* 121 (2017), pp. 4139–4145.
- [45] Hsain, H. A., Lee, Y., Materano, M., Mittmann, T., Payne, A., Mikolajick, T., Schroeder, U., Parsons, G. N., and Jones, J. L. “Many routes to ferroelectric HfO<sub>2</sub>: A review of current deposition methods”. In: *Journal of Vacuum Science & Technology A* 40.1 (Dec. 2021). ISSN: 1520-8559. DOI: 10.1116/6.0001317.
- [46] Xu, L., Nishimura, T., Shibayama, S., Yajima, T., Migita, S., and Toriumi, A. “Kinetic pathway of the ferroelectric phase formation in doped HfO<sub>2</sub> films”. In: *Journal of Applied Physics* 122.12 (2017), p. 124104. DOI: 10.1063/1.5003918.

- 
- [47] Mart, C., Kühnel, K., Kämpfe, T., Zybell, S., and Weinreich, W. “Ferroelectric and pyroelectric properties of polycrystalline La-doped HfO<sub>2</sub> thin films”. In: *Applied Physics Letters* 114 (2019), p. 102903. DOI: 10.1063/1.5089821.
- [48] Chernikova, A. G., Kuzmichev, D. S., Negrov, D. V., Kozodaev, M. G., Polyakov, S. N., and Markeev, A. M. “Ferroelectric properties of full plasma-enhanced ALD TiN/La:HfO<sub>2</sub>/TiN stacks”. In: *Applied Physics Letters* 108.24 (2016), p. 242905. DOI: 10.1063/1.4953787.
- [49] Olsen, T., Schröder, U., Müller, S., Krause, A., Martin, D., Singh, A., Müller, J., Geidel, M., and Mikolajick, T. “Co-sputtering yttrium into hafnium oxide thin films to produce ferroelectric properties”. In: *Applied Physics Letters* 101.8 (2012), p. 082905. DOI: 10.1063/1.4747209.
- [50] Park, M. H., Chung, C.-C., Schenk, T., Richter, C., Opsomer, K., Detavernier, C., Adelman, C., Jones, J. L., Mikolajick, T., and Schroeder, U. “Effect of Annealing Ferroelectric HfO<sub>2</sub> Thin Films: In Situ, High Temperature X-Ray Diffraction”. In: *Advanced Electronic Materials* 4.7 (2018), p. 1800091. DOI: 10.1002/aelm.201800091.
- [51] Pesic, M., Fengler, F., et al. “Physical mechanisms behind the field-cycling behavior of HfO<sub>2</sub>-based ferroelectric capacitors”. In: *Advanced Functional Materials* 26 (2016), pp. 4601–4612.
- [52] Park, M., Kim, H., et al. “Ferroelectric properties and switching endurance of Hf<sub>0.5</sub>Zr<sub>0.5</sub>O<sub>2</sub> films”. In: *Physica Status Solidi RRL* 8.6 (2014), pp. 532–535.
- [53] Kozodaev, M., Chernikova, A., Korostylev, E., et al. “Ferroelectric properties of lightly doped La: HfO<sub>2</sub> thin films grown by plasma-assisted atomic layer deposition”. In: *Applied Physics Letters* 111.13 (2017), p. 132903.
- [54] Wang, L., Tu, H., et al. “The effect of dopants on the dielectric constant of HfO<sub>2</sub> and ZrO<sub>2</sub> from first principles”. In: *Journal of Applied Physics* 116.12 (2014), p. 123505.
- [55] Hoffmann, M., Schroeder, U., et al. “Ferroelectric phase transitions in nanoscale HfO<sub>2</sub> films enable giant pyroelectric energy conversion”. In: *Nano Energy* 18 (2015), pp. 154–164.

- [56] Chouprik, A., Negrov, D., Tsybal, E. Y., and Zenkevich, A. “Defects in ferroelectric HfO<sub>2</sub>”. In: *Nanoscale* 13.27 (2021), pp. 11635–11678. ISSN: 2040-3372. DOI: 10.1039/d1nr01260f.
- [57] Gusev, E. P., ed. *Defects in High-k Gate Dielectric Stacks: Nano-Electronic Semiconductor Devices*. Springer, 2006. ISBN: 1-4020-4366-X.
- [58] Yan, F., Wu, Y., Liu, Y., Ai, P., Liu, S., Deng, S., Xue, K.-H., Fu, Q., and Dong, W. “Recent progress on defect-engineering in ferroelectric HfO<sub>2</sub>: The next step forward via multiscale structural optimization”. In: *Materials Horizons* 11.3 (2024), pp. 626–645. ISSN: 2051-6355. DOI: 10.1039/d3mh01273e.
- [59] Materlik, R., Künneth, C., Falkowski, M., Mikolajick, T., and Kersch, A. “Al-, Y-, and La-doping effects favoring intrinsic and field induced ferroelectricity in HfO<sub>2</sub>: A first principles study”. In: *Journal of Applied Physics* 123.16 (Apr. 2018). ISSN: 1089-7550. DOI: 10.1063/1.5021746.
- [60] Zhou, Y., Zhang, Y., Yang, Q., Jiang, J., Fan, P., Liao, M., and Zhou, Y. “The effects of oxygen vacancies on ferroelectric phase transition of HfO<sub>2</sub>-based thin film from first-principle”. In: *Computational Materials Science* 167 (Sept. 2019), pp. 143–150. ISSN: 0927-0256. DOI: 10.1016/j.commatsci.2019.05.041.
- [61] Schroeder, U., Park, M. H., Mikolajick, T., and Hwang, C. S. “The fundamentals and applications of ferroelectric HfO<sub>2</sub>”. In: *Nature Reviews Materials* 7.8 (Mar. 2022), pp. 653–669. ISSN: 2058-8437. DOI: 10.1038/s41578-022-00431-2.
- [62] Jiang, P., Luo, Q., Xu, X., Gong, T., Yuan, P., Wang, Y., Wei, W., Tai, L., Lv, H., and Gao, Z. “Wake-Up Effect in HfO<sub>2</sub>-Based Ferroelectric Films”. In: *Advanced Electronic Materials* 7.1 (2021), p. 2000728. DOI: 10.1002/aelm.202000728.
- [63] Schroeder, U., Park, M. H., Mikolajick, T., and Hwang, C. S. “The fundamentals and applications of ferroelectric HfO<sub>2</sub>”. In: *Nature Reviews Materials* 7.8 (Mar. 2022), pp. 653–669. ISSN: 2058-8437. DOI: 10.1038/s41578-022-00431-2.
- [64] Chen, H., Zhou, X., Tang, L., Chen, Y., Luo, H., Yuan, X., Bowen, C. R., and Zhang, D. “HfO<sub>2</sub>-based ferroelectrics: From enhancing performance, material design, to

- applications”. In: *Applied Physics Reviews* 9.1 (Feb. 2022). ISSN: 1931-9401. DOI: 10.1063/5.0066607.
- [65] Clima, S., McMitchell, S., Florent, K., Nyns, L., and Pourtois, G. In: *IEEE International Electron Devices Meeting (IEDM)*. San Francisco, CA, 2018.
- [66] Wei, J., Jiang, L., Huang, M., Wu, Y., and Chen, S. “Intrinsic Defect Limit to the Growth of Orthorhombic HfO<sub>2</sub> and (Hf, Zr)O<sub>2</sub> with Strong Ferroelectricity: First-Principles Insights”. In: *Advanced Functional Materials* 31.42 (July 2021). ISSN: 1616-3028. DOI: 10.1002/adfm.202104913.
- [67] Grimley, E., Schenk, T., et al. “Structural changes underlying field-cycling phenomena in ferroelectric HfO<sub>2</sub> thin films”. In: *Advanced Electronic Materials* 2.11 (2016), p. 1600173.
- [68] Carl, K. and Hardtl, K. H. In: *Ferroelectrics* 17 (1977), p. 473.
- [69] Hamouda, W., Pancotti, A., Lubin, C., Tortech, L., Richter, C., Mikolajick, T., Schroeder, U., and Barrett, N. “Physical chemistry of the TiN/Hf<sub>0.5</sub>Zr<sub>0.5</sub>O<sub>2</sub> interface”. In: *Journal of Applied Physics* 127.6 (Feb. 2020). ISSN: 1089-7550. DOI: 10.1063/1.5128502.
- [70] Kozodaev, M. G., Chernikova, A. G., Korostylev, E. V., Park, M. H., Khakimov, R. R., Hwang, C. S., and Markeev, A. M. “Mitigating wakeup effect and improving endurance of ferroelectric HfO<sub>2</sub>-ZrO<sub>2</sub> thin films by careful La-doping”. In: *Journal of Applied Physics* 125.3 (Jan. 2019). ISSN: 1089-7550. DOI: 10.1063/1.5050700.
- [71] Hoffmann, M., Schroeder, U., Schenk, T., Shimizu, T., Funakubo, H., Sakata, O., Pohl, D., Drescher, M., Adelman, C., Materlik, R., Kersch, A., and Mikolajick, T. “Stabilizing the ferroelectric phase in doped hafnium oxide”. In: *Journal of Applied Physics* 118.7 (Aug. 2015). ISSN: 1089-7550. DOI: 10.1063/1.4927805.
- [72] Warren, W. L., Dimos, D., Tuttle, B. A., Pike, G. E., Schwartz, R. W., Clews, P. J., and McIntyre, D. C. “Polarization suppression in Pb(Zr,Ti)O<sub>3</sub> thin films”. In: *Journal of Applied Physics* 77.12 (1995), pp. 6695–6702. DOI: 10.1063/1.359083.
- [73] Chun, M. C., Park, S., Park, S., Park, G., Kim, M. J., Cho, Y., and Kang, B. S. “Effect of wake-up on the polarization switching dynamics of Si-doped HfO<sub>2</sub> thin films with

- imprint". In: *Journal of Alloys and Compounds* 823 (2020), p. 153777. DOI: 10.1016/j.jallcom.2020.153777.
- [74] Dutta, S., Buragohain, P., Glinsek, S., Richter, C., Aramberri, H., Lu, H., Schroeder, U., Defay, E., Gruverman, A., and Íñiguez, J. "Piezoelectricity in hafnia". In: *Nature Communications* 12.1 (Dec. 2021). ISSN: 2041-1723. DOI: 10.1038/s41467-021-27480-5.
- [75] Liu, J., Liu, S., Liu, L. H., Hanrahan, B., and Pantelides, S. T. "Origin of pyroelectricity in ferroelectric HfO<sub>2</sub>". In: *Physical Review Applied* 12 (2019), p. 034032. DOI: 10.1103/PhysRevApplied.12.034032.
- [76] Liu, J., Liu, S., Yang, J.-Y., and Liu, L. "Electric auxetic effect in piezoelectrics". In: *Physical Review Letters* 125 (2020), p. 197601. DOI: 10.1103/PhysRevLett.125.197601.
- [77] Chouprik, A., Kirtaev, R., Korostylev, E., Mikheev, V., Spiridonov, M., and Negrov, D. "Nanoscale doping and its impact on the ferroelectric and piezoelectric properties of Hf<sub>0.5</sub>Zr<sub>0.5</sub>O<sub>2</sub>". In: *Nanomaterials* 12.9 (2022), p. 1483. DOI: 10.3390/nano12091483.
- [78] Lu, H., Kim, D.-J., Aramberri, H., Holzer, M., Buragohain, P., Dutta, S., Schroeder, U., Deshpande, V., Íñiguez, J., Gruverman, A., and Dubourdieu, C. "Electrically induced cancellation and inversion of piezoelectricity in ferroelectric Hf<sub>0.5</sub>Zr<sub>0.5</sub>O<sub>2</sub>". In: *Nature Communications* 15.1 (Jan. 2024). ISSN: 2041-1723. DOI: 10.1038/s41467-024-44690-9.
- [79] Müller, J., Böschke, T. S., Schröder, U., Mueller, S., Bräuhaus, D., Böttger, U., Frey, L., and Mikolajick, T. "Ferroelectricity in simple binary ZrO<sub>2</sub> and HfO<sub>2</sub>". In: *Nano Letters* 12.8 (2012), pp. 4318–4323. DOI: 10.1021/nl302049k.
- [80] Trentzsch, M., Flachowsky, S., Richter, R., Paul, J., Reimer, B., Utess, D., Jansen, S., Mulaosmanovic, H., Müller, S., Slesazeck, S., Ocker, J., Noack, M., Müller, J., Polakowski, P., Schreiter, J., Beyer, S., Mikolajick, T., and Rice, B. "A 28nm HKMG super low power embedded NVM technology based on ferroelectric FETs". In: *IEEE International Electron Devices Meeting (IEDM)* (2016), pp. 11.5.1–11.5.4.

- [81] Yurchuk, E., Müller, J., Müller, S., Paul, J., Pesic, M., Bentum, R. van, Schroeder, U., and Mikolajick, T. “Charge-trapping phenomena in HfO<sub>2</sub>-based FeFET-type nonvolatile memories”. In: *IEEE Transactions on Electron Devices* 63.9 (2016), pp. 3501–3507. DOI: 10.1109/TED.2016.2588439.
- [82] Mulaosmanovic, H., Ocker, J., Mueller, S., Pesic, M., Flachowsky, S., Müller, J., Polakowski, P., Jansen, S., Kolodinski, S., Richter, C., Piontek, S., Schenk, T., Kersch, A., Künneth, C., Bentum, R. van, Schroeder, U., and Mikolajick, T. “Evidence of single domain switching in hafnium oxide based FeFETs: Enabler for multi-level FeFET memory cells”. In: *IEEE International Electron Devices Meeting (IEDM)* (2015), pp. 26.8.1–26.8.3.
- [83] Park, M. H., Kim, H. J., Kim, Y. J., Moon, T., Kim, K. D., and Hwang, C. S. “Thin Hf<sub>x</sub>Zr<sub>1-x</sub>O<sub>2</sub> films: A new lead-free system for electrostatic supercapacitors with large energy storage density and robust thermal stability”. In: *Advanced Energy Materials* 4.16 (2014), p. 1400610. DOI: 10.1002/aenm.201400610.
- [84] Mart, C., Kampfe, T., Zybell, S., and Weinreich, W. “Layer thickness scaling and wake-up effect of pyroelectric response in Si-doped HfO<sub>2</sub>”. In: *Applied Physics Letters* 112.5 (2018), p. 052905. DOI: 10.1063/1.5017200.
- [85] Schenk, T., Godard, N., Mahjoub, A., Girod, S., Matavz, A., Bobnar, V., Defay, E., and Glinsek, S. “Toward Thick Piezoelectric HfO<sub>2</sub> -Based Films”. In: *physica status solidi (RRL) – Rapid Research Letters* 14.3 (Dec. 2019), p. 1900626. DOI: 10.1002/pssr.201900626.
- [86] Hoffmann, M., Fengler, F. P. G., Herzig, M., Mittmann, T., Schroeder, U., Negrea, R., Slesazeck, S., and Mikolajick, T. “Unveiling the double-well energy landscape in a ferroelectric layer”. In: *Nature* 565 (2019), pp. 464–467. DOI: 10.1038/s41586-018-0854-z.
- [87] Swerts, J., Peys, N., Nyns, L., Delabie, A., Franquet, A., Maes, J. W., Van Elshocht, S., and De Gendt, S. “Impact of precursor chemistry and process conditions on the scalability of ALD HfO<sub>2</sub> gate dielectrics”. In: *Journal of The Electrochemical Society* 157.1 (2010), G26. DOI: 10.1149/1.3258664.

- [88] Park, J., Cho, M., Kim, S. K., Park, T. J., Lee, S. W., Hong, S. H., and Hwang, C. S. "Influence of the oxygen concentration on atomic-layer-deposited HfO<sub>2</sub> thin films". In: *Applied Physics Letters* 86 (2005), p. 112907. DOI: 10.1063/1.1885167.
- [89] Materano, M., Mittmann, T., Lomenzo, P. D., Zhou, C., Jones, J. L., Falkowski, M., Kersch, A., Mikolajick, T., and Schroeder, U. "Influence of oxygen content on the structure and reliability of Hf<sub>0.5</sub>Zr<sub>0.5</sub>O<sub>2</sub> thin films". In: *ACS Applied Electronic Materials* 2.11 (2020), pp. 3618–3626. DOI: 10.1021/acsaem.0c00680.
- [90] Ramesh, R., Salahuddin, S., Datta, S., Diaz, C. H., Nikonov, D. E., Young, I. A., Ham, D., Chang, M.-F., Khwa, W.-S., Lele, A. S., Binek, C., Huang, Y.-L., Sun, Y.-C., Chu, Y.-H., Prasad, B., Hoffmann, M., Hu, J.-M., Yao, Z. (, Bellaiche, L., Wu, P., Cai, J., Appenzeller, J., Datta, S., Camsari, K. Y., Kwon, J., Incorvia, J. A. C., Asselberghs, I., Ciubotaru, F., Couet, S., Adelman, C., Zheng, Y., Lindenberg, A. M., Evans, P. G., Ercius, P., and Radu, I. P. "Roadmap on low-power electronics". In: *APL Materials* 12.9 (Sept. 2024). ISSN: 2166-532X. DOI: 10.1063/5.0184774.
- [91] Zhao, D., Chen, Z., and Liao, X. "Microstructural evolution and ferroelectricity in HfO<sub>2</sub> films". In: *Microstructures* (2022). ISSN: 2770-2995. DOI: 10.20517/microstructures.2021.11.
- [92] Mittmann, T., Materano, M., Lomenzo, P. D., Park, M. H., Stolichnov, I., Cavalieri, M., Zhou, C., Chung, C.-C., Jones, J. L., Szyjka, T., Müller, M., Kersch, A., Mikolajick, T., and Schroeder, U. "Origin of Ferroelectric Phase in Undoped HfO<sub>2</sub> Films Deposited by Sputtering". In: *Advanced Materials Interfaces* 6.11 (Apr. 2019). ISSN: 2196-7350. DOI: 10.1002/admi.201900042.
- [93] Kim, M. G. and Ohmi, S.-i. "Ferroelectric properties of undoped HfO<sub>2</sub> directly deposited on Si substrates by RF magnetron sputtering". In: *Japanese Journal of Applied Physics* 57.11S (Sept. 2018), 11UF09. ISSN: 1347-4065. DOI: 10.7567/jjap.57.11uf09.
- [94] Lee, Y. H., Kim, H. J., Moon, T., Kim, K. D., Hyun, S. D., Park, H. W., Lee, Y. B., Park, M. H., and Hwang, C. S. "Preparation and characterization of ferroelectric Hf<sub>0.5</sub>Zr<sub>0.5</sub>O<sub>2</sub> thin films grown by reactive sputtering". In: *Nanotechnology* 28.30 (July 2017), p. 305703. ISSN: 1361-6528. DOI: 10.1088/1361-6528/aa7624.

- [95] Bouaziz, J., Rojo Romeo, P., Baboux, N., and Vilquin, B. “Characterization of ferroelectric hafnium/zirconium oxide solid solutions deposited by reactive magnetron sputtering”. In: *Journal of Vacuum Science amp; Technology B, Nanotechnology and Microelectronics: Materials, Processing, Measurement, and Phenomena* 37.2 (Feb. 2019). ISSN: 2166-2754. DOI: 10.1116/1.5060643.
- [96] Shimizu, T., Katayama, K., Kiguchi, T., Akama, A., Konno, T. J., and Funakubo, H. “Growth of epitaxial orthorhombic YO<sub>1.5</sub>-substituted HfO<sub>2</sub> thin film”. In: *Applied Physics Letters* 107.3 (July 2015). ISSN: 1077-3118. DOI: 10.1063/1.4927450.
- [97] Willmott, P. R. and Huber, J. R. “Pulsed laser vaporization and deposition”. In: *Reviews of Modern Physics* 72.1 (Jan. 2000), pp. 315–328. ISSN: 1539-0756. DOI: 10.1103/revmodphys.72.315.
- [98] Shimizu, T., Katayama, K., Kiguchi, T., Akama, A., Konno, T. J., and Funakubo, H. “The demonstration of significant ferroelectricity in epitaxial Y-doped HfO<sub>2</sub> film”. In: *Scientific Reports* 6 (2016), p. 32931. DOI: 10.1038/srep32931.
- [99] Lyu, J., Fina, I., Fontcuberta, J., and Sánchez, F. “Epitaxial integration on Si(001) of ferroelectric Hf<sub>0.5</sub>Zr<sub>0.5</sub>O<sub>2</sub> capacitors with high retention and endurance”. In: *ACS Applied Materials & Interfaces* 11 (2019), pp. 6224–6229. DOI: 10.1021/acsaami.8b18762.
- [100] Zhang, Z., Hsu, S. L., Stoica, V. A., and al., et. “Epitaxial ferroelectric Hf<sub>0.5</sub>Zr<sub>0.5</sub>O<sub>2</sub> with metallic pyrochlore oxide electrodes”. In: *Advanced Materials* 33.10 (2021), e2006089. DOI: 10.1002/adma.202006089.
- [101] Wei, Y., Nukala, P., Salverda, M., Matzen, S., Zhao, H. J., Momand, J., Everhardt, A. S., Agnus, G., Blake, G. R., Lecœur, P., Kooi, B. J., Íñiguez, J., Dkhil, B., and Noheda, B. “A rhombohedral ferroelectric phase in epitaxially strained Hf<sub>0.5</sub>Zr<sub>0.5</sub>O<sub>2</sub> thin films”. In: *Nature Materials* 17.12 (2018), pp. 1095–1100. DOI: 10.1038/s41563-018-0196-0.
- [102] Estandía, S., Dix, N., Gazquez, J., Fina, I., Lyu, J., Chisholm, M. F., Fontcuberta, J., and Sánchez, F. “Engineering Ferroelectric Hf<sub>0.5</sub>Zr<sub>0.5</sub>O<sub>2</sub> Thin Films by Epitaxial Stress”. In: *ACS Applied Electronic Materials* 1.8 (July 2019), pp. 1449–1457. ISSN: 2637-6113. DOI: 10.1021/acsaelm.9b00256.

- [103] Zhang, Y., Yang, Q., Tao, L., Tsymbal, E. Y., and Alexandrov, V. “Effects of Strain and Film Thickness on the Stability of the Rhombohedral Phase of  $\text{HfO}_2$ ”. In: *Physical Review Applied* 14.1 (July 2020), p. 014068. DOI: 10.1103/PhysRevApplied.14.014068.
- [104] Katayama, K., Shimizu, T., Sakata, O., Shiraishi, T., Nakamura, S., Kiguchi, T., Akama, A., Konno, T. J., Uchida, H., and Funakubo, H. “Growth of (111)-oriented epitaxial and textured ferroelectric Y-doped  $\text{HfO}_2$  films for downscaled devices”. In: *Applied Physics Letters* 109.11 (2016), p. 112901.
- [105] Mimura, T., Shimizu, T., and Funakubo, H. “Ferroelectricity in  $\text{YO}_{1.5}$ - $\text{HfO}_2$  films around 1  $\mu\text{m}$  in thickness”. In: *Applied Physics Letters* 115.3 (July 2019). ISSN: 1077-3118. DOI: 10.1063/1.5097880.
- [106] Bassiri-Gharb, N., Bastani, Y., and Bernal, A. “Chemical solution growth of ferroelectric oxide thin films and nanostructures”. In: *Chem. Soc. Rev.* 43.7 (2014), pp. 2125–2140. ISSN: 1460-4744. DOI: 10.1039/c3cs60250h.
- [107] Chen, H., Chen, Y., Tang, L., Luo, H., Zhou, K., Yuan, X., and Zhang, D. “Obvious ferroelectricity in undoped  $\text{HfO}_2$  films by chemical solution deposition”. In: *Journal of Materials Chemistry C* 8.8 (2020), pp. 2820–2826. DOI: 10.1039/c9tc06400a.
- [108] Schenk, T., Bencan, A., Drazic, G., Condurache, O., Valle, N., Adib, B. E., Aruchamy, N., Granzow, T., Defay, E., and Glinsek, S. “Enhancement of ferroelectricity and orientation in solution-derived hafnia thin films through heterogeneous grain nucleation”. In: *Applied Physics Letters* 118.16 (Apr. 2021), p. 162902. DOI: 10.1063/5.0045966.
- [109] Starschich, S., Griesche, D., Schneller, T., and Böttger, U. “Chemical Solution Deposition of Ferroelectric Hafnium Oxide for Future Lead Free Ferroelectric Devices”. In: *ECS Journal of Solid State Science and Technology* 4.12 (2015), P419–P423. ISSN: 2162-8777. DOI: 10.1149/2.0061512jss.
- [110] Samanta, S., Anoop, G., Joh, H., Seol, W., Park, S. M., Unithrattil, S., Lee, J. Y., Kim, T. Y., Kim, H., Yeom, J., Hong, S., and Jo, J. Y. “Multi-Step Chemical Solution Deposition-Annealing Process Toward Wake-Up Free Ferroelectricity in  $\text{Y:HfO}_2$  Films”. In: *Advanced Materials Interfaces* 8.18 (Aug. 2021), p. 2100907. DOI: 10.1002/admi.202100907.

- [111] Schwartz, R. W., Schneller, T., and Waser, R. "Chemical solution deposition of electronic oxide films". In: *Comptes Rendus. Chimie* 7.5 (May 2004), pp. 433–461. ISSN: 1878-1543. DOI: 10.1016/j.crci.2004.01.007.
- [112] Badillo, M., Taleb, S., Mokabber, T., Rieck, J., Castanedo, R., Torres, G., Noheda, B., and Acuautila, M. "Low-toxicity chemical solution deposition of ferroelectric Ca:HfO<sub>2</sub>". In: *Journal of Materials Chemistry C* 11.3 (2023), pp. 1119–1133. ISSN: 2050-7534. DOI: 10.1039/d2tc04182k.
- [113] Hasenkox, U., Hoffmann, S., and Waser, R. "Influence of Precursor Chemistry on the Formation of MTiO<sub>3</sub> (M = Ba, Sr) Ceramic Thin Films". In: *Journal of Sol-Gel Science and Technology* 12.2 (Oct. 1998), pp. 67–79. ISSN: 1573-4846. DOI: 10.1023/a:1026480027046.
- [114] Howard, S. M. *Ellingham Diagrams: Standard Gibb's Energies of Formation*. Internet Resource for MET 320 - Metallurgical Thermodynamics. Data from Thomas B. Reed, *Free Energy of Formation of Binary Compounds*, MIT Press, Cambridge, MA, 1971 and D. R. Stull and H. Prophet, *JANAF Thermochemical Tables*, NSRDS-NBS 37, U.S. Dept of Commerce, National Bureau of Standards, 1971. 2006.
- [115] Mohit, Murakami, T., Haga, K.-i., and Tokumitsu, E. "Impact of annealing environment on electrical properties of yttrium-doped hafnium zirconium dioxide thin films prepared by the solution process". In: *Japanese Journal of Applied Physics* 59.SP (July 2020), SPPB03. DOI: 10.35848/1347-4065/aba50b.
- [116] Wani, W. A., Lam, N. K., Holsgrove, K. M., Bejger, G., Alem, T., Burns, K., McDonnell, S. J., Rost, C. M., Kumar, A., Ihlefeld, J. F., and Rodriguez, B. J. "Environmental Control of Ferroelectricity in Hafnia Films". In: *Advanced Materials* (Aug. 2025). ISSN: 1521-4095. DOI: 10.1002/adma.202503852.
- [117] Yano, M., Inoue, T., Ota, H., Kawamoto, T., Hirofuji, Y., Koyama, M., and Koike, K. "Characteristics of the Hf<sub>0.5</sub>Zr<sub>0.5</sub>O<sub>2</sub> Thin Films Grown by a Chemical Solution Deposition Method". In: *Journal of the Society of Materials Science, Japan* 68.10 (Oct. 2019). In Japanese, pp. 745–750.

- [118] Weeks, S. L., Pal, A., Narasimhan, V. K., Littau, K. A., and Chiang, T. “Engineering of Ferroelectric HfO<sub>2</sub>–ZrO<sub>2</sub> Nanolaminates”. In: *ACS Applied Materials & Interfaces* 9.15 (Apr. 2017), pp. 13440–13447. ISSN: 1944-8252. DOI: 10.1021/acsami.7b00776.
- [119] Kim, B. S., Hyun, S. D., Moon, T., Do Kim, K., Lee, Y. H., Park, H. W., Lee, Y. B., Roh, J., Kim, B. Y., Kim, H. H., Park, M. H., and Hwang, C. S. “A Comparative Study on the Ferroelectric Performances in Atomic Layer Deposited Hf<sub>0.5</sub>Zr<sub>0.5</sub>O<sub>2</sub> Thin Films Using Tetrakis(ethylmethylamino) and Tetrakis(dimethylamino) Precursors”. In: *Nanoscale Research Letters* 15.1 (Apr. 2020). ISSN: 1556-276X. DOI: 10.1186/s11671-020-03301-4.
- [120] Yoneda, S., Hosokura, T., Usui, T., Kimura, M., Ando, A., and Shiratsuyu, K. “High dielectric permittivity of HfO<sub>2</sub>-based films with (La, Bi, Nb) substitution”. In: *Japanese Journal of Applied Physics* 57.11S (Aug. 2018), 11UF03. ISSN: 1347-4065. DOI: 10.7567/jjap.57.11uf03.
- [121] Nakayama, S., Funakubo, H., and Uchida, H. “Crystallization behavior and ferroelectric property of HfO<sub>2</sub>–ZrO<sub>2</sub> films fabricated by chemical solution deposition”. In: *Japanese Journal of Applied Physics* 57.11S (Sept. 2018), 11UF06. ISSN: 1347-4065. DOI: 10.7567/jjap.57.11uf06.
- [122] Wei, A. Q., Chen, C., Tang, L., Zhou, K. C., and Zhang, D. “Regulating crystal structure and ferroelectricity in Sr-doped HfO<sub>2</sub> thin films”. In: *Journal of Alloys and Compounds* 731 (2018), pp. 546–553. DOI: 10.1016/j.jallcom.2018.01.063.
- [123] Tang, L., Chen, C., Wei, A., Li, K., Zhang, D., and Zhou, K. “Regulating crystal structure and ferroelectricity in Sr-doped HfO<sub>2</sub> thin films fabricated by metallo-organic decomposition”. In: *Ceramics International* 45 (2019), p. 3140. DOI: 10.1016/j.ceramint.2018.10.214.
- [124] Mimura, T., Takahashi, Y., Shiraishi, T., Kodera, M., Shimura, R., Ishihama, K., Okamoto, K., Moriwake, H., Taguchi, A., Shimizu, T., Fujii, Y., Koreeda, A., and Funakubo, H. “Phase Identification of 850 nm Thick 7%YO<sub>1.5</sub>–93%HfO<sub>2</sub> Films by Surface and Cross-Sectional Raman Spectroscopies”. In: *ACS Applied Electronic Materials* 6.4 (2024), pp. 2500–2506. ISSN: 2637-6113. DOI: 10.1021/acsaelm.4c00134.

- [125] Fan, S., Singh, S., Xu, X., Park, K., Qi, Y., Cheong, S. W., Vanderbilt, D., Rabe, K. M., and Musfeldt, J. L. "Vibrational fingerprints of ferroelectric HfO<sub>2</sub>". In: *npj Quantum Materials* 7.1 (Mar. 2022). ISSN: 2397-4648. DOI: 10.1038/s41535-022-00436-8.
- [126] Materano, M., Reinig, P., Kersch, A., Popov, M., Deluca, M., Mikolajick, T., Boettger, U., and Schroeder, U. "Raman Spectroscopy as a Key Method to Distinguish the Ferroelectric Orthorhombic Phase in Thin ZrO<sub>2</sub>-Based Films". In: *physica status solidi (RRL) – Rapid Research Letters* 16.4 (2022). ISSN: 1862-6270. DOI: 10.1002/pssr.202100589.
- [127] Luo, C.-Q., Kang, C.-Y., Song, Y.-L., Wang, W.-P., and Zhang, W.-F. "Large remanent polarization in Ta-doped HfO<sub>2</sub> thin films by reactive sputtering". In: *Applied Physics Letters* 119.4 (2021). ISSN: 1077-3118. DOI: 10.1063/5.0055068.
- [128] Raeliarijaona, A. and Cohen, R. E. "First-principles calculations of Raman and infrared spectroscopy for phase identification and strain calibration of hafnia". In: *Applied Physics Letters* 120.24 (2022). ISSN: 1077-3118. DOI: 10.1063/5.0092247.
- [129] Pečnik, T., Benčan, A., Glinšek, S., and Malič, B. "Tailoring the microstructure and dielectric properties of Ba<sub>0.5</sub>Sr<sub>0.5</sub>TiO<sub>3</sub> thin films by solution-based processing in the frame of the Microstructural Zone Model". In: *Journal of Alloys and Compounds* 743 (Apr. 2018), pp. 812–818. ISSN: 0925-8388. DOI: 10.1016/j.jallcom.2018.01.333.
- [130] Hoffmann, S., Hasenkox, U., Waser, R., et al. "Chemical Solution Deposited BaTiO<sub>3</sub> and SrTiO<sub>3</sub> Thin Films With Columnar Microstructure". In: *MRS Online Proceedings Library* 474 (Dec. 1997), pp. 9–14. DOI: 10.1557/PROC-474-9.
- [131] Schuler, T., Krajewski, T., Grobelsek, I., and Aegerter, M. A. "A microstructural zone model for the morphology of sol-gel coatings". In: *Journal of Sol-Gel Science and Technology* 31 (2004), pp. 235–239.
- [132] Lee, J. Y., Anoop, G., Lee, H. J., Kwak, J. H., and Jo, J. Y. "Structural properties of solution-processed Hf<sub>0.5</sub>Zr<sub>0.5</sub>O<sub>2</sub> thin films". In: *Current Applied Physics* 17.5 (May 2017), pp. 704–708. ISSN: 1567-1739. DOI: 10.1016/j.cap.2016.11.029.

- [133] Woods, K. N., Chiang, T.-H., Plassmeyer, P. N., Kast, M. G., Lygo, A. C., Grealish, A. K., Boettcher, S. W., and Page, C. J. “High-K Lanthanum Zirconium Oxide Thin Film Dielectrics from Aqueous Solution Precursors”. In: *ACS Applied Materials & Interfaces* 9.12 (Mar. 2017), pp. 10897–10903. ISSN: 1944-8252. DOI: 10.1021/acsami.7b00915.
- [134] Jiang, K., Anderson, J. T., Hoshino, K., Li, D., Wager, J. F., and Keszler, D. A. “Low-Energy Path to Dense HfO<sub>2</sub> Thin Films with Aqueous Precursor”. In: *Chemistry of Materials* 23.4 (Jan. 2011), pp. 945–952. ISSN: 1520-5002. DOI: 10.1021/cm102082j.
- [135] Matavž, A., Bradeško, A., Rojac, T., Malič, B., and Bobnar, V. “Self-assembled porous ferroelectric thin films with a greatly enhanced piezoelectric response”. In: *Applied Materials Today* 16 (Sept. 2019), pp. 83–89. ISSN: 2352-9407. DOI: 10.1016/j.apmt.2019.04.008.
- [136] Scherrer, P. “Title of the Article”. In: *Nachr. Ges. Wiss. Göttingen, Math.-Phys. Kl.* 98 (1918).
- [137] Müller, J., Polakowski, P., Mueller, S., and Mikolajick, T. “Ferroelectric Hafnium Oxide Based Materials and Devices: Assessment of Current Status and Future Prospects”. In: *ECS Journal of Solid State Science and Technology* 4.5 (2015), N30–N35. ISSN: 2162-8777. DOI: 10.1149/2.0081505jss.
- [138] Kim, S. J., Mohan, J., Summerfelt, S. R., and Kim, J. “Ferroelectric Hf<sub>0.5</sub>Zr<sub>0.5</sub>O<sub>2</sub> Thin Films: A Review of Recent Advances”. In: *JOM* 71.1 (Sept. 2018), pp. 246–255. ISSN: 1543-1851. DOI: 10.1007/s11837-018-3140-5.
- [139] Reyes-Lillo, S. E., Garrity, K. F., and Rabe, K. M. “Antiferroelectricity in Thin-Film ZrO<sub>2</sub> from First Principles”. In: *Physical Review B* 90.14 (Oct. 2014). ISSN: 1550-235X. DOI: 10.1103/physrevb.90.140103.
- [140] Lin, B.-T., Lu, Y.-W., Shieh, J., and Chen, M.-J. “Induction of ferroelectricity in nanoscale ZrO<sub>2</sub> thin films on Pt electrode without post-annealing”. In: *Journal of the European Ceramic Society* 37.3 (Mar. 2017), pp. 1135–1139. ISSN: 0955-2219. DOI: 10.1016/j.jeurceramsoc.2016.10.028.

- [141] Fan, Z., Deng, J., Wang, J., Liu, Z., Yang, P., Xiao, J., Yan, X., Dong, Z., Wang, J., and Chen, J. "Ferroelectricity emerging in strained (111)-textured ZrO<sub>2</sub> thin films". In: *Applied Physics Letters* 108.1 (Jan. 2016). ISSN: 1077-3118. DOI: 10.1063/1.4939660.
- [142] Park, J. Y., Lee, D. H., Yang, K., Kim, S. H., Yu, G. T., Park, G. H., Lee, E. B., Kim, K. H., and Park, M. H. "Engineering Strategies in Emerging Fluorite-Structured Ferroelectrics". In: *ACS Applied Electronic Materials* 4.4 (Nov. 2021), pp. 1369–1380. ISSN: 2637-6113. DOI: 10.1021/acsaelm.1c00792.
- [143] Ahn, C. H., Rabe, K. M., and Triscone, J.-M. "Ferroelectricity at the Nanoscale: Local Polarization in Oxide Thin Films and Heterostructures". In: *Science* 303.5657 (Jan. 2004), pp. 488–491. ISSN: 1095-9203. DOI: 10.1126/science.1092508.
- [144] Bousquet, E., Dawber, M., Stucki, N., Lichtensteiger, C., Hermet, P., Gariglio, S., Triscone, J.-M., and Ghosez, P. "Improper ferroelectricity in perovskite oxide artificial superlattices". In: *Nature* 452.7188 (Apr. 2008), pp. 732–736. ISSN: 1476-4687. DOI: 10.1038/nature06817.
- [145] Kim, J., Kim, Y., Kim, Y. S., Lee, J., Kim, L., and Jung, D. "Large nonlinear dielectric properties of artificial BaTiO<sub>3</sub>/SrTiO<sub>3</sub> superlattices". In: *Applied Physics Letters* 80.19 (May 2002), pp. 3581–3583. ISSN: 1077-3118. DOI: 10.1063/1.1477934.
- [146] Tsurumi, T., Harigai, T., Tanaka, D., Nam, S.-M., Kakemoto, H., Wada, S., and Saito, K. "Artificial ferroelectricity in perovskite superlattices". In: *Applied Physics Letters* 85.21 (Nov. 2004), pp. 5016–5018. ISSN: 1077-3118. DOI: 10.1063/1.1825057.
- [147] Dawber, M., Lichtensteiger, C., Cantoni, M., Veithen, M., Ghosez, P., Johnston, K., Rabe, K. M., and Triscone, J.-M. "Unusual Behavior of the Ferroelectric Polarization in PbTiO<sub>3</sub>/SrTiO<sub>3</sub> Superlattices". In: *Physical Review Letters* 95.17 (Oct. 2005). ISSN: 1079-7114. DOI: 10.1103/physrevlett.95.177601.
- [148] Park, M. H., Kim, Y. J., Kim, H. J., Moon, T., Kim, K. D., Lee, Y. H., and Hwang, C. S. "The Ferroelectric Properties of HfO<sub>2</sub>/ZrO<sub>2</sub> Nanolaminate Systems". In: *ISAF-ISIF-PFM-2015*. Conference held May 24–27, 2015. Singapore, May 24, 2015.

- [149] Li, J., Deng, S., Ma, L., Si, Y., Zhou, C., Wang, K., Huang, S., Yang, J., Tang, Y., Ku, Y.-C., Kuo, C.-Y., Li, Y., Das, S., Liu, S., and Chen, Z. “Enhancing ferroelectric stability: wide-range of adaptive control in epitaxial HfO<sub>2</sub>/ZrO<sub>2</sub> superlattices”. In: *Nature Communications* 16.1 (July 2025). ISSN: 2041-1723. DOI: 10.1038/s41467-025-61758-2.
- [150] Gent, J. van, Mukherjee, B., Veer, E. van der, Kiens, E. M., Koster, G. G., Kooi, B. J., Íñiguez-González, J., and Noheda, B. *Guidelines for the optimization of hafnia-based ferroelectrics through superlattice engineering*. 2025. DOI: 10.48550/ARXIV.2507.05174.
- [151] Lehninger, D., Prabhu, A., Sünbül, A., Ali, T., Schöne, F., Kämpfe, T., Biedermann, K., Roy, L., Seidel, K., Lederer, M., and Eng, L. M. “Ferroelectric [HfO<sub>2</sub>/ZrO<sub>2</sub>] Superlattices with Enhanced Polarization, Tailored Coercive Field, and Improved High Temperature Reliability”. In: *Advanced Physics Research* 2.9 (Feb. 2023). ISSN: 2751-1200. DOI: 10.1002/apxr.202200108.
- [152] Cüppers, F., Hirai, K., and Funakubo, H. “On the switching dynamics of epitaxial ferroelectric CeO<sub>2</sub>-HfO<sub>2</sub> thin film capacitors”. In: *Nano Convergence* 9 (2022), p. 56. DOI: 10.1186/s40580-022-00344-4.
- [153] Lübben, J., Berg, F., and Böttger, U. “Investigation of the large-signal electromechanical behavior of ferroelectric HfO<sub>2</sub>-CeO<sub>2</sub> thin films prepared by chemical solution deposition”. In: *Journal of Applied Physics* 135.9 (2024). Published 7 March 2024, p. 094103. DOI: 10.1063/5.0188897.
- [154] Shiraishi, T., Konno, T. J., and Funakubo, H. “Ferroelectric and piezoelectric properties of 100 nm-thick CeO<sub>2</sub>-HfO<sub>2</sub> epitaxial films”. In: *Applied Physics Letters* 120.13 (2022). Published 28 March 2022, p. 132901. DOI: 10.1063/5.0088491.
- [155] Hirai, K., Shiraishi, T., Yamaoka, W., Tsurumaru, R., Inoue, Y., and Funakubo, H. “Composition dependence of ferroelectric properties in (111)-oriented epitaxial HfO<sub>2</sub>-CeO<sub>2</sub> solid solution films”. In: *Japanese Journal of Applied Physics* 61.SN (2022). Published 2 August 2022, SN1019. DOI: 10.35848/1347-4065/ac80e9.

- [156] Zheng, S., Zhao, Z., Liu, Z., Zeng, B., Yin, L., Peng, Q., Liao, M., and Zhou, Y. "Improvement of remanent polarization of  $\text{CeO}_2\text{-HfO}_2$  solid solution thin films on Si substrates by chemical solution deposition". In: *Applied Physics Letters* 117.21 (Nov. 2020). ISSN: 1077-3118. DOI: 10.1063/5.0028200.
- [157] Dutta, S., Aramberri, H., Schenk, T., and Íñiguez, J. "Effect of Dopant Ordering on the Stability of Ferroelectric Hafnia". In: *Physica Status Solidi (RRL) – Rapid Research Letters* 14.6 (2020), p. 2000047. DOI: 10.1002/pssr.202000047.
- [158] Kumar, P. and Lee, J. "Hybrid improper ferroelectricity in a Si-compatible  $\text{CeO}_2/\text{HfO}_2$  artificial superlattice". In: *npj Computational Materials* 10 (2024), p. 294. DOI: 10.1038/s41524-024-01487-0.
- [159] Zhang, Y., Zheng, X., Jiao, F., and Hu, H. "The effect of strain and dead layer on the nonlinear electric-mechanical behavior of ferroelectric thin films". In: *Computational Materials Science* 77 (Sept. 2013), pp. 377–383. ISSN: 0927-0256. DOI: 10.1016/j.commatsci.2013.04.062.
- [160] Al-Shareef, H. N., Dimos, D., Warren, W. L., and Tuttle, B. A. "A model for optical and electrical polarization fatigue in  $\text{SrBi}_2\text{Ta}_2\text{O}_9$ , and  $\text{Pb}(\text{Zr,Ti})\text{O}_3$ ". In: *Integrated Ferroelectrics* 15.1-4 (1997), pp. 53–67. DOI: 10.1080/10584589708015696.
- [161] International Centre for Diffraction Data (ICDD). *PDF-4+ v4.23 Database*. PDF-4+ Database, ICDD. Version 4.23. 2023.
- [162] Müller, J., Böske, T. S., Schröder, U., Mueller, S., Bräuhäus, D., Böttger, U., Frey, L., and Mikolajick, T. "Ferroelectricity in Simple Binary  $\text{ZrO}_2$  and  $\text{HfO}_2$ ". In: *Nano Letters* 12.8 (July 2012), pp. 4318–4323. ISSN: 1530-6992. DOI: 10.1021/nl302049k.
- [163] Lu, Y., Shieh, J., and Tsai, F. "Induction of ferroelectricity in nanoscale  $\text{ZrO}_2/\text{HfO}_2$  bilayer thin films on Pt/Ti/SiO<sub>2</sub>/Si substrates". In: *Acta Materialia* 115 (Aug. 2016), pp. 68–75. ISSN: 1359-6454. DOI: 10.1016/j.actamat.2016.05.029.
- [164] Max, B., Pesic, M., Slesazek, S., and Mikolajick, T. "Interplay between ferroelectric and resistive switching in doped crystalline  $\text{HfO}_2$ ". In: *Journal of Applied Physics* 123 (2018), p. 134102. DOI: 10.1063/1.5015985.

- [165] Xu, Z., Zhu, X., Zhao, G.-D., Zhang, D. W., and Yu, S. "Oxygen vacancies stabilized 180° charged domain walls in ferroelectric hafnium oxide". In: *Applied Physics Letters* 124 (2024), p. 012902. DOI: 10.1063/5.0179879.
- [166] Lee, J., Yang, K., Kwon, J. Y., Kim, J. E., Han, D. I., Lee, D. H., Yoon, J. H., and Park, M. H. "Role of oxygen vacancies in ferroelectric or resistive switching hafnium oxide". In: *Nano Convergence* 10 (2023), p. 55. DOI: 10.1186/s40580-023-00403-4.
- [167] Sun, Z., Ma, C., Liu, M., Cui, J., Lu, L., Lu, J., Lou, X., Jin, L., Wang, H., and Jia, C.-L. "Ultrahigh Energy Storage Performance of Lead-Free Oxide Multilayer Film Capacitors via Interface Engineering". In: *Advanced Materials* 29.5 (2017), p. 1604427. DOI: 10.1002/adma.201604427.
- [168] Bao, K., Liao, J., Yan, F., Jia, S., Zeng, B., Yang, Q., Liao, M., and Zhou, Y. "Enhanced Endurance and Imprint Properties in  $\text{Hf}_{0.5}\text{Zr}_{0.5}\text{O}_2$  Ferroelectric Capacitors by Tailoring the Oxygen Vacancy". In: *ACS Applied Electronic Materials* 5.8 (2023), pp. 4615–4623. DOI: 10.1021/acsaelm.3c00433.
- [169] Kang, M., Peng, Y., Wenwu, W., Zhang, Y., Wang, Z., Du, P., Jiang, H., Liu, F., Liu, Y., Hao, Y., and Han, G. "HfO<sub>2</sub>-ZrO<sub>2</sub> Ferroelectric Capacitors with Superlattice Structure: Improving Fatigue Stability, Fatigue Recovery, and Switching Speed". In: *ACS Applied Materials & Interfaces* 16.2 (2024), pp. 2954–2963. DOI: 10.1021/acsaami.3c23711.
- [170] Lakin, K. M. and Wang, J. S. "Acoustic bulk wave composite resonators". In: *Applied Physics Letters* 38 (1981), pp. 125–127.
- [171] Lakin, K. M., Kline, G. R., and McCarron, K. T. "High-Q microwave acoustic resonators and filters". In: *IEEE Transactions on Microwave Theory and Techniques* 41 (1993), pp. 2139–2146.
- [172] Bailey, D., Driscoll, M., Jelen, R., and McAvoy, B. "Frequency stability of high-overtone bulk-acoustic resonators". In: *IEEE Transactions on Ultrasonics, Ferroelectrics, and Frequency Control* 39 (1992), pp. 780–784.
- [173] Machado, D. H. O., Crespo-Poveda, A., Kuznetsov, A. S., Biermann, K., Scalvi, L. V., and Santos, P. V. "Generation and propagation of superhigh-frequency bulk acoustic waves in GaAs". In: *Physical Review Applied* 12 (2019), p. 044013.

- [174] Daugey, T., Friedt, J.-M., Martin, G., and Boudot, R. “A high-overtone bulk acoustic wave resonator-oscillator-based 4.596 GHz frequency source: Application to a coherent population trapping Cs vapor cell atomic clock”. In: *Review of Scientific Instruments* 86 (2015), p. 114703.
- [175] Wu, J., Zhang, S., Zhou, H., Zheng, P., Zhang, L., Li, Z., Wang, Y., You, T., Huang, K., Wu, T., et al. “A new class of high-overtone bulk acoustic resonators using lithium niobate on conductive silicon carbide”. In: *IEEE Electron Device Letters* 42 (2021), pp. 1061–1064.
- [176] Driscoll, M., Jelen, R., and Matthews, N. “Extremely low phase noise UHF oscillators utilizing high-overtone, bulk-acoustic resonators”. In: *IEEE Transactions on Ultrasonics, Ferroelectrics, and Frequency Control* 39 (1992), pp. 774–779.
- [177] Zhou, C., Pang, W., Li, Q., Yu, H., Hu, X., and Zhang, H. “Extracting the electromechanical coupling constant of piezoelectric thin film by the high-tone bulk acoustic resonator technique”. In: *IEEE Transactions on Ultrasonics, Ferroelectrics, and Frequency Control* 59 (2012), pp. 958–962.
- [178] Zhang, H., Pang, W., Yu, H., and Kim, E. S. “High-tone bulk acoustic resonators on sapphire, crystal quartz, fused silica, and silicon substrates”. In: *Journal of Applied Physics* 99 (2006), p. 124911.
- [179] Kongbrailatpam, S. S., Goud, J. P., and Raju, K. J. “The effects of a coated material layer on high-overtone bulk acoustic resonator and its possible applications”. In: *IEEE Transactions on Ultrasonics, Ferroelectrics, and Frequency Control* 68 (2020), pp. 1253–1260.
- [180] Rabus, D., Friedt, J., Ballandras, S., Baron, T., Lebrasseur, É., and Carry, É. “High-overtone bulk-acoustic resonator gravimetric sensitivity: Towards wideband acoustic spectroscopy”. In: *Journal of Applied Physics* 118 (2015), p. 114505.
- [181] Chu, Y., Kharel, P., Renninger, W. H., Burkhart, L. D., Frunzio, L., Rakich, P. T., and Schoelkopf, R. J. “Quantum acoustics with superconducting qubits”. In: *Science* 358 (2017), pp. 199–202.

- [182] Kervinen, M., Rissanen, I., and Sillanpää, M. “Interfacing planar superconducting qubits with high overtone bulk acoustic phonons”. In: *Physical Review B* 97 (2018), p. 205443.
- [183] MacQuarrie, E. R., Gosavi, T. A., Moehle, A. M., Jungwirth, N. R., Bhave, S. A., and Fuchs, G. D. “Coherent control of a nitrogen-vacancy center spin ensemble with a diamond mechanical resonator”. In: *Optica* 2 (2015), pp. 233–238.
- [184] Chen, H., Opondo, N. F., Jiang, B., MacQuarrie, E. R., Daveau, R. S., Bhave, S. A., and Fuchs, G. D. “Engineering electron–phonon coupling of quantum defects to a semiconfocal acoustic resonator”. In: *Nano Letters* 19 (2019), pp. 7021–7027.
- [185] Hashimoto, K. *RF Bulk Acoustic Wave Filters for Communications*. Artech House, 2009.
- [186] Sorokin, B. P., Asafiev, N. O., Kvashnin, G. M., Scherbakov, D. A., Terentiev, S. A., and Blank, V. D. “Toward 40 GHz excitation of diamond-based HBAR”. In: *Applied Physics Letters* 118 (2021), p. 083501.
- [187] Sotnikov, A. V., Sorokin, B. P., Asafiev, N. O., Shcherbakov, D. A., Kvashnin, G. M., Suhak, Y., Fritze, H., Weihnacht, M., and Schmidt, H. “Microwave acoustic attenuation in CTGS single crystals”. In: *IEEE Transactions on Ultrasonics, Ferroelectrics, and Frequency Control* 68 (2021).
- [188] Gokhale, V. J., Downey, B. P., Katzer, D. S., Nepal, N., Lang, A. C., Stroud, R. M., and Meyer, D. J. “Epitaxial bulk acoustic wave resonators as highly coherent multi-phonon sources for quantum acoustodynamics”. In: *Nature Communications* 11 (2020), pp. 1–9.
- [189] Ghatge, M., Walters, G., Nishida, T., and Tabrizian, R. “An ultrathin integrated nanoelectromechanical transducer based on hafnium zirconium oxide”. In: *Nature Electronics* 2 (2019), pp. 506–512. DOI: 10.1038/s41928-019-0305-3.
- [190] Ghatge, M., Walters, G., Nishida, T., and Tabrizian, R. “A 30-nm thick integrated hafnium zirconium oxide nano-electro-mechanical membrane resonator”. In: *Applied Physics Letters* 116.4 (2020), p. 043501. DOI: 10.1063/1.5134856.

- [191] Tharpe, T., Hershkovitz, E., Hakim, F., Kim, H., and Tabrizian, R. “Nanoelectromechanical resonators for gigahertz frequency control based on hafnia–zirconia–alumina superlattices”. In: *Nature Electronics* 6.8 (July 2023), pp. 599–609. ISSN: 2520-1131. DOI: 10.1038/s41928-023-00999-9.
- [192] Baron, T., Lebrasseur, E., Bassignot, F., Martin, G., Ptrini, V., and Ballandras, S. “High-Overtone Bulk Acoustic Resonator”. In: *Modeling and Measurement Methods for Acoustic Waves and for Acoustic Microdevices*. InTech, Aug. 2013. ISBN: 9789535111894. DOI: 10.5772/56175.
- [193] Pijolat, M., Reinhardt, A., et al. “Large  $Q \times f$  product for HBAR using Smart-Cut™ transfer of  $\text{LiNbO}_3$  thin layers onto  $\text{LiNbO}_3$  substrate”. In: *IEEE Ultrasonics Symposium (2008)*. 2008, pp. 201–204.
- [194] Gachon, D., Courjon, E., Martin, G., Gauthier-Manuel, L., Jeannot, J.-C., Daniau, W., and Ballandras, S. “Fabrication of high frequency bulk acoustic wave resonator using thinned single-crystal lithium niobate layers”. In: *Ferroelectrics* 362.1 (2008), pp. 30–40.
- [195] Ma, Z., Becker, A. J., Polakos, P., Huggins, H., Pastalan, J., Wu, H., Watts, K., Wong, Y. H., and Mankiewich, P. “RF Measurement Technique for Characterizing Thin Dielectric Films”. In: *IEEE Transactions on Electron Devices* 45.8 (Aug. 1998), pp. 1811–1816.
- [196] Mulaosmanovic, H., Ocker, J., Müller, S., and Noack, M. “Novel ferroelectric FET based synapse for neuromorphic systems”. In: *Symposium on VLSI Technology*. June 2017, T176–T177. DOI: 10.23919/VLSIT.2017.7998165.
- [197] Li, Z., Zhou, D., Wang, J., Sun, N., and Zhang, W. “Ferroelectricity in hafnium oxide films doped with magnesium by chemical solution deposition”. In: *Journal of Applied Physics* 131.7 (Feb. 2022). ISSN: 1089-7550. DOI: 10.1063/5.0077616.
- [198] Badillo, M., Taleb, S., Carreno Jimenez, B., Mokabber, T., Castanedo Pérez, R., Torres-Delgado, G., Noheda, B., and Acuautla, M. “(001)-Oriented  $\text{Sr:HfO}_2$  Ferroelectric Films Deposited by a Flexible Chemical Solution Method”. In: *ACS Applied Electronic Materials* 6.3 (Mar. 2024), pp. 1809–1820. ISSN: 2637-6113. DOI: 10.1021/acsaelm.3c01725.

- [199] Mukherjee, B., Fedorova, N. S., and Íñiguez-González, J. “Towards structural softness and enhanced electromechanical responses in HfO ferroelectrics”. In: *Physical Review B* 112.6 (Aug. 2025). ISSN: 2469-9969. DOI: 10.1103/ndxt-xyz3.
- [200] Björck, M. and Andersson, G. “GenX: an extensible X-ray reflectivity refinement program utilizing differential evolution”. In: *Journal of Applied Crystallography* 40.6 (2007), pp. 1174–1178. DOI: 10.1107/S0021889807045086.
- [201] Jaffe, B., Cook, W. R., and Jaffe, H. *Piezoelectric Ceramics*. Ed. by Roberts, J. P. and Popper, P. 1st. London: Academic Press INC. (London) LTD, Nov. 1971.
- [202] Schenk, T., Yurchuk, E., Mueller, S., Schroeder, U., Starschich, S., Bottger, U., and Mikolajick, T. “About the deformation of ferroelectric hystereses”. In: *Applied Physics Reviews* 1.4 (2014), p. 041103. DOI: 10.1063/1.4903984.
- [203] Defay, E., ed. *Ferroelectric Dielectrics Integrated on Silicon*. English. London: ISTE, 2011.
- [204] Prume, K., Tiedke, S., and Schmitz-Kempen, T. “Double-beam and four-point: Piezoelectric thin-film characterization for MEMS applications”. In: *Mikroniek* 50 (2010), pp. 31–35.
- [205] Sivaramakrishnan, S., Mardilovich, P., Mason, A., Roelofs, A., Schmitz-Kempen, T., and Tiedke, S. “Electrode size dependence of piezoelectric response of lead zirconate titanate thin films measured by double beam laser interferometry”. In: *Applied Physics Letters* 103.13 (2013), p. 132904. DOI: 10.1063/1.4821948.

